Recherche de nouveaux quarks lourds avec l'expérience ATLAS a u LHC - Mise en oeuvre d'algorithmes d'identification de jets issus de quarks b

N. Bousson

CPPM-T-2012-006

UNIVERSITÉ D'AIX-MARSEILLE
FACULTÉ DES SCIENCES DE LUMINY
163 avenue de Luminy
13288 MARSEILLE Cedex 09

THÈSE DE DOCTORAT

Spécialité : *Physique et Sciences de la Matière*

Mention : *Physique des Particules et Astroparticules*

présentée par

Nicolas BOUSSON

en vue d'obtenir le grade de docteur de l'Université d'Aix-Marseille

Recherche de nouveaux quarks lourds avec l'expérience ATLAS au LHC - Mise en oeuvre d'algorithmes d'identification de jets issus de quarks b

(Search for new heavy *top*-like quarks with the ATLAS experiment at the LHC - Commissioning of high-performance *b*-tagging algorithms)

soutenue le 18 décembre 2012 devant le jury composé de :

Dr.	H. Bachacou	Examinateur
Prof.	J. Boudreau	Examinateur
Dr.	E. Kajfasz	Examinateur
Dr.	A. Rozanov	Co-directeur de thèse
Dr.	Y. Sirois	Rapporteur
Dr.	L. Vacavant	Directeur de thèse
Dr.	C. Weiser	Rapporteur

À mes parents,

Remerciements

Je tiens tout d'abord à remercier le plus chaleureusement Laurent Vacavant, mon encadrant de thèse. Ce travail t'appartient autant qu'à moi. Merci pour ta patience infinie, ton aide inconditionnelle, ton soutien et ton amitié. J'ai eu une chance immense de travailler avec toi durant plus de 3 années.

Mes plus sincères remerciements vont ensuite bien sûr à Alexandre Rozanov, mon co-encadrant. Merci pour ta confiance, ton soutien, ta gentillesse, toutes les opportunités que tu m'as offertes, et tes conseils qui m'ont toujours guidé.

Je remercie aussi sincèrement Mossadek Talby, le directeur du groupe ATLAS du CPPM. Merci de m'avoir accepté au sein du Master 2, et pour tout ton soutien et ta confiance par la suite.

Merci à tous mes collègues de travail du CPPM, en particulier Cécile Lapoire et Nancy Tannoury, pour leur aide immense et leur amitié. Merci Cécile pour tout ce que tu m'as transmis. Tu auras bien sûr reconnu aussi ton travail dans cette thèse. Nancy, ce fut une chance incroyable de faire ce master et cette thèse en même temps que toi. Merci à tous mes autres collègues thésards, sans qui vivre cette thèse n'aurait évidemment pas été la même chose.

Merci à Eric Kajfasz, le directeur du CPPM, et à tout le personnel du laboratoire pour l'atmosphère qu'ils y distillent. Merci pour votre écoute, votre soutien et vos actions qui ont rendu le travail plus efficace, et ces trois années bien plus agréables.

Un immense merci à mes collègues du groupe ATLAS de l'IFAE de Barcelone: Clément Helsens, Aurelio Juste et Antonella Succurro. Votre aide, vos idées et votre énergie furent inestimables pour mener à bien notre analyse physique. Merci pour votre soutien en particulier dans les moments qui étaient les plus difficiles pour moi. Merci également à Lan, Jean-Baptiste et Snezana pour leur aide. Merci grandement, même si indirectement, à Bob Holdom pour ses papiers qui ont inspiré l'ossature de notre analyse. Ses idées furent d'une aide essentielle.

Merci à tous mes collègues de travail du CERN, en particulier ceux des groupes *b*-tagging et Exotics, pour leur gentillesse et leur aide. Merci aux *conveners* pour la saine atmosphère qu'ils parviennent à établir dans un environnement des plus complexes. Merci pour votre soutien, votre confiance, vos conseils et votre reconnaissance. Merci d'avoir su gérer en particulier les moments les plus difficiles, merci pour votre patience.

Un grand merci à mes rapporteurs, Yves Sirois et Christian Weiser, pour le travail que vous avez accompli. Merci à tous les membres du jury, en particulier Henri Bachacou et Joe Boudreau que je n'ai pas encore cités, pour vos corrections, vos conseils et vos encouragements.

Merci à mes amis qui m'ont soutenu dans les moments difficiles (Alex, merci pour tes poêlées!), vous saurez vous reconnaître. Pardon à ceux que j'aurais pu blesser par ma *geek-attitude* parfois. Cela n'a jamais été mon intention. Merci à tous ceux qui se sont déplacés à ma soutenance, pour en faire un moment inoubliable.

Le plus grand merci va enfin à ma famille, mes parents Geneviève et Hervé, ma soeur Laury et mon frère Romain, et à toi Jehanne. Que dire tant je vous dois ? Merci de m'avoir toujours tout donné, de m'avoir supporté en toutes circonstances, d'avoir compris mes absences, et d'avoir cru en moi. Je ne vous en serai jamais assez reconnaissant.

Que dire pour terminer de tous les membres d'une collaboration telle ATLAS, des milliers de membres qui interagissent tous, et offrent chacun leur pièce à un tel édifice ? Merci à toutes les personnes qui ont contribué à construire le LHC et ses détecteurs, et à leur permettre de fonctionner. Merci à tous ceux qui les ont précédées, et à toutes les idées qui les ont inspirés. Je sais la chance infinie que j'ai eue de démarrer cette thèse à un moment aussi propice de la physique des particules.

Contents

Résumé

Le modèle dit 'Standard' (MS) de la physique des particules s'attache à décrire les constituants élementaires de la matière, ainsi que leurs interactions. Durant les 40 dernières années, il a permis de décrire les observations expérimentales avec une incroyable précision. Cependant, malgré ses nombreux succès, de nombreuses interrogations restent en suspens pour comprendre la totalité de notre univers *physique*. Cette thèse s'interroge sur la possible existence d'une quatrième famille de *fermions* – les particules de *matière* – dans le contexte d'une extension du MS. Nous recherchons la production d'une paire de quarks t' de charge $+2/3$ ayant des propriétés similaires au quark top, et se désintégrant chacun en un boson W et un quark b. L'analyse, effectuée au sein de l'expérience ATLAS au Large Hadron Collider (LHC), s'appuie sur un travail de mise en oeuvre des algorithmes d'identification des jets résultants de la fragmentation de quarks b. Le travail a également porté sur l'opération présente et future du détecteur à pixels d'ATLAS, dans le cadre notamment de l'étude d'un système visant à protéger son fonctionnement actuel, et de l'étude des performances attendues d'identification des jets b avec la nouvelle partie du détecteur à pixels, dénommée *IBL*, actuellement en construction.

Au-delà de l'interrogation fondamentale sur le nombre de génération de fermions – fixé à 3 par les observations expérimentales du dernier siècle – cette recherche de nouvelle physique est importante car une quatrième génération pourrait permettre de répondre à certaines questions essentielles, notamment sur la composition de l'univers. Cette extension du MS est également un des plus simples modèles de nouvelle physique encore non exclu, accessible au démarrage du LHC. L'identification des jets b quant à elle, en plus de servir à notre recherche de nouveaux quarks, revêt une importance primordiale au sein de l'expérience ATLAS pour la redécouverte du MS, pour l'observation du boson scalaire du MS (se désintégrant en paire $b\bar{b}$), ainsi que pour de nombreuses autres recherches de nouvelle physique, telle la Supersymétrie. Les algorithmes utilisés exploitent les propriétés spécifiques des quarks b, en comparaison avec les jets de quarks plus légers. Ils se basent sur la reconstruction très précise de la trajectoire des particules chargées, des vertex d'interactions primaires et des vertex de désintégrations secondaires présents au sein des jets, qui repose essentiellement sur les performances du détecteur à pixels d'ATLAS. Ce dernier est situé au plus proche du point des collisions du LHC, ce qui lui permet notamment de mesurer le paramètre d'impact des traces avec une résolution transverse incroyable d'environ 10 μm, mais qui le soumet en contre-partie aux plus hauts niveaux de radiations. Son intégrité apparaît donc primordiale à notre étude, ainsi qu'à toute l'expérience ATLAS, d'où l'intérêt particulier porté à ce détecteur. Son extension *IBL* permettra de compenser les défauts déjà subis depuis le début du fonctionnement du LHC, et d'améliorer les performances actuelles.

La mise en oeuvre des algorithmes d'identification des jets b, *i.e.* l'étiquetage-b, s'est tout d'abord appuyée sur une étude approfondie des propriétés des traces de particules chargées, en particulier celles qui satisfont les critères de qualité exigés par les différents algorithmes d'étiquetage-b. Cette étude s'est basée sur les toutes premières données du LHC collectées à une énergie $\sqrt{s} = 900$ GeV en décembre 2009, et sur les premiers 15 nb^{-1} collectés à $\sqrt{s} = 7$ TeV entre mars et juin 2010. L'accord entre les données réelles et les données simulées a été montré très encourageant étant donné le stade de maturité de l'expérience. Sur ces bases, et avec le même jeux de données, un travail de validation et d'optimisation du fonctionnement d'un algorithme dit 'robuste', *JetProb*, a été réalisé. Cet algorithme exploite d'une manière simple la significance du paramètre d'impact des traces associées aux jets, et a pu être utilisé pour les analyses des premières données de physique dans ATLAS. Le travail s'est ensuite porté sur la mise en oeuvre d'algorithmes s'appuyant sur des méthodes statistiques avancées, combinant en un rapport de vraisemblance, ou grâce à des réseaux de neurones, les variables associées aux jets en exploitant les connaissances acquises par la simulation Monte-Carlo. Typiquement, ces algorithmes permettent d'identifier correctement 70% des jets b, pour un taux d'identification incorrect

des jets légers de $\sim$0.68%. En comparaison, l'algorithme *JetProb* permet un taux de mauvaise identification d'$\sim$5% pour le même point de fonctionnement. Le travail de validation, basé sur 330 pb^{-1} de données 7 TeV, a permis d'identifier certaines sources de désaccord entre les données réelles et la simulation, et de déclarer que ces algorithmes pouvaient être calibrés et utilisés officiellement dans les analyses de physique d'ATLAS. Une étude de prospective sur les performances attendues d'étiquetage-b de ces algorithmes avancés avec le nouveau détecteur *IBL* a également été réalisée. Il a été démontré que, même dans des scénarios très pessimistes, les performances d'étiquetage-b sont toujours améliorées, ce qui a contribué à motiver la construction de ce détecteur, dont l'installation est prévue en 2014.

La recherche de nouveaux quarks d'une hypothétique quatrième famille de fermions s'est focalisée sur le processus de production d'une paire quark-antiquark $t'\bar{t'}$, où chacun des quarks lourds se désintègre dans 100% des cas via Wb. L'analyse a utilisé l'ensemble des 4.7 fb^{-1} de données 7 TeV collectées par ATLAS en 2011. Elle a considéré les états finaux leptons + jets + impulsion transverse manquante, *i.e.* les cas où un des deux bosons W se désintègre en voie leptonique, et l'autre en voie hadronique, donnant des états finaux avec plusieurs jets dont au moins deux jets b, un lepton de grand moment transverse, et une impulsion transverse manquante signant la présence d'un neutrino. Afin d'améliorer la précédente analyse ATLAS qui a exclu des masses pour le quark t' en-dessous de $\sim$400 GeV, l'analyse s'est focalisée sur le domaine des très hautes masses, où la production peut être distinguée de la production de bruit de fond d'une paire de quark top en exploitant la cinématique des produits de désintégration (énergie transverse de tous les objets de l'événement, ouverture angulaire entre le boson W et le quark b, collimation des produits de la désintégration des bosons W, etc). L'utilisation de l'étiquetage-b, précédemment mis en oeuvre, permet de rejeter de nombreux autres bruits de fond (*e.g.* multi-jets). La stratégie d'analyse est principalement basée sur la reconstruction de bosons W de haute impulsion transverse, qui a pour effet de rejeter naturellement le bruit de fond $t\bar{t}$. Cette reconstruction a été envisagée de plusieurs manières lors d'études prototypes utilisant notamment des algorithmes de jet à grande ouverture angulaire, permettant de 'capter' deux jets proches en tant qu'un seul et même jet reconstruit. L'analyse finale, pour des raisons pratiques, a retenu une solution utilisant des jets de plus petite taille, en considérant principalement des combinaisons de jets spatialement proches. Le rapport signal sur bruit obtenu avec cette nouvelle stratégie est supérieur à celui du type d'analyse qui a précédé cette étude par de nombreux ordres de grandeurs. Bien que n'ayant pas observé de signal significatif de nouvelle physique, cette analyse, complétée par une étude exhaustive des sources d'erreurs systématiques, a permis d'établir une limite inférieure à la masse du quark t' de 656 GeV, ce qui est la meilleure limite à ce jour en recherche directe.

Les implications de ce résultat sont diverses. D'un point de vue théorique, cette limite dépasse la limite dite de 'perturbativité' de la théorie sur laquelle est basée le MS. Bien qu'une quatrième génération 'non-perturbative' puisse exister à de plus hautes masses, il n'est plus possible de réaliser de prédiction physique précise dans ce régime. Un nouveau scénario envisageable apparaît dès lors attractif, celui dit des quarks 'vecteurs', notamment dans le contexte de la récente observation d'une particule compatible avec le boson scalaire du MS. L'analyse présentée précédemment a pu être directement appliquée et sensible à ce type de signal, et a débouché sur une des premières limites pour ce nouveau type d'hypothétique quark. D'un point de vue expérimental, cette analyse a démontré la faisabilité d'une nouvelle stratégie d'analyse exploitant les topologies d'événements dites 'boostées' à travers l'étiquetage-W. La sensibilité grandement améliorée, et les possibilités d'améliorations, sont très prometteuses pour les futures recherches au LHC. On peut par exemple imaginer que l'étiquetage-W pourra servir à des recherches de signatures avec davantage de bosons W dans l'état final (*e.g.* pour des désintégrations $t' \to b'$), scénarios où de nouveaux quarks lourds peuvent encore se cacher.

Introduction

Science gives us *models* of the world. Particle physics has its own, called the 'Standard Model', that describes the elementary bricks of matter, and their interactions. During the past 40 years, it has never been contradicted by experimental data[1]. However, despite its great successes, this model cannot account for many observational data one has about the Universe, and is likely an approximation of a more global theory. New physics beyond the Standard Model must exist.

The Large Hadron Collider (LHC) is opening a new era for fundamental science: after only 3 years of operation, it has already discovered a new particle compatible with the scalar particle[2] resulting from the *electroweak symmetry breaking* mechanism in the Standard Model. It is also testing numerous models of new physics, scanning an energy domain up to the TeV scale. Among them, the addition of a fourth family of *fermions* – the *matter* particles – is one of the simplest extensions to the Standard Model, and could be quickly accessible at the start of the LHC. This model shows several attractive features that strongly motivate searching for it. In particular, it could help to solve several issues one has in cosmology about the composition and formation of the Universe. Even after the recent discovery of the scalar particle, this model is still viable in many scenarios. Quarks of *vector*-like nature could also exist and would have similar decay signatures. They would be a novel form of matter.

For many of the searches carried out at the LHC, which are looking at the decay products of some known or still undiscovered particles produced at the interaction points, it is of primary importance to detect the production of particles called *bottom* quarks, or *b*-quarks. Many algorithms intended to detect such quarks efficiently had been developed before the start of the LHC. In this work, we will commission and optimize a simple so-called '*b*-tagging' algorithm with the first LHC data. With more data collected in 2011, we will commission algorithms exhibiting much increased performance, that will be used officially by the ATLAS experiment.

In this document, we will start with a brief introduction to the Standard Model, and show some of its limitations, and how they could be overcome with the existence of a fourth generation of quarks, hence motivating all this work.

Then, we will describe the experimental framework, introducing the functioning of the LHC, and of the ATLAS detector. We will stop by a more detailed description of one detector which is crucial for proper *b*-tagging performance: the *pixel* detector, and we will describe some work we did on a system intended to detected some cooling fluid leaks that could potentially alter its performance during operation.

Then, we will present the commissioning of the ATLAS *b*-tagging algorithms. A section will be

[1] At the exception of neutrino oscillations (see later).

[2] This particle is also widely referred to as the 'Higgs' boson. While acknowledging the work of the people who lead to theorize its existence in 1964, including physicists R. Brout, F. Englert, P. Higgs, C. R. Hagen, G. S. Guralnik and T. W. B. Kibble, we prefer to employ in this document the more generic term 'SM scalar boson' given the fact that its prediction and discovery can only be the fruit of the work of thousands of people over decades.

dedicated to assess the b-tagging performance in the perspective of a detector upgrade called IBL. This study contributed to motivate the construction of this sub-detector (currently being built).

Finally, we will present a search for new heavy quarks. We will search for an up-type quark t' decaying 100% of the time to a W boson and a b-quark, with one lepton, one b-tagged jet, missing transverse energy and two or three other jets in the final state of the events. The search strategy that will be presented is novel compared to previous similar searches, taking its strength mainly from the explicit reconstruction of a high-p_T W boson decaying hadronically, and also from the use of the b-tagging algorithms that we commissioned previously. It will be seen to show a much increased sensitivity compared to previous searches and results of competitive experiments, yielding the world most stringent exclusion limits for the model of fourth generation, with also an interpretation in the framework of Vector-Like quarks.

Chapter 1

Physics context

Physics is one of the oldest academic disciplines, studying matter and its motion through space and time. In the past century, Particle physics has seen tremendous progress with the advent of Einstein theories of relativity, quantum mechanics, and quantum field theory. In the current understanding, particles are described as excitations of quantum fields and interact following their dynamics.

In this chapter, we will first give a brief introduction to the so-called Standard Model (SM) of Particle Physics – a model encompassing our current knowledge about elementary building-blocks of matter and their interaction – trying to explain the basic concepts of the underlying theory. In particular, we will try to explain the features that are important for the rest of this work. Then, we will briefly explain the limitations of the SM, and speak about one of its most simple extension that could answer several important issues: fourth generation. We will discuss the allowed phase space still open for this model, notably in the context of the recent discovery of a particle compatible with the SM scalar boson. At the end of this chapter, we hope it will be clear why we need to produce extremely high-energy collisions in order to discover these new particles.

1.1 The Standard Model of Particle Physics

The Standard Model (SM) [1, 2, 3, 4] of Particle Physics describes the elementary constituents of matter and their interactions. With the exception of gravity, it describes the three known fundamental interactions: the weak interaction, responsible for β radioactivity, the strong interaction, ensuring the cohesion of nuclei, and the electro-magnetic interaction, responsible for upholding atomic and molecular structure, and for chemical interactions. For a pedagogical introduction to the SM, the reader is referred to *e.g* [24]. We give here only an overview of the important notions, concepts and properties that will be useful later.

1.1.1 Notions of Quantum Field Theory

Quantum fields Quantum Field Theory (QFT) provides the mathematical framework of the Standard Model, in which a Lagrangian[1] controls the dynamics and kinematics of the theory. It is fundamentally a theory of *fields*, a field being a physical quantity that has a value for each point in space-time. The application of quantum mechanics to fields has profound consequences. Unlike a classical field, such as the electric field $E(x,t)$, whose propagating waves can have any amplitude,

[1] The Lagrangian of a dynamical system can be seen as a function that summarizes the dynamics of the system. The trajectory of a system of particles is derived by solving the Euler-Lagrange equations.

the stable propagating states of a quantum field are constrained to have discrete energies. This provides a natural framework for the understanding of elementary particles: under certain conditions, this discreteness can give rise to particulate appearance to nature, which one interprets as composed of elementary particles. For example, the particles of light, *photons*, are propagating waves of the quantized electromagnetic field (see later). Similarly, all particles in nature represent discrete states of excitation of their respective underlying quantum fields.

Figure 1.1 illustrates the energy levels of a quantum field. The least excited state of a field corresponds to a state of no particle, and is also called *vacuum state*. The first excited state of a field corresponds to the presence of a single particle with energy[2] $E = \sqrt{m^2 + |\vec{p}_1|^2}$, where m is the mass of the particle and $\vec{p}_1$ its momentum. The second excited state corresponds to the presence of two particles, with total energy $E = \sqrt{m^2 + |\vec{p}_1|^2} + \sqrt{m^2 + |\vec{p}_2|^2}$, etc.

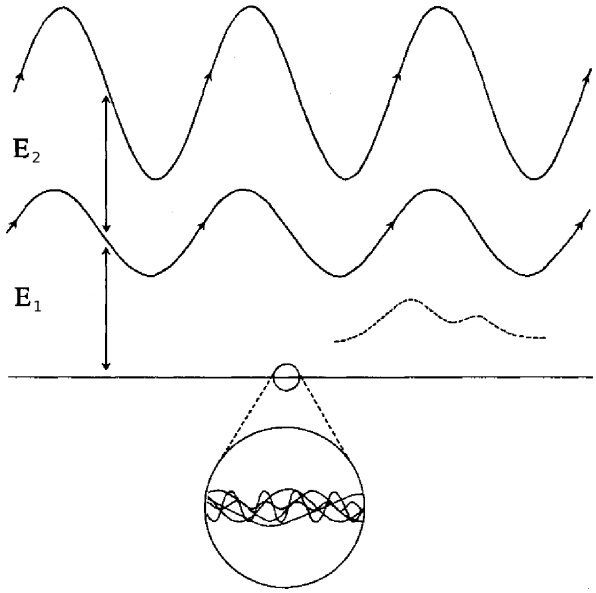

Figure 1.1: The modes of activity of a quantum field include 1) the stable, propagating states of the field with well-defined, discrete energies, which have a natural interpretation as elementary particles; 2) transient field configurations which do not propagate and play the role of forces between particles (dashed); and 3) vacuum fluctuations: the continuous, quantum-mechanical activity of the field present in the vacuum state and in all the excited states [23].

Feynman diagrams A quantum field can also sustain other form of activity, corresponding to quantum-mechanical superposition of particle states. These kind of configurations, illustrated in dashed line in Fig. 1.1 are unstable: they do not propagate, and do not possess well defined-energy. Therefore, they do not have a natural interpretation in terms of particles, but are rather sometimes called 'virtual' states. These transient modes of activity play the role of forces between particles.

This dual characteristic of a quantum field as 'particle' and 'force' is illustrated in Figs. 1.2(a) and 1.2(b), which respectively display the *Feynman* diagrams of the scattering of electrons and photons. A Feynman diagram is a pictorial representation of the time evolution of all the quantum fields involved

[2]We work using so-called Planck units in which $c = \hbar = 1$, where c is the speed of light and $\hbar$ is the reduced Planck constant.

in any basic scattering process. For a given process, there are usually many contributing diagrams. The one shown in Fig. 1.2(a) is the most important contribution, called *tree* diagram[3], of electron scattering. It shows two incoming electron lines exchanging energy and momentum through the exchange of a virtual photon, followed by two outgoing lines, the final state of the decay. The *external* lines are the physical particle states of the fields, while the *internal* line is a transient, non-propagating state of the photon (or electromagnetic) field playing the role of force carrier[4]. The amplitude of this tree level diagram is proportional to the square of $\alpha \simeq 1/137$, the coupling constant characterizing the strength of the electromagnetic interaction. The sum of all diagrams contributing to a given process is called the *perturbation* series, which is expressed as sets of power series in α. Because α is here much less than one, higher powers of α are soon unimportant, making the perturbation theory extremely practical in this case.

Fig. 1.2(b) shows the dominant contribution to the scattering of photons, a situation where the roles of the electron and electromagnetic fields are reversed compared to our previous example. In this uniquely quantum-mechanical process, the electron fields act as force carriers, while the photon fields play the role of incoming and out-coming particles. The amplitude of this diagram, showing a closed 'loop', is proportional to α^4, hence expected to happen at a very suppressed rate[5].

One can therefore conclude that any quantum field can assume either the role of particle or force, depending on whether that quantum field is in a physical particle state or 'virtual' state. In practice, fields are however commonly distinguished between *force fields*, such as the photon field, and *matter fields*, such as the electron field, due to their different quantum properties (as we will see later).

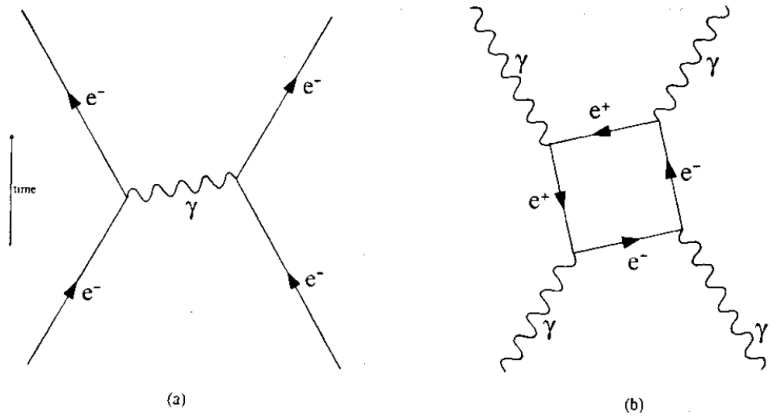

Figure 1.2: The dominant Feynman contributions to electron scattering and photon scattering. Figure (a) shows the scattering of two electrons through the exchange of a virtual photon. Figure (b) shows the scattering of two photons through a virtual electron-positron loop [23].

Vacuum fluctuations A second important consequence of the application of quantum mechanics to fields follows from the uncertainty principle, which states that one cannot simultaneously specify the value of two or more properties of a system if they are quantum-mechanically correlated[6]. In QFT, at every point in space the amplitude of the field is described by a 'wave functional' that expresses the

[3]Tree diagrams are diagrams without closed 'loops' (as in 1.2(b)).

[4]Virtual particles corresponding to internal propagators in a Feynman diagram typically do not fulfill $E^2 = m^2 + p^2$.

[5]While predicted by the SM, light-by-light elastic scattering has actually never been observed yet.

[6]*i.e.* if the operators corresponding to those properties do not commute with each other.

indefiniteness of the field and rate of change of the field at that particular point. When considering the vacuum state of a field, an amplitude being zero everywhere is hence highly unnatural from the standpoint of the uncertainty principle. The vacuum state must therefore correspond to a coexistence, or superposition, of field shapes, as illustrated in Fig. 1.1. It also must possess the dynamics of empty space, *i.e*. being *Poincare invariant*, which includes invariance with respect to translations, rotations, and 'boosts' (changes in velocity of an observer's frame of reference). The vacuum state hence consists of a very definite balance of field shapes which is stable in time, uniform in space, etc. These energetic field shapes, which are present in the vacuum state as well as in all the excited states of the field, are referred to as *vacuum fluctuations* [23]. They give rise to a large vacuum energy, which is usually subtracted out of the theory. This should not hide the fact that these fluctuations are *actually* existing and play a crucial role in our understanding of the universe, as we will see later.

Quantum field theory thereby provides a profound view of nature, in which the previously unrelated concepts of 'particle' and 'force' are naturally unified as corresponding to different modes of activity of an underlying quantum field.

1.1.2 Field content

1.1.2.1 Fermions

The SM includes 12 elementary 'particle' fields of spin $1/2$ called *fermions*, each having a corresponding antiparticle[7]. Fermions are classified depending on the way they interact.

Quarks In an attempt to simplify the large number of strongly interacting particles (or *hadrons*) by a few fundamental sub-constituents, physicists Murry Gell-Mann and George Zweig introduced the *quark* model in 1964 [11, 12]. There are six quark fields (up, down, charm, strange, top, bottom), organized in three families:

$$\begin{pmatrix} u \\ d \end{pmatrix} \begin{pmatrix} c \\ s \end{pmatrix} \begin{pmatrix} t \\ b \end{pmatrix}$$

Each family comes in three identical replications or 'colors': red R, green G and blue B (with associated *anti*-colors), and quarks are by definition carrying color charge, meaning they interact via the strong interaction (see thereafter). Quarks also carry electric charge and weak isospin, hence interacting with other fermions via both the electromagnetic and weak interactions.

Due to a dynamical phenomenon called 'color confinement', quarks cannot be isolated singularly, and are inextricably confined within the interior of hadrons: for example $q^1_R q^2_{\bar{R}}$ for a *meson* (made of one quark and one antiquark), or $q^1_R q^2_G q^3_B$ for a *baryon* (made of three quarks). This property has practical consequences for particle colliders phenomenology, as we will see later.

The quark model validity started to be experimentally verified in 1968 with deep inelastic scattering experiments at the Standford Linear Accelerator Center (SLAC), which showed that the proton should contain much smaller, 'point-like' objects which would later be identified as up and down quarks. The existence of the strange quark was also indirectly validated, as a necessary component of the Gell-Mann and Zweig's three-quark model. The existence of the charm quark was predicted in 1970 [4], and discovered by two teams at SLAC and Brookhaven National Laboratory in 1974 [13, 14], in the form of a $c\bar{c}$ meson called J/ψ. The supposition of the existence of a third quark generation was made in 1973 [21]. The discovery of the bottom quark in 1977, under the form of a $b\bar{b}$ meson [15],

[7] Quantum states of a particle and an antiparticle can be interchanged by applying the charge conjugation (C), parity (P), and time reversal (T) operators. Particle and antiparticle must hence have same mass, same spin, but opposite charges.

was hence a strong indicator of the existence of the top quark, which was discovered in 1995 [26, 27], further demonstrating the predictive power of the SM.

Leptons The remaining six fermions, called *leptons*, do not carry color charge. They are named electron, electron neutrino, muon, muon neutrino, tau and tau neutrino, organized in three families:

$$\begin{pmatrix} \nu_e \\ e^- \end{pmatrix} \begin{pmatrix} \nu_\mu \\ \mu^- \end{pmatrix} \begin{pmatrix} \nu_\tau \\ \tau^- \end{pmatrix}$$

The three neutrinos do not carry electric charge, so their dynamics are determined only by the weak interaction. The strength of this force being extremely low compared to the electromagnetic force at low energy (see later), neutrinos can traverse directly through the earth or the sun with very little chance of scattering. Electrons, muons and taus carry an electric charge, hence interact electromagnetically.

Figure 1.3 summarizes these three generations of fermion fields, shown together with their approximate masses[8]. It can be seen that each member of a generation has greater mass than the corresponding particles of lower generations, so the first generation charged particles do not decay. All ordinary matter that surrounds us is hence made of such particles, *e.g.* atoms that consist of electrons orbiting around nuclei formed schematically of up and down quarks. Second and third generations charged particles, on the other hand, decay with very short lifetime, and can only be observed in very high-energy scatterings. As far as neutrinos are concerned, the SM had initially assumed that neutrinos are massless and cannot change flavor. The discovery of neutrino flavor oscillations (see *e.g.* [25]) – *i.e.* neutrinos oscillating among the three available flavors when propagating – implied that they must have a mass, which is expected to be tiny from the current experimental bounds[9].

1.1.2.2 Gauge bosons

So-called *gauge* bosons fields are the force carriers that mediate the fundamental interactions. Mathematically, these fields are appearing in the Lagrangian of the theory to ensure its invariance under a continuous group of local transformations. The gauge fields fall into different representations of the various symmetry groups of the Standard Model. The gauge bosons all have spin 1, and are briefly described here:

- The *photon* γ mediates the electromagnetic force between electrically charged particles. The photon is massless and is well-described by the theory of quantum electrodynamics (QED), which is an Abelian[10] gauge theory with the symmetry group U(1). QED is certainly one of the most successful theories, sometimes called the *jewel of physics*, for its extremely accurate predictions, such as the anomalous magnetic moment of the electron (and muon), which is the most accurately verified prediction in the history of physics, with a precision of better than one part in a billion.

[8]The determination of quark masses is quite ambiguous. The theory of strong interaction (QCD, see later) does not predict masses in physical units, so only dimensionless combinations (such as mass ratios) can be calculated (*e.g.* in lattice QCD), and the overall physical scale depends on an external input. It is common to quote masses at the renormalization scale evaluated at a scale equal to $\mu \sim 2$ GeV (for light quarks), or at the quark mass (b- and c-quarks). For the b-quark, the mass sometimes quoted is 4.7 GeV, half the mass of the $\Upsilon(1S)$ ($b\bar{b}$) meson.

[9]The absolute neutrino mass scale is still not known, because neutrino oscillations are sensitive only to the difference in the squares of the masses of the different flavors.

[10]Meaning the symmetry group is commutative.

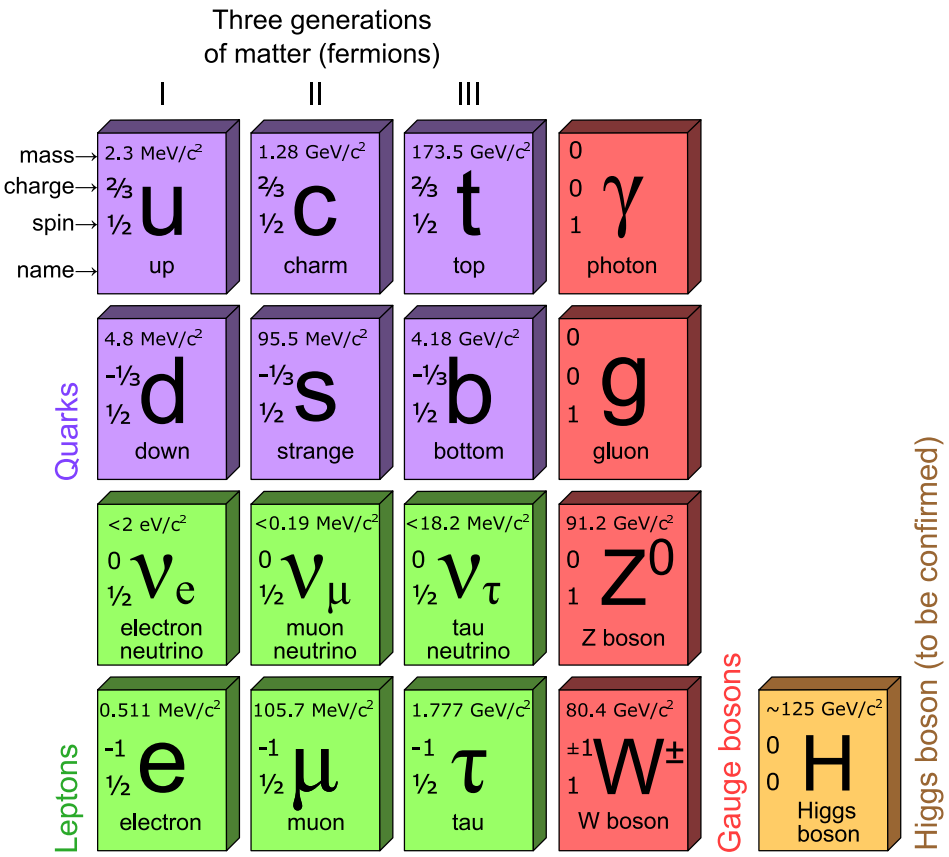

Figure 1.3: Field content of the Standard Model. Masses are updated from [47].

- The W^+, W^-, Z^0 bosons mediate the weak interactions between particles of different flavors (all quarks and leptons). They are massive, with the Z^0 being more massive than the $W^\pm$. Furthermore, the $W^\pm$ carry an electric charge of $+1$ and -1 and couple to the electromagnetic interaction. The Z^0 boson is electrically neutral. These three gauge bosons along with the photons are grouped together, as collectively mediating the electroweak interaction, a gauge theory with the symmetry group SU(2)×U(1). The prediction of weak interaction through neutral current [4], which was verified three years later in 1973 at CERN [10] was a great success of the SM, as well as the discovery of the $W^\pm$ and Z^0 bosons in 1983 at the SPS proton-antiproton collider (CERN) [16, 17, 18, 19].

- Eight *gluons* mediate the strong interactions between color charged particles (the quarks). Gluons are massless, and have an effective color charge, so they can also interact among themselves. The gluons and their interactions are described by the theory of quantum chromo-dynamics (QCD), which is a non-Abelian gauge theory with the symmetry group SU(3).

1.1.2.3 Scalar boson

The existence of a massive scalar (with spin 0) field was theorized by R. Brout, F. Englert, P. Higgs, C. R. Hagen, G. S. Guralnik and T. W. B. Kibble in 1964 [5, 6, 7, 8, 9]. It plays a very unique role in the SM, explaining why the electromagnetic and weak forces are different, and explaining why the

photon has no mass, while the $W^{\pm}$ and Z^0 bosons are heavy. It also allows to generate the masses of the leptons (at the exception of neutrinos) and quarks.

On 4 July 2012, the two experiments ATLAS and CMS (cf. Chap. 2) both observed a new particle with a mass of about 126 GeV compatible with the SM scalar boson [52, 53]. Further investigations are nevertheless needed to determine the spin of this particle and confirm that the production and decay modes are indeed compatible with the SM prediction, and not with a more exotic model. Such confirmation would be an immense success for the SM.

1.1.3 Electro-weak unification

The model of Glashow, Salam and Weinberg [1, 2, 3] describes the electromagnetic and weak interactions in a similar way, and unifies further the different fields of nature. To illustrate this, figure 1.4 shows the dominant contribution to the scattering of neutrinos through the exchange of a virtual Z^0 boson. In comparison to the electron scattering via the electromagnetic field we saw in Fig. 1.2(a), it is observed to be very much weaker. This is due to the fact that Z^0 bosons have a mass of about 90 GeV, where 1 GeV is comparable to the mass of the proton, so there is not generally enough energy to excite the Z^0 field at ordinary scales and temperatures, where the decay can only occur via a virtual non-propagating state. However, the strengths of neutrino scattering and electron scattering become close at high energies when the energy of the incoming particles is very large compared to the Z^0 mass. This example shows that this is the mass of the Z^0 field that makes the weak interaction so weak, and thereby leads to the apparent asymmetry between the electron and the neutrino. If the Z^0 were massless like the photon, the electron and the neutrino would behave as similar interaction strength components of a unified field called the left-handed lepton doublet. The unified electroweak theory, when assuming massless $W^{\pm}$ and Z^0 bosons, also provides unification of the muon and the tau with their associated neutrinos, as well as the up-type quarks with their associated down-type quark, as two components of isospin doublet.

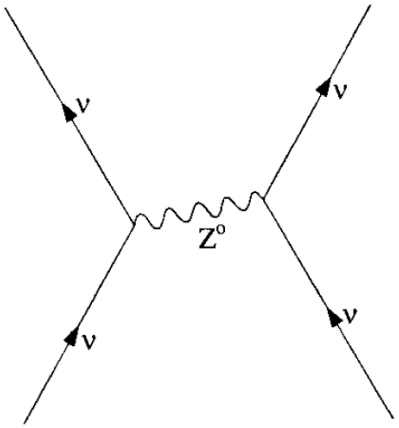

Figure 1.4: The dominant Feynman contribution to neutrino scattering involving the exchange of a massive virtual Z^0 boson [23].

1.1.4 Spontaneous symmetry breaking

In the SM, the four massless gauge bosons mediating the electroweak interaction are the generators of the symmetry groups SU(2) ($W^i_\mu, i = 1,3$) and U(1) (B_μ). The massive $W^\pm$ and Z^0 bosons, and the massless photon, are produced by the so-called *spontaneous symmetry breaking* of the electroweak symmetry SU(2)×U(1). It causes the W^3_μ and B_μ bosons to mix together into the Z^0 boson and the photon, as follows:

$$\begin{pmatrix} \gamma \\ Z^0 \end{pmatrix} = \begin{pmatrix} cos\theta_W & sin\theta_W \\ -sin\theta_W & cos\theta_W \end{pmatrix} \begin{pmatrix} B_\mu \\ W^3_\mu \end{pmatrix}$$

where θ_W is called the *weak mixing angle*. The $W^\pm$ bosons are the results of the following mixing:

$$W^\pm = \frac{W^1_\mu \pm iW^2_\mu}{\sqrt{2}} \tag{1.1}$$

The electroweak symmetry breaking (EWSB) mechanism could happen in a number of ways. In the SM, the preferred theory postulate the existence of the scalar field previously stated[11], and likely discovered by the ATLAS and CMS experiments. This field has a non-zero strength, or *vacuum expected value* (v.e.v.) – even in otherwise empty space – and $W^\pm$ and Z^0 acquire a mass interacting with it, separating the electromagnetic and weak forces.

Fermion masses can also be generated adding in the theory Yukawa interactions between the scalar field and the fermion fields, which are proportional to the v.e.v. and to arbitrary constants translating the observed masses of the particles.

For the quarks, the mechanism is similar. However, the variety of observed quark masses allow the weak decay of a quark of the generation i to a lighter quark of the generation j. This is taken into account in the Lagrangian of the theory in the so-called Cabibbo-Kobayashi-Maskawa (CKM) unitary matrix [20, 21] V^{CKM}, which expresses the quantum states of quarks when they weakly interact as a function of the quantum states when they propagate freely[12], *e.g.* for up-type quarks:

$$d'^i = V^{CKM}_{ij} d^j \tag{1.2}$$

The various V^{CKM}_{ij} terms represent the coupling of the charged weak current to the quarks i and j. Applying different constraints, it can be shown that three mixing angles and one complex phase allow to parametrize the CKM matrix. The phase translates the violation of the CP-symmetry (charge conjugation + parity) in the SM. Historically, this is the necessity of this phase to explain the CP violation observed in neutral kaon systems [21] that conducted to postulate the existence of a third generation, discovered a few years later.

Imposing the SM constraints (*i.e.* three generation unitarity), the CKM matrix elements can be most precisely determined by a global fit using all the available measurements [47]:

$$\begin{pmatrix} |V_{ud}| & |V_{us}| & |V_{ub}| \\ |V_{cd}| & |V_{cs}| & |V_{cb}| \\ |V_{td}| & |V_{ts}| & |V_{tb}| \end{pmatrix} = \begin{pmatrix} 0.97427 \pm 0.00015 & 0.22534 \pm 0.00065 & 0.00351^{0.00015}_{-0.00014} \\ 0.22520 \pm 0.00065 & 0.97345 \pm 0.00016 & 0.0412^{+0.0011}_{-0.0005} \\ 0.00867^{+0.00029}_{-0.00031} & 0.0404^{+0.0011}_{-0.0005} & 0.999146^{+0.000021}_{-0.000046} \end{pmatrix}$$

[11] The SM allows for extensions where the details of the scalar field and number of fields can differ.

[12] This matrix was introduced for three generations of quarks by M. Kobayashi and T. Maskawa, adding one generation to the matrix previously introduced by N. Cabibbo.

which tells us that, for example, the top quark decays $\sim$100% of the time into a W boson and a b-quark in the SM with three generations of fermions (SM3)[13].

This kind of mixing does not occur for leptons for a SM without neutrino masses. However, the discovery of the existence of neutrino masses requires an equivalent of the CKM matrix: the Pontecorvo, Maki, Nakagawa, Sakata (PMNS) matrix [50, 51] for the lepton sector.

Let us now come back to the matter of electroweak unification we introduced previously. We have seen that the EWSB occurs from a non-zero v.e.v. of the SM scalar field. In the standard Big Bang cosmological model, the universe began with an extremely rapid exponential expansion, called *inflation*. In the first one-billionth of a second in the evolution of the universe, it is believed that the extremely high temperatures could have add the effect to reduce to zero the v.e.v. of the SM scalar field, restoring the electroweak symmetry. In this *electroweak epoch*, massless W and Z bosons would be created, and as the universe expanded and cooled down, they would have then acquired mass at the EWSB, and the weak interaction, separated from the electromagnetic force, would have become a short range-force.

1.1.5 Quantum Chromo-Dynamics

As stated above, QCD describes the strong interactions, mediated by gluon fields exchanging a color charge between fields sensitive to this interaction. Contrary to the electromagnetic interaction, for which the photon does not carry an electric charge, gluons carry a color charge, making them able to couple to each other, reflecting the non-Abelian nature of the SU(3) group governing QCD.

The coupling constant α_s that describes the intensity of the force between two fields is low at small distance (or at high momentum transfer Q^2), a property called *asymptotic freedom*, and increases at high distance (low Q^2), explaining the confinement of quarks inside hadrons. Figure 1.5 illustrates this showing a summary of measurements of $\alpha_s(Q)$ as a function of Q. For $\alpha_s(Q^2) >> \mathcal{O}(1)$, the perturbative approach (that we introduced briefly about QED) does not work anymore for QCD, and non-perturbative approaches have to be used to predict physical observables, such as *lattice* computations.

QCD is an extremely successful theory, that plays a crucial role in physics. As we will see in great extent in the next chapters, QCD will allow to describe interactions occurring at extremely high energy, in the QCD perturbative regime. In its non-perturbative regime, QCD allows *e.g.* to explain the inner structure of protons and neutrons. In the current understanding, protons (neutrons) are composed of two (one) valence up quark(s) and one (two) valence down quark(s), in a 'sea' of quark-antiquark pairs and gluons randomly created/annihilated from vacuum fluctuations. This is pictured in Fig. 1.6. However, the sum of the rest masses of the valence quarks contributes only to $\sim$1% of the total nucleon mass[14], while the gluons have zero rest mass. Lattice QCD computations have demonstrated recently that the binding energy of gluons and sea quarks is responsible for the missing $\sim$99% of the mass [77]. As more than 99% of the mass of the *visible* universe[15] is made up of protons and neutrons, one

[13] The top quark is unique because its decay lifetime is much shorter than the time for it to interact via strong interaction. For all the *lighter* quarks, the opposite is true, as will be explained in Sec. 2.2.6.

[14] The proton mass is $\sim$938.27 MeV; the neutron mass is $\sim$939.56 MeV. The small difference between the two appears fine-tuned for the stability of nuclear matter.

[15] As introduced in the next section, visible matter is expected to account for $\sim$4% of the total mass-energy content of the

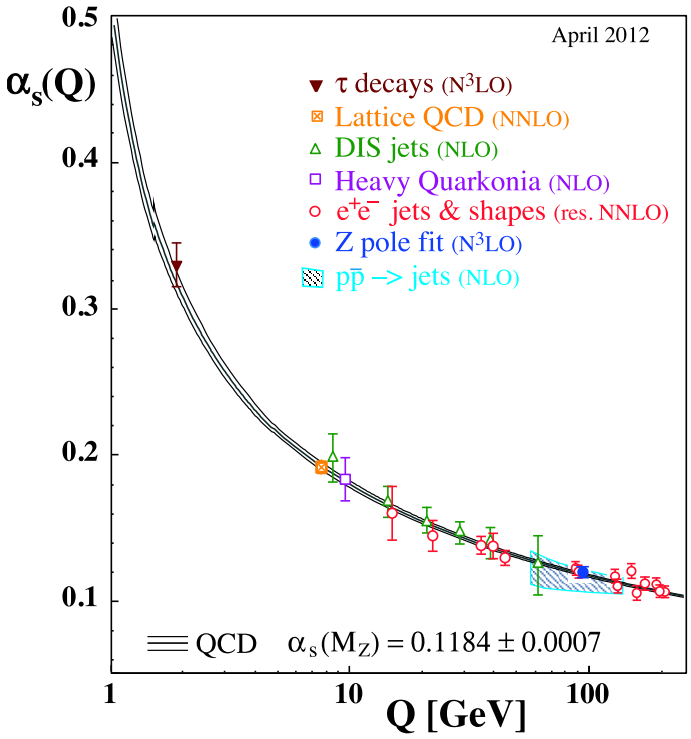

Figure 1.5: Summary of measurements of $\alpha_s(Q)$ as a function of the respective energy scale Q [47].

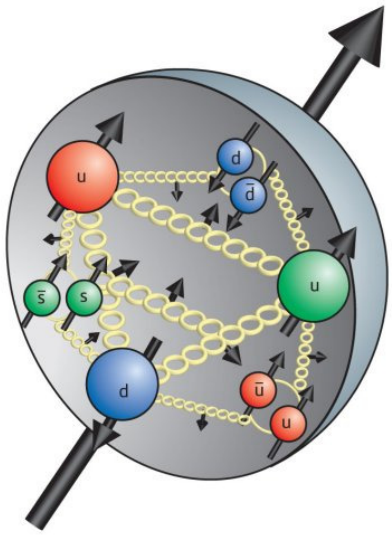

Figure 1.6: Artist view of the composition of a proton, made of two valence up quarks and one valence down quark in a 'sea' of quark-antiquark pairs and gluons created/annihilated from vacuum fluctuations.

can conclude that the vast majority of baryon mass in our world comes from the confinement energy of QCD.

1.1.6 Issues in the Standard Model

Despite its great successes, there are several reasons to believe that the SM is not the ultimate theory of particle physics, but an effective approximation (excellent up to the energy scaled probed up to today) of a more global theory. Major dissatisfaction is primary due to the fact that the SM describes correctly the observations, but often does not explain them. In particular, it has 19 numerical constants whose values are arbitrary and not predicted by the theory. Explaining the neutrino masses in the SM would add additional such parameters. Among the other conceptual issues and questions without answers, one can quote:

- it does not incorporate gravity (described by the General Relativity of Einstein), *i.e.* there is no satisfactory quantum theory of gravitation available at the moment;
- the CP violation in the electroweak sector is not sufficient to explain the matter-antimatter asymmetry seen in the universe: $\sim 10^{13}$ to 10^{15} more CP violation would be needed to explain the current asymmetry;
- the SM does not provide any candidate for *dark* matter [30]; dark matter being the matter that cannot be seen directly with telescopes. Its existence and properties are inferred from its

universe, complemented with ∼73% of *dark* energy and ∼23% of *dark* matter.

gravitational effects on visible matter and large scale structures of the universe. It is estimated to constitute $\sim$23% of its mass-energy content; visible matter being expected to represent $\sim$4% only;

- the energy associated with vacuum fluctuations is expected to have gravitational effect that could play the role of the cosmological constant of the universe. However, the level of this *dark* energy [30] (estimated to account for $\sim$73% of the total mass-energy of the universe) is over-estimated by more than a hundred orders-of-magnitude compared to the level one would expect from observations;

- the SM does not explain the so-called *hierarchy problem*, which wonders why is there 17 orders-of-magnitude difference between the weak scale and the Planck scale. In other words, why is the gravity so weak compared to the other interactions, without invoking some fine-tuning of the theory ?

- the SM only accounts for CP violation in the weak interaction. In the strong interaction, no CP violation has been observed experimentally, while this is in principle possible in the theory. This fine-tuning can also be considered unnatural;

- the SM does not fix the number of quark and lepton generations: why would there be only three generations ?

1.2 New heavy quarks

1.2.1 SM4 perturbative scenario

1.2.1.1 Fourth generation definition

In the assumption that neutrinos are massless, or fulfilling $m_\nu << m_Z/2$, the LEP measurements at the Z-pole[16] determined the number of neutrino species to be 2.9840 ± 0.0082 [28, 29], which implied the existence of only three generations of leptons, and therefore of three generations of quarks.

However, considering massive neutrinos, it became evident that extra generations are possible provided the additional neutrinos fulfill $m_\nu > m_Z/2$, *i.e.* $m_\nu > 46$ GeV. In addition, after reconsidering and reevaluating in the recent years the electroweak precision data, it became clear that a fourth generation of fermions is not ruled out experimentally by precision measurements [60, 61, 62, 66, 67, 68], in contradiction with what was commonly accepted for a long time (PDG [47] article from Langacker and Erler).

The model we consider consists of simply adding to the SM3 a chiral fourth generation of fermions. The 'SM4' fermionic content hence become:

$$\begin{pmatrix} u \\ d \end{pmatrix} \begin{pmatrix} c \\ s \end{pmatrix} \begin{pmatrix} t \\ b \end{pmatrix} \begin{pmatrix} u_4 \\ d_4 \end{pmatrix} \qquad \begin{pmatrix} \nu_e \\ e^- \end{pmatrix} \begin{pmatrix} \nu_\mu \\ \mu^- \end{pmatrix} \begin{pmatrix} \nu_\tau \\ \tau^- \end{pmatrix} \begin{pmatrix} \nu_4 \\ \ell_4^- \end{pmatrix}$$

Note that we assume perturbativity of the Yukawa couplings, and suppose Dirac[17] heavy neutrinos.

[16] The LEP is an electron-positron collider which operated until 2000 at the center-of-mass energy $\sqrt{s}$ =209 GeV. For the number of neutrinos measurement, it operated at the Z-pole, *i.e.* $\sqrt{s} \sim$91 GeV.

[17] A 'Dirac' particle is different in some way from its antiparticle. Fourth generation models with Majorana (*i.e.* the particle is its own antiparticle) neutrinos are also possible, but not considered here.

1.2.1.2 Physics implications

An extra generation of fermions would provide several attractive features in terms of model-building beyond the Standard Model (see *e.g.* [36] for a summary). Among others, it could:

- help to explain the baryon asymmetry of the Universe: CP-violation is one of the three so-called Sakharov criteria that allow the dynamical creation of the matter and antimatter at different rates. In the assumption that the universe evolved from an originally perfectly symmetric situation, it could explain why we observe now a universe composed almost entirely of matter. With three generations, the amount of CP-violation, measured by the phase of the CKM matrix, is too low by more than 10 orders of magnitude. In SM4, the amount of CP-violation could be enhanced by $\sim$13 to 15 orders of magnitude, to explain the current baryon asymmetry of the universe [32]. Long-lived fourth generation particles ($\tau_4 > 10^{-11}$ s) also save baryon asymmetry generated at the early universe from erasure by sphaleron transitions ($B-L$ conserving) [71];

- provide a candidate for dark matter (DM): for example, new fermions could either decouple completely from their SM counterparts and serve as cold DM, or may be stable particles, such as some heavy $+2/3$ charge, that could form bound neutral atomic states and serve as composite DM [33, 34];

- provide new perspective into the fermion mass hierarchy problem: the current Yukawa couplings in the SM spread over an unnaturally wide range of values. The so-called Democratic Mass Matrix (DDM) [35] approach would allow to start from couplings of the same order for all fermions families;

- relieve some tension in flavor physics precision measurements. For example, mixing-dependent CP-violation in $B_s \to J/\psi\phi$ might exhibit contributions of loops with fourth generation quarks [37, 38], as illustrated in the Feynman diagram of B_s^0 mixing in Fig. 1.7.

  Similar arguments also hold for the measurement of the $B_s \to \mu^+\mu^-$ branching fraction, which is expected extremely rare, but which could be enhanced due to heavy quarks entering loop diagrams;

- dynamically break the electroweak symmetry of the SM [141, 144]: very heavy fourth generation quark condensates could play the role of the SM scalar field via some strong interaction (see Sec. 1.2.2). Obviously, if the discovery of the SM scalar boson is confirmed, this argument does not hold any longer, but this was an interesting motivation at the time this work began.

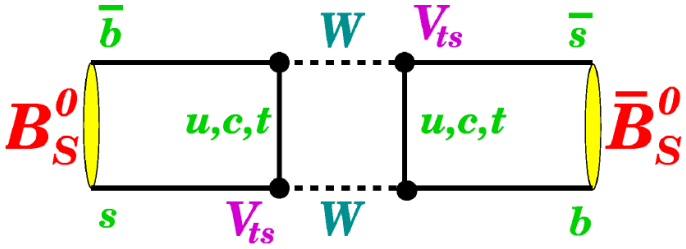

Figure 1.7: Feynman diagram describing B_s^0 mixing. New physics, if present, would be expected to contribute to the $b \to s$ transition.

Given all these attractive features, there has been an enormous interest in the phenomenology of fourth generation, with more than 500 papers in the last decades. Surprisingly, this model went through several 'deaths' and 'resurrections' among the physics community. For an history of such statements, see *e.g.* [36, 39, 54].

1.2.1.3 Phenomenology and Electroweak constraints

CKM4 matrix and mixing with SM3 The introduction of the fourth generation allows to drop the requirement of the unitarity of the 3×3 CKM matrix in the SM3 ('CKM3' matrix), which extends to a 4×4 matrix V_{CKM4}. Nine parameters, including six angles θ_{ij} and three phases δ_{j4}, allow to determine this CKM4 matrix [58]. One possible way to parametrize it uses the following quantities:

$$s_{ij} = sin\theta_{ij}, \quad c_{ij} = cos\theta_{ij}, \quad \text{and} \quad \delta_{j4} \;\; ; \quad i = 1..3 \tag{1.3}$$

One first major question we have to wonder is *how strongly the new fourth generation fermions will mix with the lighter generation fermions ?*

Assuming a predominant mixing with the third generation, this can in principle be quantified in the angle θ_{34}, or equivalently in the parameter $s_{34} \simeq |V_{b't}|$. In order to estimate such parameter, and all the coefficients of the CKM4 matrix, the direct measurements of the coefficients of the CKM3 matrix in the SM3 can be used, without assuming unitarity of the CKM3 matrix. For example, the direct determination of $|V_{tb}|$ is possible from the single top-quark production cross section. The cross-sections [48, 49] measured by the D0, CDF and CMS experiments yields on average:

$$|V_{tb}| = 0.89 \pm 0.07 \tag{1.4}$$

For the other CKM3 coefficients, a summary of the most precise measurements can be found in [47]. Regarding the s_{34} parameter, one can thus get the limit [55]:

$$s_{34} \leq 0.8 \tag{1.5}$$

It has also been shown recently, *e.g.* in [57, 58, 59], that fourth generation loops in $Zb\bar{b}$ vertices influence:

$$R_b = \frac{\Gamma(Z \to b\bar{b})}{\Gamma(Z \to hadrons)} \tag{1.6}$$

In order to fit experimental values on R_b, it was shown [58, 59] that the s_{34} mixing, which depends on the fourth generation quark masses, should be even smaller than the bound in Eq. 1.5. Fig. 1.8, from [58] shows the evolution of s_{34} with the mass of the u_4 quark, and puts an upper limit at 95% C.L.[18]:

$$s_{34} \leq 0.24 \tag{1.7}$$

It can be seen that this limit is tighter than the so-called $S-T$ constraints [57].

Applying now the unitarity constraint to the CKM4 matrix, and the latter s_{34} constraint in Eq. 1.7, [58] has obtained the following V_{ij}^{CKM4} element magnitudes at 95% C.L.:

$$\begin{pmatrix} |V_{ud}| & |V_{us}| & |V_{ub}| & |V_{ub'}| \\ |V_{cd}| & |V_{cs}| & |V_{cb}| & |V_{cb'}| \\ |V_{td}| & |V_{ts}| & |V_{tb}| & |V_{tb'}| \\ |V_{t'd}| & |V_{t's}| & |V_{t'b}| & |V_{t'b'}| \end{pmatrix} = \begin{pmatrix} 0.97425 \pm 0.04\% & 0.2252 \pm 0.8\% & 3.89 \times 10^{-3} \pm 23\% & \leq 0.042 \\ 0.22 \pm 4\% & \geq 0.95 & 40.6 \times 10^{-3} \pm 6\% & \leq 0.22 \\ \leq 0.04 & \leq 0.09 & \geq 0.97 & \leq 0.24 \\ \leq 0.08 & \leq 0.21 & \leq 0.25 & \geq 0.94 \end{pmatrix}$$

[18] This assumes that t' quark with mass below 300 GeV are excluded, which is the case from direct searches as we will see later.

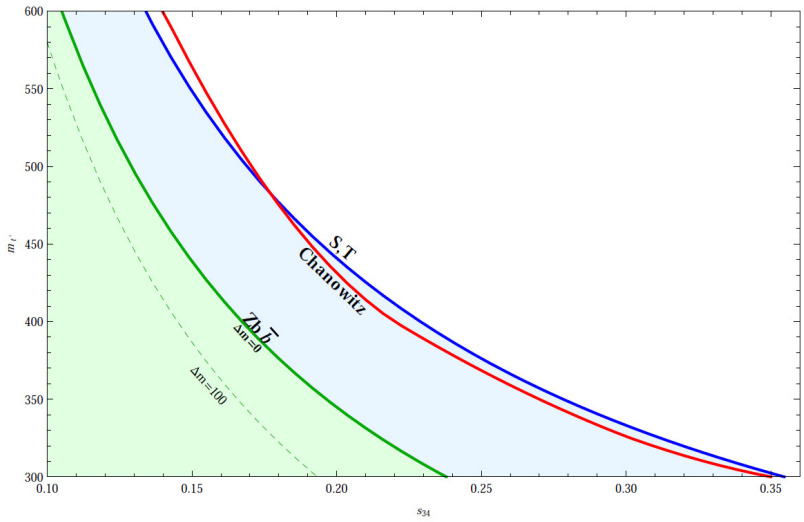

Figure 1.8: Upper limits at 95% C.L. on s_{34} depending on $m_{t'}$. The tighter constraint (green) is shown for two values of mass splitting $\Delta m = m_{t'} - m_{b'}$ [58].

We can notice that the terms $|V_{t's}|$ and $|V_{cb'}|$ are allowed to be sizable, translating a potential mixing with the second generation. However, we will not consider this possible in the following, in analogy with the mixing observed between the three known generations.

Note that these results, especially the bound in Eq. 1.7, should be revisited in view of the recent observation of the 126 GeV scalar boson, as the bound $s_{34} < 0.24$ was obtained assuming $m_{\nu'} > 90\ GeV$ and $m_H \in [117, 1000]$ GeV. As we will emphasize a bit later (Sec. 1.2.1.5), in the present situation, one should assume $46 < m_{\nu'} < 63$ GeV, where $S-T$ formulae are not valid, and apply latest NLO corrections.

Production mode At the LHC, a proton-proton collider (see Secs. 2.1 and 2.2 for a description of the experimental framework and phenomenology), the heavy quarks can be pair-produced via strong interaction, as shown in Fig. 1.9 (a), or via electroweak single-production, as shown in Figs. 1.9 (b) and (c). While the strong production is independent of the CKM4 mixing elements, the electroweak $t'\bar{b}$ ($\bar{t}'b$) and $\bar{t}b'$ ($t\bar{b}'$) productions scale by a factor $|V_{t'b}|^2 \simeq |V_{tb'}|^2$ and are strongly suppressed if these CKM mixing elements are negligibly small. For the small s_{34} values considered in the previous section, *e.g.* below 0.1, the $t'\bar{b}'$ ($\bar{t}'b'$) electroweak production overtakes $t'\bar{b}$ ($\bar{t}'b$) production by two orders of magnitude.

Table 1.1 shows LO and NLO predictions[19] of the cross-section of strong production and electroweak $t'\bar{b}'$ and $\bar{t}'b'$ productions (assuming a maximal $|V_{t'b'}|^2 = 1$), for $\sqrt{s} = 7, 8$ and 14 TeV. It is interesting to notice that the total electroweak production considered here amounts to $\sim 20\%$ of the sum of the three cross-sections. Nevertheless, as it is dominant and has a much simpler final state, we will only consider the strong production in our search in Chap. 4.

[19] It is interesting to compare the LO and NLO values quoted here to the NNLO cross-sections we will show in Sec. 4.5.2 to illustrate the functioning of perturbation theory.

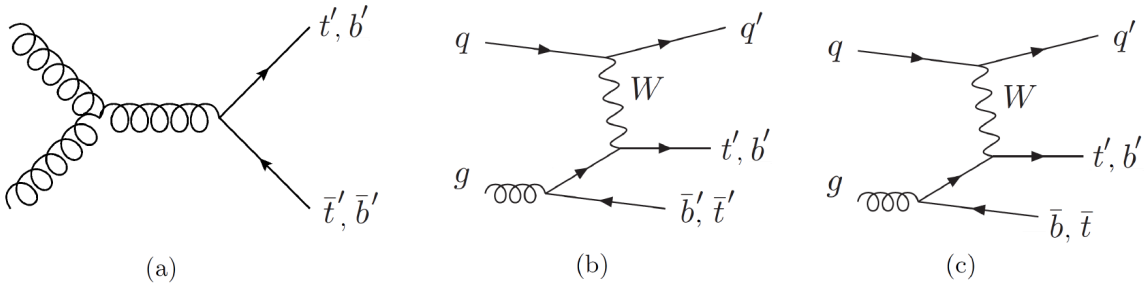

Figure 1.9: Feynman diagrams at tree level for the production of fourth generation quarks: (a) Strong pair production ; (b) $2 \to 3$ diagrams contributing to $t'\bar{b}'$ and $\bar{t}'b'$ electroweak production in the t-channel ; (c) $t'\bar{b}$ and $\bar{t}b'$ electroweak production in the t-channel (and the charge-conjugate processes) [59].

$m_{t'}$	$m_{b'}$	$\sigma^{7\text{TeV}}_{t'\bar{b}'}$ (fb)	$\sigma^{8\text{TeV}}_{t'\bar{b}'}$ (fb)	$\sigma^{14\text{TeV}}_{t'\bar{b}'}$ (fb)
500	450	(32.9) $49.7^{+7.8+8.8}_{-4.6-6.1}$	(57.1) $92.6^{+11.1+12.6}_{-6.4-9.3}$	(468) 610^{+32+40}_{-17-35}
$m_{t'}$	$m_{b'}$	$\sigma^{7\text{TeV}}_{\bar{t}'b'}$ (fb)	$\sigma^{8\text{TeV}}_{\bar{t}'b'}$ (fb)	$\sigma^{14\text{TeV}}_{\bar{t}'b'}$ (fb)
500	450	(12.2) $18.9^{+4.0+5.0}_{-1.7-2.4}$	(23.4) $42.3^{+5.9+8.1}_{-1.6-3.8}$	(239) 300^{+23+32}_{-9-17}
$m_{Q\bar{Q}}$		$\sigma^{7\text{TeV}}_{Q\bar{Q}}$ (fb)	$\sigma^{8\text{TeV}}_{Q\bar{Q}}$ (fb)	$\sigma^{14\text{TeV}}_{Q\bar{Q}}$ (fb)
500		(228) $314^{+70.8+81}_{-37.1-48}$	(393) $542^{+107+124}_{-59-76}$	(2767) $3861^{+422+510}_{-257-368}$

Table 1.1: $\sqrt{s} = 7, 8$ and 14 TeV NLO predictions for the electroweak $t'\bar{b}'$ and $\bar{t}'b'$ productions, assuming $|V_{t'b'}|^2 = 1$, and for $Q\bar{Q}$ strong production. LO predictions are given in parentheses. From [59]. See reference for details about simulation and errors quoted.

Decay modes In addition to the CKM4 mixing parameters, the decay modes of the new quarks will depend on their masses. Typically, this will depend on the mass splitting $\Delta m_{q'} = m_{t'} - m_{b'}$:

- if $\Delta m_{q'} > m_W$, one would expect naively the decay $t' \to Wb'$ to occur directly;
- if $-\Delta m_{q'} > m_W$, one would instead expect the decay $b' \to Wt'$ to occur;
- if $|\Delta m_{q'}| < m_W$, one can expect the fourth-generation quarks to decay to the third generation quarks: $t' \to Wb$ or $b' \to Wt$. This scenario is in accordance with the actual mass and mixing patterns of the known quarks.

These different scenarios would lead in principle in numerous signatures depending on the production modes of the new quarks, with *e.g.* up to six W bosons in the final state (see *e.g.* [59] for a study of these signatures at the LHC). Fortunately, electroweak precision observables constraint the mass splitting of the fourth-generation quarks. Figure 1.10 from [54] shows such constraints on the mass splittings $\Delta m_{q'}$ and $\Delta m_{l'} = m_{\nu_4} - m_{l_4}$, allowing for CKM mixing and free lepton masses (see reference for details about the fit hypotheses). One can see that the fit favors the scenario in which $|\Delta m_{q'}| < m_W$, with a mass of the t' quark slightly higher than the b' mass. In our search in Chap. 4, we will hence consider this scenario in which $t' \to Wb$ and $b' \to Wt$.

However, even if $|\Delta m_{q'}| < m_W$, the $t' \to Wb'$ ($b' \to Wt'$) can occur via exchanging virtual W bosons and compete for example with the CKM suppressed decay $t' \to Wb$ ($b' \to Wt$) when $|V_{t'b}| \simeq$

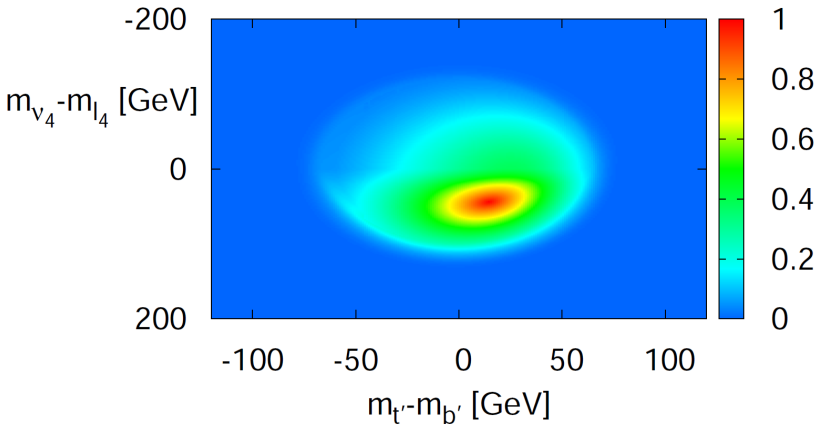

Figure 1.10: Allowed mass splitting of fourth generation fermions according to the constraints from electroweak precision observables, allowing for CKM mixing and free lepton masses [54].

$|V_{tb'}| << |V_{t'b'}|$. To quantify such statement, formulae for computing the two-body decay widths of a heavy t' and b' are given in [59] for a classical quark mass ordering ($\Delta m_{q'} > 0$):

$$\Gamma(t' \to Wq) = \frac{G_F m_{t'}^3}{8\pi\sqrt{2}} |V_{t'q}|^2 f_1(\frac{m_q}{m_{t'}}, \frac{m_W}{m_{t'}}), \tag{1.8}$$

$$\Gamma(t' \to b'W^{(*)}) = \frac{G_F^2 m_{t'}^5}{192\pi^3} |V_{t'b'}|^2 f_2(\frac{m_{t'}^2}{m_W^2}, \frac{m_{b'}^2}{m_W^2}, \frac{\Gamma_W^2}{m_W^2}), \tag{1.9}$$

where f_1 and f_2 are parametric functions that can be found in the reference. Figure 1.11, also from [59], shows the relative fraction $\Gamma_{t' \to b'W^{(*)}}/\Gamma_{t' \to Wb}$ versus the mass difference $\Delta m_{q'}$ for $m_{t'} =$ 500 GeV.

We clearly see that the $t' \to b'W$ decays can compete with the $t' \to Wb$ decays when $\Delta m_{q'} >$ 80 GeV for $s_{34} < 0.1$, and systematically dominate for $s_{34} < 10^{-3}$. However, for our benchmark scenario where $\Delta m_{q'} < m_W$, the $t' \to Wb$ decays dominate. The relative fractions $\Gamma_{b' \to t'W^{(*)}}/\Gamma_{b' \to tW}$ versus $m_{b'} - m_{t'}$ lead to similar results considering the same mass scale. For these reasons, we will consider branching ratios $\mathrm{BR}(t' \to Wb) = 100\%$ and $\mathrm{BR}(b' \to Wt) = 100\%$ in our search in Chap. 4, keeping in mind that for very high quark masses, the *actual* branching ratio might be lower for very low mixing.

It has also been pointed out in *e.g.* [70, 71] that if mixing angles are tiny ($\sim 10^{-13} < \theta_{34} <\sim 10^{-8}$ and $m_{t'} \sim m_{b'}$, heavy quarks could have a proper lifetime of $\sim 10^{-11} < \tau'_q <\sim 1$ s. Their decay lenght could hence range at the LHC (cf. Chap. 2) from a few millimeters to many meters. Such scenario would require to revisit the conventional search strategies.

1.2.1.4 Direct limits

Assuming $\mathrm{BR}(t' \to bW) = 100\%$ and $\mathrm{BR}(b' \to tW) = 100\%$, current best direct searches at high-energy hadron colliders excluded $m_{t'} < 570$ GeV [138] and $m_{b'} < 611$ GeV [139] at 95% CL (see also Sec. 4.3.2 for more details). Both searches require the identification of at least one b-quark in the final state. Without this requirement, another search looked recently for pair-produced heavy quarks $Q\bar{Q}$

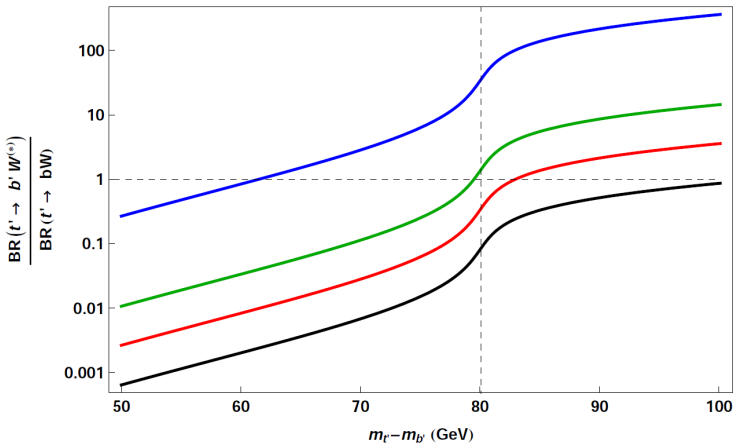

Figure 1.11: Ratio of the $t' \to b'W^{(*)}$ and $t' \to Wb$ decay widths for a classical quark mass ordering, for $m_{t'} = 500$ GeV with $|V_{t'b}| = 0.2$ (black), $|V_{t'b}| = 0.1$ (red), $|V_{t'b}| = 0.05$ (green), and $|V_{t'b}| = 0.01$ (blue) [59].

with $\mathrm{BR}(Q \to qW) = 100\%$, allowing $q = d,s,b$ for up-type Q final states, or $q = u,c$ for down-type Q final states [43]. It excluded $m_Q < 350$ GeV at 95% CL, and provides a more conservative bound.

Note that before this work began, the best limits were $m_{t'} > 450$ GeV [136] and $m_{b'} > 495$ GeV [137].

Regarding the fourth generation lepton sector, the LEP put a lower bound $m_{\tau'} > 100$ GeV [31]. Assuming Dirac masses, we previously stated the limit $m_{\nu'} > 46$ GeV for new heavy stable neutrinos.

1.2.1.5 Constraints from SM scalar boson searches

Recent results of SM scalar boson searches at the LHC have significantly impacted the prospects and focus of heavy-quark searches. In particular, the observation of a new boson by the ATLAS [52] and CMS [53] Collaborations with a mass of ~126 GeV and couplings close to those expected for the SM scalar boson disfavors [64, 65, 69, 59] perturbative chiral fourth-generation models.

This is due to the fact that a new family of fermions significantly modifies the SM scalar boson production and decay rates with respect to the SM. At leading order, the SM scalar boson production cross-section via gluon-gluon fusion increases by a factor of 9 due to the additional t' and b' fermion loops. However, this argument must not hide that the decay rates can also be altered, and might leave the product:

$$\sigma(gg \to H) \cdot BR(H \to XX) \tag{1.10}$$

for the SM4 comparable to the one in SM3. Generally, here are important considerations illustrating that it is not possible to fully exclude perturbative fourth generation yet:

- **SM scalar boson invisible decay**: if a new neutral lepton ν_4 is lighter than half the SM scalar boson mass, the opening of the new invisible mode $H \to \nu'\bar{\nu}'$ increases the total width, and can overtake the $H \to WW, ZZ$ and $f\bar{f}$ with a substantial branching ratio (*e.g.* [63, 59]). Assuming $m_H = 126$ GeV, a neutrino fulfilling $46 < m_{\nu'} < 63$ GeV constitutes a crucial region of the parameter space that could escape the constraints from electroweak corrections, and should be considered carefully;

- **NLO electroweak corrections**: as seen previously, current direct limits on the fourth generation quark indicate roughly $m_{t',b'} \geq 500$ GeV. Even if these limits are model dependent (*e.g.* assuming unity branching ratios as we have seen) and could *actually* be lowered, for such high masses (see next section), perturbation computations are difficult and NLO predictions typically suffer very large uncertainty. For example, the NLO rate $\sigma(gg \to H) \cdot BR(H \to \gamma\gamma)|_{SM4}$ is suppressed by one order of magnitude with respect to the LO result due to accidental cancellation of boson and fermion loop diagrams [59]. Such behavior raises legitimate concerns about the stability of the NLO predictions for $BR(H \to \gamma\gamma)$, especially considering very high fourth generation quark masses.

Given the fact that the couplings of the new particle discovered at the LHC are not known yet with great precision, it becomes fairly clear that the perturbative fourth generation model may still remain viable in various scenarios. While the motivations for directly searching for such model were already very strong prior to the new boson observation, these direct search are still well motivated.

1.2.2 SM4 non-perturbative scenario

As introduced hereabove, for very heavy fermions, the weak interaction would become strong, and the perturbation expansion would fail (non-perturbative Yukawa couplings). The bound from partial wave unitarity is reached at some high fermion mass scale, which is around 500 GeV for quarks and 1 TeV for leptons [56]. While this is not attractive from the theory point of view, there is no fundamental reason that quarks with masses much higher than $\sim$500 GeV might not exist in nature, so direct searches must be pursued also in this scenario.

1.2.3 SM4 + new physics scenario

An easy way to avoid bounds on the fourth generation from SM scalar boson observations is to extend the scalar sector. For example, a fourth generation can be compatible with two scalar doublets [72, 67], or SUSY models.

1.2.4 Vector-Like quarks scenario

As we have seen, a fourth-generation of chiral quarks in the perturbative regime is not favored by the recent observation at the LHC, and might soon be excluded if the experiments measure precisely the scalar boson couplings as in the SM. Another possibility is the addition of weak-isospin singlets or doublets of so-called *vector-like* quarks, which have vector-like couplings to the weak interaction.

To understand this, we need to complete the picture of the SM that we gave in Sec. 1.1 by mentioning that all physical fermion fields propagating through space are actually a superposition, or quantum mixture, of two field states called 'left-chiral' and 'right-chiral'[20] (at the exception of neutrinos that have only been observed as left-chiral for the time being). In the SM, left-chiral fields do carry a weak (isospin) charge: $+1/2$ for up-type fields and $-1/2$ for down-type fields; while right-chiral fields do not carry any, which means that the weak force only interact with left-chiral particles[21]. Chirality implies that *e.g.* an electron can be either observed as a left-chiral electron or a right-chiral electron in

[20] The notion of fermion chirality refers to the two types of spin-1/2 representations of the Poincaré group. The physical meaning of this can be schematized considering the phase of a particle wave-function: when the fermion is rotated, its quantum wave-function is shifted in a way that depends on its chirality.

[21] The SM is hence called a *chiral* theory, and explains for example why nuclear beta decays (mediated by the W bosons) always produce left-chiral neutrinos.

the mass-basis. Such oscillations between the two field states, that break isospin charge conservation, are due to the SM scalar field non-zero v.e.v. arising from EWSB. Formally, left-chiral up and down quarks and leptons are grouped in SU(2) doublets, *e.g.* $(e,\nu_e)_L$ or $(u,d)_L$. The right-chiral counterparts of quarks and up-type leptons are left in SU(2) singlets, *e.g.* e_R, or u_R and d_R. Regarding the strong and electromagnetic interactions, they behave in the same way with respect to left-chiral and right-chiral particles.

Vector-like, *i.e.* non-chiral, quarks are quarks for which both chiralities have the same transformation properties under the electroweak group $SU(2) \times U(1)$. Such quarks receive a mass that is independent of the EWSB mechanism, hence can naturally have masses of the order of 1 TeV, and escape most of the theoretical and experimental constraints compared to chiral quarks. In addition, they do not enhance the SM scalar boson production by gluon fusion at the LHC and are decoupled from EW observables. While being physics 'beyond Standard Model', vector-like quark models have SM $SU(3) \times SU(2) \times U(1)$ quantum numbers and effective Lagrangians invariant under the SM gauge symmetry. They appear in many extensions of the SM such as 'Little Higgs' or extra-dimensional models (see e.g. [171] and references therein). In these models, a top-partner quark often plays a key role in canceling the quadratic divergence in the SM scalar boson mass induced by radiative corrections involving the top quark.

The simplest model we will test in Chap. 4 is the addition to the SM of massive $SU(2)$ up-type singlets t'_L and t'_R of electric charge 2/3. Such quarks can decay through Yukawa couplings with the ordinary SM quarks. As the mixing is proportional to the mass of the SM quark [172], our vector-like quark will mix preferentially with third-generations quarks, and has *a priori* three possible decay modes:

$$t' \to W^+ b, \qquad t' \to tH, \qquad t' \to tZ \tag{1.11}$$

with branching ratios that vary as a function of $m_{t'}$. Contrary to fourth-generation chiral quarks where the first mode is dominant, the proportions of W, Z and H bosons produced will be close to $2:1:1$ [173]. This is also true of other varieties of vector-like quarks and top partners [144].

Such vector-like quarks could also decay through magnetic moment couplings [173], in which case the dominant decays for the t' would be:

$$t' \to gt, \qquad t' \to \gamma t, \qquad t' \to Z^0 t, \tag{1.12}$$

with the latter decays having branching ratios of several percent. However, we will not consider this kind of decays, but focus on the W^+b, Zt and Ht decays as they share common features with chiral fourth-generation quarks, as we will see later in much extent.

1.2.5 Conclusion

In all previously stated scenarios, it appeared justified to search directly for the production and decay of new heavy quarks. We isolated one of the most interesting processes: pair-produced up-type quarks t' decaying promptly to a W boson and a b-quark, which can be interpreted in a number of ways, including the vector-like quark model. This will be the signature that we will search for in Chap. 4, with the experimental framework that we will now describe in Chap. 2. The identification of b-quarks will be done thanks to algorithms that we will commission in Chap. 3. Note also that we have identified scenarios less 'favored' for the moment, but that would certainly be worth studying in the future, such as signatures with long-lived quarks in the final state (due to very tiny mixing between the fourth and lighter generations), or signatures with more W bosons in the final state (*e.g.* considering $t' \to b'$ decays, or electroweak $t'\bar{b}'$ single production).

Chapter 2

Experimental framework

We will now describe the experimental framework, starting by a description of the Large Hadron Collider and notions of proton-proton collision phenomenology.

We will then describe the ATLAS experiment we belong to. During its description, we will focuse at some point (Sec. 2.3.3) on a contribution we made to a system intended to protect the innermost sub-detector of the ATLAS detector. In the context of this work, the following papers were published in scientific journals [73, 74, 75].

Then, we will give an overview of the ATLAS detector upgrade plans, and focuse on the major coming upgrade, called IBL, as we have contributed to evaluate the performance of b-quark identification (see next Chapter in Sec. 3.7) with this new detector layer. In the context of this work, the author presented a poster about *ATLAS Upgrade Plans* [91] at the 105^{th} LHCC meeting that took place at CERN on March 23-24^{th} 2011.

2.1 The Large Hadron Collider

The Large Hadron Collider (LHC) [76] is a particle collider located at CERN near Geneva, Switzerland. It is designed to collide proton beams with a center-of-mass energy $\sqrt{s}$ of 14 TeV, and lead ions with an energy of 2.8 TeV per nucleon. Since December 2009, it is the world most powerful Particle Physics collider, superseding the Tevatron collider[1]. The LHC is located $\sim$100 meters beneath the Franco-Swiss border in the 27 km in circumference tunnel that used to host the LEP collider.

2.1.1 Interest of proton-proton collisions

The choice of protons for the collisions at the LHC was made mainly for the following reasons:

- it allows to reach a much higher energy than using electrons. This is due to the fact that relativistic charged particles of mass m and energy E accelerated in a ring of radius R are losing energy through synchrotron radiation:

$$\Delta E \propto \frac{E^4}{m^4 R} \tag{2.1}$$

  As protons are $\sim$ 1836 times heavier than electrons, the energy loss per tunnel round is $\sim 10^{13}$ times lower, becoming negligible compared to the proton beams energy.

[1] A proton-antiproton which operated until September 2011 at $\sqrt{s}$ =1.96 TeV near Chicago, USA.

- it is much more easy to produce protons than antiprotons. At the Tevatron, this was a limiting factor to the number of collisions observed per unit of time, due to a production rate of antiprotons ∼50k times lower than the one of protons.

However, protons are composite objects, which is also the source of difficulties, as we will see later. One of them is that the energy *available* at each collision is not known with precision, and follows a wide spectrum around the third of $\sqrt{s}$.

2.1.2 Proton acceleration chain

In the following, we will sometimes make the approximation that the LHC is a circular ring of radius $R \simeq 4.3$ km, and consider a moving referential attached to the protons circulating along this ring: the $\overrightarrow{z}$ unit-vector lies along the proton direction, the $\overrightarrow{x}$ unit-vector points from the proton to the center of the ring, and the $\overrightarrow{y}$ unit-vector is vertical pointing upwards, $\{\overrightarrow{x};\overrightarrow{y};\overrightarrow{z}\}$ being a direct coordinate system. At the point where the protons will collide, the plan formed by the $\overrightarrow{x}$ and $\overrightarrow{y}$ vectors will be called the *transverse* plane, and the $\overrightarrow{z}$ direction the *longitudinal* direction. The component in the transverse plane of the momentum of particles will be denoted p_T.

The CERN accelerator complex is illustrated in Fig. 2.1. Protons are created from a hydrogen gas ionized by an electron beam, pre-accelerated by the LINAC2 to 50 MeV, and sent to the Proton Synchrotron (PS) BOOSTER where their energy is increased to 1.4 GeV. They are then sent to the PS, in which bunches of $\sim 10^{11}$ protons are formed, spaced nominally by 25 ns (*i.e.* at a frequency of ∼40 MHz)[2], and accelerated to reach an energy of 26 GeV. The next synchrotron, the SPS (Super PS), accelerates them to an 'injection' energy of 450 GeV. At this point, protons are ready to be injected into the LHC as two bunched beams in opposite directions.

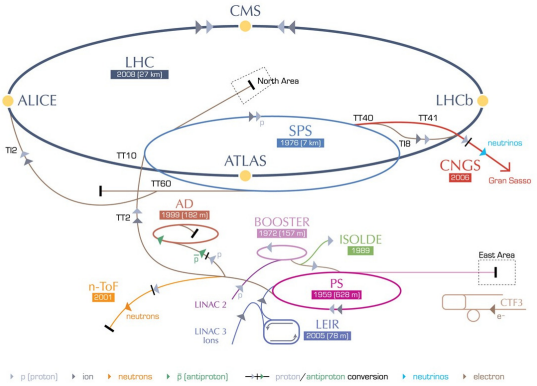

Figure 2.1: The CERN accelerator complex.

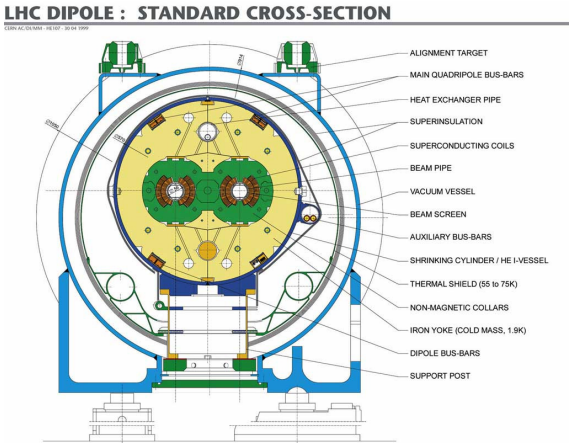

Figure 2.2: Sectional view of a dipole magnet, showing the two separate vacuum chambers.

The acceleration of the beams to their 'final' energy is done thanks to superconducting Radio Frequency (RF) cavities (8 per beam), which provide RF energy to the beams and keep the bunches tightly bunched to ensure optimal conditions at the collision points (see next section). The RF system

[2]This duration is much smaller than the time of ∼89μs needed for a proton to make a complete revolution around the LHC. This would in principle allow to place 3564 proton bunches in the LHC, but for practical reasons, a maximum of 2808 bunches will be nominally used.

works by 'capturing' the beam, speeding up the slower moving particles and slowing down the faster ones so that the beam remains bunched into fine threads about 11 cm long. Without it, the beam quickly dissipates and cannot be used for physics.

The maximum energy the protons can reach is limited by the magnetic field which has to be applied in order to bend the trajectory of the protons and keep them in the LHC ring. For 7 TeV beams, the magnetic field has to be $\sim$8.4 T for the 17.6 km of the LHC ring that can be equipped with superconducting magnets. This technological prowess relies on 1232 15-meter long dipole[3] magnets made of superconducting coils in NbTi circulating a current of $\sim$12 kA. Because two protons beams cannot circulate in opposite directions in the same vacuum chamber with a single bending magnetic field, a 'two-in-one' design was chosen for the dipole magnets, as illustrated in Fig. 2.2. Two superconducting dipole magnets and two beam pipes lie in a single cryostat cooled down to the super-fluid Helium temperature of 1.9 K, making the LHC the largest cryogenic facility in the world.

In addition, 392 quadrupole[4] magnets are used to keep the beams focused, as well as higher multi-pole magnets for various corrections.

2.1.3 Interaction points

Along the LHC ring, there are four straight sections in which the beams are crossing each other. Four detectors are placed at these interaction points (see Fig. 2.1):

- ATLAS [79], A Toroidal LHC ApparatuS: a general purpose experiment (see Sec. 2.3).
- CMS [80], Compact Muon Solenoid: a general purpose experiment, with same goals as ATLAS.
- ALICE [78], A Large Ion Collider Experiment: experiment intended to observe heavy ion collisions and study the properties of the quark-gluon plasma. This is the state of the universe which is believed to have existed in the early universe, a high-temperature phase, which would have essentially disappeared through expansion and cooling until the current low-temperature phase dominated by hadrons.
- LHCb [81]: experiment intended mainly to study the parameters of CP violation in the decays of hadrons containing bottom quarks. As we briefly introduced in Chap. 1, new physics can be searched indirectly studying electroweak decays (such as $B_s \to \mu^+\mu^-$, $B_s \to J/\psi\phi$ etc).

In the center of these four detectors, the size of the beams is squeezed down as much as possible to increase the chances of proton-proton collisions. The relative beam sizes around the interaction point are illustrated *e.g.* for ATLAS in Fig. 2.3. Beams are crossing with a small crossing angle of the order of 150-200 μm in order to avoid the occurence of parasitic collisions.

While proton collisions are occurring at an incredible rate, as we will see in much detail later, most protons miss each other and carry on around the ring time after time. Typically, the beams are kept circulating for hours, and their intensity slightly decreases due to the protons 'lost' in the collisions.

2.1.4 Luminosity

Besides its center-of-mass energy $\sqrt{s}$, the most important feature of a particle collider such as the LHC is called its *instantaneous luminosity* $\mathscr{L}$, which directly translates the number of collisions that the collider is able to produce per unit of time, given by the formula $N = \mathscr{L} \cdot \sigma$, where $\mathscr{L}$ is expressed

[3] Two coils are ensuring the magnetic field direction to be along the y-axis.

[4] Four coils are ensuring the magnetic field lines to point toward the beam pipe.

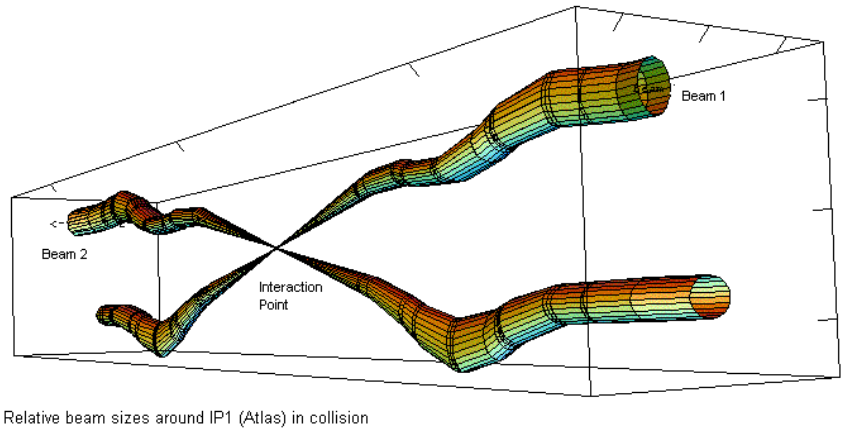

Figure 2.3: Relative beam sizes around the interaction point of ATLAS in collision.

in $\mathrm{cm}^{-2}\mathrm{s}^{-1}$, and σ is the cross-section of a physics process, expressed in barns[5]. For colliding beams of proton bunches with Gaussian dimensions, $\mathscr{L}$ is given by the formula:

$$\mathscr{L} = \frac{N^2 \cdot B \cdot f_r}{4\pi \cdot \sigma_x \cdot \sigma_y} F \tag{2.2}$$

where:

- N is the number of protons per bunch;
- B is the number of bunches in the LHC ring per round;
- f_r is the revolution frequency of the bunches around the LHC ring;
- σ_x and σ_y are the width of the Gaussian distributions of the beams in the transverse plane at the interaction point;
- F is a geometrical factor due to the crossing angle of the beams at the interaction point.

One can also integrate $\mathscr{L}$ over time to get the so-called *integrated* luminosity $\mathscr{L}_{int} \equiv \int \mathscr{L}(t)dt$. Table 2.1 summarizes the main LHC features for the 2010, 2011, 2012 and design functioning. Figure 2.4 shows the integrated luminosities as a function of the time.

2.1.5 Start-up and first collisions

On September 10^{th} 2008, proton beams were successfully circulated in the main ring of the LHC for the first time. 9 days later, operations were halted due to a magnet quench incident resulting from an electrical fault. The ensuing helium gas explosion damaged over 50 superconducting magnets and their mountings, and contaminated the vacuum pipe. On November 20^{th} 2009 proton beams were successfully circulated again, with the first recorded proton-proton collisions occurring 3 days later at the injection energy of 450 GeV per beam. On November 30^{th} 2009, the first collisions took place between two 1.18 TeV beams, setting the world record for the highest-energy man-made

[5] $1\ \mathrm{b} = 10^{-24}\ \mathrm{cm}^2$

Parameter	2010	2011	2012	nominal
$\sqrt{s}$ (TeV)	7	7	8	14
N	$1.2{\cdot}10^{11}$	$1.2{\cdot}10^{11}$	$1.2{\cdot}10^{11}$	$1.2{\cdot}10^{11}$
B	368	1380	-	2808
bunch spacing (ns)	50	50	50	25
f_r (kHz)	11	11	11	11
$\sigma_{x,y}$ (μm)	$\sim$60	-	-	$\sim$16
$\mathscr{L}$ (cm^{-2}s^{-1})	$2.1{\cdot}10^{32}$	$3.2{\cdot}10^{33}$	$7.73{\cdot}10^{33}$	10^{34}
$\mathscr{L}_{int}$/year	48.1 pb^{-1}	5.61 fb^{-1}	23 fb^{-1}	100 fb^{-1}

Table 2.1: Main features of the LHC, in nominal functioning, and during the peak instantaneous luminosity records in 2010, 2011 and 2012, shown together with the integrated luminosities per year.

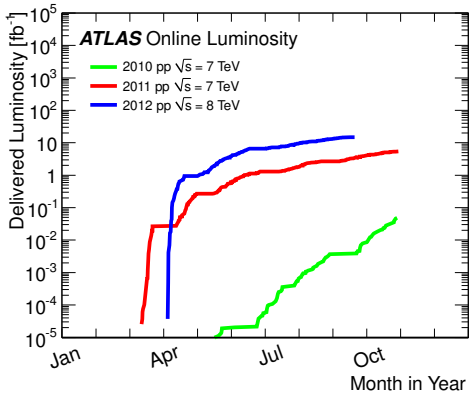

Figure 2.4: Cumulative luminosity versus day delivered to ATLAS during stable beams and for p-p collisions. This is shown for 2010 (green), 2011 (red) and 2012 (blue) running.

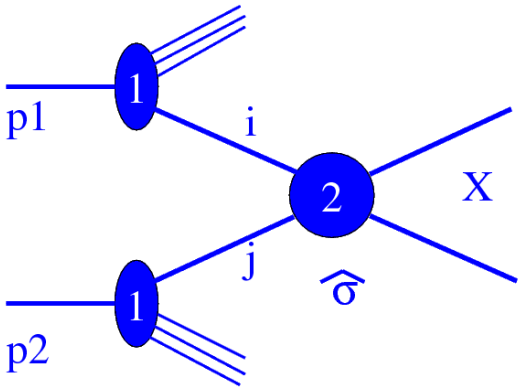

Figure 2.5: Illustration of the principle of a proton-proton collision.

particle collisions. On March 30th 2010, the two beams collided at 7 TeV (3.5 TeV per beam). The half designed energy was decided to start safely the LHC physics program even before a complete upgrade of the magnetic systems that was diagnosed to be needed for a safe operation at the design luminosity of 14 TeV (7 TeV per beam). On April 5th 2012, it was decided to run the LHC at 4 TeV per beam to improve the physics reach of the experiments.

2.2 Proton-proton collisions phenomenology

Hadron colliders are today the only machines able to produce collisions with such high energy and luminosity. This comes at a price. Contrary to electron-positron, for which one can assume the initial particles as point-like, the protons are composite objects, so the energy *used* during the hard-interaction is not the one from the proton-proton center-of-mass $\sqrt{s}$. As a consequence, the longitudinal momentum of the particles in the initial state is not known *a priori*. The remnants of the protons are carrying the largest part of the available energy. While this energy is usually lost in the beam pipe, it can also contaminate the interesting event (so-called 'underlying event', see later).

2.2.1 Parton model

At the energies accessible at the LHC, the proton can be considered as a gas of quasi-free partons i (quarks and gluons), each one having a fraction $x_i \in [0,1]$ of the total momentum. These partons constitute the initial state of the collision, and the cross-section of the process $pp \to X$ can be factorized as follows:

$$d\sigma(pp \to X) = \sum_{i,j} \int_0^1 dx_i dx_j f_i(x_i, Q^2) f_j(x_j, Q^2) d\hat{\sigma}(q_i q_j \to X, \hat{s}, Q^2) \tag{2.3}$$

where $\sqrt{\hat{s}} = \sqrt{x_i x_j s}$ is the energy in the center-of-mass of the two incoming partons q_i and q_j, as illustrated in Fig. 2.5. The sum is done over all the combinations of pairs of partons able to lead to the final state in question. The associated partonic cross-sections $d\hat{\sigma}$ are 'easily' computable at the lowest order in the perturbation theory (*Leading Order*, LO). While the order of magnitude is correct using only a LO estimate, higher order computations (*Next^n Leading Order*, N^{n}LO) are necessary to get a more precise estimate. Q is the typical energy scale used in these computations. The functions f_i, called the *parton distribution functions* (PDFs), define the probability density functions of finding a particle with a certain longitudinal[6] momentum fraction x_i at momentum transfer Q^2. These PDFs are not computable using perturbation theory, and have to be determined using experimental inputs (*e.g.* HERA, Tevatron)[7].

2.2.2 Minimum bias events

Cross-sections for various physics processes at the LHC are shown in Fig. 2.6. Let us focus first on the total proton-proton cross-section, amounting to $\sim$100 mb, which can be broken down into two contributions:

- *elastic* scattering: *i.e.* collisions of particles in which the total kinetic energy of the particles is conserved. In other words, nothing new is produced during this kind of scattering. Proton elastic scatterings cannot be detected by experiments such as ATLAS, as they do not give rise to particles at sufficient high angles with respect to the beam axis[8]. We will not consider this kind of scattering in the following.

- *inelastic* scattering: In this case, the protons will convert part of their kinetic energy into the creation of new particles. One usually distinguishes[9]: single-diffractive (SD) $pp \to pX$, double-diffractive (DD) $pp \to XY$ (in which both protons dissociate with no net color flow between the systems X and Y), and non-diffractive (ND) $pp \to XY$ events (in which color flow is present between the two initial-state protons). Except for the very 'hard'[10] processes that we will describe in the next sections, the immense majority of these scatterings are 'soft' interactions, for which cross-sections can not yet be calculated by QCD, hence requiring non-perturbative phenomenological models to estimate them. The model used *e.g.* by the PYTHIA simulator[11] predicts cross-sections of 13.7 mb, 9.3 mb and 48.5 mb for the SD, DD and ND processes, respectively,

[6] The transverse momentum of the partons inside the protons is neglected.

[7] Major collaboration providing these PDFs are named *e.g.* CTEQ or MRST.

[8] However, 'forward' detectors placed very close to the beam pipe and far from the interaction point can detect elastic scatterings to measure σ_{tot} and the LHC absolute luminosity (*e.g.* the ALPHA detector for ATLAS).

[9] Neglecting so-called central-diffraction, estimated to be of the order of 1 mb.

[10] In the sense that the decay products have high energy, especially in the transverse plane of the detector. Similarly, 'soft' interaction have very low-p_T decay products.

[11] Pythia 6 [167] and Pythia 8 [168].

for a total of 71.5 mb. ATLAS has measured this value to be $\sigma_{inel} = 69.4 \pm 2.4(\text{exp.}) \pm 6.9(\text{extr.})$ mb [82], where (extr.), the biggest uncertainty, is due to the extrapolation from previous models to the LHC.

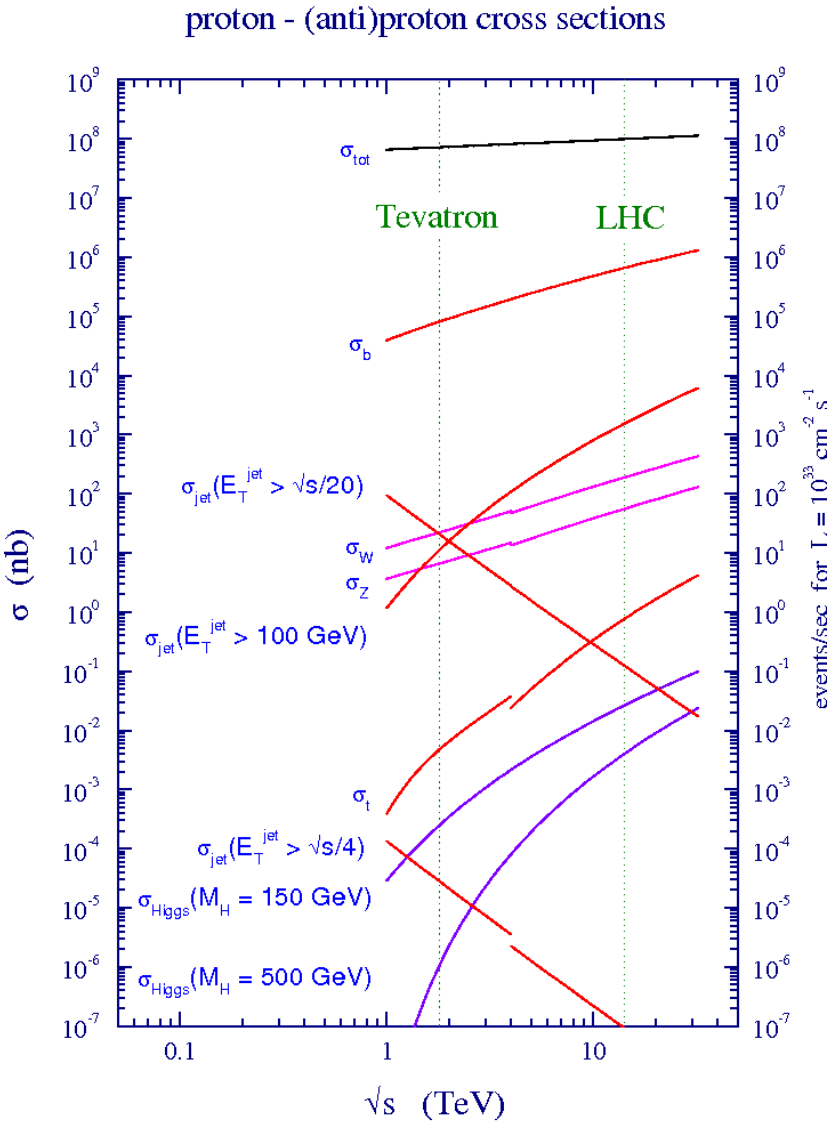

Figure 2.6: Production cross-sections of different processes at the Tevatron (proton-antiproton collisions) and at the LHC (proton-proton collisions) as a function of $\sqrt{s}$ [83]

Events from DD and ND events (or equivalently Non-SD events) are usually referred to as 'Minimum Bias' (MB) events, as they are the ones that will pollute the more our interesting collisions. A MB event is in principle what one would see with a totally inclusive selection of events, but the experimental definition depends on the way events are selected. Modeling MB in simulation is very important for high-p_T physics measurements, because due to its huge cross-section compared to rarer

events, it can become a major background to physics analyzes, especially at very high luminosities. In the following, we will sometimes refer to this background as 'QCD background', or 'QCD multijet' events.

2.2.3 Hard-scattering process

Looking back at Fig. 2.6, one can see that the second biggest cross-section shown is the production of b-quarks. Examples of Feynman diagrams for such production are shown in Fig. 2.7 at the LO ($\mathcal{O}(\alpha_s^2)$) and in Fig. 2.8 at NLO ($\mathcal{O}(\alpha_s^3)$). These series of diagrams are typically the ones that fit in the "2" box of Fig. 2.5. Subsequently, jets with higher and higher transverse energy, and particles with higher and higher masses (W, Z, SM scalar bosons, heavy quarks, etc) are produced with lower and lower cross-sections. All these processes are significantly different from minimum-bias events, and are very hard processes, well described by perturbative QCD, as we have seen previously. Note that given how rare all the interesting processes are compared to minimum bias events, it is extremely unlikely that more than one high-p_T interaction will occur during a same BC, and in practice this is considered to never be the case.

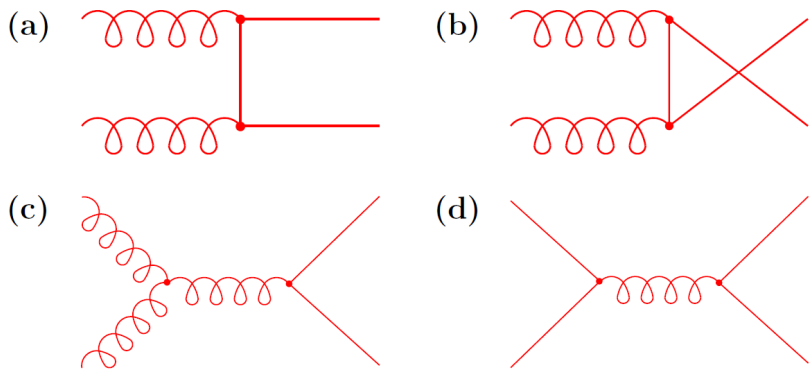

Figure 2.7: Leading order (LO) $\mathcal{O}(\alpha_s^2)$ Feynman diagrams for heavy quark production through (a)-(c) gluon-gluon fusion and (d) quark-antiquark annihilation [84].

2.2.4 Underlying-event

As seen previously, two partons are interacting during the hard-scattering process, but the remnants of the interacting protons can also contribute to the activity in the detector, and the interactions associated to this activity are collectively termed the *underlying event* (UE). The UE may involve contributions from both hard and low-p_T transfer between the scattering particles, the latter being difficult to account for by using perturbative QCD methods only. As it was the case for minimum-bias event, models based on experimental inputs have to be used, but this is even more challenging as subtle effects, such as color correlation with the hard-scattering, have to be taken into account. The modeling of the UE is very important for precise high-p_T measurements at the LHC, as *e.g.* jets from the UE can impact the calibration of the energy of jets from the hard process.

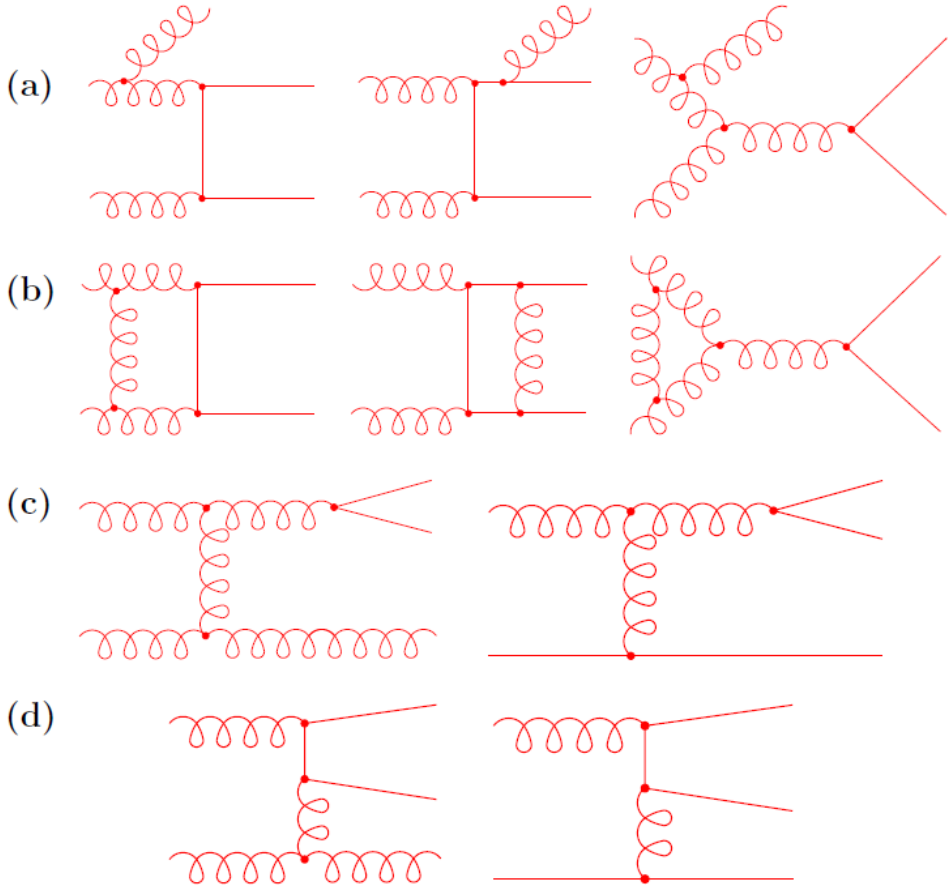

Figure 2.8: Examples of Feynman diagrams for heavy quark production at Next-to-Leading Order (NLO): (a) real emission, (b) virtual emission, (c) gluon splitting, and (d) flavour excitation [84].

2.2.5 Pileup

Let us now come back to the minimum-bias events, and see how many of them can occur in a bunch crossing (BC) at the LHC. Fig. 2.9 shows the luminosity-weighted distribution of the mean number of interactions per crossing for the 2011 and 2012 data. The mean number of interactions per crossing corresponds the mean of the Poisson distribution on the number of interactions per crossing calculated for each bunch. It is calculated from the instantaneous per bunch luminosity $\mathscr{L}_{bunch} \equiv \mathscr{L}/B$ as $\mu = \mathscr{L}_{bunch} \cdot \sigma_{inel}/f_r$ where σ_{inel} is taken to be 71.5 mb for 7 TeV collisions and 73.0 mb for 8 TeV collisions. From this figure, one can realize that much more than one collision occur per BC. Most important, it means that many minimum-bias events *add* to the interesting hard-process. Such MB events are referred to as *pileup* events. Note that contrary to the UE, minimum-bias pileup events are completely independent from the hard-process.

All the MB events occurring in the same BC as the hard-process are referred to as *in-time* pileup, and are polluting the final state of the event. At its designed luminosity, the LHC is expected to have on average 25 pileup interactions per BC. We will come back in details on some effects of in-time pileup in Sec. 3.7.

As seen previously, BCs are designed to be separated by 25 ns. However, the response from

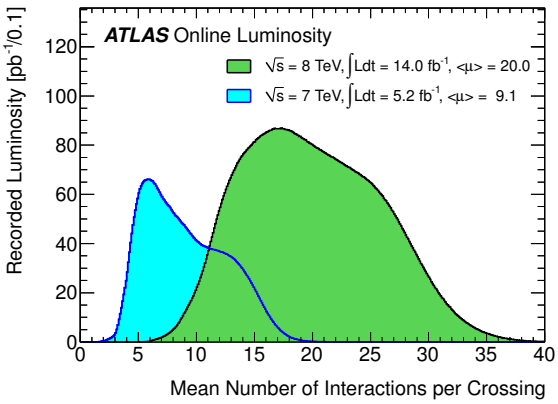

Figure 2.9: Shown is the luminosity-weighted distribution of the mean number of interactions per crossing for the 2011 and 2012 data. This shows the full 2011 run and 2012 data taken between April 4th and September 17th. The integrated luminosities and the mean μ values are given in the figure.

various sub-detectors can be significantly higher than this duration, so pileup events from a previous hard collision could spread electric signals to a subsequent hard collision. The polluting pileup events are referred to as *out-of-time* pileup.

2.2.6 From partons to hadrons

Let us now come back to the properties of QCD in order to understand what will happen to the external lines of the Feynam diagrams of our hard-interaction processes (seen *e.g.* in Figs. 2.5, 2.7 and 2.8) when it consists of quarks or gluons. Due to the property of confinement, free quarks (*i.e.* existing on their own) are never observed: if up, down, strange, charm, or bottom quarks are produced during extremely high-energy collisions at the LHC, they will initiate cascade reactions to lose progressively their energy; the top quark will instead decay before it has time to hadronize. Due to the equivalence between mass and energy, the cascade will necessarily translate in the production of numerous particles with lower energies, and the cascade will stop when the particles produced are in a 'stable' state. The cascade process, also referred to as *fragmentation*, can be factorized in two distincts steps, that we detail now.

Parton shower During the first phase, the partons (quarks and gluons) radiate gluons that in turn emit further gluons or produce quark-antiquark pairs, leading to the formation of *parton showers*. This is illustrated in Fig. 2.10, which shows parton showers from the output external lines of the hard-process diagram, also called *Final State Radiations* (FSR). During this phase, the energy of the partons is high enough so that perturbative QCD can be used. Each particle can produce two daugther particles as in these three basic processes: $q \rightarrow qg$, $g \rightarrow gg$ and $g \rightarrow q\bar{q}$. The probability of occurence of each process is proportionnal to the Altarelli-Parisi *splitting* functions $P_{a\rightarrow bc}$ which depend on the fraction of energy z carried by the partons. Parton showering can also occur for the input external lines of the diagram in Fig. 2.10, and terminates when they collide to initiate the hard subprocess. This is referred to as *Initial State Radiations* (ISR).

Looking back to Fig. 1.5, the parton shower phase corresponds to high momentum transfer where the QCD coupling constant α_s is low. During parton showering, the interaction scale falls and the strong interaction coupling rises, eventually triggering the process of *hadronization*.

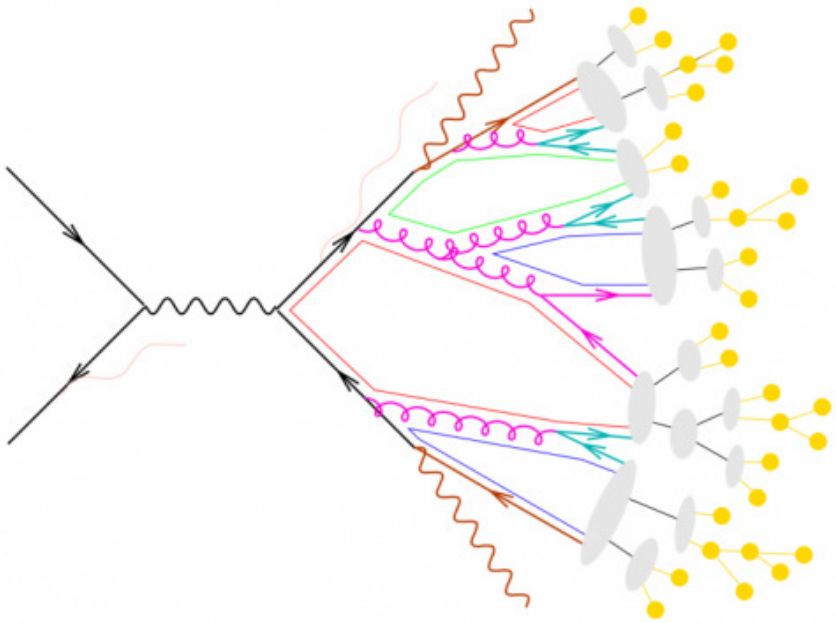

Figure 2.10: Illustration of the process of fragmentation: initial partons first initiate a parton 'shower' (colored quark and gluons lines), until triggering the process of *hadronization* that forms 'stable' particles (grey ellipses and yellow points and lines). See text for details.

Hadronization When the energy of the partons issued from the cascade reaction decreases to roughly 1 GeV, the QCD coupling constant is high and the energy available will start to create hadrons. In this non-perturbative regime, exact computations are not feasable and models have to be used. One of the most popular is the Lund 'string' model, which models the coupling between quarks by a color flux tube, as depicted in Fig. 2.11. This approximation is actually quite realistic when comparing to the result of lattice QCD simulation shown on the same figure. The potential energy accumulated in the string increases linearly with the separation of the two quarks. When produced at an annihilation point, quark and antiquark are moving rapidly apart. As the gluonic string is stretched between them, its potential energy grows at the expense of their kinetic energy. When the potential energy becomes of the order of hadron masses, it becomes energetically favourable for the string to break at some point along its length, through the creation of a new quark-antiquark pair. The two string segments then begin to stretch and break again, and so on until all the energy has been converted into quark-antiquark pairs connected by short string segments, which can be identified with hadrons. One iteration of this process is shown in Fig. 2.12 and Fig. 2.10 illustrates the repetition of such process in a more global picture, until stable hadrons are produced (in yellow).

Jets Due to the extremely high energy-momentum of the initial quarks produced in the hard-process, the cascade of particles produced during the fragmentation are very localized in space, typically contained in a cone whose axis is collinear with the direction of the initial quark. Such spread of particles associated to an incoming parton is referred to as a *jet*. It can also happen that a very hard gluon radiation may initiate a sufficiently energetic cascade to slightly modify this direction, or even create another jet.

During the hadronization process, the quark-antiquark pairs production in string breaking can be regarded as arising from vacuum fluctuations, so there is a preference for production of light flavours

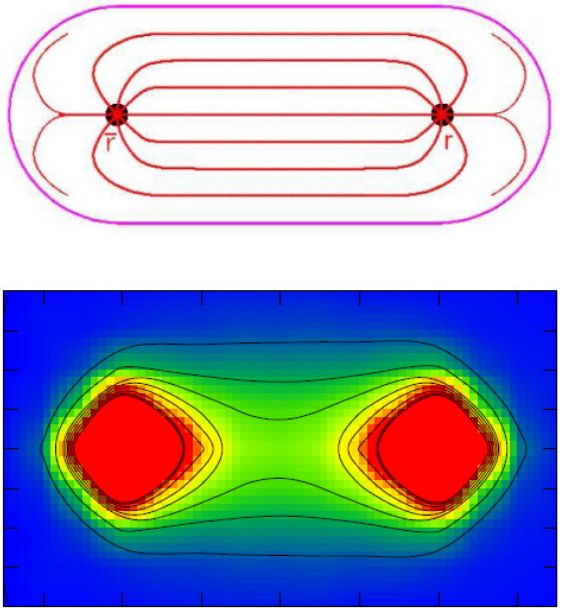

Figure 2.11: (top) Modelisation of the coupling between two quarks as a color flux tube. (bottom) Result from lattice QCD simulation of a quark and antiquark (red) 'glued' together (green) [87].

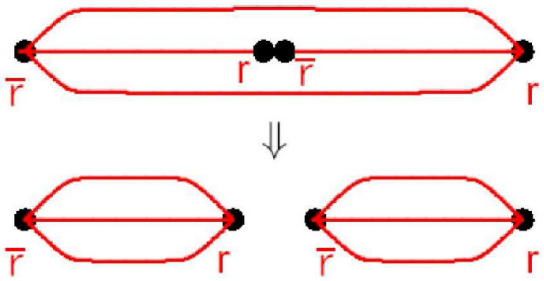

Figure 2.12: Illustration of the basic process of hadronization: as quark and antiquark are moving apart, the potential energy of the string increases until a point where a new quark-antiquark pair is produced from the vacuum. The two resulting string segments then each repeat this process until stable hadrons are produced.

with low transverse momentum relative to the string axis. This means that the probability that a jet issued from a light quark (or light-jet) is contaminated by a c or b quark is negligible. For jets issued from gluons, processes like $g \to c\bar{c}$ or $g \to b\bar{b}$ can contaminate, but the probability is very low ($< 4\%$).

2.3 The ATLAS experiment

2.3.1 General description

ATLAS is the biggest experiment ever built at a particle collider, being 46 m long, 25 m high and 7000 t heavy. Its construction started in 1997, and its installation in the 80 m deep experimental cavern began in 2003. Test beams studies, followed by extensive commissioning with cosmic muons allowed the ATLAS collaboration to be ready for the first LHC circulating beams in 2008. In 2009, it recorded the first collisions at $\sqrt{s} = 900$ GeV, and in 2010 the first 7 TeV collisions. The ATLAS collaboration involves roughly 3000 physicists at 175 institutions in 38 countries.

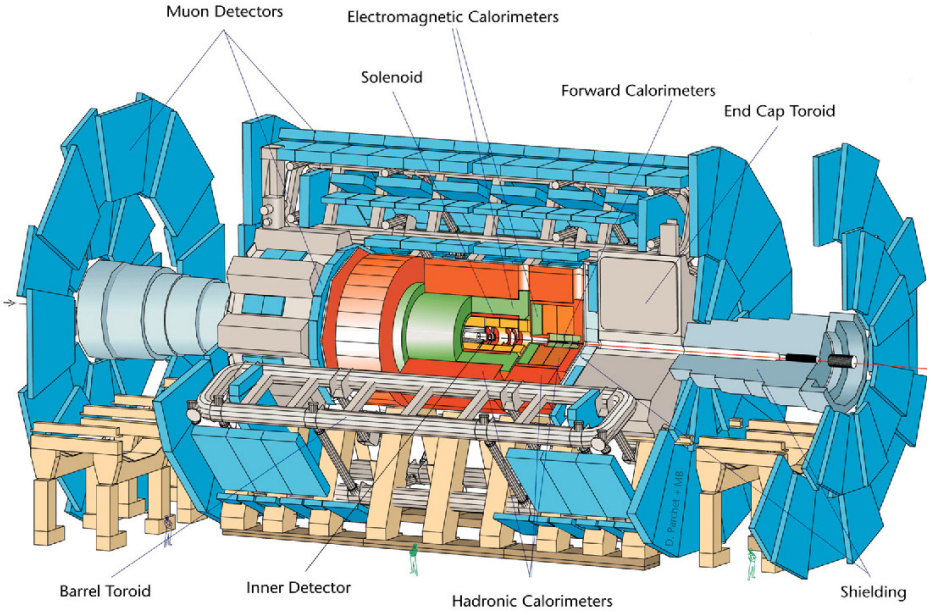

Figure 2.13: Overview of the ATLAS detector.

The ATLAS detector has an 'onion-like' structure, as displayed in Fig. 2.13, with different layers of sub-detectors placed around the LHC beam, and centered around the interaction point. The layers are made up of detectors of different types, each of which being designed to observe and measure properties (energy, momentum, charge, etc) of specific types of particles, as summarized in Fig. 2.14.

The closest to the interaction point, the Inner Detector system, surrounded by a 2 T solenoidal magnetic field used to bend the trajectory of charged particles, is composed of a high granularity Pixel detector, a silicon micro-strip tracker (SCT), and a Transition Radiation Tracker (TRT). It provides high precision tracking of charged particles, vertex reconstructions, as well as electron identification with the TRT.

Further from the interaction, the electromagnetic (EM) calorimeter allows to identify and measure the energy of electrons and photons. It is surrounded by an hadronic calorimeter that collects the energy of jets which was not lost in the EM calorimeter. The calorimetry systems also provide trigger capabilities, *i.e.* abilities to select interesting events (cf. Sec. 2.3.6), from the reconstructed objects.

For the muons escaping all the previous detectors, strong bending power in the volume of the muon spectrometer is provided by three large air-core toroid systems (one barrel, composed of an eight-fold

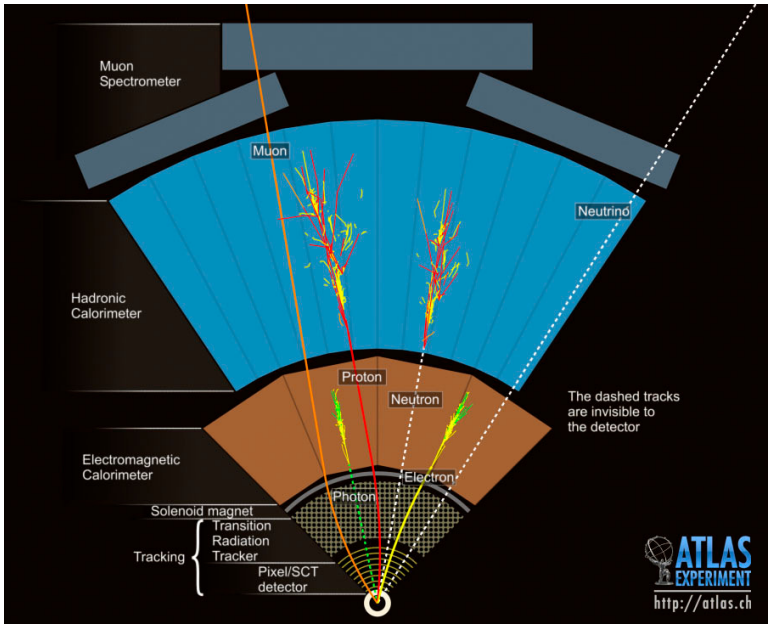

Figure 2.14: Illustration of particle detection in the subsystems of the ATLAS detector.

structure, as seen in Fig. 2.15, and two end-caps, as seen in Fig. 2.16). The muon spectrometer consists of chambers placed all around the toroid magnets, and allows both to trigger and perform high-precision tracking of muons, the only charged particles escaping the detector.

Neutrinos are traversing the detector without interacting with it, thus 'leaving' missing energy that can be measured. This could also be the case for other still un-discovered particles. The total balance can only be computed in the transverse plane, because as we have seen, due to the proton compositeness, the longitudinal sum (along the beam axis) of the energy of the partons involved in the initial state of a hard proton-proton interaction is unknown, and a priori non-zero. In the transverse plane however, the sum of the energies of these partons is assumed to be perfectly equal to zero before the collision, because the protons are traveling along the beam axis[12]. From the law of conservation of energy, the transverse energy of all the objects produced in a collision should hence be equal to zero.

Nomenclature The ATLAS coordinate system is defined as follows. Its origin is the nominal interaction point. The beam direction defines the z-axis, and the x-y plane is the plane transverse to the beam direction. The positive x-axis is defined as pointing from the interaction point to the center of the LHC ring, and the positive y-axis is pointing upwards. The *azimuthal* angle ϕ is measured around the beam axis, and the *polar* angle θ is the angle from the beam axis. The *pseudo-rapidity* is defined as $\eta = -\ln\tan(\theta/2)$. The transverse momentum p_T and the transverse energy E_{T}, as well as the missing energy $E_{\mathrm{T}}^{\mathrm{miss}}$ and other transverse variables, are defined in the x-y plane. The distance ΔR in the pseudo-rapidity-azimuthal angle space is defined as $\Delta R = \sqrt{\Delta^2\eta + \Delta^2\phi}$.

Specifications In addition to the functional abilities stated above for the reconstruction of the various physics objects, the ATLAS detector must also have fast and radiation hard electronics to cope with the

[12]Formally, the proton beams have however a small crossing angle, as we saw in Sec. 2.1.3.

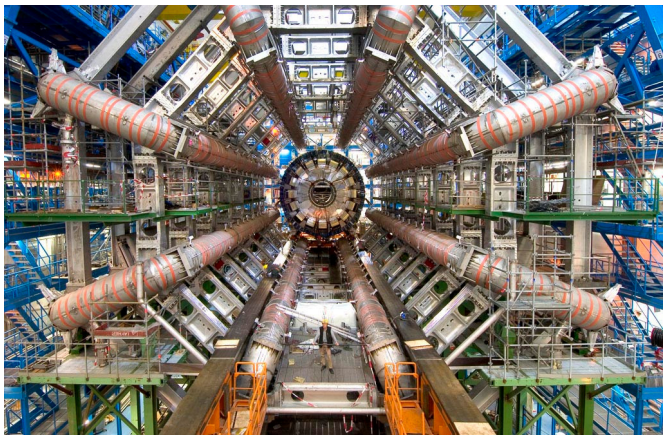

Figure 2.15: The eight barrel toroidal magnets (during ATLAS installation).

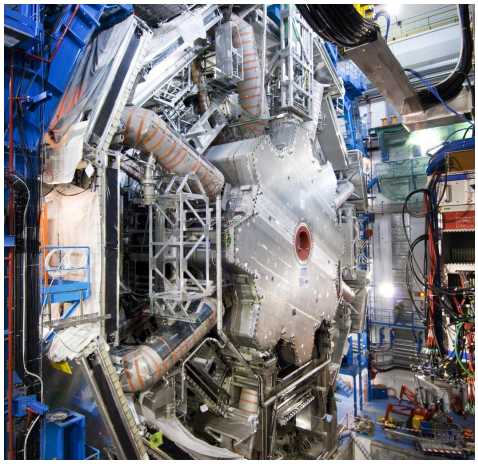

Figure 2.16: View of the ATLAS Cavern with the end-cap toroid magnets in place.

high LHC luminosity. Full azimuthal coverage and a large acceptance in pseudo-rapidity must also be fulfilled for full event reconstruction. This is especially important for missing energy determination. Table 2.2 summarizes the performance requirements of the ATLAS detector. A noteworthy point is that most of these requirements have to be fulfilled for a very wide range of energies, from a few GeV to the order of the TeV.

Sub-detector	Resolution	Coverage	
		Measurement	Trigger L1
Inner detector	$\sigma_{p_T}/p_T = 0.05\% p_T \oplus 1\%$	$\|\eta\| < 2.5$	-
EM calorimeter	$\sigma_E/E = 10\%\sqrt{E} \oplus 0.7\%$	$\|\eta\| < 3.2$	$\|\eta\| < 2.5$
Hadronic calorimeter	$\sigma_E/E = 50\%\sqrt{E} \oplus 3\%$	$\|\eta\| < 3.2$	$\|\eta\| < 3.2$
Forward calorimeter	$\sigma_E/E = 100\%\sqrt{E} \oplus 10\%$	$3.1 < \|\eta\| < 4.9$	$3.1 < \|\eta\| < 4.9$
Muon spectrometer	$\sigma_{p_T}/p_T = 10\%$ at $p_T = 1$ TeV	$\|\eta\| < 2.7$	$\|\eta\| < 2.4$

Table 2.2: Design performance and coverage of the ATLAS sub-detectors.

2.3.2 Tracking systems

The Inner Detector begins a few centimeters from the proton beam axis, extends to a radius of 1.2 meters, and is seven meters in length along the beam pipe. Its basic function is to track charged particles by detecting their interaction with material at discrete points, revealing detailed information about the types of particles and their momentum. The magnetic field surrounding the entire inner detector causes charged particles to curve; the direction of the curve reveals a particle's charge and the degree of curvature reveals its momentum. The Inner Detector is composed of three sub-detectors which are described in the next sections. Figure 2.17 shows the overall layout of their active (detection) areas, together with trajectory of tracks stemming from the interaction point.

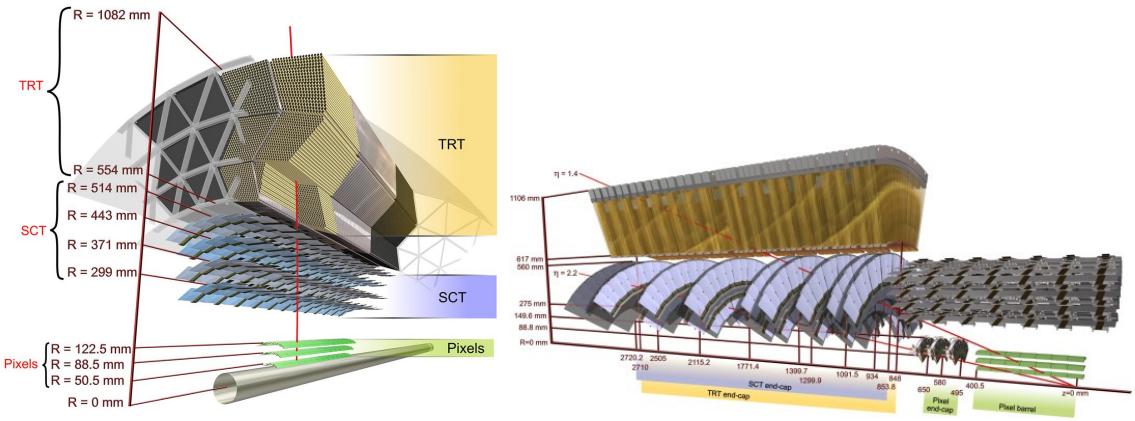

Figure 2.17: Cutaway views of the ATLAS inner detector. Shown are the barrel region (left) and one of the two end-caps organized as planar disks (right).

2.3.2.1 Pixel detector

Specifications The Pixel detector is the one situated the closest to the collisions, and therefore has to provide the most accurate tracking measurements. Its most important requirements are:

- provide on average three measurements per track over a pseudo-rapidity of $|\eta| < 2.5$;
- high detection efficiency close to 100% with a low noise rate;
- intrinsic resolution of about 10 μm in R-ϕ and 115 μm in the z-direction;
- transverse impact parameter (see Sec. 3.2 for exact definition) better than 15 μm. This is needed to separate tracks stemming directly from the interaction point, from tracks stemming from the decay of long-lived particles (b- and c-quarks), which will be the major focus of our next chapter.
- radiation hardness of all detector components, the first pixel layer, situated at $\sim$5 cm from the interaction point, being expected to accumulate a total dose of 500 KGy after 5 years of operation;
- minimal amount of material in order to reduce multiple scattering and secondary interactions in front of the other ATLAS sub-detectors.

Layout The pixel detector detection area is $\sim$1.8 m^2 divided in three barrel layers covering the central region of the detector, and three end-cap layers, called *disks*, on both sides covering the forward regions. A light mechanical support in carbon composites supports the active parts as represented in Fig. 2.18. It also supports cooling tubes, various services on both sides, and the LHC beam pipe in its core. The detection area is segmented in 1744 modules of 6.08×1.64 cm^2 each. Each module counts 46080 individual channels called *pixels*, for a total of more than 80M detection units.

In the barrel region, 13 modules are mounted on a *stave*. The staves are mounted on a cylindrical support with a tilt angle of 20° to form a layer, as illustrated in Fig. 2.19. This geometry allows overlaps between the modules, hence a full coverage with no gaps among the layers. The position of each of the barrel layers and the numbers of corresponding staves and modules are listed in Tab. 2.3.

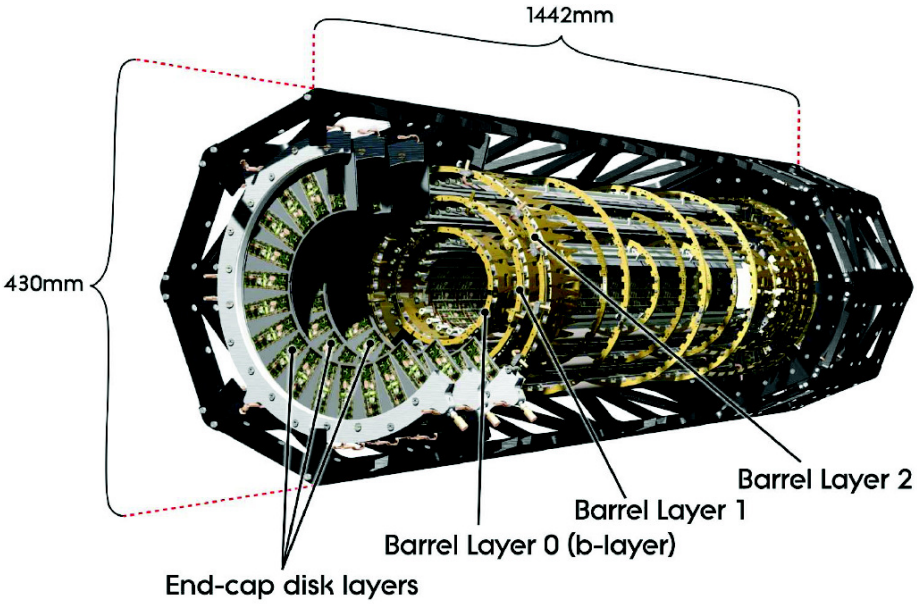

Figure 2.18: Layout of the ATLAS pixel detector [92].

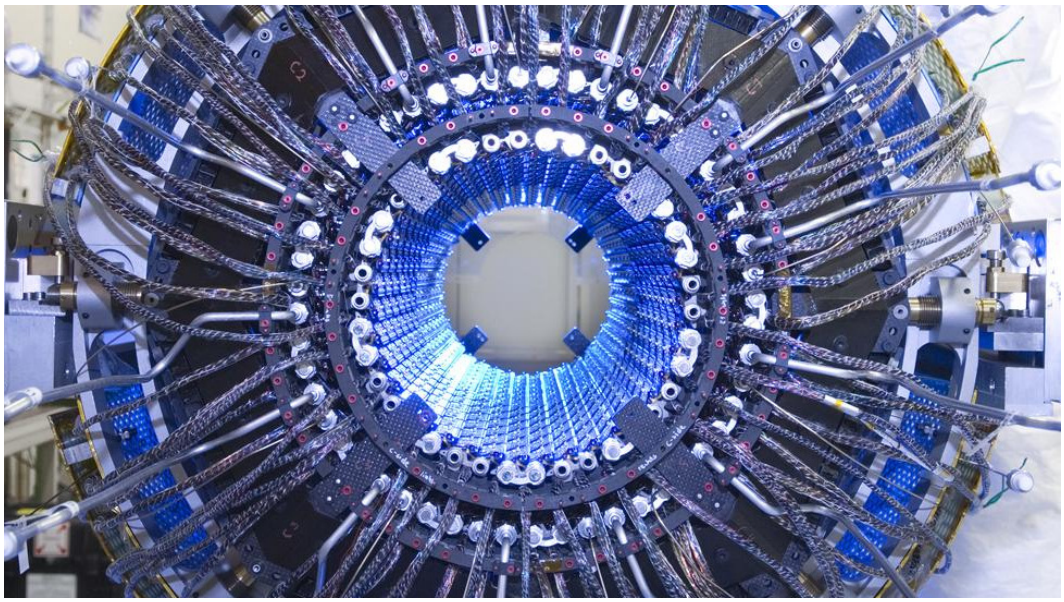

Figure 2.19: Pixel barrel sub-assembly in November 2006. The Layer 2 and Layer 3 are installed. Staves and cooling tubes serving bi-staves are clearly visible.

Each of the disks of the end-caps consist of 8 sectors with six modules each. Two groups of three modules are mounted side-by-side with the long module side in the radial direction. The modules are rotated with a tilt angle of 7.5° to ensure overlap between neighboring modules, hence full coverage. The position of each of the disks in one end-cap and the number of corresponding sectors and modules are listed in Tab. 2.4.

Layer	Radius (mm)	Staves	Modules	Active area (m^2)
0	50.5	22	286	0.28
1	88.5	38	494	0.49
2	122.5	52	676	0.67

Table 2.3: Properties of the pixel detector barrel layers.

Disk	$\|z\|$ (mm)	Sectors	Modules	Active area (m^2)
0	495	8	48	0.0475
1	580	8	48	0.0475
2	650	8	48	0.0475

Table 2.4: Properties of the pixel detector disks for each of the end-caps.

Modules As illustrated in Fig. 2.20(a), each module consists of:

- a sensor layer which is a Metal Oxide Semiconductor (MOS) structure. The principle of detection uses one of the most basic component of integrated circuit technology: a silicon p-n junction (formed at the boundary between a p-type and an n-type semiconductor), or *diode*. Reverse-biased, the diode becomes a *depletion* region, free of charge carriers, in which a strong electric field lies. This is the perfect environment for detecting a charged-particle crossing this region, which will create electron/hole pairs: the holes derive in the direction of the electric field, and the electrons in opposite direction. This collected signal can then be amplified and treated by dedicated electronics. In the high-radiation environment of the LHC, the following n^+-n-p^+ structure has been chosen: n^+-doped implants are arranged in an n-type bulk silicon layer, and the back-side of the bulk is p^+-doped, as illustrated in Fig. 2.20(b)[13]. This configuration will allow to operate even partially depleted after type inversion of the n-bulk due to radiations[14]. In the ATLAS pixel detector, the sensor tile contains 47232 n^+ implants, most of them with a pitch[15] of 400×50 μm^2. In the $\sim$250 μm-thick silicon layer, a minimum ionizing particle (MIP) will deposit about 19600 electrons. The bias voltage at the start of the LHC was about 150 V. The n^+-implants are connected via the technique of bump-bonding to the readout electronics;

- a readout electronics layer, composed of 16 *Front-End* (FE) chips. Each FE chip contains 2880 readout channels, each one being intended to extract the signal collected on a n^+-implant of the sensor layer, and traveling through the bump. An implant, its bump, and its associated readout electronics is called a *pixel*. The pixel cell electronics is represented in Fig. 2.21, in which one can see the bump-bond pad connected to a charge sensitive preamplifier with a 5 fF feedback capacitor. The two transistors on top of it are acting as a nearly constant current source which discharges linearly the capacitor when charges are collected. The time to discharge the capacitor is in this way proportional to the collected charge. The preamplifier is connected to a discriminator with a programmable threshold. When the deposited charge exceeds the threshold, the logical output state of the pixel switches. Figure 2.22 illustrates the shape of the

[13]This is the structure of the detector before irradiation, which will inevitably transform an n-type silicon to a p-type silicon under strong irradiation, a phenomenon called *type inversion*.

[14]After type-inversion, the n^+-n-p^+ configuration will 'transform' into a n-p-p^{++} one, so the localization of the p-n junction will move from the back-side of the bulk, to the top-side where the n-implants are, and in both configurations the signal can be collected individually by each implant.

[15]The actual area of the implants is obviously lower than the pitch size.

signal at the output of the preamplifier[16], in which one can notice the leading (trailing) edge LE (TE) of a 'hit' signal, which is the time-stamp of the discriminator output passing above (below) the threshold. When a LE is detected, a hit is detected and temporarily stored in memory. The difference TE-LE is defined as the Time-over-Threshold (ToT), and is proportional to the collected charge. Note that the LE needs to be lower than 25 ns in order to be associated to the correct bunch crossing, while the ToT can last more than 25 ns. The hit information (LE, TE, pixel address) is then transferred to the hit buffers at the chip periphery. If a L1 trigger is received within 3.2 μs, the hit information is transferred to the next layer, otherwise it is cleared.

- an electronic card called the *flex*, connected to the FE chips via the technique of wire-bonding. The most important part of the flex is the Module Control Chip (MCC), which controls the FE chips, receives the hit signals from them, and takes in charge the communication with the rest of the data acquisition chain.

Opto-boards Electric signals from the MCCs are transferred thanks to Kapton cables and converted in optical signals via so-called *opto-boards* situated at $|z| = 80$ cm on both sides of the detector. These signals are then transmitted outside the ATLAS cavern.

Resolution Assuming only one pixel only per particle track crossing the pixel detector fires a hit, the resolution on the track position equals to $p/\sqrt{12}$, where p is the pitch of the detector [93]. As a consequence, the 400×50 μm^2 pitch of the pixels yields a resolution of $\sim115\times14$ μm^2.

In practice, more than one adjacent pixels can fire a hit at the same time, especially tracks crossing with a low incidence angle, which will deposit electron/hole charges on a longer distance in the silicon compared to track with normal incidence. This phenomenon, referred to as geometrical *charge sharing*[17], allows an ever better resolution on the track position. The ensemble of neighboring pixel hits created from the passage of a particle is commonly called a *cluster*.

Calculating the position of the charge barycenter using the information of the ToT, proportional to the charge collected, can further improve the resolution on the track position, allowing to fulfill the needed requirements for physics.

2.3.2.2 Silicon micro-strip tracker (SCT)

The Semi-Conductor Tracker (SCT) surrounds the Pixel detector for charged-particle tracking. It consists of four barrel layers ($|\eta| < 1.4$) and nine end-cap disks ($1.1 < |\eta| < 2.5$) on each side, on which 4088 SCT modules are mounted. Fig. 2.23 shows the layout of a barrel module. It consists of two pairs of silicon micro-strip planes glued together back-to-back. The planes are rotated with respect to each other by a 40 mrad angle, which allows measurements along the length of a strip. The micro-strip pitch is approximately 80 μm, and the intrinsic accuracy is 16 μm (R-ϕ)$\times$580 μm (z). The SCT has approximately 6.2M readout channels.

2.3.2.3 Transition-radiation tracker (TRT)

The Transition-Radiation Tracker (TRT) is the outermost part of the Inner detector. It is made of 351k individually read out straw tubes of 4 mm in diameter. In the barrel region, 144 cm long tubes are

[16] In Fig. 2.22, the output voltage was converted in a 'number of electrons'.

[17] Charge sharing is increased by the tilted layout of the pixel modules, and reduced by the magnetic field lying in the Inner detector volume, which bends the trajectory of the charge carriers during their collection.

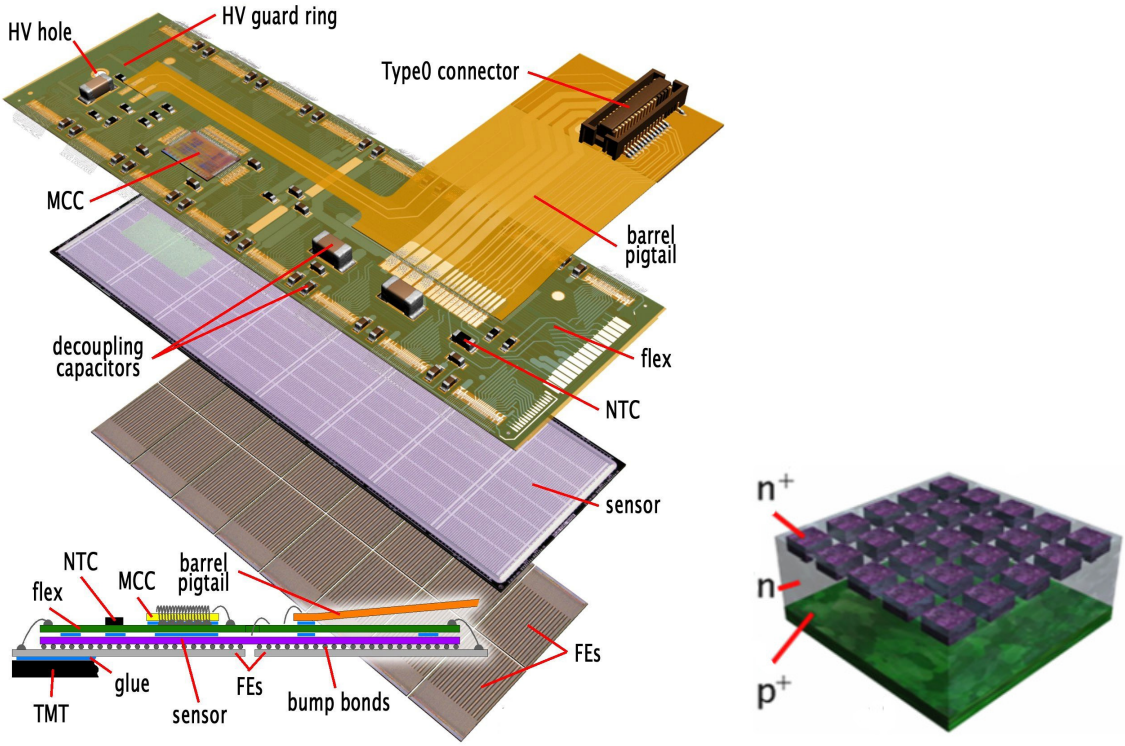

(a) (b)

Figure 2.20: (a) Layout of an ATLAS pixel module [92]. (b) Doping configuration of the sensor layer before irradiation. The dimensions are not to scale. The actual pitch of the n^+-implants is 400×50 μm^2, and the thickness of the bulk is $\sim$250 μm.

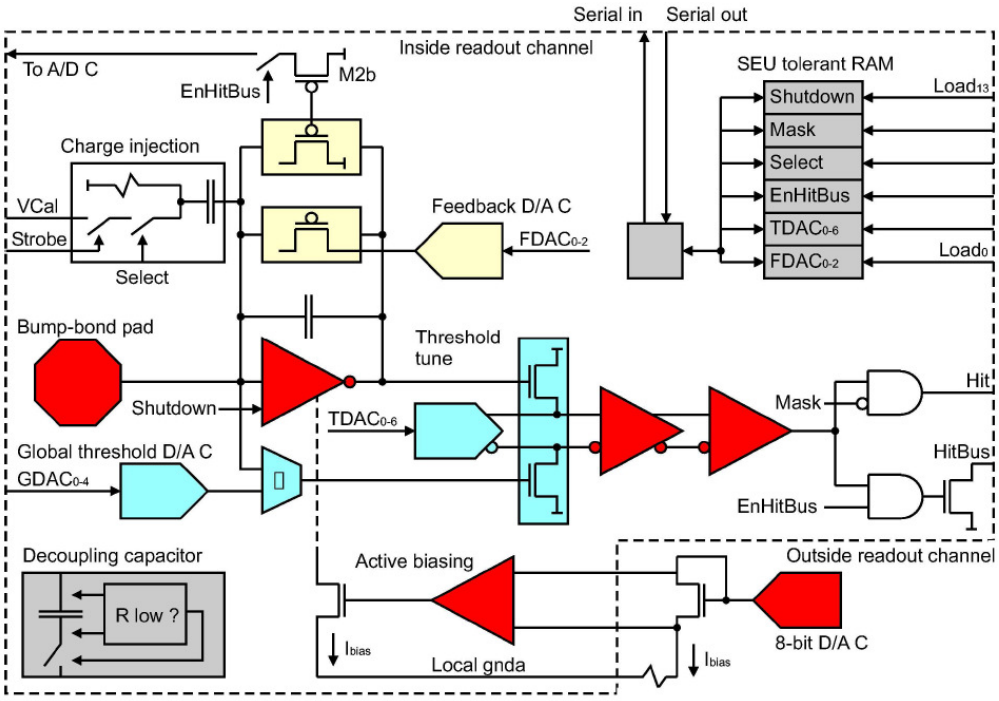

Figure 2.21: Scheme of the electronic part of a pixel.

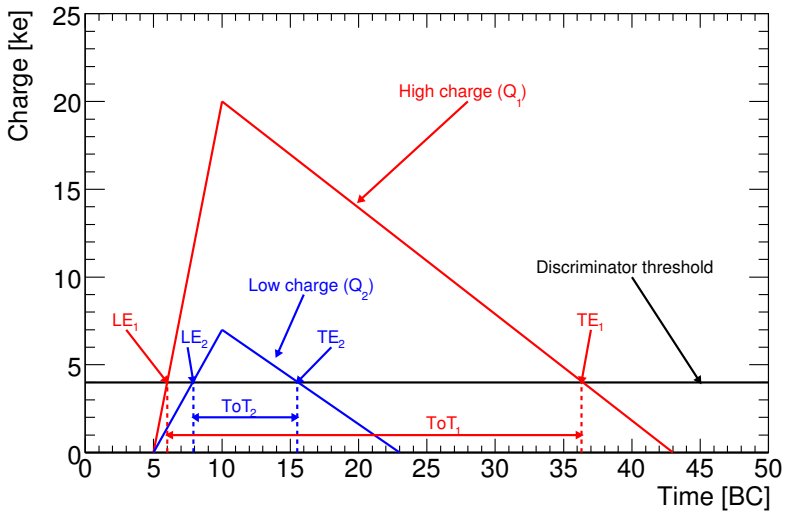

Figure 2.22: Shape of a 'hit' signal at the output of the preamplifier connected to a pixel sensor. A high collected charge (Q_1) can be seen to have a shorter Leading Edge (LE) time and a longer Time-over-Threshold (ToT≡TE-LE) compared to a lower collected charge (Q_2).

aligned along the beam axis. In the end-caps, the 37 cm long tubes are arranged radially. Each tube is filled with a gas mixture of $Xe/CO_2/O_2$, and contains a gold plated tungsten anode at its center.

The TRT functioning is based on the detection of avalanche currents on the anode wire initiated by

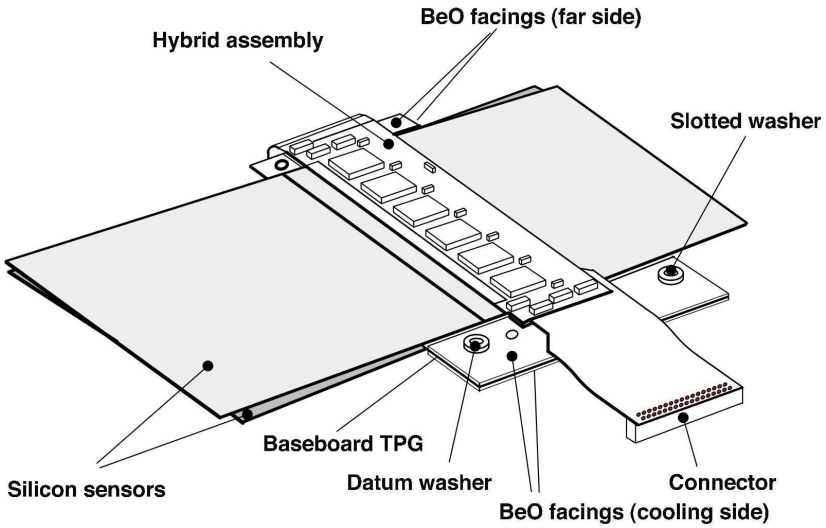

Figure 2.23: SCT barrel module.

clusters of primary ionization electrons from charged-particle crossing the tube. The operative voltage of about 1500 V applied to the cathode yields a gain of approximately 2.5×10^4. The drift time of the cluster depends upon the distance from the wire of the primary ionization, hence allowing a more precise tracking measurement. A minimum of $\sim$36 straws will be traversed in the barrel region (22 in the end-caps). The intrinsic resolution was designed to be $\sim$130 μm in R-ϕ. In addition, between the straws, materials with widely varying indices of refraction cause ultra-relativistic charged particles to produce transition radiation X-rays which are absorbed in some straws. Xenon gas is used to absorb such radiations and effectively increase the number of straws with strong signals. Since the amount of transition radiation is proportional to $\gamma' = E/m$, electrons are identified as tracks with high number of strong signals.

2.3.2.4 Matter in the Inner detector

High-energy electrons ($>\sim$10 MeV) predominantly lose energy in matter by bremsstrahlung, and high-energy photons by e^+e^- pair production. The characteristic amount of matter traversed for these related interactions is called the radiation length X_0, usually measured in g·cm^{-2}. It is both the mean distance over which a high-energy electron loses all but $1/e$ of its energy by bremsstrahlung, and $7/9$ of the mean free path for pair production by a high-energy photon. It is also the appropriate scale length for describing high-energy electromagnetic cascades [89]. Figure 2.24 shows the distribution of the matter traversed by a particle moving in straight line through the Inner Detector in radiation lengths X_0, as a function of η. The relatively high quantity of matter at the transitions from barrel to end-caps for the different sub-detectors of the Inner detector is due in a great extent to the passage of services (cooling, electric cables, etc). It has an important effect on the reconstruction of *e.g.* electrons, photons, and also pions with momentum of a few GeV.

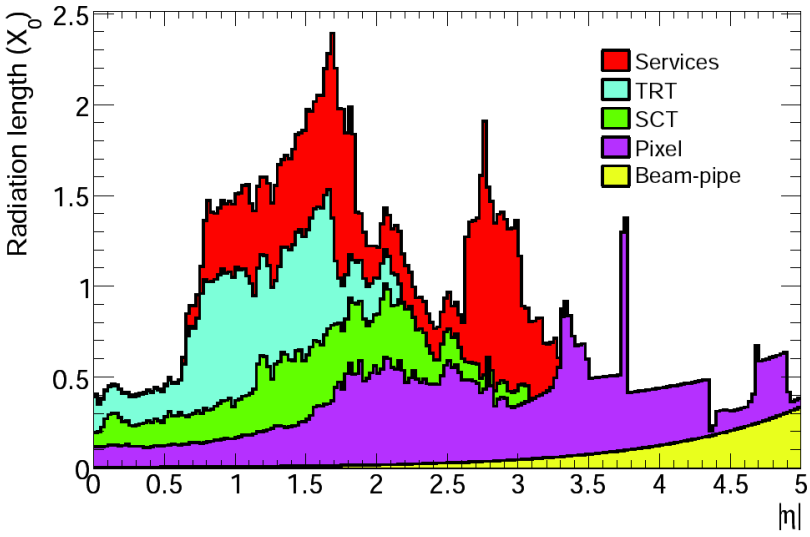

Figure 2.24: Distribution of the matter in the Inner Detector in radiation lengths X_0, as a function of η [79].

2.3.3 Inner detector cooling and SONAR system

2.3.3.1 Cooling

To maintain stable operation and prevent Silicon detector irradiation damages, the Inner detector is equipped with an efficient cooling system, whose purpose is to dissipate the 85 kW of heat from the ID electronics at nominal luminosity and increase the lifetime of the sensors.

The Pixel and SCT detectors share the same evaporative cooling system, using C_3F_8 as coolant. The choice of saturated fluorocarbons was done because of their radiation resistance, non-flammability, low viscosity and low toxicity, despite their enthalpy of evaporation lower than the one of less radiation-stable refrigerant. The silicon sensors of the pixels are expected to operate at about -7°C to minimize the impact of radiations. In the pixel barrel, two adjacent staves share the same cooling loops, as could be seen in Fig. 2.19. For the disks, one cooling loop serves two disks sectors.

Both Pixel and SCT detectors are operating in a dry N_2 gas flow, which ensures a low dew point and therefore no accumulation of humidity on the sensors and the front-end electronics.

2.3.3.2 Detection of coolant leaks using SONAR

In the pixel volume, the presence of C_3F_8 in the N_2 gas has been detected [96], indicating that some a priori unknown cooling loops are leaking. Due to radiations, especially high in the pixel volume, the presence of Hydrogen in case of dissociation of C_3F_8 can generate hydrofluoric acid (HF) that is very corrosive and penetrating. This could damage *e.g.* the very complex structure of the pixel modules (wires, bonds, etc). While the leak level is known to be very small at the moment ($\lesssim 0.05\%$, see later), a very high increase of the leaking of some cooling loops would be a catastrophic scenario threatening the whole experiment. Monitoring the concentration of C_3F_8 in the N_2 gas would hence be very useful to prevent such damages, in particular if it could allow to detect the cooling loops leaking the most, which could then be turned off (hence together with all the associated modules) to protect the operation of the rest of the detector.

Principle An astute means to measure the concentration of saturated fluorocarbons gas is to measure the speed of sound (SoS) in it, which is strongly affected even for very little concentration [94]. In practice, this is done by 'sniffing' the N_2 environmental of the pixel and SCT detectors using a small vacuum pump to aspirate the vapor through 150 m of tube until a measurement volume in the ATLAS USA15 underground service cavern. The measurement volume is a tube equipped with a sonar which will measure the travel time of a sound wave from one side of the tube to the other one, as illustrated in Fig. 2.25. The tube has a length known with high precision, and is also equipped with 10 temperature sensors along the tube. An illustrative example of the sensitivity of such system happened between September 13 and 16, 2009, when a shutdown of the pixel cooling system occurred. Before that, the sound velocity in the gas had been observed very stable, but during the shutdown, the SoS increased from 350.39 m/s to 350.95 m/s, and then decreased when the cooling system was re-activated. The higher speed corresponded exactly to the SoS in pure N_2 at the temperature of the gas, and the lower speed allowed to infer that the leak concentration of C_3F_8 is about 0.05% when the cooling system operates normally [96].

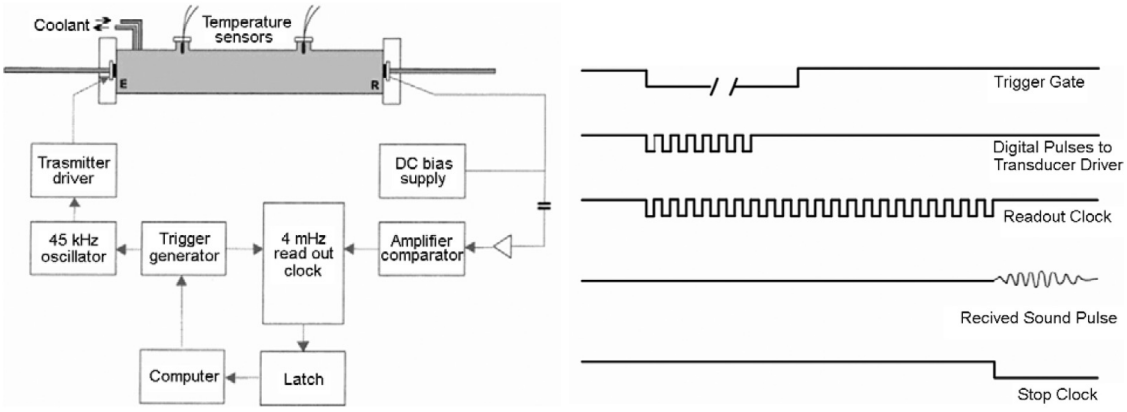

Figure 2.25: Simplified scheme of modified sonar analyzer and its timing sequence [94].

Speed of sound prediction The relation between speed of sound and the concentration $c(C_3F_8/N_2)$ of C_3F_8 in the mixture C_3F_8/N_2 can be derived using equations of state (EoS) based on statistical associating fluid theory (SAFT), especially the perturbed-chain (PC)-SAFT model [97]. In practice, SoS can be computed using complex formula in the form of $(SoS, c(C_3F_8/N_2), T)$ look-up tables. In order to achieve sufficient precision for the concentration ($< 0.1\%$), such table can count more than tens of thousands of lines. In this work, we propose a simplified model to compute the tabulated values of SoS. We start from the ideal gas equation for the SoS (V_s):

$$V_s = (\frac{\gamma RT}{M})^{1/2} \tag{2.4}$$

where γ is the adiabatic index of the noble gas, R the molar gas constant (8.3145 J$\cdot$ mol$^{-1} \cdot K^{-1}$), T the absolute temperature in kelvin, and M the molar mass in kg/mol. For our mixture of two components i, we replace:

$$\gamma \rightarrow \gamma_m = \frac{Cp_m}{Cv_m} = \frac{\sum_i W_i Cp_i^0}{\sum_i W_i Cp_i^0} \tag{2.5}$$

$$M \rightarrow M_m = \sum_i f_i^V \cdot M_i \tag{2.6}$$

where C_p is the isobaric heat capacity, C_v the volumetric heat capacity ($C_v = C_p - R/M$), W_i the mass fraction of component i and f_i^V the volume fraction of component i.

The isobaric heat capacity, C_p (J/K/kg) can be derived, for N_2, thanks to the following approximation [95]:

$$C_p(T)/M = C_p(T_0)/M + \frac{dC_p}{dT}(T - T_0)/M \text{ with } T_0 = 25°C \text{ and } \frac{dC_p}{dT} = 1.27 \cdot 10^{-3} \tag{2.7}$$

and from the following correlation for saturated fluorocarbons, from [98]:

$$\frac{C_p M}{R} = a_0 + \sum_{k=1}^{3} a_k \left(\frac{b_k}{T}\right)^2 \frac{exp(b_k/T)}{[exp(b_k/T) - 1]^2} \tag{2.8}$$

Formula	a_0	a_1	a_2	a_3	b_1	b_2	b_3
C_2F_6	4	2.4818	7.0622	7.9951	190	622	1470
C_3F_8	4	7.2198	7.2692	11.599	326	595	1489

We can now compute the SoS for any concentration of C_3F_8 for a given temperature. Figure 2.26 shows the result of our approximated formula, compared to PC-SAFT predictions, and real SoS values that had been measured at CPPM. The agreement can be seen to be excellent between the three curves.

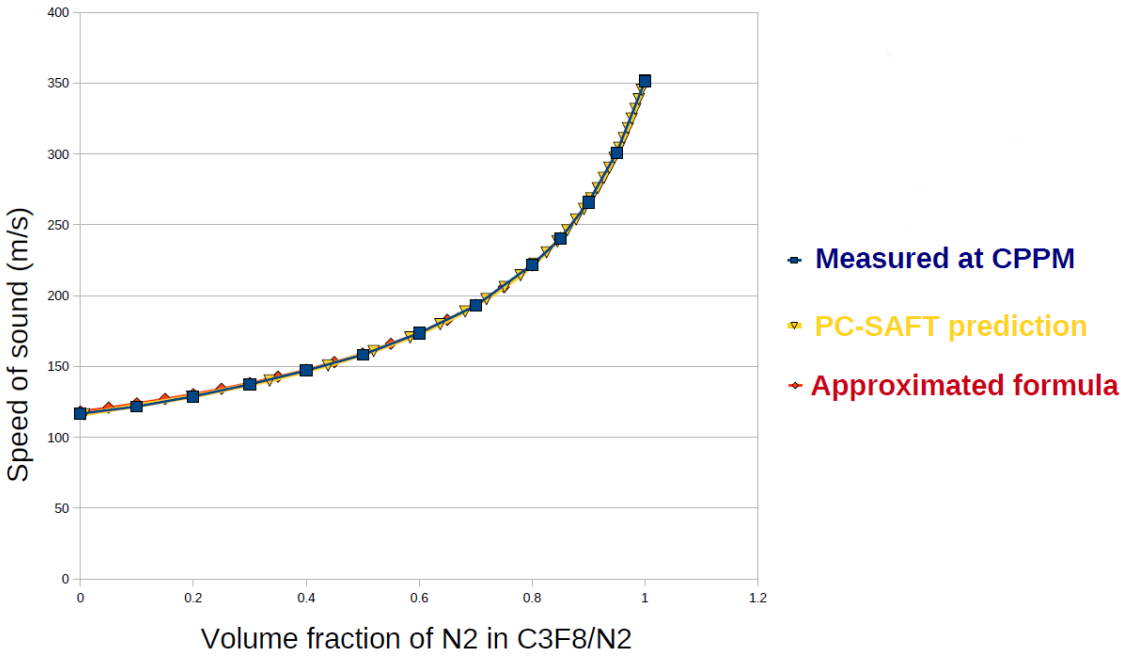

Figure 2.26: Speed of sound versus volume fraction of N_2 in C_3F_8, as measured at CPPM laboratory (blue), as approximated by PC-SAFT (yellow), and as approximated by us (red), for a temperature of 25.7°C.

Future operations of the pixel detector will require a lower operating temperature while using the same installed plant. A mixture adding 10-20% of C_2F_6 to the C_3F_8 is foreseen for the ATLAS

pixel detector [96]. For this reason, it is interesting to investigate the use of the sonar that could be used to monitore the C_2F_6 concentration in the C_2F_6/C_3F_8 new coolant mixture. We applied our approximated formula to these two components, and show the results in Fig. 2.27. We observe again a very satisfactory agreement with measured values and PC-SAFT predictions, (relative error between 0.6 and 1.7%), even if the agreement is slightly worse than for the C_3F_8/N_2 mixture.

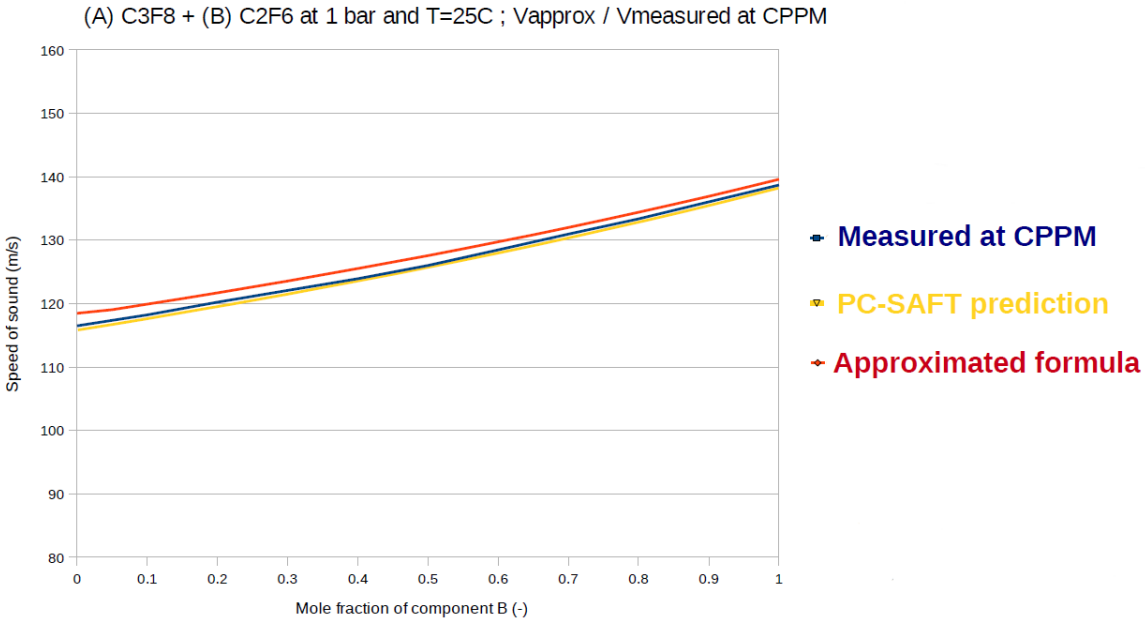

Figure 2.27: Speed of sound versus molar fraction of C_2F_6 in C_3F_8, as measured at CPPM laboratory (blue), as approximated by PC-SAFT (yellow), and as approximated by us (red).

2010 Feb 3-4 cooling leak tests On February 3 and 4, 2010, a technical stop of the LHC offered nice conditions to make the following study. As we have seen, some C_3F_8 leaks are detected in the N_2 gas from pixel and SCT detectors. However, we would like to separate leaks inside the pixel volume (danger of corrosion by HF) from leaks outside the pixel volume, and identify the leaking loops. For this reason, special settings of the compressors allowed to clean the pixel loops prior to our test, and all pixel loops were put in OFF state. The SCT loops were also effectively disconnected. The plan was then to turn ON successively one by one cooling loops suspected (from previous studies) to be leaking the most. From the sonar measurement during the September 13-16 2009 cooling plant failure described previously, the response time of the sonar system[18] had been estimated of about 2 h. Figure 2.28 shows the concentration calculated from SoS and temperature measurements during the test, together with the instants were different cooling loops were opened. We can clearly see that until the opening of 'Loop 32', there is a significant increase of the C_3F_8 concentration, up to a level of $\sim 0.015\%$. Before that, the concentration was compatible with noise around zero. Note that just after the first opening of Loop 32, a DSS (Detector Safety System) alarm occurred around 11am, which turned off all cooling loops, before all previously opened loops were re-opened at $\sim$1:15pm. Given the time response of delay of about 2 h, the causality of the opening of Loop 32 and the increase of concentration is nevertheless clear, and indicate that this loop can very likely be identified as leaking,

[18] *i.e.* the time for a leak to spread in the N_2 volume and be sniffed by the 150 m long tube.

and responsible of about one third of the total leak ($\sim 0.05\%$). Unfortunately, the LHC did not allow us to continue further our investigations, and we had to stop the test.

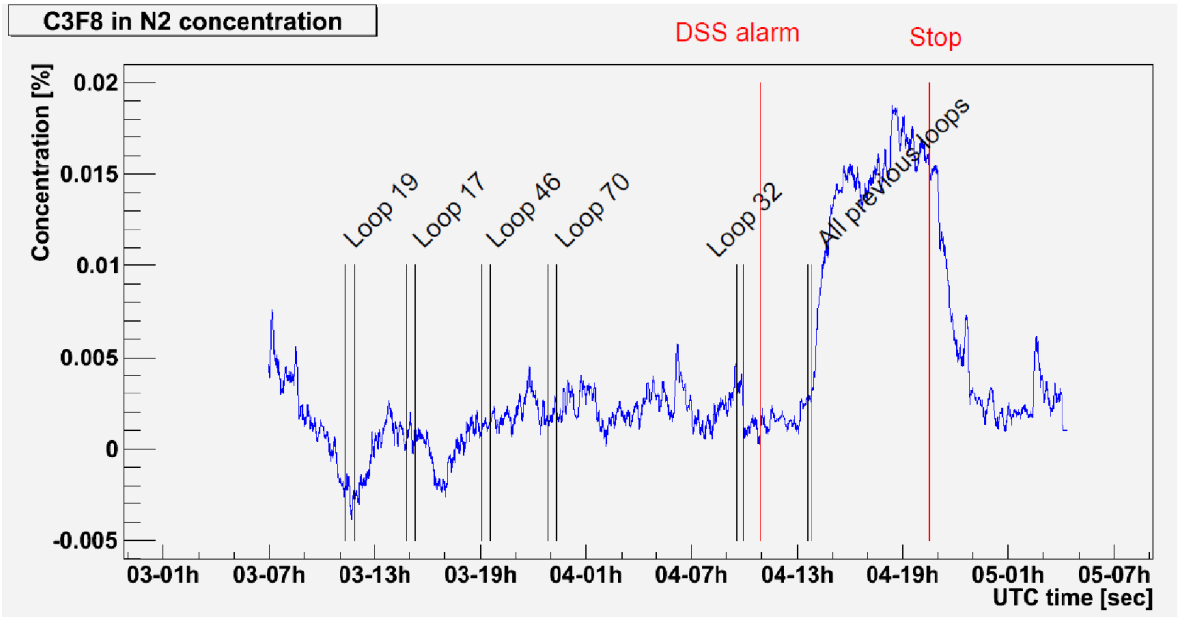

Figure 2.28: C_3F_8 in N_2 concentration measured by the SONAR system during the 3-4 February 2010 leaking test.

In order to increase the precision of the sonar system below the 0.005% level, the sonar tube was immersed in a water flow to stabilize the temperature measurements along the tube on February 10, 2010. We also recommended to increase the readout clock to frequency higher than 4 MHz.

2.3.4 Calorimetry systems

The ATLAS calorimeters cover the large pseudo-rapidity range $|\eta| < 4.9$. An overview of the different sub-detectors can be seen in Fig. 2.29. Their design was dictated by physics searches such as $H \to \gamma\gamma$, where H denotes the SM scalar boson, or Z' and W' bosons, which involve electrons, photons, and constraint their expected performance as quantified previously in Tab. 2.2. The EM and hadronic calorimeters are both *sampling* calorimeters; that is, they absorb energy in high-density metal and periodically sample the shape of the resulting particle shower, inferring the energy of the original particle from this measurement.

2.3.4.1 Electromagnetic calorimeter

The electromagnetic (EM) calorimeter absorbs energy from particles that interact electromagnetically, which include charged particles and photons. It has high precision, both in the amount of energy absorbed and in the precise location of the energy deposited. It is divided into a central barrel ($|\eta| < 1.475$) and two end-caps ($1.375 < |\eta| < 3.2$). In the forward region ($3.15 < |\eta| < 4.3$), the first module of the forward calorimeter (FCal) is part of the EM calorimeter. The EM barrel and end-caps are made of succession of lead absorbers and copper electrodes, with gaps of liquid argon (LAr) in between. Each gap harbors an electric field provided by a dedicated high-voltage system. The FCal

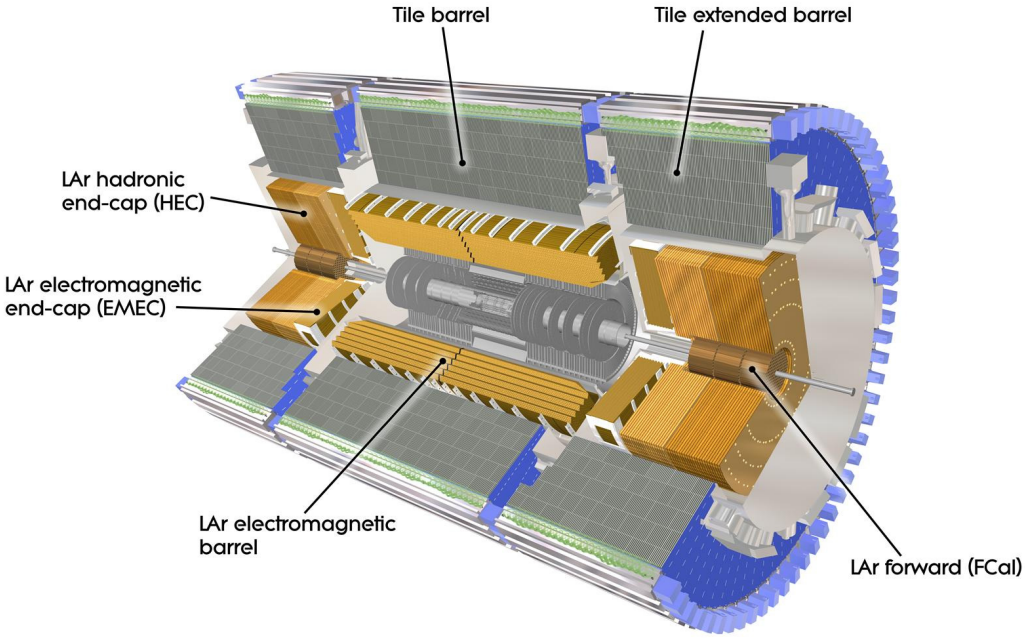

Figure 2.29: Overview of the ATLAS calorimeter systems.

layout consists of electrode tubes, arranged along the beam axis, in copper/tungsten. A cryostat is surrounding the EM calorimeter to keep it sufficiently cool.

Barrel The barrel is segmented in three compartments in depths, as illustrated in Fig. 2.30. The first layer (as seen from the interaction point), has a length of 4.3 radiation lengths X_0. It is very finely segmented in thin strips of size $(\Delta\eta \times \Delta\phi) = (0.0031 \times 0.098)$, which is crucial for photon/π^0 separation. The second sampling layer has a depth of 16 radiation lengths X_0, and absorbs the majority of the energy. Clusters with energy below 50 GeV are fully contained in it. For the position measurement of the clusters, the two coordinates are equally important resulting in square cells of size $(\Delta\eta \times \Delta\phi) = (0.0245 \times 0.0245)$. Only the highest energy particles will reach the third layer. The clusters are at this point wide and the cell size can be doubled in the η direction without loss of resolution. An additional detector layer is installed in front of the EM barrel: the Pre-Sampler (PS). It consists of a single thin layer of argon, whose purpose is to correct for the energy loss in the Inner Detector, solenoid magnet and cryostat vessel. The *accordion* geometry of the electrodes allows fast signal collection and full ϕ-coverage without gap.

End-cap The EM end-caps (EMEC) extend the EM calorimetry to higher pseudo-rapidity. The EMEC is divided in two coaxial wheels: the outer wheel covers $1.375 < |\eta| < 2.5$, and the inner wheel covers $2.5 < |\eta| < 3.2$. The main feature of the EMEC is its variable LAr gap size and high-voltage, which vary with the radius in order to obtain a η-uniform response.

Forward The Forward Calorimeter (FCal) covers the pseudo-rapidity range $3.1 < |\eta| < 4.9$. It is made of three modules sharing the same design: an absorber matrix filled with electrode tubes

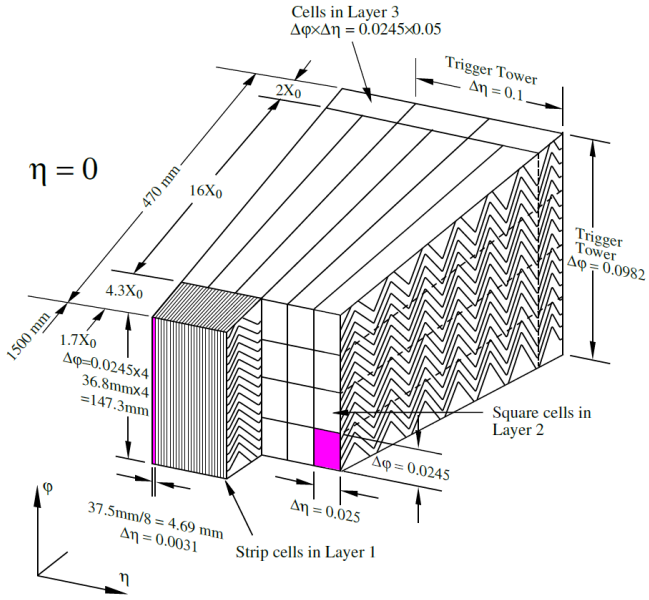

Figure 2.30: The structure of the barrel *accordion* EM calorimeter. The presampler is in front of the accordion.

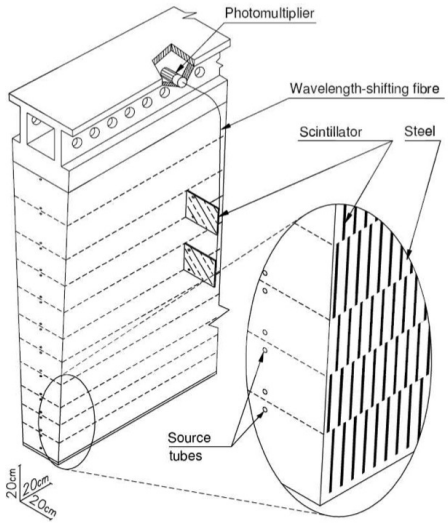

Figure 2.31: A Tile Calorimeter module with the iron absorbers, the scintillating tiles, the optical fibers and the photomultipliers.

arranged along the beam axis. For the first module, dedicated to forward electrons and energy measurements, the absorber is made of copper. The two other modules, used for hadronic energy measurements, the absorber is made of tungsten. Inside each tube is a rod, where the high-voltage is applied. The gap between the rod and its tube is filled with liquid argon. The small gap (250-500 μm) limits the sensitivity to pile-up effects which are large close to the beam pipe where energetic jets often hit the same area of the calorimeter.

2.3.4.2 Hadronic calorimeter

The hadron calorimeter absorbs energy from particles that pass through the EM calorimeter, but do interact via the strong force; these particles are primarily hadrons.

Tile calorimeter The so-called Tile calorimeter (TileCal) is divided into three parts: a barrel, covering $|\eta| < 1$, and two extended barrels on each side, covering $0.8 < |\eta| < 1.7$. It consists of steel absorbers and scintillating plastic tiles as active material, as illustrated in Fig. 2.31. The light created in the tiles is read out with wavelength shifting fibers to photo-multipliers placed on the outside of the calorimeter. The fibers absorb the blue light from the scintillators and re-emit it at longer wavelengths where it reaches the photo-multipliers through total internal reflection inside the fibers. The energy of jets deposited in the TileCal is proportional to the number of photons collected.

The pseudo-projective segmentation (longitudinally and in depth) lead to cell sizes of $\Delta\eta \times \Delta\phi = 0.1 \times 0.1$ in the first two compartments, and $\Delta\eta \times \Delta\phi = 0.2 \times 0.1$ in the last one. The TileCal has approximately 9600 read-out channels, extends from a radius of 2.28 m to 4.25 m, and weights $\sim$2900 tons.

Hadronic End-cap The Hadronic End-Cap (HEC) calorimeter is installed with the same endcap cryostat as the EMEC and FCal. It cover the pseudo-rapidity range $1.5 < |\eta| < 3.2$. It is a sampling calorimeter with copper absorbers and liquid argon as an active medium. In contrast to the EM calorimeter, the electrodes are flat and arranged orthogonally with respect to the beam axis.

2.3.5 Muon spectrometers

The muon spectrometer is the outermost part of the ATLAS detector. It consists of four different types of muon chambers, as illustrated in Fig. 2.32. The chambers are operating in a toroidal magnetic field, whose purpose is to bend the trajectory of the muons, allowing a precise measurement of their momentum and the determination of their charge. The magnetic field is generated by three air-core toroids, whose geometry has been chosen so that the fields are almost always perpendicular to the muon trajectory. Two toroids forming the end-caps are inserted in the larger toroid that covers the barrel region.

For precision measurements, two types of chambers are used: the Monitored Drift Tubes (MDTs), covering all the range $|\eta| < 2.7$, except for the innermost layer of the end-caps region ($2.0 < |\eta| < 2.7$), where Cathode Strip Chambers (CSCs) are installed. The MDTs are chambers comprised of aluminum tubes of 30 mm in diameter filled with an Ar/CO_2 gas mixture and a tungsten anode. The tubes operate at a pressure of 3 bar and a voltage of 3080V, resulting in an amplification gain of $\sim 2\times 10^4$. The average spatial resolution of one of the 350k tubes of the MDT is approximately 80 μm. The CSCs are multi-wire proportional chambers with cathodes segmented into strips. Wires perpendicular to the strips provide the precision coordinate with a resolution of ~ 60 μm. Wires parallel to the strips provide the transverse coordinate with a resolution of ~ 5 mm. At $|\eta| > 2$, the particle rate exceeds the MDT maximum allowed counting rate, while CSC can safely operate.

For trigger purposes, two types of chambers are used: the Resistive Plate Chambers, used in the barrel region ($|\eta| < 1.05$), and the Thin Gap Chambers (TGC) in the end-cap region ($1.05 < |\eta| < 2.4$). The RPC is a gaseous parallel electrode-plate detector. Two plastic resistive plates are separated by a 2 mm gas mixture where lies an electric field of 4.9 kV/mm. The TGCs are multi-wire proportional chambers operated in quasi-saturated mode: the wires are 1.4 mm away from graphite cathodes, put at a potential of 2.9 kV and surrounded by a highly quenching gas mixture, resulting in an amplification gain of $\sim 3\times 10^5$. This allows very good timing resolution. Seven layers complement the MDT measurement in the middle end-cap wheel, and two in the innermost η region.

All the chambers are aligned with respect to each other thanks to an embedded infrared optical system, allowing a constant monitoring of the detectors position in the cavern and achieving a precision on the relative position of the chambers of ~ 30 μm.

2.3.6 Triggering system

Principle As we have seen previously, at the LHC design luminosity, trains of bunches of protons spaced by 25 ns will circulate in each direction of the LHC ring close to the speed of light. On average, the 2808×2 bunches (out of 3564×2 possible) contained in the LHC ring will cross each other $\sim$31M times per second, producing $\sim$790M collisions per second[19]. Assuming raw data from an event can be stored using 1.6 megabytes, this would require to store 1.3 petabytes of raw-data per second.

[19] Assuming an average number of 25 minimum-bias collisions per BC (cf. Sec. 2.2.5), and a revolution time around the LHC for the protons of ~ 88.9 μs

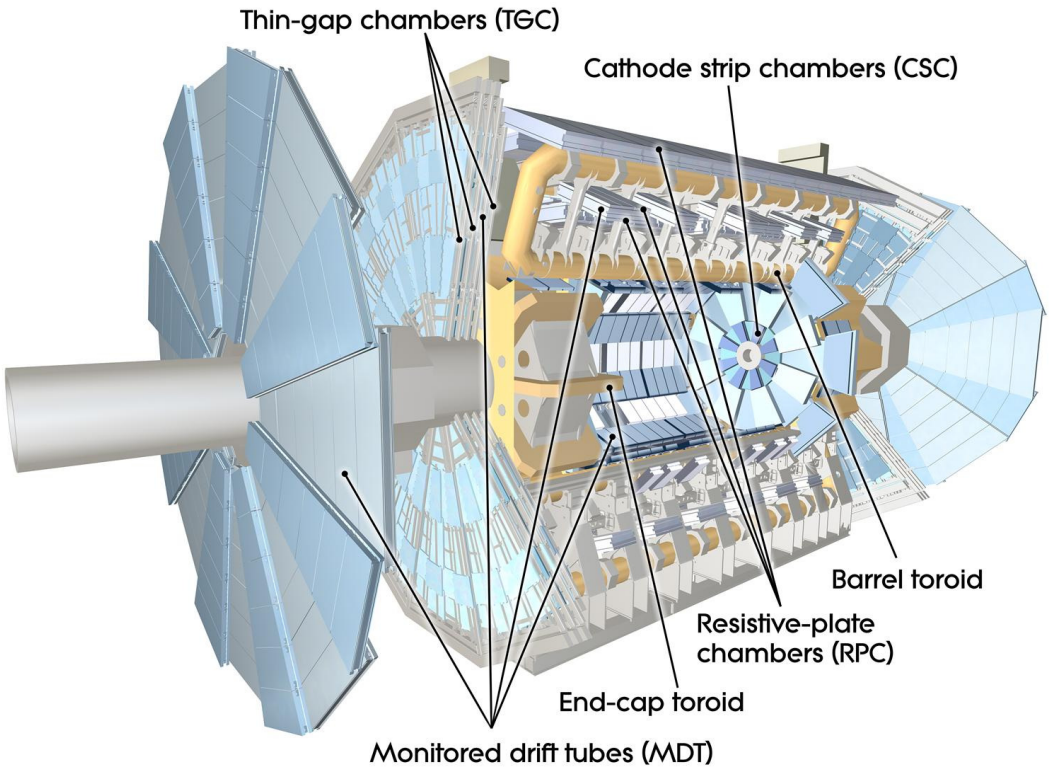

Figure 2.32: Overview of the ATLAS muon spectrometer components.

The ATLAS trigger system is intended to select, in real time, the most interesting events (*i.e.* the very rare processes, including the hypothetical new physics ones), allowing to reduce the amount of data to be stored to a manageable level. In clear, the trigger system is the crucial system on which all the data acquisition relies.

As illustrated in Fig. 2.33, the trigger system is divided in three stages: L1, L2 and Event Filter (EF), the two latter being referred to as High Level Trigger (HLT):

- The calorimetry, muon and tracking systems front-end electronics acquire the lowest level of signals, gather them, and send them to the L1 trigger. The L1 looks for basic patterns that could identify muons, electrons, photons, jets, or missing transverse energy. If found, it makes the decision to keep the event, referred to as a *L1 Accept* (L1A). The time allowed for the L1 to provide a L1A (2.5μs) is limited by the design overall L1 output rate of $\sim$100 kHz.
- Once the L1A has been issued, the buffered data is sent to the L2 together with regions of interest (RoI), defined as η-ϕ regions of the detector where information has been deemed interesting. The L2 processes further the information from the L1 by applying refined algorithms. This step takes $\sim$40 ms, limited by the design overall output rate of $\mathcal{O}(1kHz)$.
- When an event is accepted by the L2, it is sent to the EF, which processes even more refined algorithms. If accepted, the raw data are meant to be permanently stored, at a maximum rate of $\mathcal{O}(100Hz)$. At this point, the raw data is available offline, to be fully reconstructed by dedicated algorithms and the most up-to-date calibrations of the various detectors.

At various stages of the trigger chain, so-called *prescales* can often be applied to reject further the rate of events: a given fraction of L1As are rejected randomly, *e.g.* a prescale of 1000 means that only 1 event out of 1000 is actually selected.

Figure 2.34 shows the different trigger rates during the highest luminosity run of 2011, including all the ATLAS triggers enabled at that time.

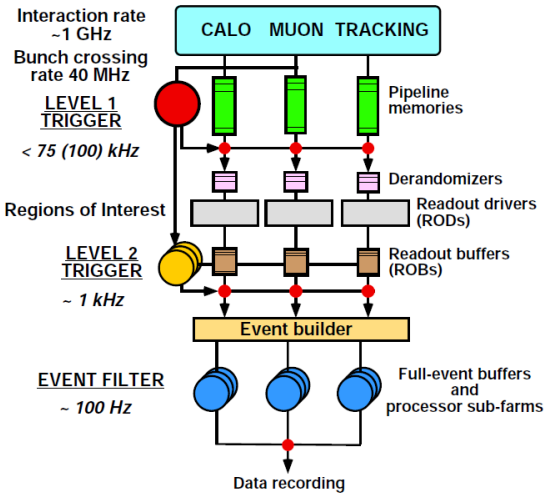

Figure 2.33: Block diagram of the Trigger/DAQ system.

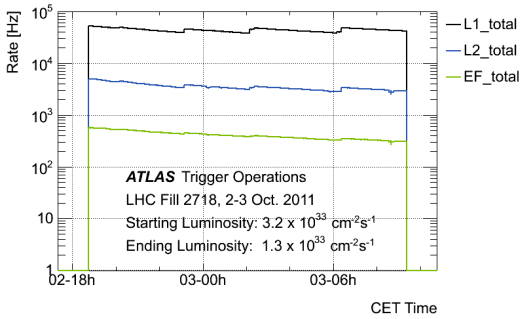

Figure 2.34: Data trigger output and recording rate at ATLAS at a luminosity of $3.2 \cdot 10^{33} cm^{-2} s^{-1}$.

Example To illustrate better the behavior of the trigger chain, we now describe the principle of a jet trigger used in 2011. At L1, proto-jets are reconstructed with a sliding-window algorithm using 4×4 trigger towers of granularity $\Delta\eta \times \Delta\phi = 0.1 \times 0.1$. The proto-jets above threshold define the Regions of Interest (RoI). The L2 algorithm looks in a $\Delta\eta \times \Delta\phi = 1.0 \times 1.0$ window centered on each L1 RoI and builds jets with a simple $\Delta R = 0.4$ cone algorithm. At the last stage of the trigger, the EF does not rely anymore on the RoI (unlike for the 2010 data taking) but performs a full scan, reading out the complete calorimeter and running the offline anti-k_t[20] jet finding algorithm with $R = 0.4$ on topological clusters.

Infrastructure The different elements of the trigger chain just described are the following: for reliability and speed of execution reasons, the L1 is purely hardware; the L2 and EF are handled by a computer farm located at the surface above the ATLAS cavern; the data are stored in the CERN Computer Centre and reconstructed there. The latter stage, called 'Tier-0', is the first stage of the LHC Computing Grid [90], which then transmits the data to the various 'Tier-1' sites around the world, which in turn are made available to all the 'Tier-2' sites. The Grid architecture has been designed to optimize availability of the data and best usage of the computing resources of all the ATLAS institutes around the world.

[20]The Anti-k_t algorithm will be introduced in Sec. 3.2.5.1.

2.4 The ATLAS Upgrade plans

2.4.1 Overview

The ATLAS detector has had a very successful start with many results produced already in 2010. The LHC will continue increasing luminosity in a series of runs interspersed with long shut-downs for installation of injector, LHC and experiment upgrades. The higher integrated luminosity made available – the target is 3000 fb^{-1} – will open access to many new physics goals. Figure 2.35 summarizes these goals and ATLAS upgrade plans from that time until the High-Luminosity LHC project around 2020. Mainly, two major reasons motivate upgrading the ATLAS detector: to replace damaged components that are altered by the high-level of radiation during operation; and to improve current detector (with new technology), or add new ones, to be able to cope with the LHC luminosity upgrades, which will cause higher detector occupancies and harsher radiation environment. The detectors operating at low radii and large η are the most affected.

The next upgrade of the ATLAS detector, called 'Phase-0' upgrade, will occur during the 2013-2014 shutdown of the LHC, whose main objective is to perform interventions which will permit the machine to operate at its design parameters: $\sqrt{s} = 14$ TeV, and $\mathscr{L} = 10^{34} cm^{-2} s^{-1}$. ATLAS main goals during this period will be to compensate the performance degradation of the detectors most affected during the past three years of operation: the Inner Detector, the Muon Spectrometer (adding a new neutron shielding), and the beam pipe (installing a new one). The central upgrade activity is the installation of a new barrel layer in the present Pixel detector, the so-called IBL project.

2.4.2 Insertable B-Layer (IBL)

On the time scale of 2013, without upgrade, the present pixel detector performance could be degraded due to both radiation damage and/or component failures. Failures could be related to issues with *e.g.* thermal cycling or opto-boards. Performance degradation will be mainly related to charge collection inefficiencies and to failed components. It could also come from limitations in the hit rate that the current pixel integrated-chip can handle at high peak luminosity.

The Insertable B-Layer (IBL) [103] is an additional 4^{th} pixel layer which will be inserted between the innermost pixel layer and the beam pipe, as shown in Fig. 2.36. To make the installation of the IBL possible, a new beam pipe built of Beryllium will be installed in the central region, with radius reduced by 4 mm compared to the current beam pipe. The baseline concept of the IBL consists of 14 staves mounted directly on the beam pipe with a tilt angle of 14°. The new layout is shown in Fig. 2.37. On each stave, 16 or 32 modules depending on the sensor type will be installed. Currently, two silicon sensor types are used: planar and 3D. The sensors will be bump-bonded with a new readout chip designed in technology 130 nm: the FE-I4 [100], which has been specially developed to function at high data transfer rates (∼160 Mb/s). Its design allows an increase of the IBL segmentation by decreasing the pixel size from 400×50 μm^2 to 250×50 μm^2, which will help to face the much higher particles fluxes (scaling with $1/R^2$). As will be explained in detail in Sec. 3.7, the IBL will compensate for defects, such as irreparable failures of modules, in the existing B-layer, ensuring tracking robustness. The smaller radius will improve the vertex reconstruction and identification of *b*-jets (*b*-tagging) performance, hence extending the reach of physics analyzes. The FE-I4 chip will also be compatible with the needs of the pixel outer layers in the years $\sim$ 2021-2022 which will see the replacement of the entire Inner Detector by a new 'all-silicon' one[21].

[21] The hit rate of particles at radii above 12 cm being expected for Super-LHC luminosities to be rather similar to the rates in the B-layer at the time of the IBL upgrade.

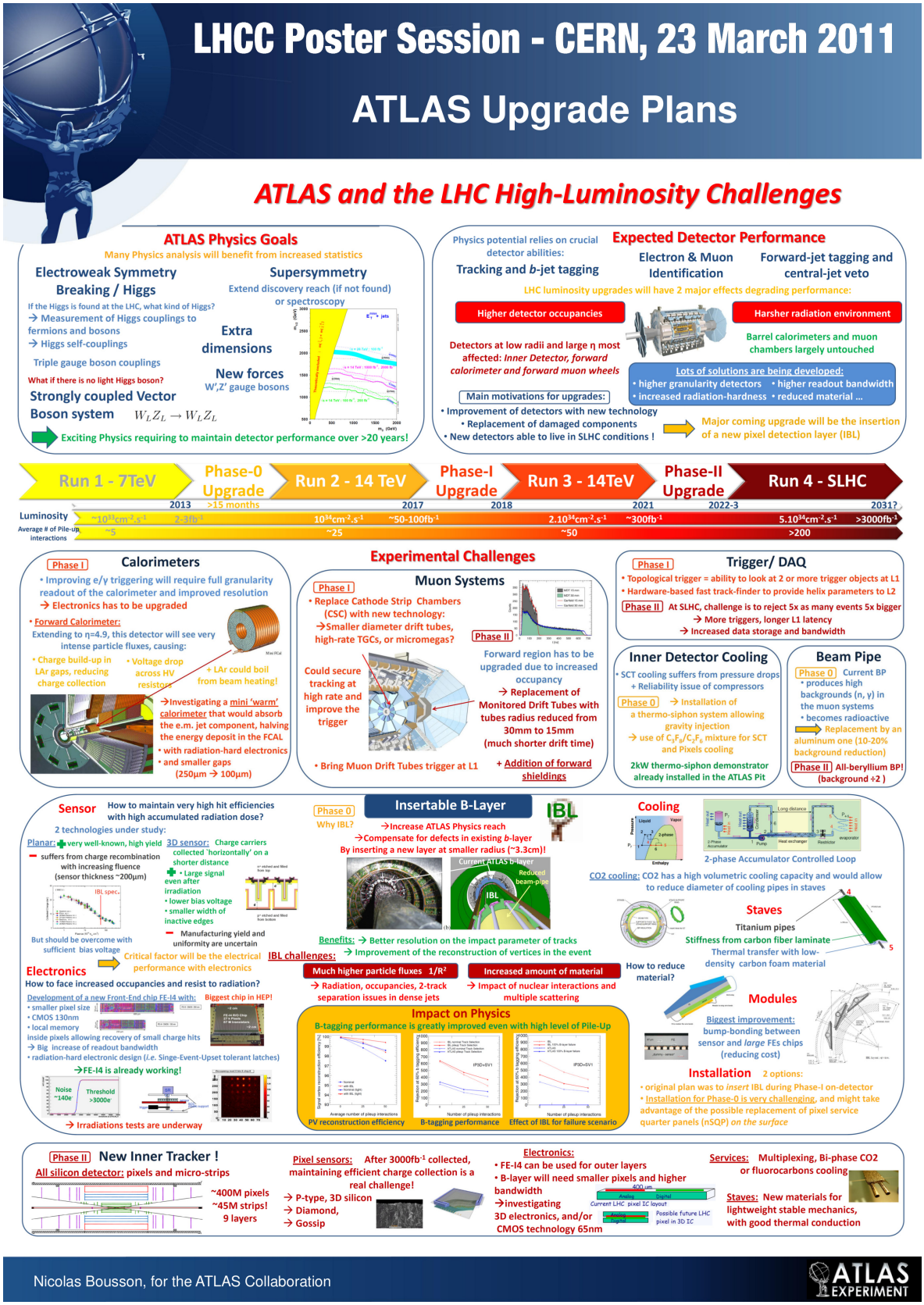

Figure 2.35: Poster presented at the CERN 105th LHCC - March 23-24th 2011 [91].

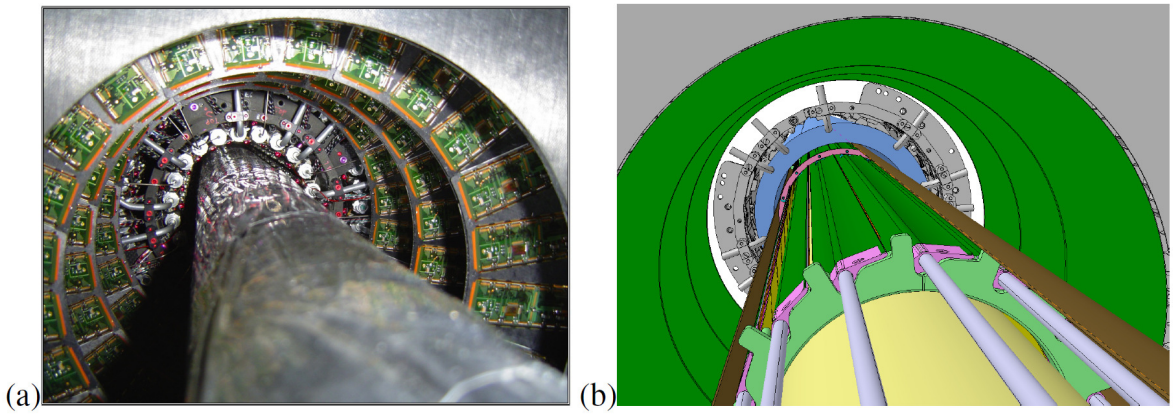

Figure 2.36: (a) Photo of the Pixel detector with the inserted beam pipe during the integration, and (b) rendering of the insertion of the IBL with the smaller beam pipe. From [103].

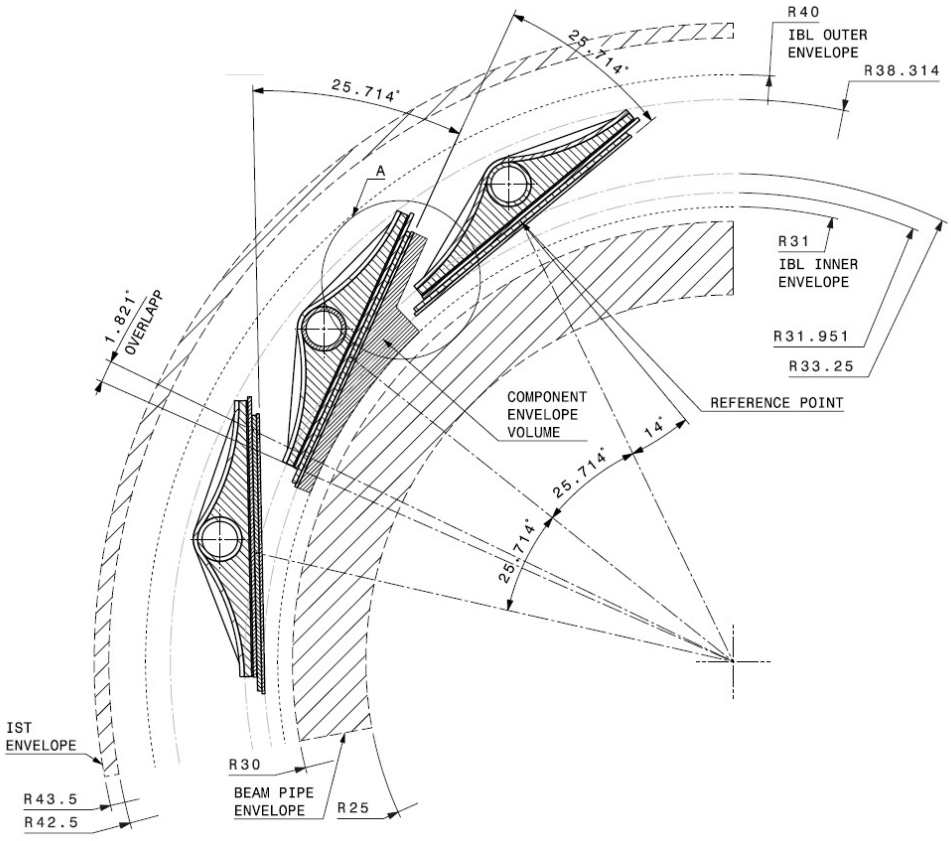

Figure 2.37: IBL layout: $r\phi$ view. From [103].

Chapter 3

Identification of b-jets

3.1 Introduction

In this chapter, we will first explain the importance of detecting jets from the hadronization of b-quarks in the LHC collisions. We will describe the specific properties of these b-jets compared to *lighter* jets, and see how they can be exploited with the ATLAS detector.

In particular, we will have a close look at the tracking performance of the Inner Detector, which plays a crucial role in the reconstruction of tracks and vertices, the basic ingredients of b-tagging.

We will then describe the so-called *early* b-tagging algorithms, that were intended to work at the start of the LHC. We will present in detail the commissioning studies for the *JetProb* algorithm.

Taggers than can achieve much higher performance will then be described, as well as a summary of all the commissioning studies we have carried out. The expected performance of all these taggers will also be shown.

Finally, we will present the improvements that the detector upgrade IBL is expected to bring. We will focus briefly on the tracking and vertexing aspects, and in detail on the b-tagging performance, both without pileup, and simulating the very high level of pileup that are expected with the coming LHC luminosity upgrades.

3.2 b-tagging key ingredients

3.2.1 Physics motivations

Why are b-quarks are so interesting, and why is it so important to detect them in a general-purpose experiment such as ATLAS ?

This can be easily understood referring to the quark masses indicated in Fig. 1.3. It can be seen that, with the exception of the top quark, which decays before hadronizing, the bottom quark is much heavier than the other quarks. This means that heavy particles could couple, hence decay, preferentially to this quark, such as the top quark, a light SM scalar boson, or hypothetical particles still unknown (*e.g.* fourth generation quarks, new heavy gauge bosons, SUSY particles etc).

As a consequence, the identification of jets arising from the hadronization of b-quarks, referred to as 'b-tagging', together with the identification of other fundamental particles coming from a collision, is the starting point to reconstruct the initial particle that decayed. In other words, the ability to identify b-jets is an essential tool to discover and study new particles.

However, this ability would be useless if b-jets were produced just as frequently in less interesting processes. So the most important reason why b-jets are important lies in hadron collider phenomenology. As we have seen in Sec. 2.2.3, in generic QCD interactions, only a percent or less of the time b-jets (see Fig. 2.6) are produced[1], and almost always, the jets are due to the hadronization of lighter quarks, or gluons, so the presence of b-jets in an event is rare. The main reason for this is that b-quarks are not components of the protons, that are composed essentially of *up* and *down* quarks as we have seen. So b-quarks exist only for vanishingly small instants of time in the quark 'sea' of the protons, and it is thus a very rare occurrence that a proton-proton collision involves one of them, gluons having to be ready to spend $\gtrsim 10$ GeV into the creation of a $b\bar{b}$ pair.

To come back to more pragmatic considerations, in addition to the searches for new physics mentioned above, b-tagging will be particularly useful to select very pure top quark samples, study the new boson discovered compatible with the Standard Model scalar boson, and to veto the large $t\bar{t}$ background for many physics channels.

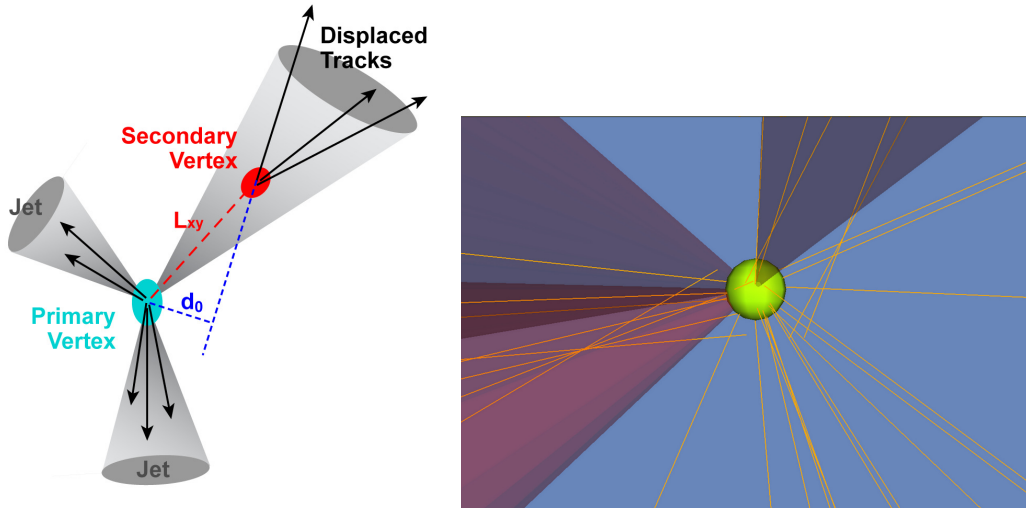

(a) *Artist view* (b) Reconstructed tracks in a 'real' b-jet.

Figure 3.1: (a) Schematic illustration of the important features a b-jet (the top-right one) and light jets. (b) Event display from a real event (snapshot from Fig. 3.2). The green 'ball' represents the primary interaction vertex, and the left part shows a reconstructed secondary vertex inside a jet.

3.2.2 Properties of b-jets

In addition to the fact that b-jets are rare and especially interesting, they also have unique features that greatly help to distinguish them from *lighter* jets:

- The fragmentation is hard, and the hadrons containing bottom quarks retain about 70% of the original b-quark momentum.
- The mass of b-hadrons is relatively high (>5 GeV). Thus, their decay products tend to have higher transverse momentum (momentum perpendicular to the original direction of the bottom

[1] $\sigma_{b\bar{b}}$ was actually one of the first physics measurements performed at the LHC

quark, and therefore of the b-jet). This causes b-jets to be wider, have higher multiplicities (numbers of constituent particles) and invariant masses.

- b-hadrons have sufficient lifetime that they travel some distance before decaying. Typically, their lifetime (τ) is of the order of 1.5 ps ($c\tau \approx 450\mu m$). A b-hadron in a jet with $p_T = 50$ GeV will therefore have a significant flight path length $< l >= \beta\gamma c\tau$, traveling on average 3 mm before decaying.

- In 40% of the cases, the decay products contain a muon or an electron, because $BR(B \to \ell X) \sim$ 20% where $\ell = e$ or μ, taking into account cascade decays ($B \to D \to \ell X$).

Experimentally, b-jet identification will hence rely on:

- measuring the impact parameters (IPs) of the tracks from the b-hadron decay products, *i.e.* the distance of closest approach of the track to the primary vertex point (*N.B.*: a more detailed definition of the IP of a track will be given in Sec. 3.2.4). The tracks from b-jets tend to have rather large IPs which can be distinguished from tracks originating from the primary vertex. This is illustrated in Fig. 3.1 (a) which depicts two light jets, with tracks arising from the primary vertex, and one b-jet with tracks, stemming from a displaced vertex, with large IP (d_0). We will come back in much detail on the algorithms exploiting the IP of tracks later in this document.

- exploiting the *flight* distance of b-hadrons in the detector. Given the great precision of the ATLAS Inner Detector, that allows to reconstruct tracks of $p_T = 1$ GeV with a spatial resolution better than ~ 100 μm, it is possible to measure this distance by reconstructing potential 'secondary vertices' (SV) displaced from the primary interaction. This is more demanding, but when such vertices can be reconstructed, this is a strong indication, as can be seen on the illustration in Fig. 3.1. In addition, a big fraction of the jet energy comes from the SV, due to the hard fragmentation, which is an important property of the SVs to exploit. We will come back in more details on the reconstruction of SVs in Sec. 3.2.6 and when describing the algorithms exploiting SVs later in this document.

- detecting leptons in jets, which due to the hard fragmentation and high mass of b-hadrons, have large transverse momentum, and large momentum relative to the jet axis. These leptons also have relative low-energy compared to leptons produced in hard interaction at the primary vertex of *physics* events. Taggers relying on the detection of such leptons in jets are hence called 'Soft-lepton' taggers, but we will not detail their functioning (please refer to [166]) nor commission them in this work[2]. This is because the performance of these taggers is intrinsically limited by the branching ratios to leptons, and by all the reconstruction efficiencies for *actually* attaching a real lepton to true b-jets, and because the IP- and SV-based taggers can reach much higher performance. However, combining these soft-lepton taggers with track-based taggers might help to reach better performance in the future.

To summarize, the most important factor impacting the b-tagging performance is the reconstruction of tracks, from which vertices can be reconstructed, and the performance of this reconstruction relies directly on the performance of the pixel detector.

[2]We will however briefly see that the Soft-muon tagger was useful in some calibration studies in Sec. 3.6.

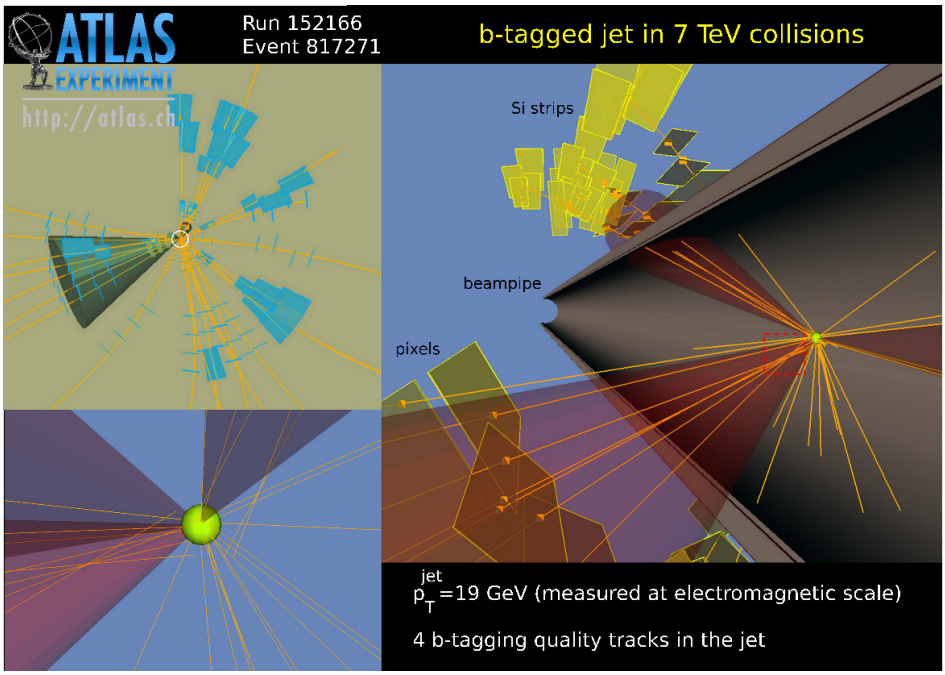

Figure 3.2: Event display of a *b*-jet candidate in one of the first 7 TeV event (number 817 271 from run 152 166.

3.2.3 Primary vertex

Reconstruction The determination of the position of the primary vertex (PV) of the event, *i.e.* the exact location of the high-p_T interaction, is a first crucial step before computing the IP of tracks or measuring the displacement of possible displaced vertices. It relies on the tracks reconstructed in the event and consists of two stages:

- first: the *vertex finding* associates reconstructed tracks to vertex candidates. An iterative approach is used to find the PV candidates, in which the tracks the most incompatible with a PV candidate are removed and used to seed another vertex candidate;
- second: the *vertex fitting* reconstructs the vertex positions (and their error matrix) and refits the tracks constraining them to originate from the reconstructed vertex. The fitting is relying on an *adaptive* vertex fitting algorithm [110].

The beam-spot information is used at both stages of the PV reconstruction, in particular to constrain the vertex fit. PV candidates are required to have at least 5 tracks. For further information about the PV reconstruction, the reader is referred to Ref. [111].

Choice One important issue for *b*-tagging is the choice of the PV, which is less trivial in the presence of additional minimum-bias events (pile-up): the primary vertex from a pile-up event may be picked-up, or a fake PV built from tracks from two different vertices may be reconstructed. The current strategy is to choose the PV candidate which maximizes $\sum_{tracks} {p_T}^2$: all candidates are ranked in decreasing order and the first candidate is considered to be the best PV and is used as the reference point for the interaction location.

3.2.4 Impact parameter

As introduced previously, the IP of a track, *i.e.* the distance of closest approach of the track to the primary vertex, is a key-ingredient for discriminating tracks originating from displaced vertices from tracks originating from the PV. In the ATLAS coordinate system, it is particularly useful to define:

- the transverse IP, d_0, which is the distance of closest approach of the track to the PV, in the r-ϕ projection.
- z_0, which is the z coordinate of the track at the point of closest approach in r-ϕ[3].

These two parameters can be computed in two ways:

- In a 'Biased' way, *i.e.* d_0 or z_0 of a track is computed w.r.t to a PV and this track was also used for the PV determination.
- In a 'Un-biased' way: if the track under consideration was initially used for the PV determination, it is first removed from the PV which is subsequently refitted, and d_0 or z_0 is then re-computed w.r.t this new PV. This is done because in the hypothesis that the track stems from a displaced vertex, *e.g.* in a b-jet, the fact that the track was included in the PV fit might bias the PV determination, hence the IP computation. Unless explicitly quoted, we will only use this determination of the track IPs in the following.

In order to give more importance to tracks well reconstructed, the IP of a track can be divided by the error on its measurement, which includes contributions from the IP resolution and the uncertainty on the reconstructed PV. The quantity obtained, assigned track-by-track, is called the IP *significance*:

$$\frac{d_0}{\sigma(d_0)} = \frac{d_0}{\sqrt{\sigma^2(d_0^{track}) + \sigma_{PV}^2}} \tag{3.1}$$

The resolution $\sigma(d_0^{track})$ of the impact parameter determined by a tracking detector can be divided into two independent sources, the intrinsic and multiple-scattering terms:

$$\sigma(d_0^{\text{track}}) = \sigma_{\text{intrinsic}} \oplus \sigma_{\text{MS}} \tag{3.2}$$

where $\sigma_{\text{intrinsic}}$ is a constant and accounts for intrinsic detector resolution and misalignment. Further discussion about the multiple-scattering term will be detailed in the study in Sec. 3.3.4.4.

3.2.5 Tracks in jets

3.2.5.1 Jets

Reconstruction As sketched in Fig. 3.3, the evolution of a jet in the ATLAS detector can be divided roughly into three stages: the *parton* level (resulting from the parton shower, cf. Sec. 2.2.6), the *particle* level (resulting from hadronization), and the *calorimeter* level (resulting from the energy deposition in the calorimeters).

Jet candidates are reconstructed by using the anti-k_t jet clustering algorithm [101] with a distance parameter of $R = 0.4$. The inputs to this algorithm are groups of calorimeter cells, called *topological energy clusters*, that are designed to follow the shower development taking advantage of the fine segmentation of the calorimeters.

[3]Formally, $z_0 \cdot sin\theta$ is the longitudinal IP of the track, but it is common to call mistakenly z_0 the longitudinal IP.

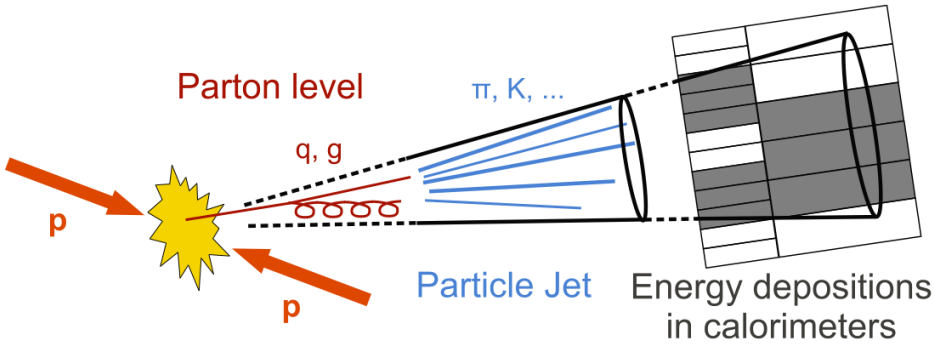

Figure 3.3: The three regimes in the evolution of a jet: parton level, particle level and calorimeter level [88].

Calibration In order to calibrate the measured calorimeter level jet energy to the particle level, the jet energies are corrected for inhomogeneities and for the non-compensating nature of the calorimeter by using p_T- and η-dependent calibration factors determined from Monte Carlo simulation [102]. This procedure is commonly referred to as Jet Energy Scale (JES) calibration.

Only jets with $p_T > 20$ GeV and within $|\eta| < 2.5$ are considered in the following, where the jet direction is properly corrected to take into account the position of the primary vertex along the z axis. These p_T and η cuts define the *taggability* requirement for jets.

3.2.5.2 Track selection

The tracks used are reconstructed from the so-called "inside-out" approach [105, 112], in which the pattern-recognition starts in the two silicon systems (pixel and micro-strip detectors) and tracks are extended in increasing radius.

The standard quality level requires at least seven precision hits (pixel or micro-strip hits) on the track. The transverse and longitudinal impact parameters defined with respect to the detector center must fulfill $|d_0| < 2$ mm and $|z_0 - z_{pv}| \sin\theta < 10$ mm respectively, where z_{pv} is the longitudinal location of the primary vertex. Only tracks with $p_T > 1$ GeV are considered.

The track selection for b-tagging is further designed to select well-measured tracks and reject fake tracks and tracks from long-lived particles (K_s, Λ and other hyperon decays) and material interactions (photons conversions or hadronic interactions).

For the so-called 'b-tagging quality' level, the extra requirements are: at least two hits in the pixel detector of which one must be in the innermost pixel layer, $|d_0| < 1$ mm and $|z_0| \sin\theta < 1.5$ mm (this time the impact parameters are expressed with respect to the primary vertex). This selection is used by all the tagging algorithms relying on the impact parameters of tracks and is referred to as the baseline b-tagging track selection.

The secondary vertex algorithms use a looser track selection[4], in particular in order to maximize the efficiency to reconstruct V^0 (neutral particles with long lifetime, such as K^0, Λ^0, etc) decays and material interactions whose corresponding tracks are subsequently removed for b-tagging purposes. The main differences in the selection cuts are the following: $p_T > 400$ MeV, $|d_0| < 3.5$ mm (no cut on

[4]The track selection for the SV0 algorithm that will be described in Sec. 3.4.1 is even looser than the one described here, see [119].

z_0), at least one hit in the pixel detector (no requirement on the innermost pixel layer), no more than one shared hit on the track. These selection cuts are summarized in Tab.3.1.

Variable	Cut IP	Cut SV
p_T	>1GeV	>400 MeV
$\|\eta\|$	<2.7	
χ^2/N_{dof}	-	<3
$\|d_0\|$	1mm	<3.5mm
$\|z_0\|sin\theta$	<1.5mm	-
N_{bla}	≥1	-
N_{Si}	≥7	
N_{pix}	≥2	≥1
N_{SCT}	-	≥4
N_{shared}	-	=0

Table 3.1: Summary of the track selection cuts for IP- and SV-based algorithms. N_{Si}, N_{pix}, N_{SCT}, N_{bla} are the numbers of hits in, respectively, the silicon detectors (pixel+SCT), the pixel detector, the SCT, the pixel *b*-layer. N_{shared} is the number of hits that are shared with another track.

3.2.5.3 Association of tracks to jets

Tracks are associated to the jets with a spatial matching in ΔR(jet, track). The association cut varies as a function of the jet p_T according to $R = 0.239 + e^{(-1.22-1.64\cdot 10^{-5}\cdot p_T^{\text{jet}})}$, in order to have a smaller cone for jets at high p_T which are more collimated [106]. For the average jet p_T of 26 GeV, the ΔR cut is 0.43. At 20 GeV, it is 0.45 while for a jet with a p_T around 150 GeV the ΔR cut is 0.26.

3.2.5.4 Signing

In order to increase the discriminating power of the IP significance, the above IP variables are given a 'lifetime' sign: positive if the track is more likely to intersect the jet flight axis 'in front' of the PV (*i.e.* is more compatible with stemming from a displaced vertex in the direction of flight expected for the *b*-hadron), or negative if the track is more likely to intersect the flight axis 'behind' the PV, opposite to the jet direction. Fig. 3.4 illustrates both cases, and defines the variables needed to define formally the lifetime sign: $\overrightarrow{p}_{jet}$, the jet direction as measured by the calorimeters, $\overrightarrow{p}_{track}$ and $\overrightarrow{r}_{IP}$ the direction and position of the track at the point of closest approach to the PV and $\overrightarrow{r}_{PV}$ the position of the PV. The sign is then given by:

$$sign_{3D} = sign([\overrightarrow{p}_{track} \times \overrightarrow{p}_{jet}] \cdot [\overrightarrow{p}_{track} \times \Delta\overrightarrow{r}_{IP}]) \,. \tag{3.3}$$

where $\Delta\overrightarrow{r}_{IP} = \overrightarrow{r}_{IP} - \overrightarrow{r}_{PV}$ is the three-dimensional IP of the track with respect to the PV.

The lifetime sign can also be defined on the transverse plane (x-y) or on the longitudinal plan ($r\phi$-z) by considering the projections of the three-dimensional IP respectively on these two planes. Fig. 3.5 shows the signed transverse IP d_0 and its signed significance $d_0/\sigma(d_0)$ using Monte-Carlo simulation at $\sqrt{s} = 14$ TeV for *b*-, *c*-, and light-jets. One can clearly see *at first glance*[5] that the experimental resolution generates a random sign for the tracks originating from the PV, while tracks

[5]Tracks originating from b/c-hadron decays also contribute to the negative part of these distributions due to cascade decays in the jets, or when the b/c-hadron deviates slightly from the jet direction.

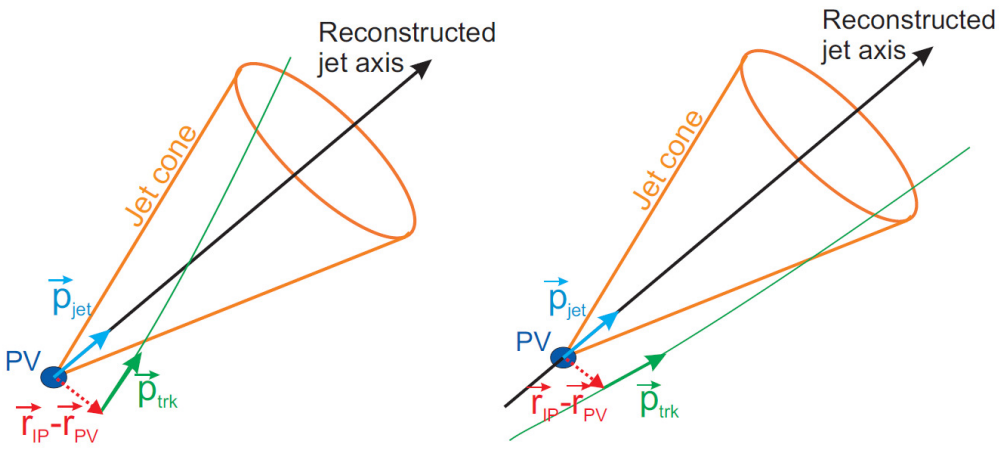

Figure 3.4: Definition of variables needed to compute the lifetime sign of a track in the three-dimensional space. In addition a positive (left) and negative (right) lifetime signed track is shown. From [110].

from the b/c hadron decay tend to have a positive sign. The signed IP significance will be a crucial variable of several of the b-tagging algorithms that we will describe later in this document.

3.2.6 Secondary vertices

As stated previously, a b-jet originates from a b-quark, which produces a b-hadron in the fragmentation. The b-hadron then decays due to electroweak interactions, which causes the transition of the b-quark preferably into a c-quark ($|V_{cb}|^2 >> |V_{ub}|^2$), which then also undergoes a weak decay. As a result, the typical topology of the particles in a b-jet is a decay chain with two vertices, one stemming from the b-hadron decay and at least one from the c-hadron decays, as illustrated in Fig. 3.6.

Trying to resolve the b- and c-hadron vertices of the decay cascade separately is very difficult for the following reasons:

- the probability to have at least two reconstructed charged particle tracks both from the b- and c-hadron decays is much less than 100%. This is both because of the charged particle multiplicities involved in these decays[6] as well as the limited track reconstruction efficiency due mainly to material interactions.

- the resolutions of the relevant track parameters, especially at low transverse momentum, are not sufficient to separate efficiently the two very close-by vertices.

Inclusive reconstruction For the reasons stated above, the default reconstruction procedure consists of fitting a single geometrical vertex formed by the decay products of the b-hadron including the products of the eventual subsequent charm hadron decay, as illustrated in Fig. 3.7. This is strictly speaking not the correct hypothesis, but this is an approximation that works well for a large fraction of the cases. The search starts by building all two-track pairs that form a good vertex, using only tracks associated to the jet and far enough from the primary vertex. Vertices compatible with a V^0 or

[6]The large b-hadron masses lead to a huge number of possible decays with very small branching ratios, many of them involving neutral particles (that cannot be used for the vertex reconstruction).

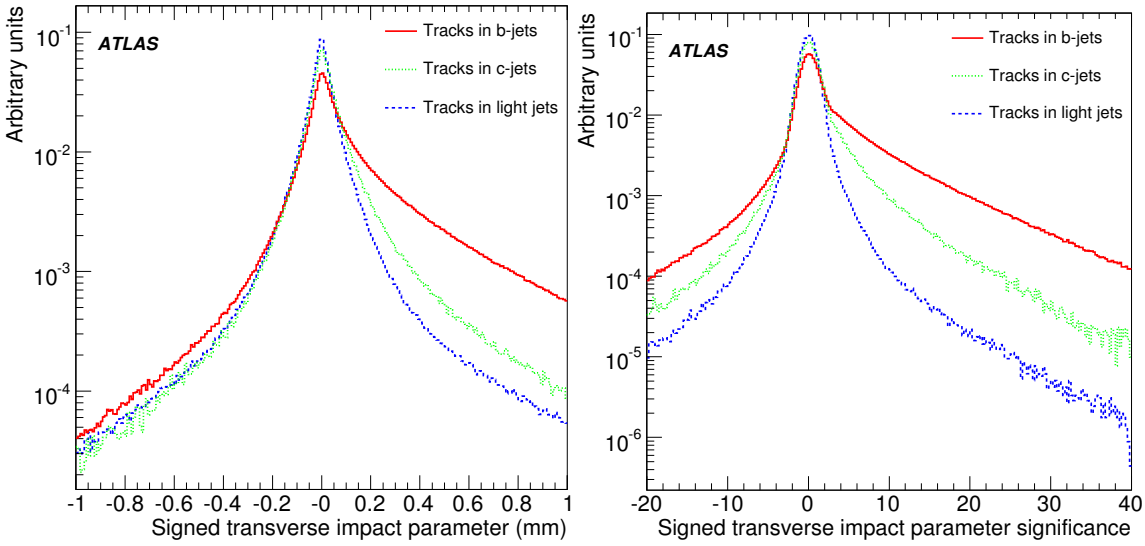

(a) (b)

Figure 3.5: Signed transverse impact d_0 (a) and signed transverse impact parameter significance d_0/σ_{d_0} distribution (b) for b-jets, c-jets and light jets.

material interaction are rejected. All tracks from the remaining two-track vertices are combined into a single inclusive vertex, using an iterative procedure to remove the worst track until the χ^2 of the vertex fit is good. This kind of reconstruction is used by the b-tagging algorithms called *SV0* and *SV1* that we will describe in Sec. 3.4.1 and 3.5.1.3.

Multi-vertex reconstruction Another approach is to make the kinematic assumption that the PV, the b- and c-hadron decay vertices lie on the same line, the flight path of the b-hadron. This has several advantages, such as increasing the chance to separate the b/c-hadron vertices (as illustrated in Fig. 3.6), or reconstructing incomplete topologies *e.g.* with a single track stemming from the b/c-hadron decay(s). This approach is used by the b-tagging algorithm called *JetFitter*, that we will describe in Sec. 3.5.1.4.

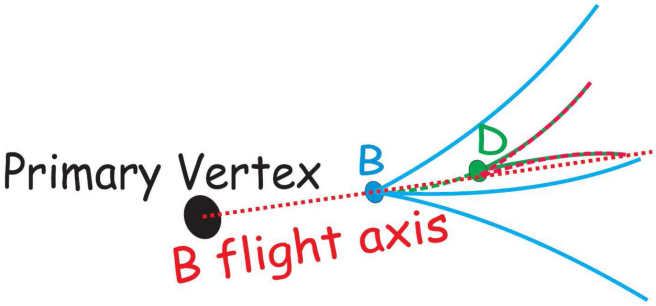

Figure 3.6: Illustration of the decay chain inside a b-jet, and of a multi-vertex fit using the b-hadron flight direction as constraint [126].

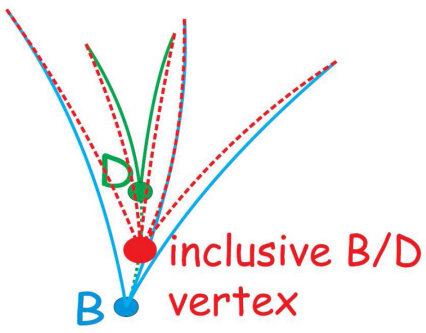

Figure 3.7: Illustration of an inclusive vertex fit inside a b-jet [126].

3.2.7 Performance estimators

3.2.7.1 Labeling

To define b-tagging performance, the Monte-Carlo event history is used to know the type of parton from which a jet originates. This *labeling* procedure is not unambiguous and is not strictly identical for different Monte Carlo generators. For all the results presented in this document, the following quark labeling has been used:

- a jet is labeled as a b-jet if a b-quark with $p_T > 5$ GeV is found in a cone of size $\Delta R = 0.3$ around the jet direction;
- If no b-quark is found, one looks for a c-quark with the same procedure. If found, the jet is labeled as a c-jet;
- If neither a b-quark nor a c-quark is found, one looks for a τ lepton, and if found, labels the jet as a τ-jet;
- If none of the above particles is found, the jet is labeled as a light-jet. No attempt is made to distinguish between u, d, s quarks and gluon since such a label is even more ambiguous.

3.2.7.2 Statistical definition

Now that we have detailed the main ideas to distinguish b-jets from lighter jets, we need to define a bit more formally what a *good* b-tagging algorithm should be able to do. In general, physics analysis will need to answer the question: *Is my jet a b-jet or not ?* So in principle an algorithm should be able to answer by *yes or no*[7], taking as input the outputs of the ATLAS detector (PVs, tracks, jets, etc). Obviously, given the complexity of what happens during a proton-proton collision at the LHC, and all the detector imperfections, we will never know with full certainty the true nature of a *real* jet, so the performance of an algorithm can only be assessed on a statistical basis.

Hypothesis testing b-tagging can hence be easily formulated in the statistical framework of *hypothesis testing* (see *e.g.* [115]), in which one tests an hypothesis H_0 (*e.g.* the jet originates from a b-quark) against its alternative hypothesis H_1 (*e.g.* the jet does not originate from a b-quark), on the basis of experimental observations. For that purpose, one can define:

- X, some function of the observations, called the *test statistic*;
- W, the space of all possible values of X;
- w, a sub-space of W, called a *rejection region*, such that observations X falling into w are regarded as implying that the hypothesis H_0 is not true;
- $W - w$, the complement of w, called *acceptance region* (of H_0).

Fig. 3.8 illustrates an example of distributions of an arbitrary test statistic for an hypothesis H_0, with *probability density function* (*p.d.f.*) $f(X|H_0)$, and its alternate H_1, with *p.d.f.* $f(X|H_1)$, as well as an acceptance region.

[7] Instead of answering to this question in such a binary manner, some analyzes might prefer to get a 'continuous' answer, translating the *likeliness* of jet to be a b-jet. This is actually not an issue at this time because all the tagging algorithm we will present in the next sections have, at an intermediate stage, an output variable translating this idea, on which the user applies a 'cut' to tag or not the jet.

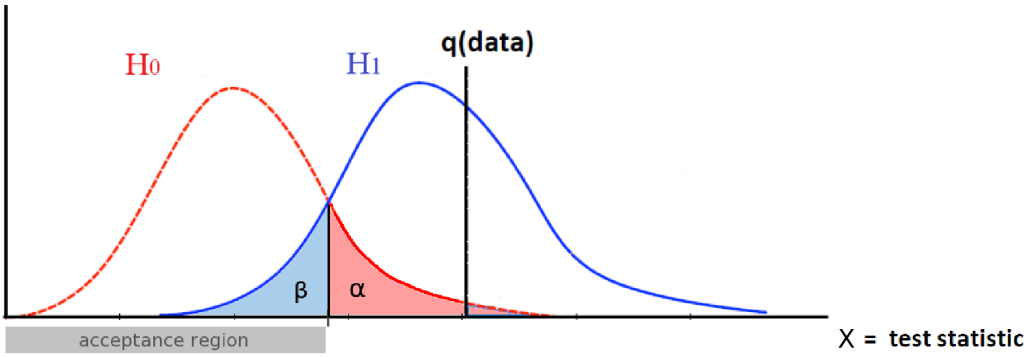

Figure 3.8: Example of the distributions of a test statistic for an hypothesis H_0 and its alternate H_1. The errors of first kind α and second kind β are displayed for a defined acceptance region, as well as the value of the test statistic for an hypothetical *real* data in black.

Defining a b-tagging algorithm is hence equivalent to building a test statistic and specifying an acceptance region such that there is no more than some (small) probability α of rejecting H_0 even if H_0 is indeed true (or equivalently, of accepting H_1 while it is false):

$$P(X \in w|H_0) = \alpha = \int_w f(X|H_0)dX \tag{3.4}$$

This probability α is often called the *level of significance*, *size of the test*, or *error of the first kind*, and is illustrated as the red integral in Fig. 3.8. In the b-tagging context, this is the probability of tagging a jet of real flavor b as non-b.

Obviously, one would like α to be as low as possible, and even for a given value, there is in principle an infinite number of possible acceptance regions giving the same value of α, so the usefulness of a test (here a b-tagging algorithm), depends on its ability to discriminate against the alternative hypothesis H_1. In practice, one wants to minimize the probability of accepting the hypothesis H_0 when it is false (or equivalently, of rejecting the hypothesis H_1 when it is true):

$$P(X \in W - w|H_1) = \beta = \int_{W-w} f(X|H_1)dX \tag{3.5}$$

This probability β is often called *error of the second kind*, or *contamination*, and $(1-\beta)$ the *power of the test*. β is also illustrated as the blue integral in Fig. 3.8. In the b-tagging context, this is the probability of tagging a jet of real flavor non-b as a b-jet.

Efficiency and rejection Equivalently to define the performance of a test by defining its level of significance α and by its contamination β, from two samples of true b-jets and true non-b-jets (from Monte Carlo simulation), one can define for a b-tagging algorithm:

- its *efficiency*:

$$\varepsilon_b = (1-\alpha) = \frac{\text{Number of jets of real flavor } b \text{ tagged as } b}{\text{Number of jets of real flavor } b} \tag{3.6}$$

- its *mis-tagging rate*:

$$\varepsilon_{\text{non-b}} = \beta = \frac{\text{Number of jets of real flavor non-}b \text{ tagged as } b}{\text{Number of jets of real flavor non-}b} \tag{3.7}$$

For historical reasons in ATLAS, we will mostly use $r_{\text{non-b}} = 1/\varepsilon_{\text{non-b}}$, called the *light-jet rejection* instead of $\varepsilon_{\text{non-b}}$ in the rest of this document.

To summarize, we would like an as high as possible b-tagging efficiency, for an as high as possible light-jet rejection. A pair $(\varepsilon_b; r_{\text{non-b}})$ is called an *operating point* of the algorithm, and defines fully on average its performance on the Monte-Carlo samples on which it has been derived. We will illustrate later on that changing the acceptance region (*i.e.* the region classifying a jet as b-jet) modifies this operating point.

In practice As we have just seen, the performance of an algorithm is first defined using Monte Carlo simulation. But how do we tag a jet from *real* data ? Exactly as for simulation: if the algorithm returns a value (the test statistic) that falls in the acceptance region, we label (or *tag*) the jet as b; if not, we label it as a light-jet (Fig. 3.8 illustrates an example of a real jet falling in the rejection region that will be tagged as a light jet). The second most important question is how do we know that the *real* performance of an algorithm will be the same as the one derived from simulation ? This is a fundamental question for any physics analysis involving b-tagging in ATLAS, and it is tackled on two fronts:

- First, the algorithms need to be *commissioned*, which means that a careful comparison has to be made between the *observed (or real)* data and the MC simulation, for all the input and output variables they are using. This is a crucial step because it means that one has looked in detail into the 'black-box', and that one understands the behavior of the algorithms and the physics behind. For example, one could observe a good data-to-simulation agreement for the outputs of an algorithm, but this might hide two mis-modeled effects that luckily compensate each other. The commissioning is successful when the conclusion can be reached that the data-to-simulation agreement is understood and judged good enough so that the physics analyzes can use it, and that their performance can be estimated, or *calibrated*, in data, which is the next step that we describe in the next point.

  Maybe more important, this is during the commissioning phase that one has to face technical problems (*e.g.* in order to make work properly the algorithms) or problems related to the simulation, and that one needs to develop solutions that will be useful for other related studies, like the calibration in data for example. This is the opportunity to isolate the biggest sources of data-to-simulation disagreement (*e.g.* mis-alignment, bad description of the matter in the detector, estimation of the error on pixel clusters, etc), and decide which areas need improvement. Ideally, one would like to recover an almost perfect agreement between simulation and data, which would give the highest confidence that the simulation reproduces well the reality.

- Secondly, the b-tagging performance needs to be checked *in data*, a step that is called *calibration* of the algorithms. This is a crucial step because, as we have seen, b-tagging will help to make important physics measurements or major discoveries (that will translate as a disagreement between the *known* theory and the observations) so one needs to estimate as accurately as possible the level of agreement between data and MC, and correct for the discrepancies. In practice, these studies, that are based on lepton tagging or on a selection of very pure $t\bar{t}$ events, yield scaling factors that one needs to apply at the analysis level to jets from MC simulation, together with some related uncertainties on these factors. This will be explained briefly in Sec. 3.6, and used in our search for fourth generation quarks in Chap. 4.

3.3 Tracking studies

We will now assess the tracking performance of the ATLAS Inner Detector presenting some studies relevant for *b*-tagging, in particular the track properties and notably the impact parameter resolution. For this we will use the first LHC data collected at $\sqrt{s} = 900$ GeV in December 2009, and the first 15 nb^{-1} of data collected at $\sqrt{s} = 7$ TeV from March to June 2010. We also performed similar studies using the first 0.4 nb^{-1} of 7 TeV data but they are not presented here since the results with 15 nb^{-1} are using an improved alignment of the ATLAS detector and a more precise error description with respect to previous data periods. We have documented all this work in the public conference notes [118, 120, 121] in which further details can be found. Given the similarity of the studies for the 900 GeV and 7 TeV data, we will start by a description of the data and event selection for both cases, but we will then present generally the results in parallel.

3.3.1 Data sample and event selection

For the 900 GeV data: the trigger relied on the combination of two different devices: the Beam Pick-up probes and the Minimum Bias Trigger Scintillators (cf. [116]). Experimental data are compared to 10 million events from a Monte Carlo simulation of non-diffractive minimum bias events, based on the PYTHIA event generator [167], and described in Ref. [116]. Experimental and simulated data were re-reconstructed, updating the primary vertex reconstruction and using the most up-to-date dead pixel module list.

In addition, events are required to have at least one reconstructed primary vertex. This is essential for *b*-tagging purposes: either to compute the impact parameters of tracks with respect to the primary vertex or to look for vertices displaced with respect to the primary vertex. To ensure a well-reconstructed primary vertex, only vertices with at least 4 tracks are considered. A sample of $\sim$300k events is available with this selection.

For the 7 TeV data: The trigger used to select events is the jet trigger with the lowest E_T threshold at the first trigger level. This trigger requires at least one jet candidate object with $E_T > 5$ GeV at the electromagnetic scale, where no hadronic jet energy correction is applied, and is referred to as J5. At the analysis level at least one jet with $E_T > 20$ GeV is required.

Experimental data are compared to dijet Monte Carlo simulation, based on the PYTHIA event generator [168]. Experimental and simulated data were reconstructed according to the version of the ATLAS reconstruction software frozen in May 2010, using improved alignment constants and a more precise cluster error description in the Inner Detector. In particular, the cluster errors used for the early commissioning of the Inner Detector at $\sqrt{s} = 900$ GeV were based on very *broad* errors, reflecting a uniform distribution corresponding to the size of the cluster considered, while the new error description makes use of a more complete parametrization of the errors as a function of the track azimuthal incidence angle and of the cluster size.

Events are required to have a reconstructed primary vertex with at least 10 tracks, while events with one or more additional reconstructed primary vertices with more than 4 tracks are removed from the sample to reduce the influence of pile-up. A sample of 3.9 million events is available with this selection.

Finally, for both sets of data, the simulated geometry corresponds to a perfectly aligned detector. Only data collected during luminosity blocks corresponding to stable beam periods in which the silicon systems were operated at full depletion voltage are used.

3.3.2 Simulation reweighting

As simulation samples are generally prepared before knowing the exact LHC parameters that will be used during data-taking, the distributions of the primary vertices of the events somewhat differ in data and in simulation. It is notably much wider in data for the PV z coordinate. Events were hence reweighted in order to recover a perfect agreement for the width and mean of the PV z coordinate.

Posterior to that treatment, the p_T spectrum of the tracks was observed to be a little harder in the simulation compared to data. A jet reweighting for this variable was hence performed in addition to the PV reweighting mentioned previously.

3.3.3 Track selection

The track selection is the IP track selection described in Sec. 3.2.5.2. The total number of selected tracks is about 458000 and 23 million for respectively the 900 GeV and 7 TeV data.

3.3.4 Track properties

3.3.4.1 Overall hit patterns

The patterns of hits on tracks have been studied using the experimental data and compared to Monte Carlo simulated data.

The distribution of the average number of hits in the pixel detector as a function of the track azimuthal angle and pseudo-rapidity are shown on Fig. 3.9.

The simulated events describe well the experimental data. There are slight discrepancies between data and Monte Carlo for the number of pixel hits on track: only one configuration of dead pixel modules was simulated while the number of dead modules fluctuated over the period of data considered, and this distribution is sensitive to this effect.

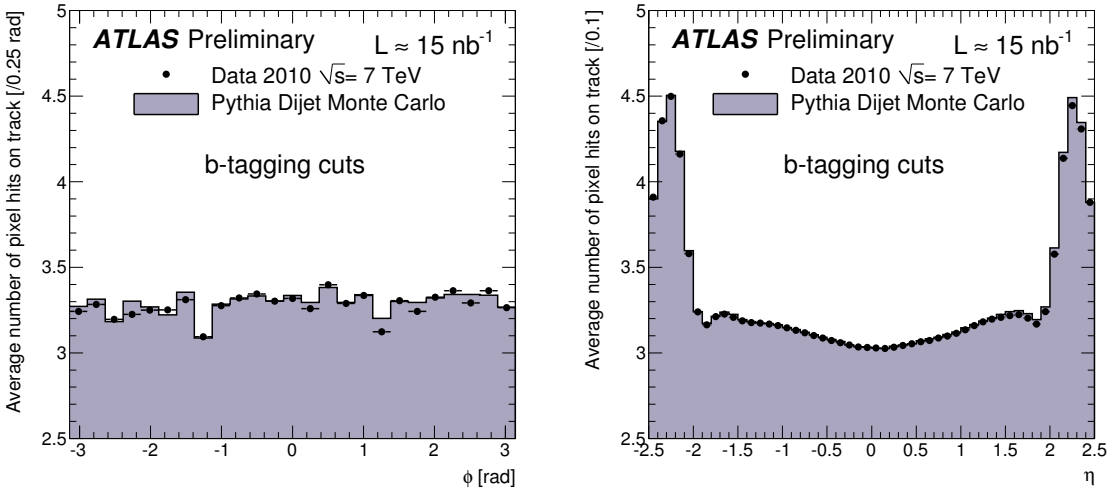

(a) Number of pixel hits versus track azimuthal angle.

(b) Number of pixel hits versus track pseudo-rapidity.

Figure 3.9: Distribution of the number of pixel hits as a function of the track azimuthal angle and pseudo-rapidity, for tracks fulfilling the *b*-tagging quality cuts. Experimental data (solid black dots) is compared to the Monte Carlo simulation (plain histogram).

The number of TRT and SCT hits on a track agree very well between experimental and simulated data.

3.3.4.2 The innermost pixel layer

The hit in the innermost pixel layer, thanks to its small radius, determines the resolution of the impact parameter of the track, and is therefore essential for b-tagging. It is therefore important to study how often a hit in this layer is attached to a track. To do so, the requirement of a hit on the innermost pixel layer is removed, but all other b-tagging quality cuts are retained. The fraction of b-tagging tracks which have such a hit is shown as a function of the track azimuthal angle and pseudo-rapidity in Figs. 3.10(a) and 3.10(b) for the 900 GeV data.

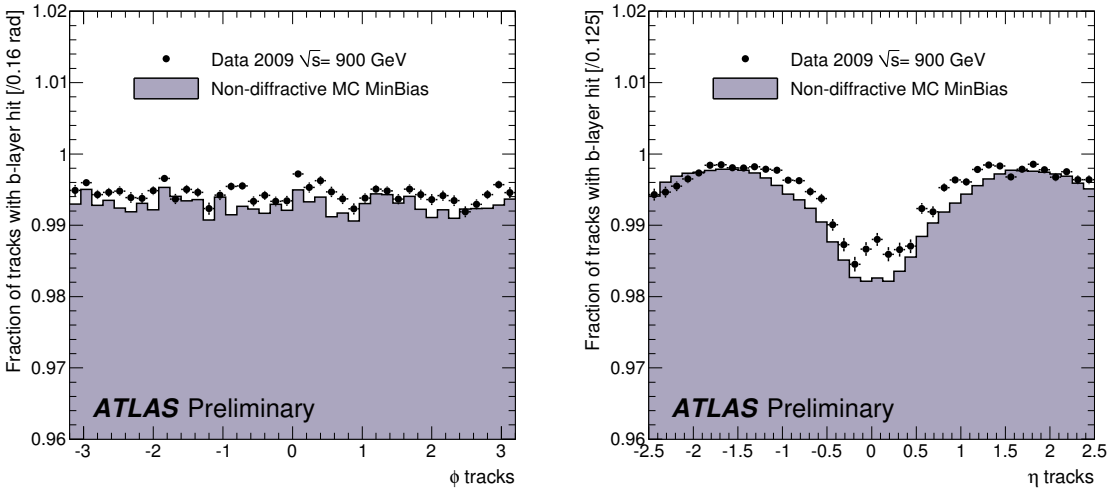

(a) As a function of the track azimuthal angle ϕ.

(b) As a function of the track pseudo-rapidity η.

Figure 3.10: Distribution of the fraction of tracks having at least one hit on the first pixel layer, while fulfilling all the other b-tagging quality criteria. Experimental data (solid black dots) are compared to the Monte Carlo simulation (plain histogram).

Tracks crossing non-instrumented regions in the innermost pixel layer or regions with a dead module or dead front-end were discarded. This was done producing maps of dead silicon in the pixel layers in data (see Fig. 3.11) and in simulation, as a function of ϕ and η. On these maps one can see un-activated modules, as well as un-activated Front-End chips ($1/16^{th}$ of a module). These maps especially emphasize the fact that dead modules in the first layer (resp. at low $|\eta|$), have much more impact in terms of loss of acceptance than modules in the higher-radius layers (resp. at higher $|\eta|$).

It can be seen that the overall fraction of tracks which could have had an innermost pixel layer hit but do not have one is of the order of 0.5 %. The small dip in the central region of the detector ($|\eta| < 0.5$) is due to very thin gaps in the b-layer between adjacent modules along z, for tracks originating from a longitudinally displaced primary vertex. Simulation and data agree reasonably well, though the fraction of tracks with an attached innermost pixel layer hit is slightly higher for the experimental data around $\eta = 0$. This is most probably due to a slightly too high fraction of pixels randomly killed in the simulation.

Similar conclusions were drawn for the 7 TeV data.

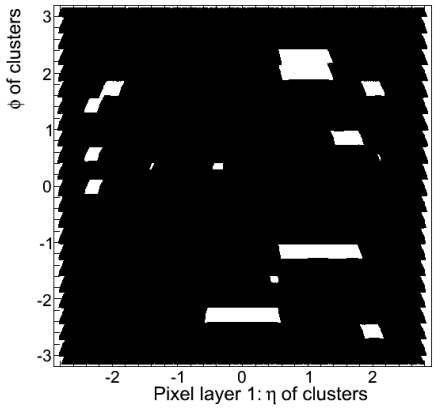

(a) *b*-layer (Layer 0)

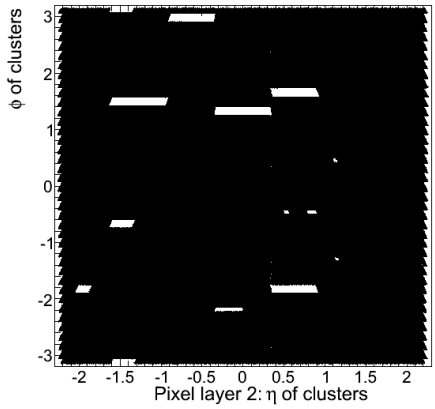

(b) Layer 2

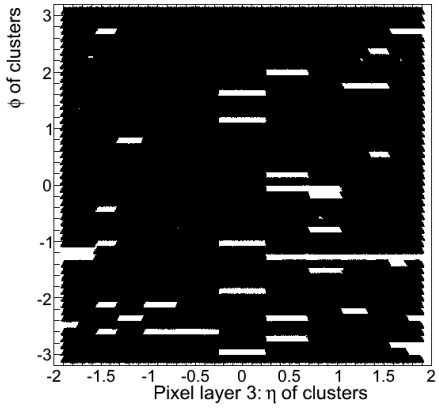

(c) Layer 3

Figure 3.11: Maps of deactivated silicon areas in the pixel detector layers, as a function of ϕ and η, derived from 900 GeV data.

3.3.4.3 Basic impact parameter distributions

The distribution of d_0 ('un-biased') for tracks fulfilling the *b*-tagging quality cuts is shown in Fig. 3.13(a) for the 7 TeV data. The distribution of the significance d_0/σ_{d_0} is shown in Figs. 3.12 and 3.13(b), for the 900 GeV and 7 TeV data, respectively. The overall agreement between data and simulation is good, though the simulated distribution of d_0 is a bit narrower.

The distribution of z_0 ('un-biased') and significance z_0/σ_{z_0} for tracks fulfilling the *b*-tagging quality cuts is shown respectively in Figs. 3.13(c) and 3.13(d), for the 7 TeV data. The agreement between data and simulation is good.

3.3.4.4 Impact parameter resolution as a function of p_T and θ

The knowledge of the IP resolution is crucial for the correct understanding of the *b*-tagging algorithms as it enters directly into the IP significance definition (Eqs. 3.1, 3.2 of Sec. 3.2.4). It has therefore been studied in detail in [118, 120, 121].

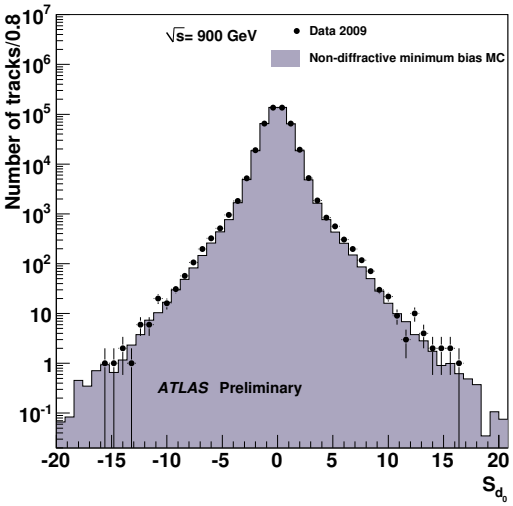

Figure 3.12: Distributions of transverse impact parameter significance d_0/σ_{d_0} for tracks passing the b-tagging quality cuts. Experimental 900 GeV data points are the solid black dots and the Monte Carlo simulation the plain histogram. The Monte Carlo is normalized to the data.

It can been shown [113, 114] that the multiple scattering contribution σ_{MS} to the impact parameter resolution can be parametrized as:

$$\sigma_{\mathrm{MS}} \quad = \quad \frac{b}{\sqrt{p^2 \sin^3\theta}} = \frac{b}{\sqrt{p_{\mathrm{T}}^2 \sin\theta}},$$

where p is the track momentum, p_T its transverse momentum and θ the track polar angle. Therefore one can write equation (3.2) in the following form:

$$\sigma^2(d_0^{\mathrm{track}}) = \sigma^2_{\mathrm{intrinsic}} + \frac{b^2}{p_{\mathrm{T}}^2 \sin\theta}\,. \tag{3.8}$$

In order to study the relation between the impact parameter resolution $\sigma(d_0^{\mathrm{track}})$, p_{T} and θ, one can fix either of the two variables, and parametrize the resolution:

- for fixed θ as
$$\sigma^2(d_0^{\mathrm{track}}) = a_1^2 + \frac{c_1^2}{p_{\mathrm{T}}^2} \qquad \text{with} \qquad c_1 = \frac{b}{\sqrt{\sin\theta}}\,; \tag{3.9}$$
- for fixed p_{T} as
$$\sigma^2(d_0^{\mathrm{track}}) = a_2^2 + \frac{c_2^2}{\sin\theta} \qquad \text{with} \qquad c_2 = \frac{b}{p_{\mathrm{T}}}\,. \tag{3.10}$$

Ideally one expects to verify relations $\sigma_{\mathrm{intrinsic}} = a_1 = a_2$ and $b = c_1\sqrt{\sin\theta} = c_2 p_{\mathrm{T}}$.

For this study, slightly different selection criteria are used than detailed earlier: the cuts on the impact parameters $|d_0|$ and $|z_0|\sin\theta$ have been removed. All other cuts remain the same. The selected tracks have been divided into 15 p_{T} bins between 1 GeV and 30 GeV and 16 θ bins. Twelve of these

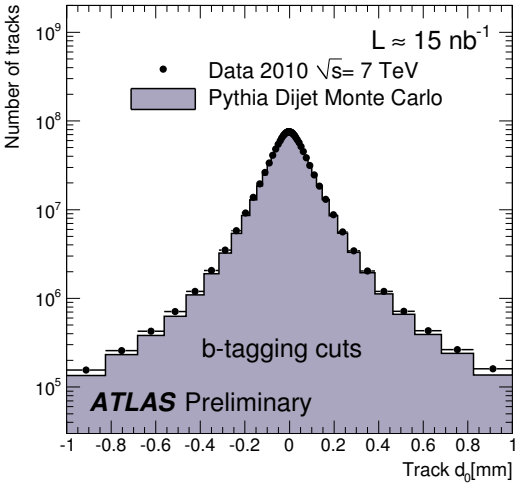

(a) Transverse impact parameter d_0.

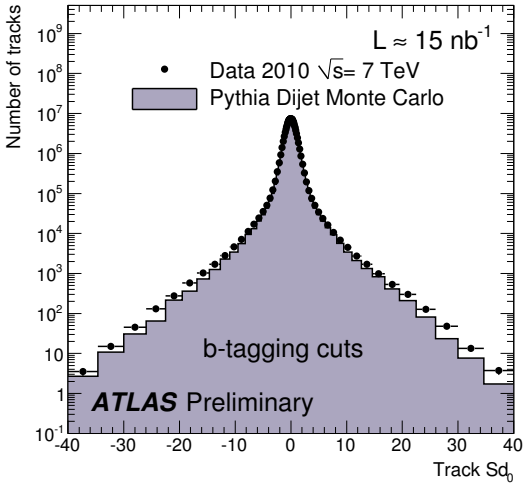

(b) Impact parameter significance d_0/σ_{d_0}.

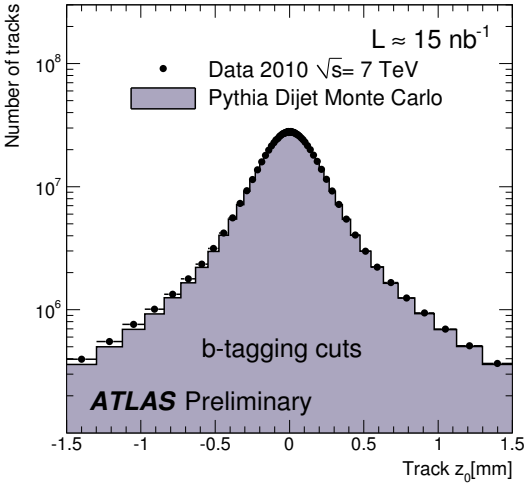

(c) Longitudinal impact parameter z_0.

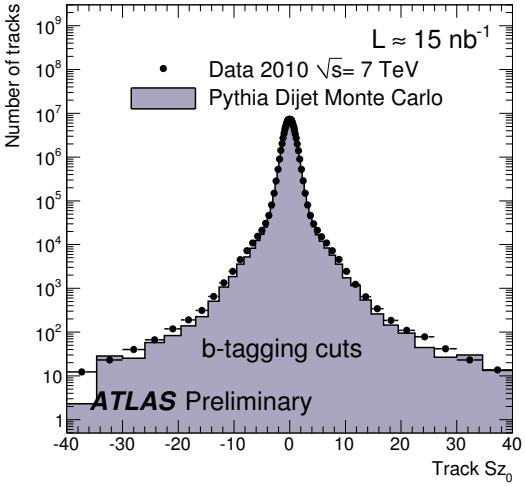

(d) Impact parameter significance z_0/σ_{z_0}.

Figure 3.13: Distributions of impact parameters and their significance for tracks passing the *b*-tagging quality cuts. The upper plots are for the transverse impact parameter, the lower ones for the longitudinal impact parameter. Experimental 7 TeV data points are the solid black dots and the Monte Carlo simulation the plain histogram. The Monte Carlo is normalized to the data.

bins are in the barrel region. The restriction to the barrel is wanted since the model in equation (3.8) is only valid for cylindrically distributed material.

The distribution of the transverse impact parameter was fitted within 2σ of its mean with a Gaussian function for each bin in θ and p_{T}. The width of this Gaussian $\sigma(d_0) = \sigma(d_0^{\mathrm{track}}) \oplus \sigma(PV)$ is understood as the impact parameter resolution convoluted with the uncertainty of the reconstructed primary vertex.

Figures 3.14 and 3.15 show the squared impact parameter resolution $\sigma^2(d_0) = \sigma^2(d_0^{\mathrm{track}}) + \sigma^2(PV)$

for the 7 TeV data.

Figure 3.14 shows it versus p_{T} for one θ bin ($0.5\ \pi < \theta < 0.55\ \pi$). Figure 3.15 shows it versus θ for one p_{T} bin (1 GeV$< p_{\mathrm{T}} <$ 1.1 GeV). As expected, the resolution is quickly falling with p_{T} and depends on the traversed detector material (i.e. θ) in the b-layer and beam-pipe.

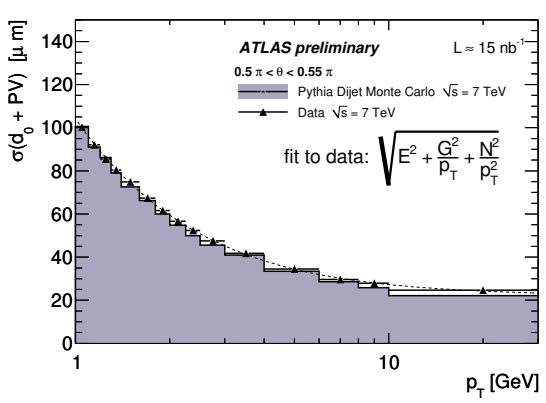

Figure 3.14: Transverse impact parameter resolution versus p_{T} for $0.5\ \pi < \theta < 0.55\ \pi$. The data have been fitted by $\sqrt{E^2 + \frac{G^2}{p_{\mathrm{T}}} + \frac{N^2}{p_{\mathrm{T}}^2}}$ (dashed line).

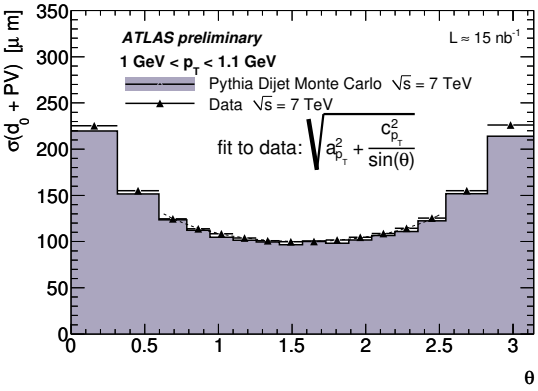

Figure 3.15: Transverse impact parameter resolution versus θ for 1 GeV$< p_{\mathrm{T}} <$ 1.1 GeV. $\theta = \frac{\pi}{2}$ refers to the center of the detector. The data have been fitted by $\sqrt{a_{p_T}^2 + \frac{c_{p_T}^2}{\sin\theta}}$ in the barrel (dashed line).

The agreement for both plots between experimental and simulated data is very good. The fits in the different p_{T} and θ bins give consistent results. Within the error of the fitted parameters, the two constant terms a_1 and a_2 agree between both fit methods and experimental and simulated data. Remaining differences are due to small mis-alignments in the detector or differences in the primary vertex resolution, which both add to the intrinsic resolution in this method.

The fitted parameters $c_1\sqrt{\sin < \theta >}$ and $c_2 < p_{\mathrm{T}} >$, with $< \theta >$ and $< p_{\mathrm{T}} >$ the mean values in the respective bins, show an agreement within their error between both fit methods and experimental and simulated data as well. This means that the multiple scattering contribution to the impact parameter resolution (i.e. the material distribution in the b-layer and beam-pipe) is well modeled in the simulation.

Additional studies were carried out in [120] to deconvolve the effect of the primary vertex from the measurement of the IP resolution itself. Similar studies were also carried out with the 900 GeV data [118], with same conclusions.

3.3.4.5 Tracks with shared hits

Complex track pattern-recognition issues may arise in a jet environment due to the high density of tracks. This may be particularly acute for narrow high-p_T jets. While the jets recorded in the 900 GeV collision data are on average very soft, it is nevertheless already possible to start assessing some of the pattern-recognition effects using the experimental data and check whether they are well-modeled when reconstructing the simulated data.

One important case for b-tagging is the case of tracks which are sharing some of their measurement points with other track(s). Shared hits occur more often in the silicon micro-strip detectors because of

the larger size of the silicon diodes, despite the fact that the measurement layers are placed at larger radii. Thanks to its high granularity, the pixel detector is more immune to this effect. Nevertheless, hit sharing in the pixel detector is actually more critical for *b*-tagging purposes since the lowest radius measurements define the impact parameter of the track. In the following, a track with shared hits is defined as a track with at least one shared hit in the pixels or at least two shared hits in the strips.

The distribution of the fraction of tracks with shared hits fulfilling the *b*-tagging quality cuts is shown as a function of their distance ΔR to the *b*-tagging track under consideration in Figure 3.16. It is clearly noticeable that the closer the tracks, the more likely they share hits, as expected. This effect is also quite well modeled by the simulation.

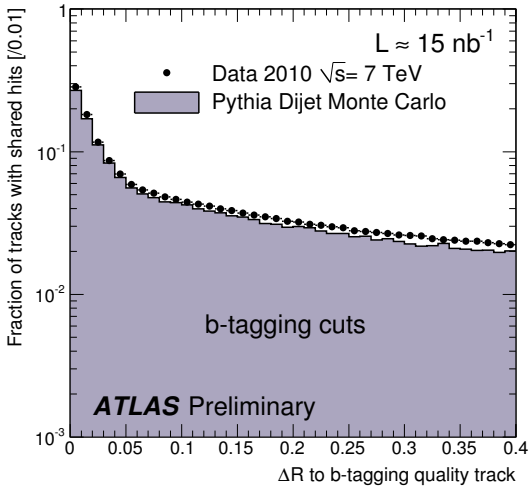

Figure 3.16: Distribution of the fraction of tracks with shared hits fulfilling the *b*-tagging quality cuts, as a function of their distance ΔR to the *b*-tagging quality track under consideration, for the 7 TeV data.

Despite being rather few, these shared tracks play a significant role in degrading *b*-tagging performance because they induce large tails in the d_0 distribution. This is shown for experimental data in Figure 3.17 where those tracks are compared to tracks without shared measurements. As can be seen in Fig. 3.18, this effect is well reproduced by the simulation especially for tracks with large d_0 (with lifetime contributions). Depending on the measurement layer where the sharing occurs, the tracks with shared hits could be either removed or treated in a special way for *b*-tagging.

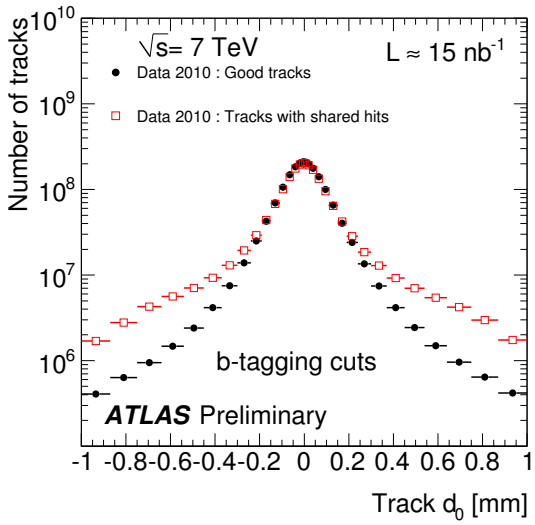

Figure 3.17: Distribution of the transverse impact parameter d_0 in experimental data for all tracks (solid black dots) and for tracks with shared hits (red open squares, plot normalized to all tracks) for the 7 TeV data.

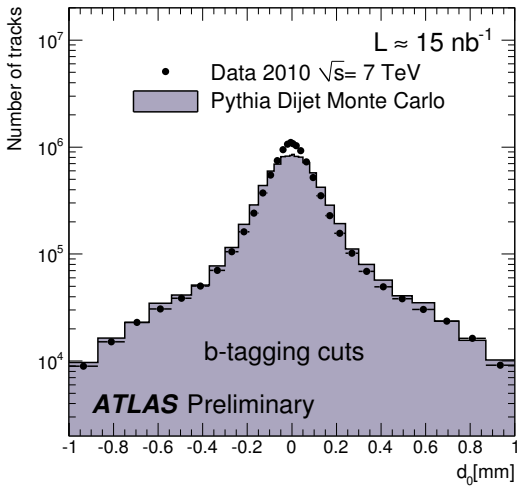

Figure 3.18: Distribution of the transverse impact parameter d_0 for tracks with shared hits in experimental data (solid black dots) and in simulated data (plain histogram) for the 7 TeV data.

3.4 Commissioning of *early* taggers

Now that we have seen that the basic ingredients for *b*-tagging are fairly well reproduced by the simulation, we will describe the so-called *early b*-tagging algorithms[8], named *SV0* and *JetProb*. We will then present the commissioning studies that were carried out with the first 900 GeV and 7 TeV LHC data for the *JetProb* algorithm. We documented all this work in the public conference notes [122, 123] in which further details can be found.

As we have emphasized at the end of section 3.2, the level of agreement between data and MC simulation is very important for practical use of *b*-tagging. Given the incredible complexity of the ATLAS detector and given the numerous parts of it that are involved for *b*-tagging (jet reconstruction, high-precision tracking, lepton identification etc), it was forecast that a relative long time would be necessary before the detector would be sufficiently well understood. For this reason, algorithms as simple as possible and relying as little (and if possible not at all) on MC simulation had been designed previously to the start of the LHC.

So how can we identify b-jets as simply as possible?

3.4.1 The *SV0* algorithm

One simple possibility to identify *b*-jets is to look at the three-dimensional distance between the PV and a reconstructed displaced SV (when found, as described in Sec. 3.2.6) and divide this distance by the error on its measurement. The quantity obtained, $SV0_{weight} \equiv L_{3D}/\sigma(L_{3D})$, gives more importance to SVs well reconstructed (as it was the case for the IP significance of tracks). It is also signed depending on the sign of the projection of the decay length vector on the jet axis. Figure 3.19 shows the distribution of the signed decay length significance in the first 0.4 nb^{-1} of the 2010 LHC data for data and simulation[9]. It can be seen that the low decay length significance region is dominated by background from *c*- and light jets, while the large decay length significance region is dominated by *b*-jets. The discriminating power of this distribution can be exploited simply by placing a cut $SV0_{OP}$ and then deciding:

- if $SV0_{weight} > SV0_{OP}$: the jet is tagged as *b*;
- if $SV0_{weight} \leq SV0_{OP}$: the jet is tagged as *non-b*.

Varying the value of $SV0_{OP}$ allows to adjust the operating point of this simple 'algorithm', *i.e.* defining its performance. As we will see in Sec. 3.5.7, 'moving' on the *SV0* performance curve in Fig. 3.49 is equivalent to change the value of $SV0_{OP}$. As can also be seen on this figure[10], the *b*-jet efficiency of this algorithm is limited to $\sim 60\%$, which is on average the efficiency of reconstructing a SV in a *b*-jet.

3.4.2 The *JetProb* algorithm

In order to be able to work at higher *b*-tagging efficiency by not paying the price for reconstructing a SV, another simple tagger exploiting the IP of tracks had been prepared before the start of the LHC. It

[8] We will actually not present an algorithm called *TrackCounting* that showed lower performance than the ones we present in the following.

[9] We have not contributed *directly* to this work. Hence, for a detailed description of the event selection used for this plot, we invite the reader to refer to [119].

[10] For a slightly different data reprocessing though, cf. [124] for details.

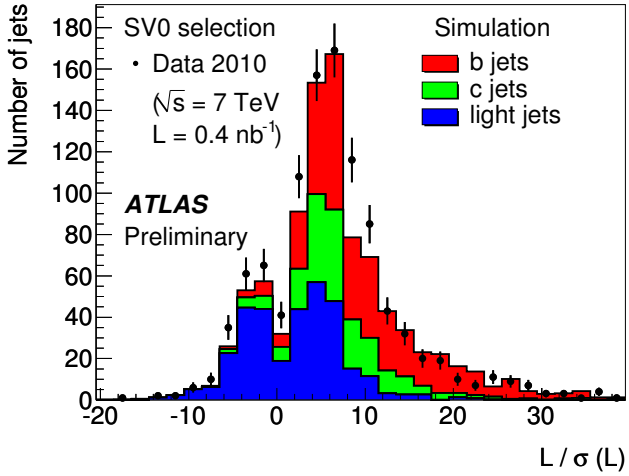

Figure 3.19: The three-dimensional decay length significance, signed with respect to the calorimeter jet axis, for all secondary vertices reconstructed in data events (markers). The expectation from simulated events (histogram) for non-diffractive minimum bias events, normalized to the number of jets in the data, is superimposed. From [119].

is called *JetProb* and is an implementation of the ALEPH tagging algorithm [117], used extensively at LEP and later at the Tevatron.

3.4.2.1 Event and jet selections

Before going to its detailed description, we wish to emphasize that in the following studies about the commissioning of this algorithm, the data samples and event selections for the 900 GeV and 7 TeV sets of data are the same as the ones used in all the previous section 3.3 for the tracking studies (cf. Sec. 3.3.1). Concerning the jet selection, this is also the same as the one that was specified in Sec. 3.2.5.1, but for the 900 GeV data, due to the very limited statistics, the requirements were loosened to $p_T > 7$ GeV and $|\eta| < 2.7$. The total number of selected jets is for the 900 GeV (resp. 7 TeV) data of 6372 (resp. 2.4M). The mean p_T of these jets is for the 900 GeV (resp. 7 TeV) data of 9.5 GeV (resp. 26 GeV).

3.4.2.2 Principle

Original definition The idea of the *JetProb* algorithm is to exploit the evident discriminating power of the signed IP significance of the tracks in a jet by testing their compatibility with the hypothesis that they come from the primary vertex, which is a priori true for light jets. Fig. 3.20 shows the signed transverse impact parameter significance $S_{d_0} \equiv d_0/\sigma_{d_0}$ for tracks in jets in the 900 GeV data and the 7 TeV data, for data and simulation.

The signed impact parameter significance S_{d_0} of each selected track in a jet is compared to a resolution function $\mathscr{R}$ for prompt tracks by computing this quantity:

$$\mathscr{P}_{\mathrm{trk}\,i} = \int_{S_{d_0}}^{+\infty} \mathscr{R}(x)dx\,. \tag{3.11}$$

The resolution function can be determined from experimental data using the negative side of the signed IP distribution, assuming the contribution from heavy-flavor particles is negligible. We will describe how this resolution function is exactly built in the next section, but one can already mention that it is symmetric with respect to 0, and have a look at what it looks like in Fig. 3.21. From this figure, one can understand that Eq. 3.11 will give:

- for tracks in light jets, *i.e.* originating from the PV: values between 0 and 1 distributed on average uniformly around 0.5 ($\mathscr{R}$ being normalized to unity).
- for tracks in *b*-jets, *i.e.* with tracks with large S_{d_0}: values distributed close to 0, and even peaked at this value.

So one understands already that the discriminating power can be extracted at the track level. In order to combine the individual weight of each of the N tracks associated to the jet to obtain a jet weight, $\mathscr{P}_{\text{jet}}$, which discriminates between *b*-jets and light jets, there are several possibilities. Originally, it was done as follows:

$$\mathscr{P}_{\text{jet}} = \mathscr{N}(N, \mathscr{P}_0) \cdot \mathscr{P}_0 \tag{3.12}$$

where

$$\mathscr{P}_0 \equiv \prod_{i=1}^{N} \mathscr{P}_{\text{trk}i} \text{ and } \mathscr{N}(N, \mathscr{P}_0) \equiv \sum_{k=0}^{N-1} \frac{(-ln\mathscr{P}_0)^k}{k!} \tag{3.13}$$

Therefore the jet weight $\mathscr{P}_{\text{jet}}$ is the product $\mathscr{P}_0$ of all the individual track weights, with a weighting factor $\mathscr{N}(N, \mathscr{P}_0)$ depending on $\mathscr{P}_0$ and the track multiplicity.

The weighting factor While the weighting factor can be surprising at first sight, it actually plays a very important role. If this term was not present in Eq. 3.12, $\mathscr{P}_{\text{jet}}$ would reduce to the product of all track weights, all comprised between 0 and 1 (because the integral of $\mathscr{R}$ from $-\infty$ to $+\infty$ equals to 1), so any jet with an arbitrarily high number of tracks would get an as small as desired jet weight $\mathscr{P}_{\text{jet}}$, independently of its flavor.

As $\lim_{N\to\infty} \mathscr{N}(N, \mathscr{P}_0) = 1/\mathscr{P}_0$ (Taylor series of the exponential function), $\lim_{N\to\infty} \mathscr{P}_{\text{jet}} = 1$ and, as a consequence, a jet with many tracks will have a higher weight than the one it would have get without the weighting factor. In this way, if it was a light jet, it is better discriminated from a jet with lifetime contributions with less tracks (that by construction gets a small jet weight).

Variation In [107], it has been shown that using only tracks in jets with positive d_0 allows to reach better performance, and Eq. 3.11 was modified as follows:

$$\mathscr{P}_{\text{trk}i} \to \mathscr{P}_{\text{trk}i} \times 2 \text{ if } d_0 > 0 \tag{3.14}$$

which had the effect to keep the track weights (that were taking values from 0 to 0.5 with the original definition) between 0 and 1. We will come back on this point in Sec. 3.5.6.1, where we will remove this transformation, and explain why, but for the moment we will keep it, as this is what was done in practice at that time.

Interpretation Before going to the details of the construction of the resolution function, we can conclude that the physical interpretation of $\mathscr{P}_{\text{jet}}$ is the *likeliness*[11] that the jet has no decay products from long-lifetime particles. In other words, the higher $\mathscr{P}_{\text{jet}}$ is, the more the jet looks like a light-jet, and reversely, the lower it is, the more it looks like a *b*-jet.

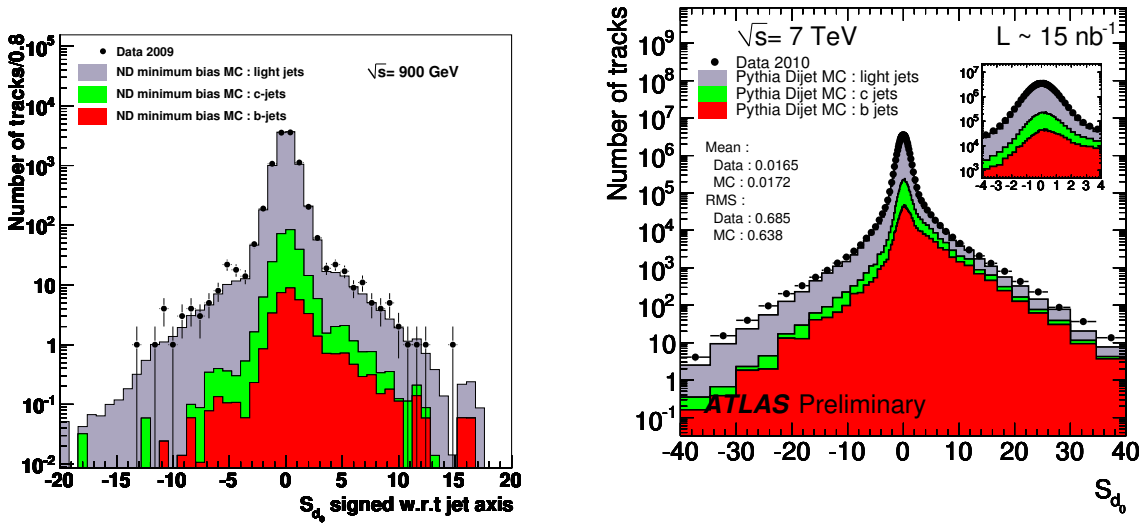

(a) S_{d_0} (900 GeV data)

(b) S_{d_0} (7 TeV data)

Figure 3.20: Distributions of the signed transverse impact parameter significance S_{d_0} for the 900 GeV data (a) and the 7 TeV data (b). Experimental data (black points) are superimposed with simulated data (plain histograms). Simulated distributions are normalized to data.

3.4.2.3 Construction of the resolution function

900 GeV data: As can be seen in Figs. 3.20(a), the data/simulation agreement is really good, so it was decided to build one single resolution function from the simulation, because the statistics is much higher than in data (hence populating better the tails of the Sd_0 distributions) and because we could use the truth to consider only tracks stemming from light jets. Among all these tracks that fulfill the *b*-tagging quality criteria and that have a negative d_0, the S_{d_0} distribution is symmetrized around $S_{d_0} = 0$ to build the complete $\mathscr{R}$ function. To make the method more robust with respect to statistical fluctuations and to avoid binning problems which typically induce rough shape and peculiar structures in the distributions of $\mathscr{P}_{\text{trk}}$ and $\mathscr{P}_{\text{jet}}$, the symmetrized S_{d_0} distribution is normalized to unity, and then fitted with a functional form corresponding to the sum of one Gaussian core and two exponential to describe the tails:

$$\mathscr{R}(x) = e^{-p_0-p_1|x|} + e^{-p_2-p_3|x|} + p_4 e^{-x^2/2p_5^2} \tag{3.15}$$

The resulting resolution function is shown in Fig. 3.21, together with the values of the fitted parameters. The χ^2/N_{dof} is not great but allowed to get very satisfactory results in the following.

7 TeV data: As can be seen in Figs. 3.20 (b), the S_{d_0} distributions in experimental data and in simulation are slightly different, so the resolution function $\mathscr{R}$ for prompt tracks must be constructed

[11] We insist on that point because the name *JetProb*, for 'Jet Probability', is misleading, as $\mathscr{P}_{\text{jet}}$ does not satisfy the Kolmogorov axioms of the theory of *probability* (cf. *e.g.* [115]).

for each, separately. In both cases the same procedure is followed: among the tracks fulfilling the *b*-tagging quality criteria, again, only those with negative d_0 are used in order to sample mostly the smearing due to resolution and to limit the contribution from long-lived decays. However, contrary to the 900 GeV data, for the Monte Carlo simulation, no specific treatment using the truth information was applied to reject heavy-flavors, other long-lived particles or material interactions, because this is not possible in data and one wants to apply the same construction procedure in both cases for consistency. The negative part of the S_{d_0} distribution is then symmetrized around $S_{d_0} = 0$, and normalized to unity to build the complete $\mathscr{R}$ function. It is then also fitted with a functional form corresponding to the sum of two Gaussian cores and two exponentials:

$$\mathscr{R}(x) = p_0 e^{-x^2/2p_1^2} + p_2 e^{-x^2/2p_3^2} + e^{-p_4 - p_5|x|} + e^{-p_6 - p_7|x|} \tag{3.16}$$

The resulting fitted values are shown in Tab. 3.2, and the resolution functions can be found in [123].

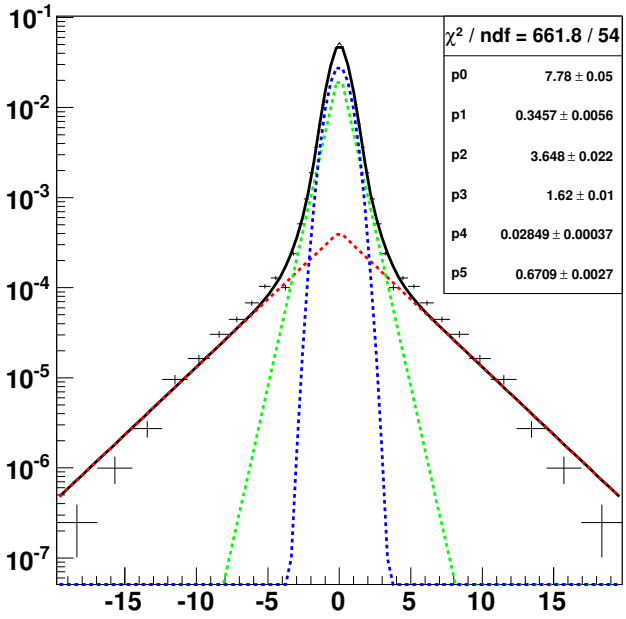

Figure 3.21: JetProb resolution function extracted from MC simulation at $\sqrt{s} = 900$ GeV and fitted with the functional form of Equation 3.15.

3.4.2.4 Track and jet weights

The number of *b*-tagging quality tracks in selected jets is for the 900 GeV (respectively 7 TeV) data $\sim$1.6 (respectively $\sim$3) on average in data and simulation. This is quite low for the 900 GeV data, but one has to keep in mind that the tight requirements, particularly the $p_T > 1$ GeV one, were optimized for jets with much higher energy. For jets with at least one track with positive d_0 (the ones that we will use for tagging), the multiplicity of tracks with positive d_0 is for the 900 GeV (respectively 7 TeV) data $\sim$1.3 (respectively $\sim$2) on average. In all cases, the simulation was seen to reproduce very well the data.

	χ^2/n	p_0	p_1	p_2	p_3
Experimental data	154.2/72	0.26 ± 0.01	0.61 ± 0.01	0.19 ± 0.01	0.92 ± 0.01
Simulation	64.0/72	0.32 ± 0.01	0.56 ± 0.01	0.19 ± 0.01	0.89 ± 0.02
		p_4	p_5	p_6	p_7
Experimental data		2.94 ± 0.04	0.79 ± 0.01	6.08 ± 0.03	0.21 ± 0.01
Simulation		3.09 ± 0.11	0.81 ± 0.03	6.07 ± 0.06	0.23 ± 0.01

Table 3.2: Goodness of the fit and fit parameters for the functional form used to describe the resolution function $\mathscr{R}$, for the experimental and simulation at $\sqrt{s} = 7$ TeV.

The *JetProb* track weight distributions are shown in Fig. 3.22 for the 7 TeV data. It can be seen that *b*-jets tend to peak at very low values, while lighter jets are uniformly distributed. The simulation is seen to describe very well the data.

The *JetProb* jet weight distributions are shown in Fig. 3.23, with the same conclusions as for the track weights. Fig. 3.24 shows the same distribution but in logarithmic scale, which appears much more convenient visually and for practical use. Similar distributions can be found in [122].

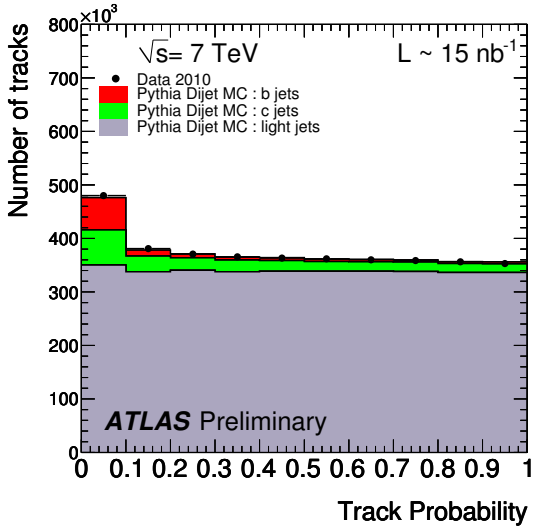

Figure 3.22: Distributions of the *JetProb* track weight $\mathscr{P}_{\text{trk}}$ for the 7 TeV data. Simulated distributions are normalized to data.

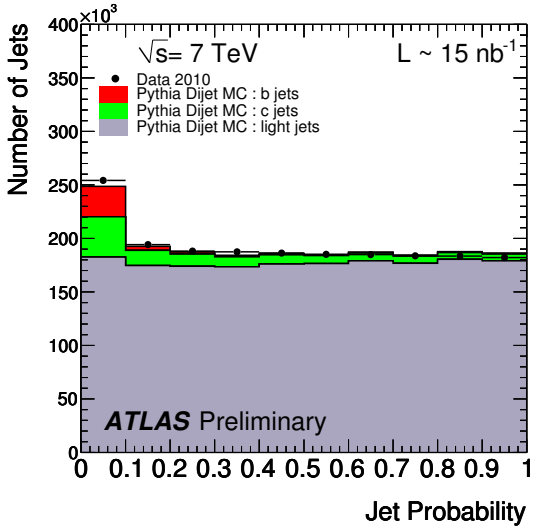

Figure 3.23: Distributions of the *JetProb* jet weight $\mathscr{P}_{\text{jet}}$ for the 7 TeV data. Simulated distributions are normalized to data.

3.4.2.5 Performance

In the 900 GeV data, the number of expected *b*-jets is just too low to estimate a meaningful performance of the algorithm. Mainly, it allowed to extract the first ATLAS *b*-jets candidates, that one can find in [107].

In the 7 TeV data, we can start to evaluate the performance using the simulation. In the same manner as for the *SV0* algorithm, the *JetProb* algorithm is defined by applying a cut on the $P_{jet} \equiv$

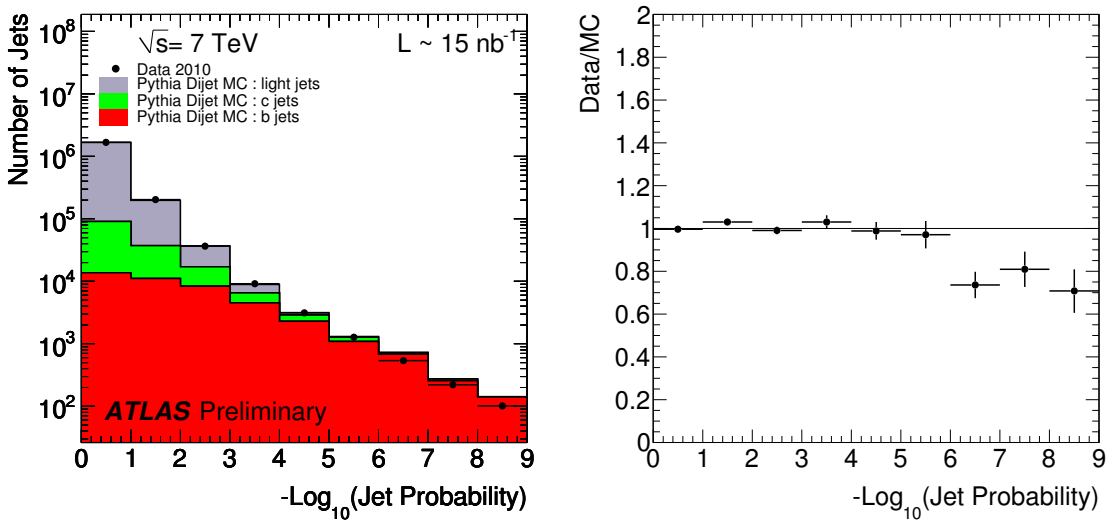

Figure 3.24: Distribution of $-log_{10}(\mathscr{P}_{\text{jet}})$ for the 7 TeV data (left). Experimental data (black points) are superimposed with simulated data (plain histograms). Simulated distributions are normalized to data. The data-to-simulation ratio is also shown (right).

$-\log_{10}(\mathscr{P}_{\text{jet}})$ weight:

- if $P_{jet} > JetProb_{OP}$: the jet is tagged as b;
- if $P_{jet} \leq JetProb_{OP}$: the jet is tagged as *non-b*.

where $JetProb_{OP}$ defines the operating point. In the present case, $JetProb_{OP} = 1.30$ selects 151 281 (resp. 148 272) jets in data (resp. simulation), and corresponds to a b-jet efficiency of 60% and a light-jet rejection of ~ 18.5.

3.4.3 Conclusion

We have contributed (together with [107]) to the commissioning of the *JetProb* algorithm. This tagger relies on the transverse impact parameter of tracks in jets, especially on the construction of a resolution function. While we constructed one of this function from simulation for comparison, it can be constructed directly from data, as was done for the 7 TeV data. This was particularly appropriate at the start of the LHC. We have made careful data-to-simulation comparisons of the quantities related to this algorithm, and found remarkable agreement.

One has also seen reasonable agreement with the expectations for the *SV0* tagger, which relies on the reconstruction of secondary vertices, in particular in regions expected to be dominated by b-jets where the agreement was seen really good.

It should be noted that these two algorithms are complementary because the *SV0* algorithm yields in principle a better rejection than *JetProb*, but cannot work at efficiencies higher than $\approx 60\%$, contrary to *JetProb* which can operate at higher values.

For these reasons, these two taggers were declared usable by physics analysis at the very start of the LHC. This was a very satisfactory result given the complexity of the ingredients required by these algorithms.

3.5 Commissioning of *high-performance* taggers

We will now describe algorithms that can achieve much higher performance compared to the *early* taggers, thanks to the fact that they are directly exploiting information from the MC simulation. We will then summarize the commissioning studies that we carried out with 330 pb^{-1} of the 7 TeV data, and show the expected performance of all the taggers. We documented all this work in the public conference note [124], and presented these results at the International Europhysics Conference on High Energy Physics, Grenoble, France, July 2011 [125].

3.5.1 Overview of the algorithms

3.5.1.1 Likelihood-ratio formalism

In the previous section, we described two algorithms exploiting simply the discriminating power of two variables: the signed IP significance of tracks, for the *JetProb* algorithm, and the signed decay length significance of SVs, for the *SV0* algorithm. While these algorithms were designed with the knowledge, obtained from simulation, that these variables are discriminant, they are actually not *using* the simulation in order to work properly.

Most importantly, it can be shown that the way these discriminating variables were used was not optimal. In Sec. 3.2.7.2, we started to introduce some notions of *hypothesis testing*, that can be directly applied in our present case, considering the discriminating variables as *test statistics*. The so-called *Neyman-Pearson* lemma (see *e.g.* [115]), states that for two *simple* hypothesis, *i.e.* that are fully specified[12], the optimal[13] scalar test statistic is defined by:

$$t(X) \equiv \frac{f(X|H_0)}{f(X|H_1)} \tag{3.17}$$

and then accepting H_0 if $t(X) > c_\alpha$, or rejecting it otherwise. c_α specifies the level of significance α of the test, which is also called a *likelihood ratio test*, because when X is specified (by the observation), the quantity $f(X|H_i)$ is a function of the hypothesis and is called a *likelihood* function. In our case, the measured value X_i of a discriminating variable can be compared to pre-defined smoothed and normalized distributions obtained from Monte Carlo simulation (that play the role of the *p.d.f.* $f(\cdot|H_0)$ and $f(\cdot|H_1)$) for both the b- and non-b hypotheses: $b(X) \equiv f(X|H_0)$ and $u(X) \equiv f(X|H_1)$ respectively. These so-called *reference histograms* can even be two- or three-dimensional for some tagging algorithms. To limit statistical fluctuations, the histograms are smoothed with an ad-hoc implementation. As an illustration in the case of the so-called IP2D impact parameter-based algorithm, X_i is the signed d_0/σ_{d_0}, whose reference histograms can be seen in Fig. 3.25. The ratios of the probabilities $b(X_i)/u(X_i)$ define the track weights. Assuming that the tracks in a jet are independent, their weight can be optimally combined into a jet weight W_{Jet} as the sum of the logarithms of the N_T individual track weights W_i:

$$W_{Jet} = \sum_{i=1}^{N_T} \ln W_i = \sum_{i=1}^{N_T} \ln \frac{b(X_i)}{u(X_i)} \tag{3.18}$$

As we have seen previously, tracks may exhibit different behavior even after the track selection, such as the tracks with shared hits. One idea to take advantage of the different properties of tracks is to arrange all tracks into various categories and use dedicated probability density functions for each

[12] In the sense that there is no unknown parameters to estimate.

[13] In the sense of getting the highest power $(1-\beta)$ for a given level of significance α. In the b-tagging context, it is equivalent to say that it gets the lowest mis-tagging rate $\varepsilon_{\text{non-b}}$, for a given b-jet efficiency ε_b.

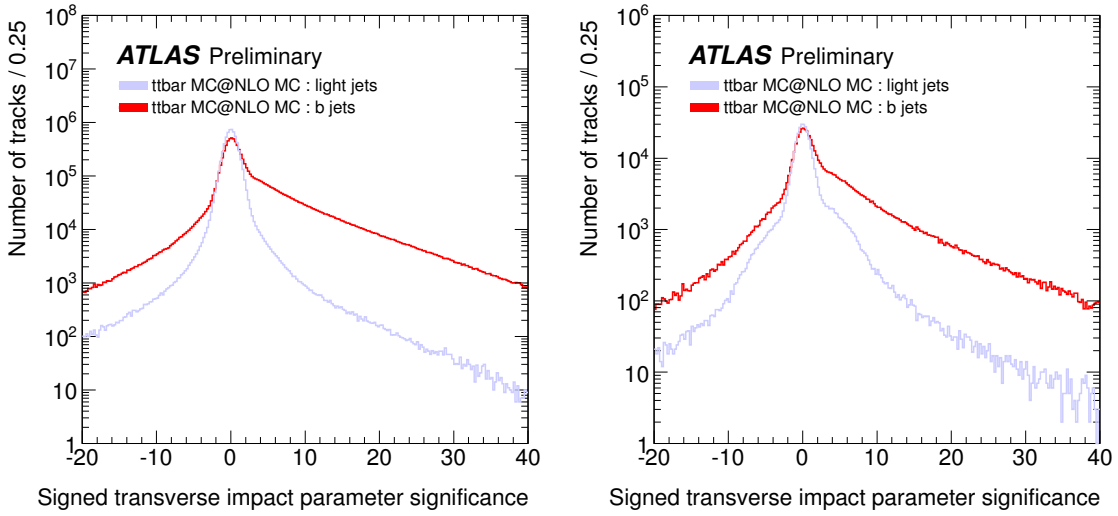

(a) regular tracks

(b) tracks with shared hits

Figure 3.25: Signed track impact parameter significance $d_0/\sigma d_0$ reference distributions for the IP2D algorithm for regular tracks (left plot) and for tracks with shared hits (right plot), obtained from simulated $t\bar{t}$ events. Red distributions can be regarded as the *p.d.f.* $b(X)$, and the blue ones as the *p.d.f.* $u(X)$. *N.B.*: The distributions are not normalized to unity here, but this is done internally in the *b*-tagging software.

category. The likelihood ratio formalism permits to incorporate such categories in a straightforward way. After the division of the tracks into disjoint categories j, where every category has its own set of reference histograms b_j and u_j, the jet weight can simply be written as the sum over all tracks in each category N_T^j and all categories N_C:

$$W_{Jet} = \sum_{j=1}^{N_C} \left(\sum_{i=1}^{N_T^j} \ln \frac{b_j(X_i)}{u_j(X_i)} \right) \tag{3.19}$$

In the present case, two track categories are used: the *Shared* tracks (tracks with shared hits), and the complementary subset of tracks called *Good* tracks. These track categories are only used for the time being for the IP2D tagger (Fig. 3.25) and the IP3D tagger that we describe now.

3.5.1.2 The *IP3D* algorithm

The IP3D algorithm uses also the signed longitudinal IP significance $z_0/\sigma(z_0)$ in addition to the signed transverse IP significance $d_0/\sigma(d_0)$. This is done in practice using two-dimensional reference histograms, that are shown in Fig. 3.26.

3.5.1.3 *SV1* algorithm

The high-performance tagging algorithm SV1 takes advantage of four of the secondary vertex properties:

- the invariant mass of all tracks associated to the vertex: M

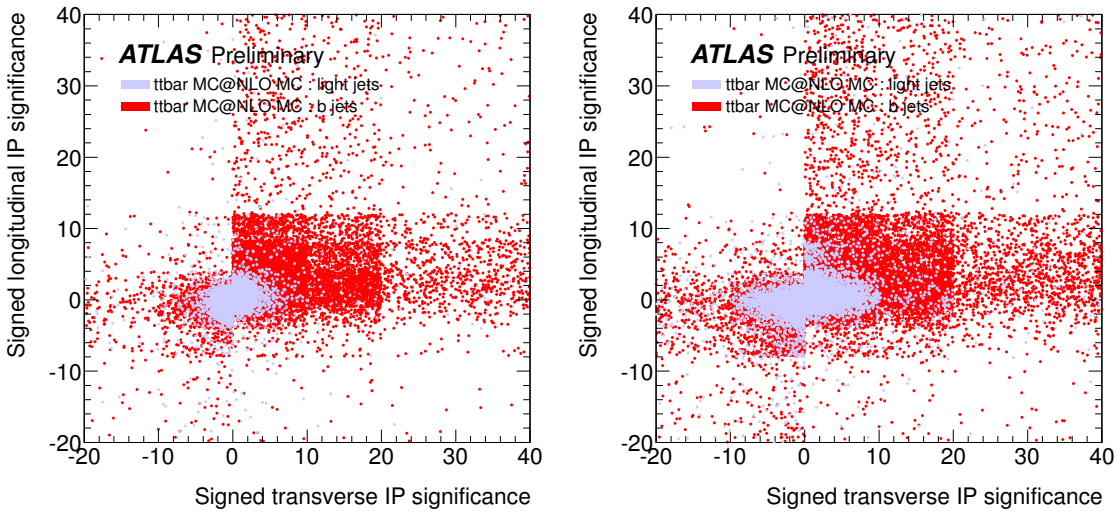

(a) regular tracks

(b) tracks with shared hits

Figure 3.26: Signed track impact parameter significances z_0/σ_{z_0} versus d_0/σ_{d_0} reference distributions for the IP3D algorithm for regular tracks (left plot) and for tracks with shared hits (right plot), obtained from simulated $t\bar{t}$ events.

- the ratio of the sum of the energies of the tracks in the vertex to the sum of the energies of all tracks in the jet: E_{frac}
- the number of two-track vertices in the jet (excluding identified V^0 decays or material interactions): N
- the distance ΔR between the jet axis and the line joining the PV to the SV.

These variables are combined using the likelihood ratio formalism described previously: for each vertex, three weights are computed using the three reference histograms that are shown in Fig. 3.27[14], and then added into a single jet weight. When no vertex is found, the SV1 tagging algorithm returns a weight of $\ln \frac{1-\varepsilon_b^{SV}}{1-\varepsilon_u^{SV}}$, where ε_b^{SV} and ε_u^{SV} are the SV finding efficiency for b- and non-b jets (typically higher than 60% for b-jets). The values have to be provided as input to the SV1 tagger.

One should also note an important feature of the SV1 algorithm, which is that it is not using the signed decay length significance of the secondary vertex $L_{3D}/\sigma(L_{3D})$, which was the discriminating variable of the *SV0* algorithm. This is because when combining variables with the log-likelihood formalism, the combination is optimal when the variables are un-correlated. However, the distance between PV and SV is strongly correlated with the IP of tracks[15], so the variables used by SV1 have been chosen to be maximally independent of track IP, and this algorithm was developed primarily for working in combination with an IP-based algorithm (see Sec. 3.5.1.5).

[14]The strange combination $M' = M/(M+1)$, $E'_{frac} = E^{0.7}_{frac}$ and $N' = log(N)$ used were chosen to facilitate the production (with limited statistics) and use of these reference histograms.

[15]One can just take a look back at Fig. 3.1 to convince ourselves.

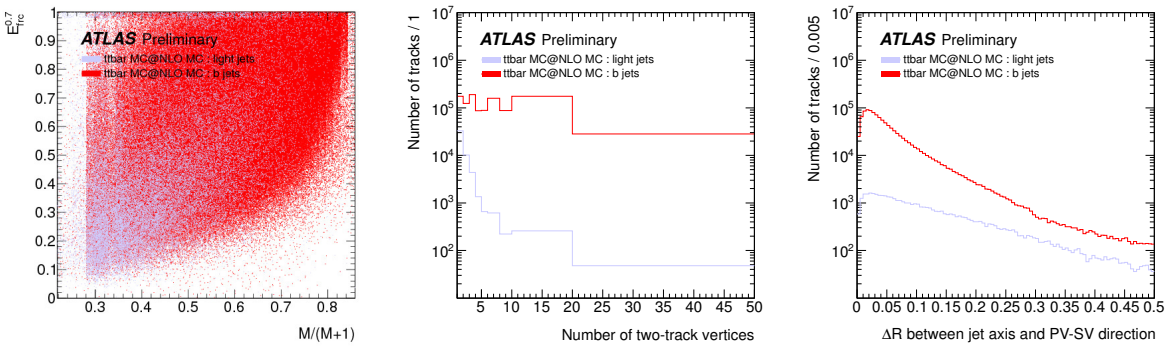

(a) energy fraction vs vertex mass (b) number of two-track vertices (c) distance $\Delta R(jet, PVSV)$

Figure 3.27: Reference histograms for the four variables used for SV1 (cf.text), obtained from simulated $t\bar{t}$ events. *N.B.*: The distributions are not normalized to unity here, but this is done internally in the *b*-tagging software.

3.5.1.4 Decay chain reconstruction with the *JetFitter* algorithm

Another algorithm, called JetFitter, exploits the topology of weak *b*- and *c*-hadron decays inside the jet, which was introduced in Sec. 3.2.6. A Kalman filter is used to find a common line on which the primary vertex and the *b*- and *c*-vertices lie, as well as their position on this line, giving an approximated flight path for the *b*-hadron. With this approach, the *b*- and *c*-hadron vertices are not necessarily merged (contrary to the case of the SV0 and SV1 algorithms that reconstruct a single inclusive vertex in the jet) even when only a single track is attached to each of them. The discrimination between *b*-, *c*- and light jets is based on a likelihood using similar variables as in the SV1 tagging algorithm above, and additional variables such as the flight length significances of the vertices. This algorithm is described in detail in Refs. [166, 126].

3.5.1.5 Combined taggers: *IP3D+SV1*, *IP3D+JetFitter* and *MV1*

- *IP3D+SV1*: Thanks to the likelihood ratio method used for IP3D and SV1, the algorithms can be easily combined: the weights of the individual tagging algorithms are simply summed up.
- *IP3D+JetFitter*: The combination IP3D+JetFitter is based on artificial neural network techniques with Monte Carlo simulated training samples and additional variables describing the topology of the decay chain [166].
- *MV1*: MV1 is a an artificial neural network combination of the IP3D, SV1 and JetFitter weights.

3.5.2 Data samples

3.5.2.1 Experimental data sample

The analysis presented now is based on a sample of proton-proton collisions at $\sqrt{s} = 7$ TeV delivered by the LHC and collected by the ATLAS experiment between March 22^{nd} and May 25^{th} 2011. Only data collected during stable beam periods in which all sub-detectors were fully operational are used. The sample amounts to approximately 93M events and corresponds to about 330 pb^{-1} of integrated luminosity. Throughout the considered period, the LHC beam parameters were relatively stable. For

instance, the average number of minimum-bias pile-up events, originating from the collisions of additional protons in the same bunch as the signal collision, was maintained at around six.

3.5.2.2 Simulated data samples

Experimental data are compared to a Monte Carlo simulation of QCD jet events generated with the Pythia program[16]. Samples were generated using an ATLAS Minimum Bias set of parameters in which the non-diffractive model has been tuned to ATLAS measurements of charged particle production at $\sqrt{s} = 900$ GeV and $\sqrt{s} = 7$ TeV. In order to have sufficient statistics over the entire p_T spectrum, eight samples were generated for different exclusive ranges of the hard-scattering partonic transverse momentum $\hat{p_T}$. The lowest-p_T sample consists of about 16M events, while the highest p_T ones have about 2M events each.

The eight samples were combined taking into account their production cross sections.

On top of these signal events, simulated minimum-bias events were superimposed to simulate pile-up, obtained from Pythia non-diffractive, single and double diffractive events. The bunch train configuration of the LHC during this period was emulated.

The particle four-vectors from these generators were passed through a full simulation of the ATLAS detector and trigger that is based on GEANT4 [132]. The beamspot position as been simulated to reproduce the period D of the 2010 data. The simulated geometry corresponds to a perfectly aligned detector and most of the disabled detector elements for data-taking, notably the pixel modules, were masked in the simulation. Small run-to-run variations of the number of disabled channels are present in data but not corrected for in simulation. For instance, on the innermost pixel layer, six modules were permanently masked in simulation, while in data the number of disabled modules fluctuates around nine.

Finally, the simulated events were reconstructed using the same version[17] of the ATLAS software as used to process the data.

3.5.3 Trigger, event and jet selections

3.5.3.1 Trigger

All the events analyzed were triggered by a jet trigger chain. At the Level 1 and Level 2, cluster-based jet triggers are used to select events. At the last stage, the so-called Event Filter performs a full scan[18], reading out the complete calorimeter and running the offline anti-k_t jet finding algorithm with $R = 0.4$ on topological clusters.

Trigger chains For this analysis, the events were required to come from one of the jet trigger Event Filter chains of type EF_jX_a4tc_EFFS where X is the p_T threshold in GeV: X $\in \{10, 15, 20, 30, 40, 55, 75, 100, 135, 180, 240\}$. For period B the chain type was EF_jX_a4_EFFS. The chain is usually a succession of triggers with slightly increasing thresholds: for instance the EF_j100_a4tc_EFFS chain is fed by L2_j95 which itself is fed by L1_J75 triggers. However the chains with the first three thresholds used in this analysis, namely X $\in \{10, 15, 20\}$, were fed by random triggers to increase the acceptance for low-p_T jets.

[16] Pythia 6.423 using the MRST LO*[169] PDF.

[17] The so-called Release 16 in ATLAS

[18] Unlike for the 2010 data, during which the Event Filter relied on the Regions-of-Interest.

Trigger prescales A further complication comes from the fact that most of these triggers, especially the low-p_T ones, were increasingly more prescaled with the fast increase in luminosity. The triggers with the lowest p_T thresholds were prescaled by up to 5 orders of magnitude, and typically the jet triggers at the end of the data sample considered were 10 times more prescaled than the jet triggers at the beginning.

Trigger selection In order to obtain sufficient statistics for our studies, a logical OR of all the EF_jX_a4tc_EFFS triggers was used for selecting the events in the following.

Offline event selection The offline event selection for this analysis consists of requiring the selected primary vertex candidate to have at least 5 tracks.

Different samples of jets are derived from the experimental data and from the simulated samples. The most commonly used sample is formed by the collection of the leading jet in all the events, provided they fulfill the requirements to potentially be tagged which are: $p_T > 20$ GeV and $|\eta| < 2.5$. This sample is referred to as the inclusive leading jet sample and consists of about 10M jets in data. The average p_T of those jets is 145 GeV. In addition, two other samples are defined to study events with a different flavor-composition, using the dijet event selection mentioned above: the heavy-flavor enriched sample (HFJ) with 100k jets in data, and the light-flavor enriched sample (LFJ) with 3M jets in data. For both these samples, the study probes the b-tagging of the second jet in the event while the leading jet was tagged or anti-tagged using the already commissioned early tagging algorithms. The heavy-flavor enrichment was obtained by requiring that the tag jet is identified as a b-jet by either the JetProb or the SV0 algorithms with high-purity cuts: $L_{3D}/\sigma_L > 8$ for SV0 or $-\log_{10}(\mathscr{P}_{\text{jet}}) > 6$ for JetProb. To enrich the LFJ sample in light jets, the tag jet must have at least 3 b-tagging quality tracks and their combination by the JetProb tagging algorithm should fulfill $-\log_{10}(\mathscr{P}_{\text{jet}}) < 3$.

3.5.4 Simulation reweighting and corrections

Since the simulation is a CPU-intensive task, simulation files are prepared in advance while some parameters, especially regarding the beam parameters of the machine, are not yet known. In addition, the modeling of the physics by the generator may not be perfect, and the simulation may not reproduce properly some specific features. To address these two aspects, the distributions obtained from simulated events are reweighted to correct for the differences with observed distributions in experimental data. Except if explicitly stated otherwise, all the distributions shown in the following have been obtained after applying the reweightings and corrections mentioned in this section.

3.5.4.1 Pile-up and primary vertices

Figure 3.28 shows the luminosity-weighted average of the Poisson distribution on the number of interactions per beam-crossing in the experimental data for periods D, E and F. The average is slightly higher in period B, but this period amounts to only 3% of the whole data sample considered here. Figure 3.29 shows the distribution of the average number of interactions per crossing in the simulated data samples. It can be seen that the Monte Carlo samples were prepared to cover data-taking periods with slightly higher bunch intensities than the ones studied in this note: the luminosity-weighted average of the Poisson distribution on the number of interactions per beam-crossing for the triggers we are using is 10.4 in simulation and 5.7 in experimental data.

To properly account for the out-of-time pile-up (pp collisions from neighboring bunches in the same train), it is recommended to reweight the simulated events by the difference of the μ distributions

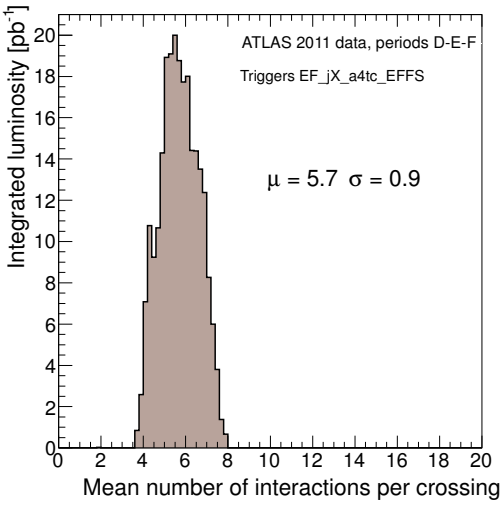

Figure 3.28: Distribution of the luminosity-weighted mean number of interactions per crossing in the experimental data from periods D to F.

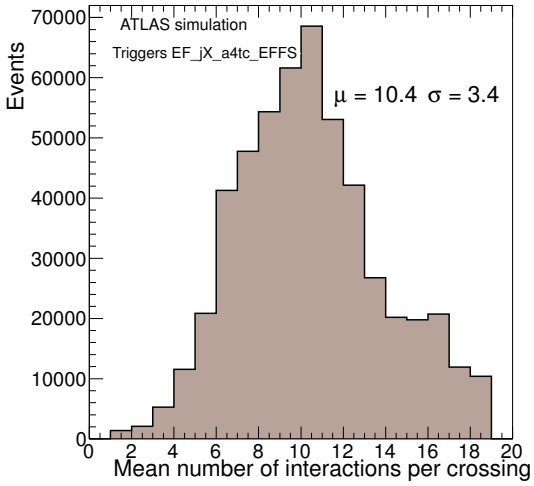

Figure 3.29: Distribution of the mean number of interactions per crossing in the simulated samples used.

(Fig. 3.28 vs Fig. 3.29). However given the time resolution of the Inner Detector, and since we require that all the jets under study have at least one track associated to them, the contribution of the out-of-time pile-up for this analysis is expected to be negligible. As a consequence, the simulated events were reweighted using the distribution of the number of reconstructed primary vertices shown on Figure 3.30.

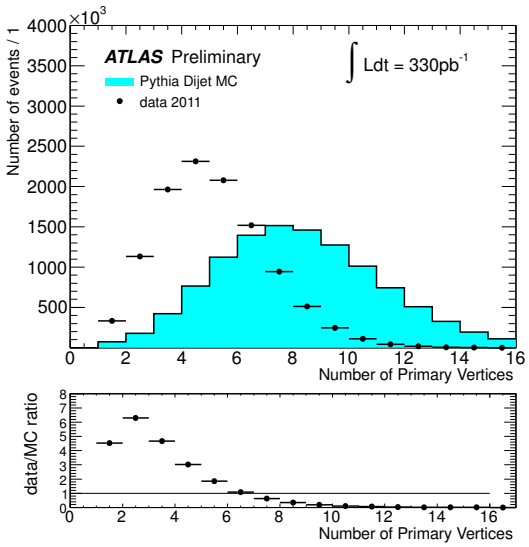

Figure 3.30: Distribution of the number of reconstructed primary vertices per event for experimental data (solid black points) and for simulated data before the event reweighting.

3.5.4.2 Jet kinematics

Another important point is that the combination of the various jet triggers used and the fact that they were prescaled, which is not modeled in the simulation, results in rather different p_T and η spectra in data and simulation. This can be seen on Figure 3.31[19] which shows the transverse momentum and pseudo-rapidity distributions of the leading jet for experimental data and for simulated events. The huge disagreement between the simulated and experimental curves is obvious, and is due to the prescaling of the triggers previously described. To account for this, and also to correct for residual discrepancies between the experimental data and the modeling of the dijet event kinematics by the particle generator, a two-dimensional reweighting in (p_T, η) of the jets in simulation is performed. Since the most energetic jet in the event is more likely to fire the jet trigger, jets are classified in three categories according to their energy rank in the event: leading jet (1^{st} rank), sub-leading jet (2^{nd} rank) or softer jets (3^{rd} rank and lower ranks). For each jet rank, a 2D reweighting map is obtained by dividing the (p_T, η) distributions in data and in simulation[20]. This procedure is applied separately for the inclusive jet sample and for the sample enriched in heavy-flavor jets. The same reweighting factor is applied to all jet flavors when reweighting the Monte Carlo, *i.e.* there is no attempt to model any possible flavor dependence. Note that the $\mathcal{O}(100)$ jets with a p_T above 800 GeV were ignored in the procedure and will not appear in the results discussed in this note.

One important remark is that these (p_T,η) reweighting are applied after the reweighting of the number of PVs. However, there is some correlation between the number of PVs of the event and the kinematic of the jets. We have checked that the (p_T,η) reweighting was not affecting substantially the reweighted number of PVs distribution, and that the observed change had no effect at all on the effects we are probing in all the following. In the future, for much higher level of pileup, we would recommend for example to use a three-dimensional (number of PV, p_T,η) reweighting.

3.5.5 Track properties

In this section, some properties of the reconstructed charged tracks are examined, since tracks are a crucial ingredient of *b*-tagging. The tracks are required to fulfill the *b*-tagging track quality requirements and to be associated with a reconstructed jet, as explained in Sections 3.2.5.2 and 3.2.5.3. Prior to this, several relevant properties of the event were checked (primary vertex, environment of jets and effects of close-by jets, etc) and in all cases the simulation was found to adequately describe the experimental data after reweighting.

3.5.5.1 Impact parameters

As seen previously extensively, the most critical track parameters for *b*-tagging are the transverse and longitudinal impact parameters. Figure 3.32 shows the distribution of the signed transverse impact parameter d_0 for *b*-tagging quality tracks in selected jets, for experimental data and simulation. The simulation reproduces well the distribution in data, within 10% for most of the d_0 range. It can be shown that the disagreement is more pronounced at higher track momentum, suggesting that it may be an effect of residual misalignments. A smearing of the simulation was under investigation at the time of this study to correct the residual discrepancy, which originates in part from the fact that in simulation the measurement modules are perfectly aligned. The material appears to be well modeled

[19] The little discontinuities of the spectra of the simulated distributions are a consequence of cuts that we applied in order to fix some artifacts of the simulation of pileup events in the *Jx* samples. These cuts became official corrections recommended by the *b*-tagging group for other studies.

[20] This reweighting procedure that we applied ended to be recommended by the *b*-tagging group for other studies.

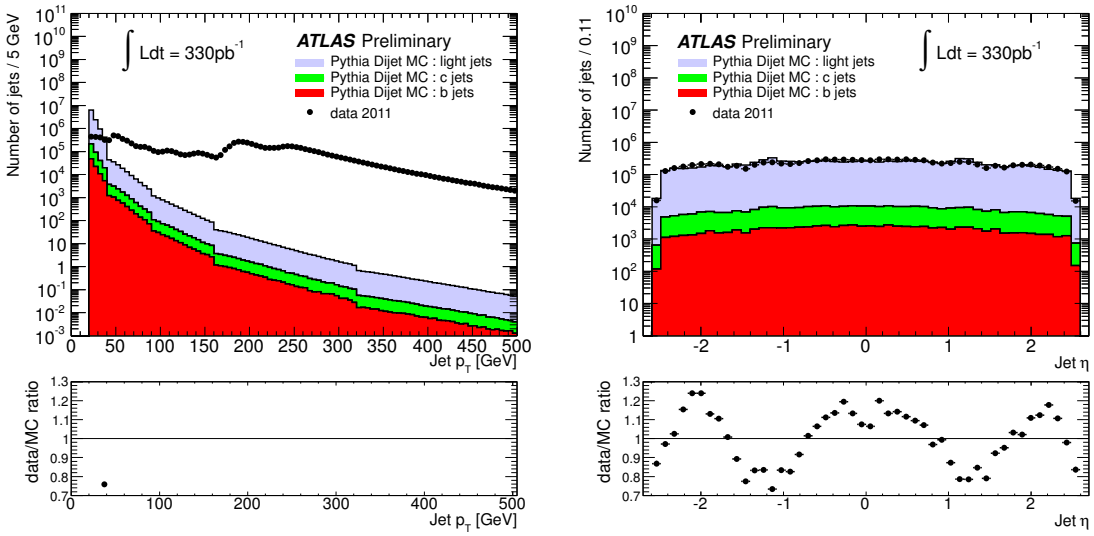

(a) Leading jet p_T

(b) Leading jet η

Figure 3.31: Distribution of the raw transverse momentum p_T and the pseudo-rapidity η of the selected leading jets for experimental data (solid black points) and for simulated data (filled histograms).

by the simulation, since the agreement is better for low-momentum tracks, as seen previously in [116]. For negative d_0, the agreement is slightly worse, as seen in previous studies from Sec. 3.3 based on 2010 data. The error on d_0 as returned by the track fit is shown in Figure 3.33 where the data-to-simulation agreement is also reasonable. Further studies in bins of $p^2 \sin^3\theta$ of the tracks show that the best description in simulation is for low-momentum tracks and/or tracks at large pseudo-rapidities. This indicates in particular that the description of the material in the simulation and its treatment in the track reconstruction are reasonable. The signed transverse impact parameter significance d_0/σ_{d_0} is shown on Figure 3.34. The moderate underestimation of the tails in the simulation is again due to high-momentum tracks: a further refined alignment could reduce the discrepancy. The significance z_0/σ_{z_0} is shown in Figure 3.35: in this case the resolution in data is better than in simulation. In both cases, the size of disagreements between the impact parameter significance distributions in data and Monte Carlo is minor and will be absorbed by the calibration procedures (see Sec. 3.6).

3.5.6 Commissioning studies

We have studied many aspects of the Monte Carlo description of the data during the commissioning of the algorithms. We present the two most important aspects: the level of agreement in the description of the tagging output discriminating variable and any associated auxiliary variables, and the description of the tagging rates in inclusive and heavy flavor-enhanced jet samples. The tagging rate is defined as the fraction of jets that are tagged out of those that could be tagged by a given algorithm, for a specific choice of its operating point. The fraction of tagged jets has some dependence on the jet p_T (and to a lesser extent on η) which is specific to each algorithm. For a typical sample with a mix of flavors and a fraction f_b of b-jets, the integrated tagging rate is the sum of the fraction of b-jets correctly tagged by the algorithm and the fraction of non-b jets tagged by mistake, *i.e.* $f_{\text{tagged}} = f_b\varepsilon_b + (1-f_b)\varepsilon_{\text{non-b}}$, where $\varepsilon_{\text{non-b}}$ is the efficiency to tag a non-b jet by mistake and is algorithm- (and also p_T- and η-)

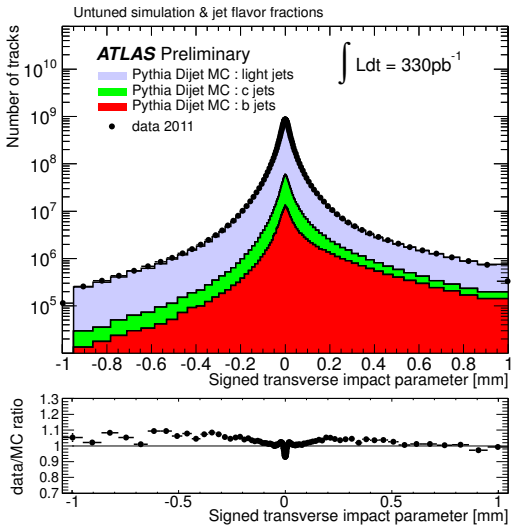

Figure 3.32: Distribution of the signed transverse impact parameter d_0 of tracks, for experimental data (solid black points) and for simulated data (filled histograms for the various flavors).

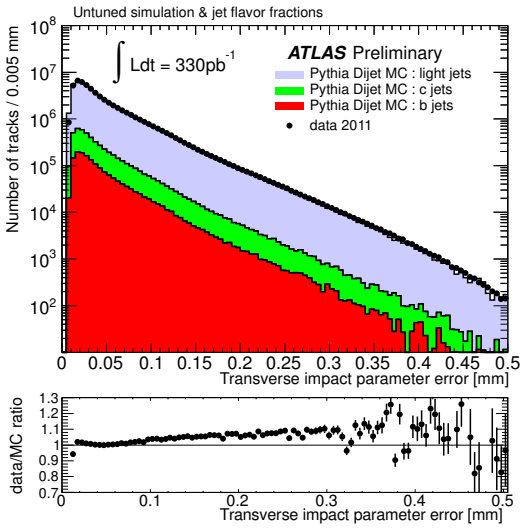

Figure 3.33: Distribution of the transverse impact parameter σ_{d_0} uncertainty of tracks.

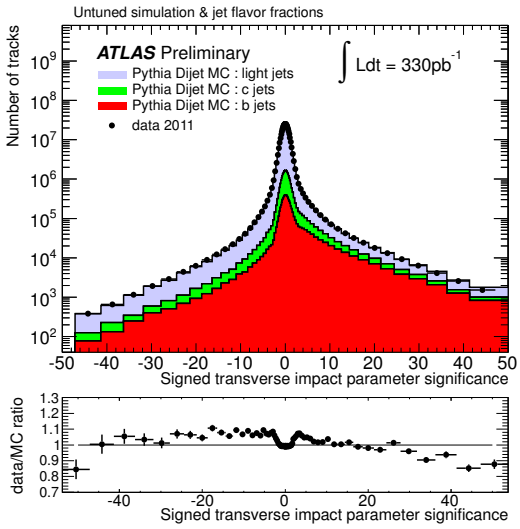

Figure 3.34: Distribution of the signed significance of the transverse impact parameter $d_0/\sigma(d_0)$ of tracks.

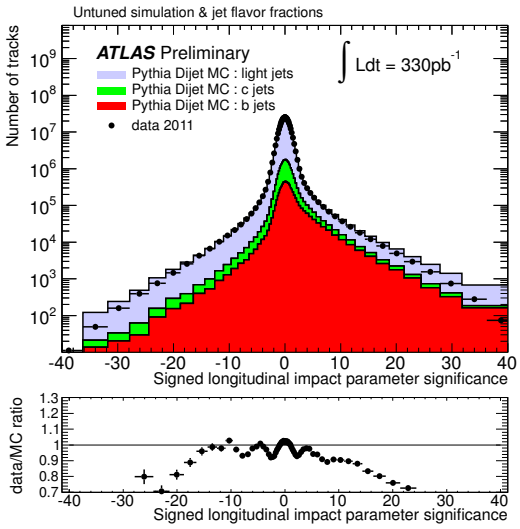

Figure 3.35: Distribution of the signed significance of the longitudinal impact parameter $z_0/\sigma(z_0)$ of tracks.

dependent.

It is important to note that for the tagging rate histograms in the following, the data and simulation plots were not normalized to the same area: both the shape and normalization contain information. For the sake of comparison the operating points are not described by the actual cut value on the output of each algorithm: instead the cuts are chosen to yield a fixed b-jet tagging efficiency (50% or 70%

for instance) on a simulated $t\bar{t}$ sample. Therefore in the following, the operating points are referred to by their corresponding $\varepsilon_b^{t\bar{t}}$ efficiency.

It is also important to note that no systematic uncertainties are shown on the Monte Carlo predictions. Two important effects can influence the details of the agreement with data — the residual discrepancies in modeling the impact parameter resolutions, and the correct modeling of the b, c and light flavor composition of the jet samples by the Pythia Monte Carlo generator. Rather than evaluating these in detail (*e.g.* by using the impact parameter smearing procedures discussed in Section 3.5.5.1), these residual discrepancies will be addressed in practice by means of the tag calibration procedures [127, 128]. This is discussed further in Section 3.5.6.4.

3.5.6.1 Come-back to the JetProb algorithm

With the much different event selection, especially the trigger selection, that we are using in this study compared to the one used during the commissioning of *JetProb* with the 0.4 nb^{-1} of 7 TeV data in Sec. 3.4.2, particularly different trigger selections, we studied again the *JetProb* algorithm previously commissioned.

Most importantly, we realized that removing the modification that was added to the original definition of JetProb, the one in Eq. 3.14 of Sec. 3.4.2.2 that multiplied the track weights by a factor of 2, lead to an increase of the b-tagging performance. At a 60% b-jet efficiency, on a $t\bar{t}$ sample, the rejection increased by $\sim 45\%$. This increase can be understood when realizing that the transformation in Eq. 3.14 was equivalent to the transformation $\mathscr{P}_0 \rightarrow \mathscr{P}_0 \times 2^N$ in the original defintion of *JetProb* in Eqs. 3.12 and 3.13, hence introducing a factor depending on the multiplicity of the jets. We have seen the crucial importance of the weighting factor $\mathscr{N}(N, \mathscr{P}_0)$ that acted to renormalize the weight of jets with high multiplicity of tracks. Given the fact that b-jets have on average a higher multiplicity than light jets, the added factor 2 in the track weight have modified differently the distributions of b-jets and light jets, affecting the performance.

The new track weight and jet weight distributions can be seen in Fig. 3.36, now ranging from 0 to 0.5. The data-to-simulation can be seen to be degraded compared to the one in Sec. 3.4.2, but this is due to the fact that in the present case, the resolution function has not been re-done compared to the immediate previous reprocessing[21] due to lack of time and due to the priority to commission the high-performance taggers. Despite this, the agreement is still very reasonable and will be absorbed in the calibration procedure.

3.5.6.2 IP3D+SV1 algorithm

Since IP3D+SV1 is a combination of two algorithms, their individual behavior is discussed first. The output of the IP3D algorithm for taggable jets is shown in Figure 3.37, for experimental data and for simulated data. The simulated sample is broken into three components: b-jets, c-jets and light jets, according to the flavor composition predicted by the Pythia generator. The simulation gives a reasonably good description of the data, within 20%, with however a discrepancy in the region with negative weights, dominated by light jets. This discrepancy arises from the non-perfect modeling of the impact parameter discussed previously in Section 3.5.5.1, which can be accounted for with an *ad hoc* smearing of the simulated impact parameters. The positive tail is also not perfectly reproduced. Currently an operating point chosen in simulation would overestimate slightly the efficiency and would lead to fewer jets being tagged in data, as can be seen in Figure 3.38. This figure shows the tagging rate for

[21] It was however redone compared to Sec. 3.4.2, and the version used here is for a reprocessing very similar to the latest one at the time of the study.

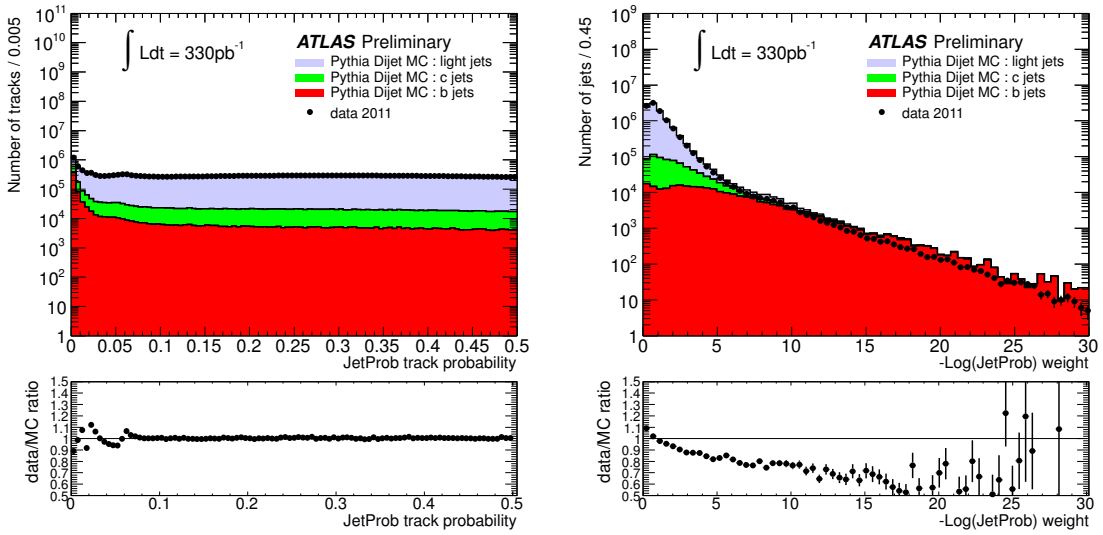

(a) (b)

Figure 3.36: Distribution of the *JetProb* track weight $\mathscr{P}_{\text{trk}}$ (a) and of $-log_{10}(\mathscr{P}_{\text{jet}})$ (b) for experimental data (solid black points) and for simulated data (filled histograms for the various flavors).

the IP3D algorithm operating at a 60% b-jet efficiency. Despite the output weight discrepancy, the shape and the fraction of tagged jets are reasonably well reproduced by the simulation.

The other ingredient is the SV1 algorithm. The reconstruction of an inclusive secondary vertex is not always successful. The fraction of jets in which such a vertex could be found is shown in Figure 3.39 for experimental and simulated data, as a function of the jet transverse momentum. Two samples with different flavor compositions are used, the inclusive leading jet sample and one enriched in heavy flavor jets. The simulated data agree reasonably well with the experimental data in the latter sample. In the sample dominated by light jets, the simulation slightly overestimates (by $\approx 10\%$) the secondary vertex reconstruction efficiency. The properties of the inclusive vertex found by SV1 are shown in Figure 3.40. The peaks at zero correspond to jets in which no secondary vertex could be reconstructed. All vertex properties shown are well modeled by the simulation within 20%.

Finally, the resulting output weight of the IP3D+SV1 combined algorithm is shown in Figure 3.41. The behavior is very similar to the IP3D case, but the level of agreement between data and simulation is improved by the SV1 component which is better modeled than IP3D. The tagging rates as a function of the jet p_T and for an operating point leading to a b-jet efficiency of 60% in $t\bar{t}$ events are shown in Figure 3.43, for jets from the inclusive leading jet sample and for jets from the heavy-flavor enriched sample. The tagging rates on the inclusive leading jet sample as a function of the jet pseudo-rapidity and jet azimuthal angle can be found in [124]. Shapes are well predicted by the simulation and the overall rates in simulation agree with the ones in data within 20%.

3.5.6.3 IP3D+JetFitter

The same checks are now performed for the IP3D+JetFitter tagging algorithm. The output of the JetFitter algorithm (not combined with IP3D) is shown in Figure 3.42. Its tagging rate distributions can be found in [124].

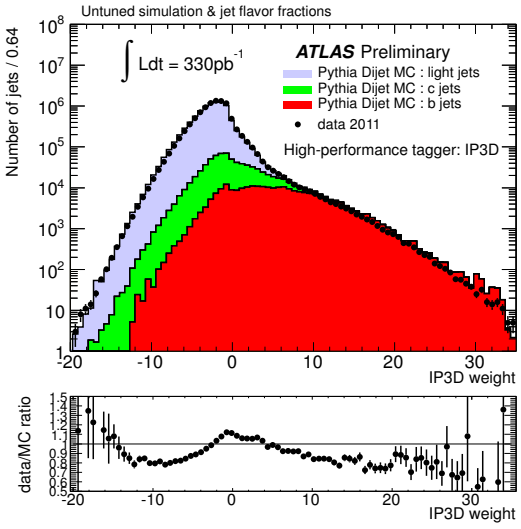

Figure 3.37: Distribution of the jet output of the IP3D tagging algorithm for experimental data (solid black points) and for simulated data (filled histograms for the various flavors). Jets are from the inclusive leading jet sample. The ratio data/simulation is shown at the bottom of the plot.

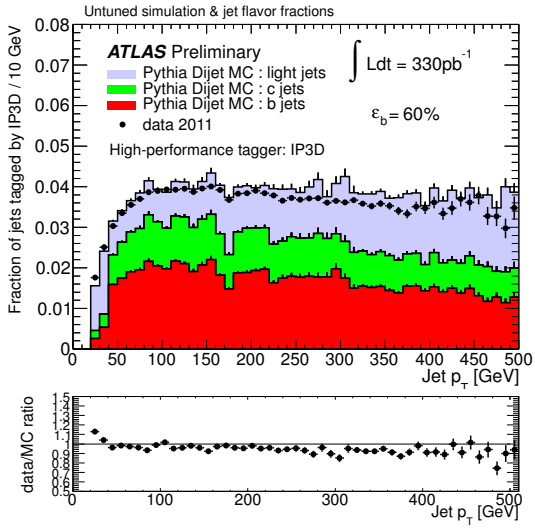

Figure 3.38: Distribution of the tagging rate for the IP3D tagging algorithm versus the jet p_T at an operating point $\varepsilon_b \approx 60\%$ for experimental data (solid black points) and for simulated data (filled histograms). Jets are from the inclusive leading jet sample.

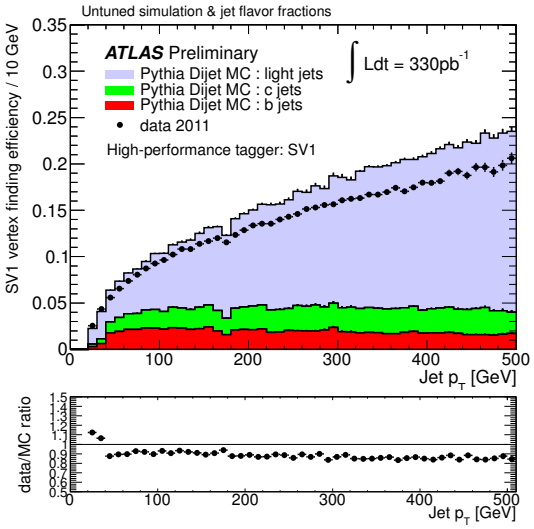

(a) inclusive leading jet sample

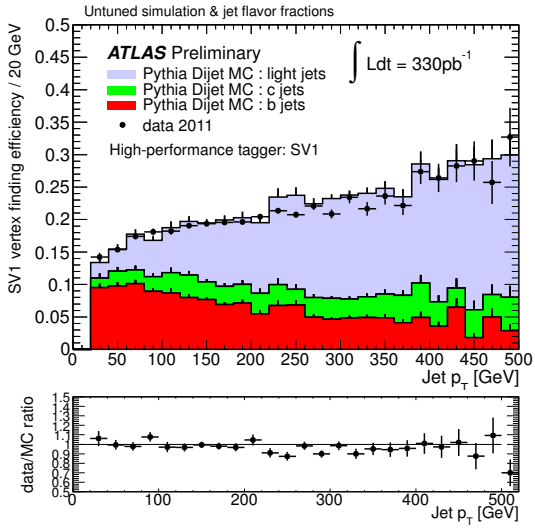

(b) heavy-flavor enriched jet sample

Figure 3.39: Distribution of the vertex finding efficiency by the SV1 tagging algorithm versus the jet transverse momentum for experimental data (solid black points) and for simulated data (filled histograms for the various flavors). The plots are for two samples: (a) inclusive leading jets sample and (b) sample enriched in heavy-flavor jets.

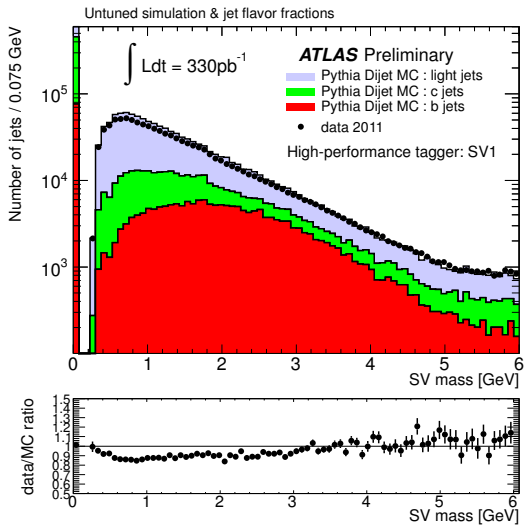

(a) vertex mass

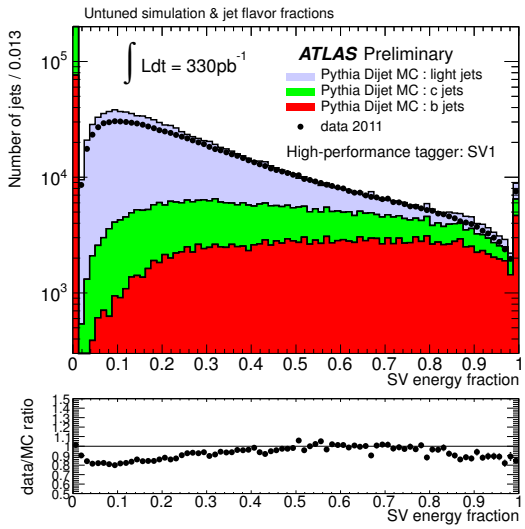

(b) vertex energy fraction

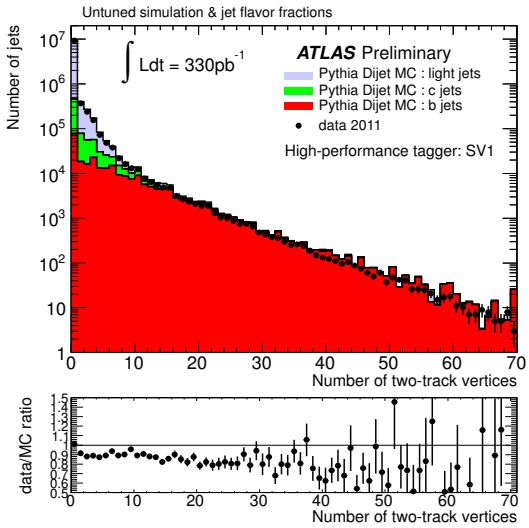

(c) number of two-track vertices

Figure 3.40: Distribution of the properties of the vertex found by the SV1 tagging algorithm for experimental data (solid black points) and for simulated data (filled histograms for the various flavors). Jets are from the inclusive leading jet sample.

Some of the properties of the decay chain found by JetFitter can be found in cite [124]: the number of vertices with two or more tracks, the number of single-track vertices, the invariant mass of the tracks used anywhere along the decay chain and the fraction of their energy compared to the jet energy. The simulation reproduces these distributions fairly well, which is remarkable given these are the results of very complex algorithms.

The jet weight resulting from the combination of JetFitter with IP3D can be seen in Figure 3.44. The shape in experimental data is closely reproduced by the simulation, except in the negative weight region, dominated by light jets, where the impact parameter resolution issue already discussed (Sec-

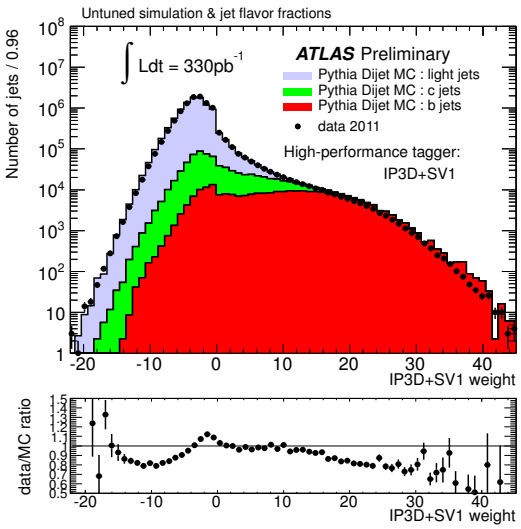

Figure 3.41: Distribution of the output of the IP3D+SV1 tagging algorithm. Jets are from the inclusive leading jet sample.

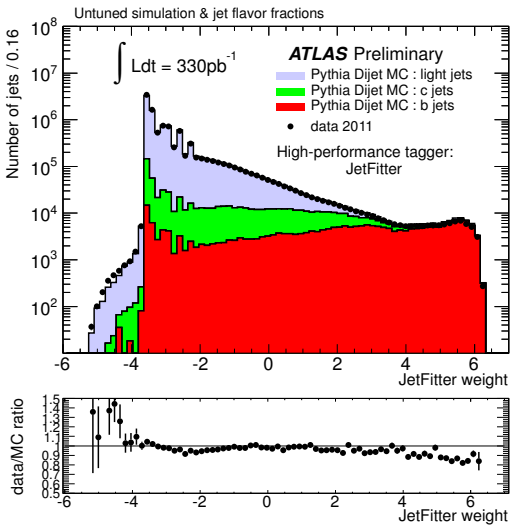

Figure 3.42: Distribution of the output of the JetFitter tagging algorithm. Jets are from the inclusive leading jet sample.

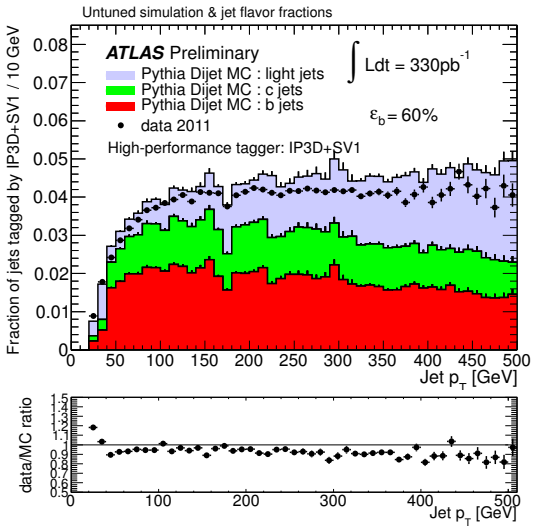

(a) inclusive leading jet sample

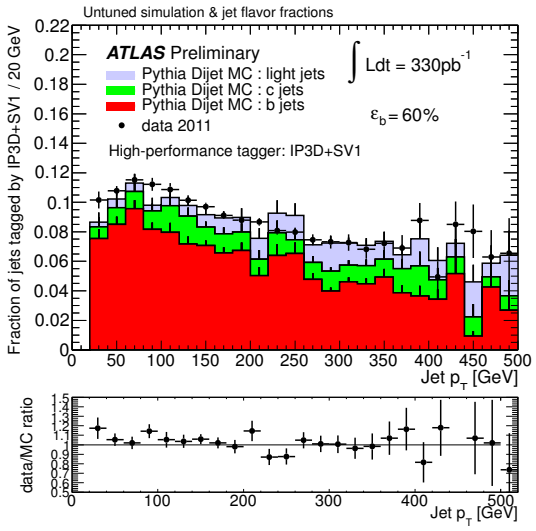

(b) heavy flavor enriched jet sample

Figure 3.43: Distribution of the tagging rate for the IP3D+SV1 tagging algorithm at an operating point $\varepsilon_b \approx 60\%$ versus the jet transverse momentum, for two jet samples: (a) the inclusive jet sample and (b) the sample enriched in heavy-flavor jets.

tion 3.5.5.1) manifests itself through the combination with IP3D. The tagging rates for the inclusive jet sample and for the one enriched in heavy-flavor jets are shown on Figure 3.45, this time with a looser configuration of the algorithm ($\varepsilon_b^{t\bar{t}} \approx 70\%$). The tagging rates as a function of the jet pseudo-rapidity and azimuthal angle are shown in Figure 3.46. In all cases, the tagging rate predicted by the simulation agrees with experimental data to within 20%.

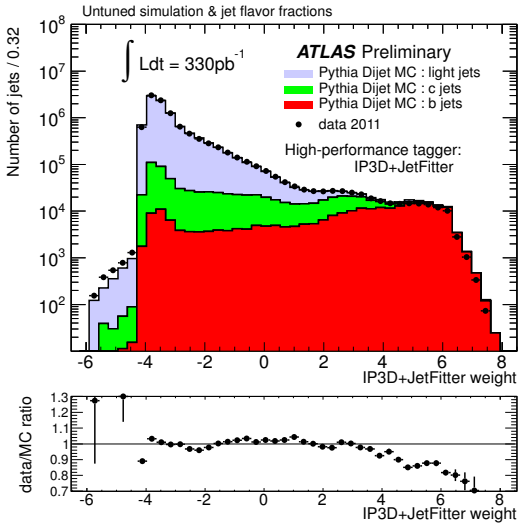

Figure 3.44: Distribution of the output of the IP3D+JetFitter tagging algorithm for experimental data (solid black points) and for simulated data (filled histograms for the various flavors). Jets are from the inclusive leading jet sample. The ratio data/simulation is shown at the bottom of the plot.

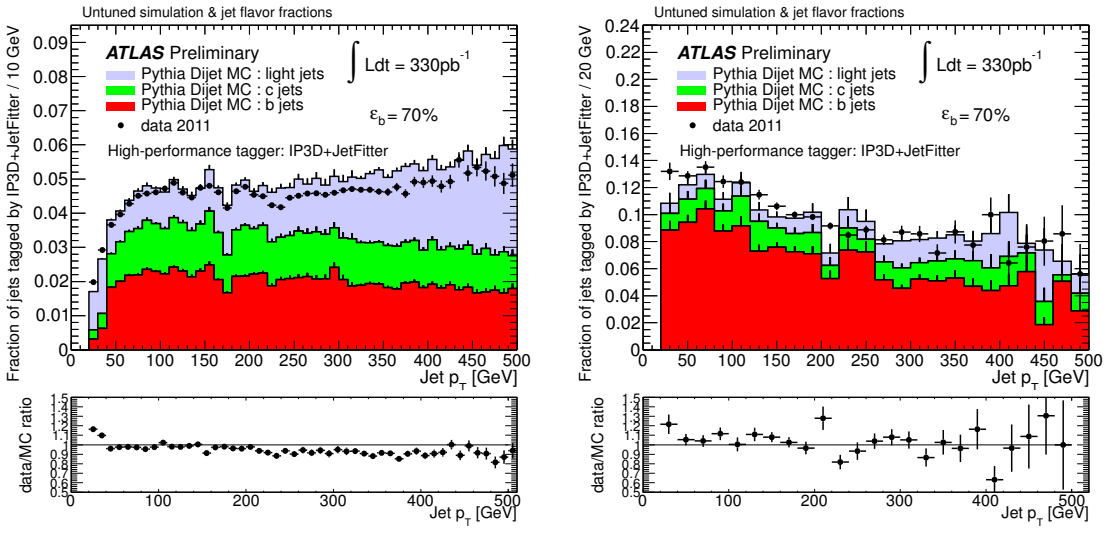

(a) inclusive leading jet sample

(b) heavy-flavor enriched jet sample

Figure 3.45: Distribution of the tagging rate for the IP3D+JetFitter tagging algorithm at an operating point $\varepsilon_b \approx 70\%$ for experimental data (solid black points) and for simulated data (filled histograms for the various flavors) versus the jet transverse momentum, for two jet samples: (a) inclusive light jet sample and (b) sample enriched in heavy-flavor jets.

3.5.6.4 Comparison of the algorithms

In this section, we discuss briefly how the performance of the high-performance tagging algorithms compares with the one of the *early* algorithms, using experimental data. As seen in Section 3.2.7.2, the performance of the tagging algorithms is characterized, for a given operating point, by the efficiency

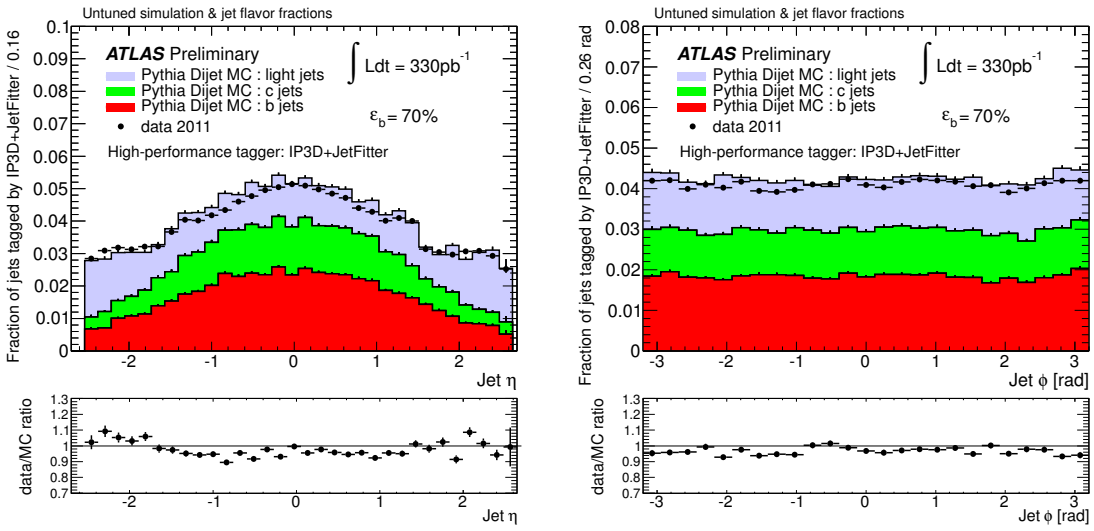

(a) versus jet η (b) versus jet ϕ

Figure 3.46: Distribution of the tagging rate for the IP3D+JetFitter tagging algorithm at an operating point $\varepsilon_b \approx 70\%$ for experimental data (solid black points) and for simulated data (filled histograms for the various flavors). Jets are from the inclusive leading jet sample.

to tag real b-jets $\varepsilon_b(p_T,\eta)$ and by the rejection of non-b jets, which is the inverse of the fraction of mistagged jets $\varepsilon_{\text{non-b}}(p_T,\eta)$. Since it is not possible to select data samples with a high-enough purity in b-jets, and even less so with a high purity of light jets, a detailed comparison would in principle require to disentangle the behavior of the taggers and the actual flavor composition of the sample. Calibration techniques to do so are described briefly in Sec. 3.6 and will be used in the future. Instead a qualitative approach is used here to give an indication of the improved performance to be expected from the high-performance b-tagging algorithms.

The SV0 algorithm, which has been used so far in many physics analysis at an operating point of $\varepsilon_b^{t\bar{t}} = 50\%$ in simulation, is compared to the new IP3D+SV1 algorithm at an operating point chosen to give the same efficiency $\varepsilon_b^{t\bar{t}}$. Figure 3.47(a) shows the SV0 tagging rate in data as a function of the jet p_T in the inclusive jet sample. For illustration, the tagging rates in the simulated samples are also shown. In Figure 3.47(b), analogous tagging rates are shown for the IP3D+SV1 algorithm. The IP3D+SV1 algorithm appears to be less prone than the SV0 algorithm to mistakenly tag light jets as b-jets. It is important to note however that the comparison is qualitative only and that it is not possible to infer for instance the ratio of the mistag rates of the two algorithms from these plots. This is because a change in the operating point leading to a minor change in the b-tag efficiency can have a large impact on the mistag rate[22]. Moreover, even if the operating points of the two algorithms were chosen to give the same inclusive b-tag efficiency in a simulated $t\bar{t}$ sample, there is no guarantee that the algorithms would operate at exactly the same tagging efficiency in data in the dijet sample. On the contrary, this is quite unlikely since the kinematics of the jet sample considered here are different from $t\bar{t}$ and the tagging efficiency depends strongly on the p_T of the jet. Slight differences between the b-tag efficiencies in data and simulation and the associated change in the light jet rejection also allow for the observed differences in the tagging rates when comparing data and Monte-Carlo without posing a major problem for the commissioning of these algorithms.

[22] This will be seen *e.g.* in Fig. 3.49.

As mentioned already, one feature of the new tagging algorithms is their ability to operate at a high b-jet tagging efficiency, *e.g.* 70%, while still achieving a high rejection of light jets. Of the early algorithms, only the JetProb algorithm could reach such high efficiencies, but with a poor light jet rejection. The SV0 algorithm efficiency is intrinsically limited to 50%-60%, which is the efficiency to reconstruct a secondary vertex. Therefore the new IP3D+JetFitter algorithm at $\varepsilon_b^{t\bar{t}} = 70\%$ is compared to JetProb operating at the same $\varepsilon_b^{t\bar{t}}$. Figure 3.48(a) shows the tagging rate as a function of the jet p_T for the JetProb algorithm in the inclusive jet sample, while Figure 3.48(b) shows the same information for the IP3D+JetFitter algorithm. The same conclusion holds, namely that the fraction of mistagged non-b jets appears to be substantially higher for JetProb than for the more powerful IP3D+JetFitter algorithm. Please however note that since there is no guarantee that the two algorithms actually tag exactly the same fraction of b-jets in the data sample considered, no quantitative conclusion on the relative mistag rates of the two algorithms should be drawn from this comparison.

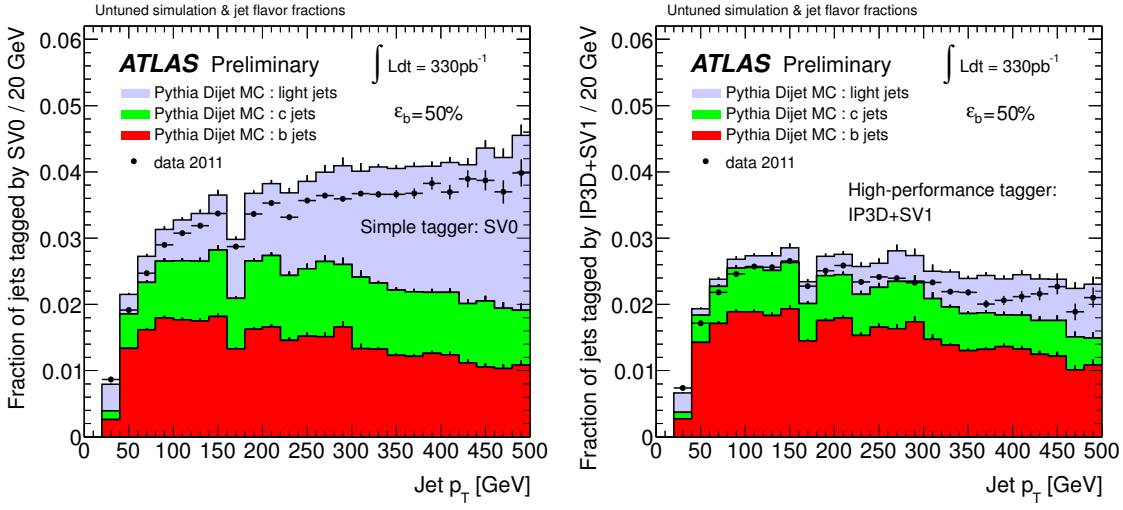

(a) SV0

(b) IP3D+SV1

Figure 3.47: Distribution of the tagging rates on the inclusive leading jet sample, for the SV0 and IP3D+SV1 tagging algorithms with their respective operating points tuned to a priori give the same 50% b-jet efficiency on a $t\bar{t}$ simulated sample.

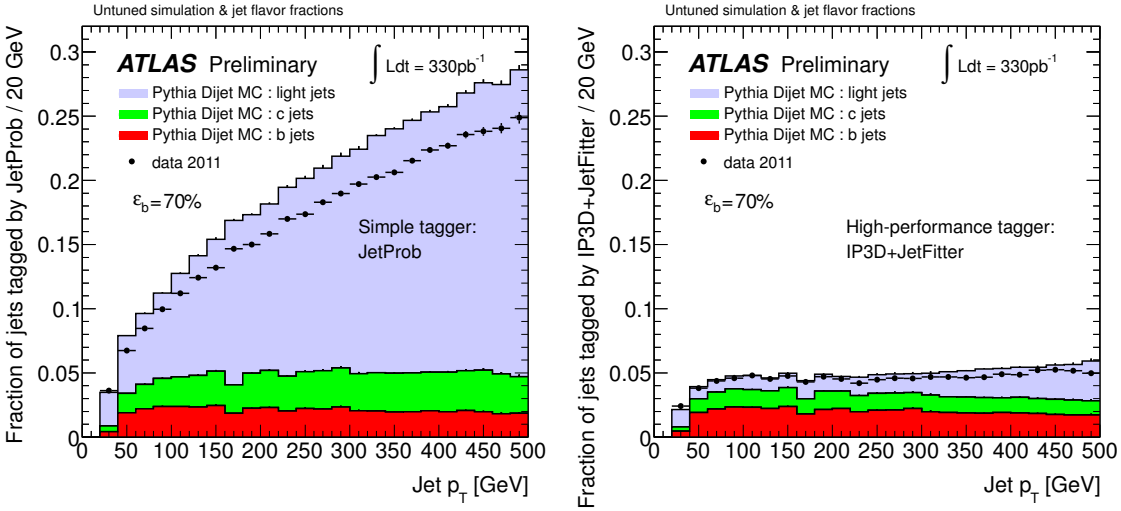

(a) JetProb (b) IP3D+JetFitter

Figure 3.48: Distribution of the tagging rates on the inclusive leading jet sample, for the JetProb and IP3D+JetFitter tagging algorithms with their respective operating points tuned to a priori give the same 70% b-jet efficiency on a $t\bar{t}$ simulated sample.

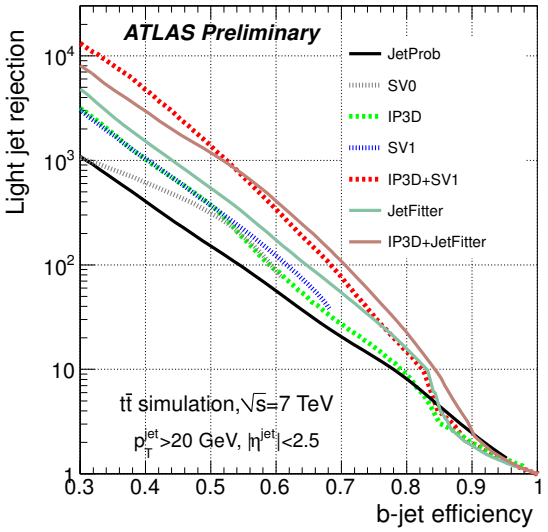

Figure 3.49: Light-jet rejection as a function of the b-jet tagging efficiency for the early tagging algorithms (JetProb and SV0) and for the high-performance algorithms, based on simulated $t\bar{t}$ events.

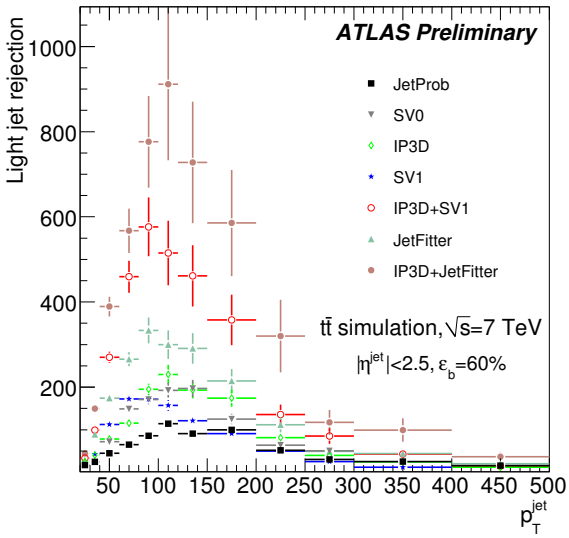

Figure 3.50: Light-jet rejection as a function of the jet transverse momentum p_T, for operating points of the various tagging algorithms leading to the same $\varepsilon_b^{t\bar{t}} = 60\%$, based on simulated $t\bar{t}$ events.

3.5.7 Expected performance

The expected improvement in b-tagging performance achieved by the high-performance tagging algorithms is discussed in this section, and is based on a sample of simulated $t\bar{t}$ events in which both W bosons either decay leptonically or one decays leptonically and the other hadronically. The events were generated with an MC@NLO generator[23] assuming a top mass of 172.5 GeV.

Figure 3.49 shows the light-jet rejection as a function of the b-jet tagging efficiency ε_b for the various ATLAS b-tagging algorithms. It is obtained by varying continuously the operating point of each tagger, *i.e.* the cut on its output discriminating variable. For the same tagging efficiency, the high-performance tagging algorithms are expected to have much lower mistagging rates than their counterpart algorithms designed for early data. In addition, by combining the vertexing techniques and the impact parameter information, the IP3D+SV1 and IP3D+JetFitter algorithms can reach very high tagging efficiencies. For a 50% (resp. 60%) b-tagging efficiency, these results show that a high-performance tagger like the IP3D+SV1 algorithm achieves a factor of five (resp. four) reduction in the mistag rate in events with $t\bar{t}$-like kinematics, compared to the early tagging algorithms used currently for physics analyses. At 70% b-tagging efficiency, the IP3D+JetFitter algorithm achieves a mistag rate lower than 1%.

Note that the results depend strongly on the kinematics of the sample under study, and that this variation is specific to each tagging algorithm, as can be seen in Figure 3.50 which shows the light jet rejection as a function of the jet p_T for the various tagging algorithms operating in such a way that they all lead to the same $\varepsilon_b^{t\bar{t}} = 60\%$. One can notice that for all algorithms, the tagging performance is optimal for ${p_T}^{\text{jet}} \sim 100$ GeV: below this threshold, tracks in jets are relatively soft and therefore multiple scattering is compromising the resolution on the impact parameter, while above this p_T value several effects such as merged pixel clusters and pattern-recognition issues conspire to reduce the performance. Further information can be found in Ref. [166].

Note also that the MV1 algorithm was not shown in the previous two figures. This is due to the fact that this tagger was developed later. We recall that this tagger is a combination of the IP3D, SV1 and JetFitter weights, and hence relies directly on the commissioning work we performed. Fig. 3.51[24] shows the performance of MV1 compared to IP3D+SV1 and IP3D+JetFitter[25] from [128], which proves that its performance is actually the best one available, and that it allows to work at higher b-tagging efficiencies.

3.6 Calibration in data

As introduced previously, as long as the description of the tracking and vertexing performance of the detector by MC simulation is not perfect, the performance of the b-tagging will have to be understood using real data. This is necessary in order to estimate the backgrounds from well known Standard Model processes after applying b-tagging algorithms in physics analyzes.

[23] See [124] for details

[24] Figure. 3.49 and Fig. 3.51 cannot be compared directly due the jet p_T cut which differs; requiring respectively to be above 20 GeV and 15 GeV.

[25] In this plot, the JetFitterCombNNc algorithm is identical to JetFitterCombNN with the exception that the neural network is trained to reject c-jets rather than light jets.

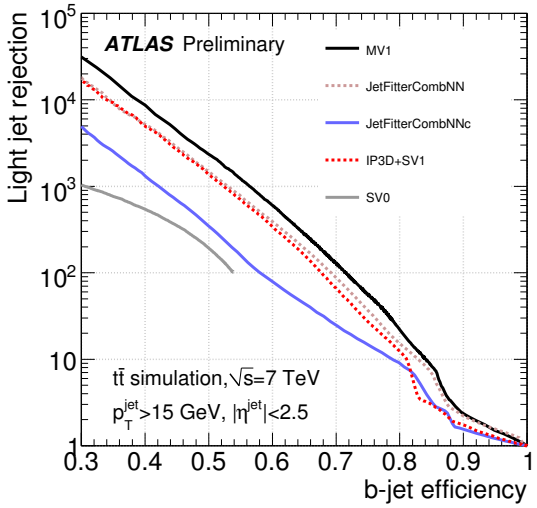

Figure 3.51: Light-jet rejection as a function of the b-tag efficiency for the b-tagging algorithms calibrated in [128], based on simulated $t\bar{t}$ events.

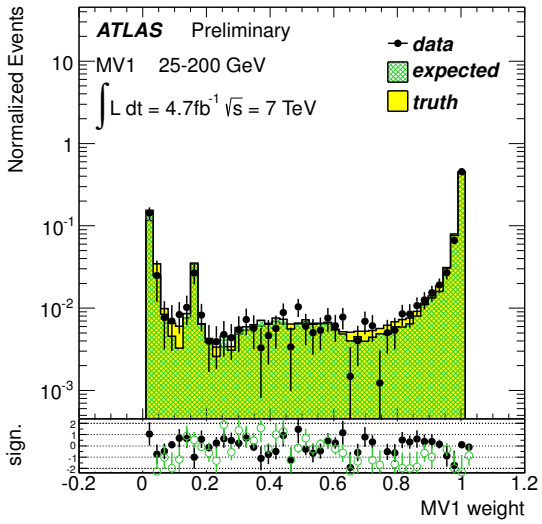

Figure 3.52: Background-subtracted MV1 weight distributions. The expected distribution is obtained by performing the kinematic fit method on simulated events while the truth distribution correspond to that for simulated b-jets [129].

3.6.1 Efficiency

Pure samples of b-jets are required to measure the b-jet tagging efficiency[26], which can be done using two kind of samples, as described now.

Using di-jet events with *Soft-muon* tag As emphasized in Sec. 3.2, b-jets are naturally produced as QCD di-jet events at the LHC, so they can in principle be used as a source of b-jets to derive the b-tagging calibration with the low integrated luminosity expected at the start of the LHC. However, $b\bar{b}$ production represents only a very small fraction of the total QCD cross section. In order to increase the fraction of b-jets, jets are required to contain a muon[27], because the major source of muons is the semi-leptonic decay of b-quarks or c-quarks resulting from the initial b-quark decay. As a consequence, this is only the semi-leptonic efficiency that is measured in data. In the techniques described hereafter, the assumption is made that it can be extrapolated to obtain the inclusive b-tagging efficiency, using MC simulation, which is actually the toughest part of these measurements.

Two methods have been used at the start of the LHC:

- The p_T^{rel} method uses MC-derived templates, for b-, c-, and light jets, of the relative p_T of a muon with respect to the jet+muon axis. The b-content of a jet data sample can then be determined by fitting the p_T^{rel} distributions of the data with these templates before and after the tagging algorithms are applied. The b-tagging efficiency is derived from the changing b-fractions (*e.g.* [128, 107, 108]);

[26] Measuring in data the c-tagging efficiency is also important, but beyond the scope of this work and not used in our analysis in Chap. 4.

[27] In practice, this is done *e.g.* using the so-called 'Soft-muon' tagger that we introduced briefly in Sec. 3.2.2.

- The *System 8* method employs two samples with different b-content and two uncorrelated tagging algorithms to construct a system of 8 nonlinear equations and 8 unknowns. One of the unknowns is the b-tagging efficiency (*e.g.* [128, 109]).

Using $t\bar{t}$ events At the LHC, the large $t\bar{t}$ production cross-section of $\sigma_{t\bar{t}} = 177 \pm 3(\text{stat.}) \, ^{+8}_{-7}(\text{sys.}) \pm 7(\text{lum.})$ pb [131] offers an interesting source of b-jets, in a distinctive topology which is relatively easy to trigger and to isolate, as we will see in Chap. 4. The b-tagging efficiency can be extracted from $t\bar{t}$ events either by counting events with different numbers of tagged jets, or by reconstructing the $t\bar{t}$ decay topology in order to identify a pure sample of b-jets [166, 129]. With the large integrated luminosity of 4.7 fb^{-1} collected in 2011, these methods have become competitive for the first time [129]. In this latter analysis, the b-tagging efficiency is measured *e.g.* from very high purity weight distributions of b-jets obtained applying a kinematic fit and using a statistical background subtraction, as can be seen in Fig. 3.52 for the MV1 algorithm.

In addition to providing calibration measurements in an inclusive b-jet sample rather than a sample of semi-leptonic b-jets, these methods also allow to extend the calibrated p_T range. Furthermore, the $t\bar{t}$ environment of high jet multiplicity and high-p_T b-jets is more similar to the final states to which b-tagging is applied generally in physics analyses than to semi-leptonic jet sample.

Both methods are yielding $\varepsilon_{data}/\varepsilon_{MC}$ scale factors, that are determined in bins of jet p_T. The systematic uncertainties on these factors are also provided. For the b-jet efficiency of the MV1 tagging algorithm, the scale factors resulted from the combination of the two methods p_T^{rel} and System8, and are shown in Fig. 3.53, and the ones obtained from $t\bar{t}$ decays are shown in Fig. 3.54.

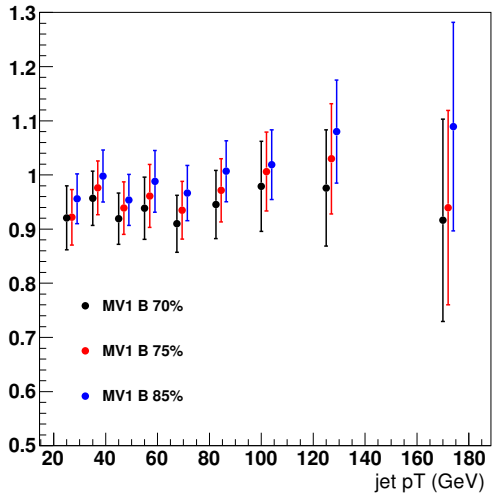

Figure 3.53: Data/MC scale factors for the b-jet tagging efficiency with MV1 as a function of the jet p_T, for 3 operating points, obtained from p_T^{rel} and *System 8* calibrations [128].

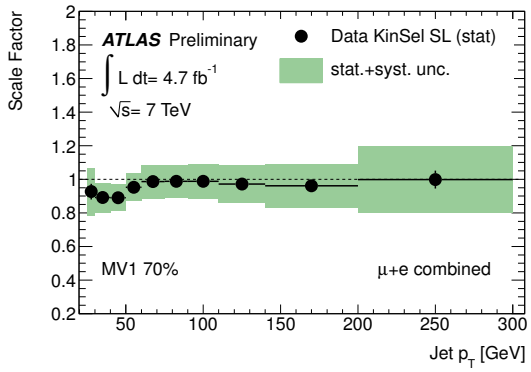

Figure 3.54: The resulting scale factors for the MV1 algorithm at 70% b-tagging efficiency in the kinematic selection single lepton $t\bar{t}$ analysis. The error bars show the statistical uncertainties while the green band indicates the total uncertainty [129].

3.6.2 Mistagging rate

The mistagging rate of the algorithms has also to be measured in data, using inclusive jet samples (where the heavy flavor content is small). This is done using two methods: the first one uses the invariant mass spectrum of tracks associated with reconstructed SV to separate light and heavy-flavor jets; the other is based on the rate at which SV with negative decay length, or tracks with negative IP, are present in data [130].

These measurements provide jet-p_T and η dependent scale factors that correct the b-tagging mistagging rate in simulation to that observed in data. The uncertainties on these scale factors range from less than 10% for the loosest operating points ($\varepsilon_b \sim$85%) to more than 100% for the tighest operating points ($\varepsilon_b \sim$60%).

The accuracy of the calibration measurements is very important because it can translate directly into large errors in physics analyzes using b-tagging. The rather large errors seen in Fig. 3.53, that are also remarkable given the maturity of the experiment, illustrate well the necessity to tackle the data-to-simulation agreement issue on two fronts in parallel: understanding and improving the basic ingredients of the algorithms (tracks, vertices, etc), and improving the measurements methods in data.

3.7 *b*-tagging performance with IBL

As introduced in Sec. 2.4, the installation of an Insertable B-Layer (IBL) has been studied for a long time. It would allow to meet ATLAS physics goals despite the inevitable degradation of the current detector with radiation doses, and despite the coming LHC luminosity upgrades.

Thanks to the lower radius of the IBL compared to the current *b*-layer, and due to the fact that each track gets in principle an extra measurement point[28], the tracking and vertexing performance are expected to be greatly improved with the installation of the IBL. As these two aspects are the main ingredients of *b*-tagging, the gain in performance is expected to be substantial, and becomes a decisive argument for the construction of the IBL. It hence has to be studied in great detail, which is the aim of this section. We provided the results[29] in this section to the official ATLAS IBL Technical Design Report [103] in which further detail can be found.

3.7.1 Impact on tracking, vertexing and *b*-tagging performance without pileup

3.7.1.1 Tracking

As seen to a great extent previously, the IP resolution of tracks is the crucial parameter that affects the *b*-tagging performance. With its smaller radius, the IBL is expected to directly improve it, which was studied in [103].

First of all, the *b*-tagging quality criteria for IBL was naturally slightly modified compared to the definition for the current ATLAS geometry (cf. Tab.3.1 in Sec.3.2.5.2): the requirement of at least one hit in the (current) '*b*-layer' was replaced by the requirement of at least one hit in the IBL.

Regarding the IP resolution, its observed p_T dependence can be described (as explained in Sec. 3.3.4.4) by the $A \oplus B/p_T$ model, for which the A term describes the intrinsic resolution of the detector visible at high p_T, while the B term describes the effect of multiple scattering in the detector material dominant at low p_T. As an example, for tracks with $0.2 < \eta < 0.4$, it was found that the IBL leads to an improvement in A by a factor of 1.2 in d_0 and a factor 1.7 in $z_0 \times sin\theta$. This illustrates the change in the z pitch between IBL and the current Pixel detector. The multiple scattering term improves by a factor 1.8 in d_0 and as well a factor 1.8 in $z_0 \times sin\theta$.

3.7.1.2 Primary Vertex reconstruction

The task of the PV reconstruction is to reconstruct the vertex position of the signal and of additional pileup interactions. The improvement in the PV resolution has been studied in [103] using the default ATLAS PV algorithm and high-multiplicity $t\bar{t}$ events without pileup. Without beam spot constraint, the resolution in x (and y) improves from 15 μm to 11 μm (RMS) with IBL compared to the current geometry, and the resolution in z improves from 34 μm to 24 μm. Adding the beam spot as a constraint to the vertex reconstruction reduces the gain in resolution with IBL in x and y, which leads to an RMS of 8 μm compared to 9 μm without IBL. The gain in resolution in z is basically unchanged: it improves from 31 μm to 24 μm with IBL.

[28] Obviously assuming no 'dead' material on the IBL

[29] At the exception of plot 3.56, whose purpose in this section is mainly to introduce the *Jet Vertex Fraction* variable of a jet, that we will use in the analysis in Chap. 4

3.7.1.3 *b*-tagging

The improvements in track IPs and PV resolution is expected to lead logically to a significant gain in *b*-tagging performance. Figure 3.55 shows the light jet rejection as a function of the *b*-jet efficiency for the *IP3D* tagger alone and for the combined *IP3D+SV1* tagger. The results are obtained using $t\bar{t}$ events without pileup. Jets used have $p_T > 15$ GeV, $|\eta| < 2.5$ and at least one *b*-tagging quality track associated. Table 3.3 summarizes the very significant improvements in the rejection of light jets at fixed *b*-jet efficiency of 60%.

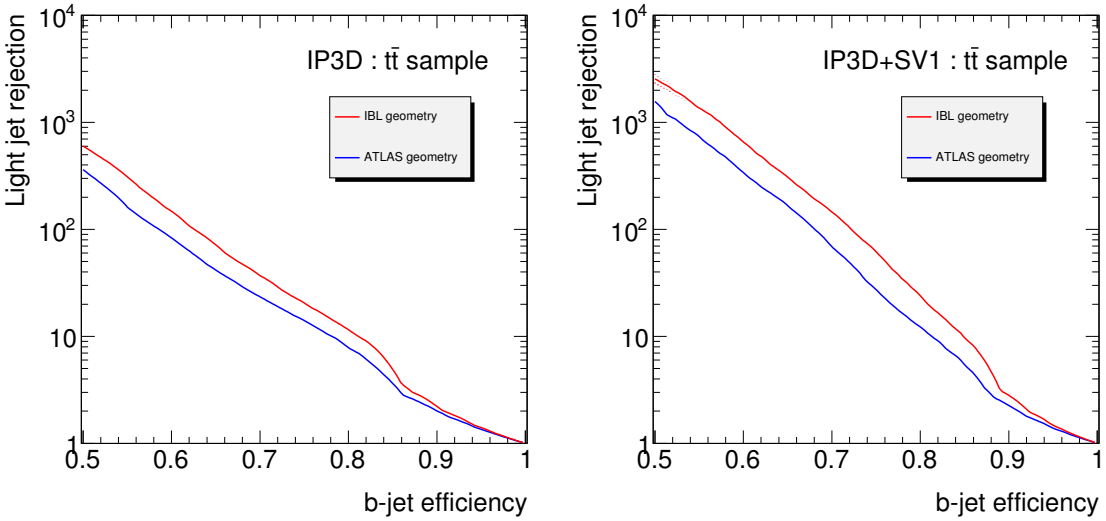

Figure 3.55: Light jet rejection as a function of *b*-jet efficiency for the *IP3D* tagger (left) and for the combined *IP3D+SV1* tagger (right). Compared are the results with and without IBL, using $t\bar{t}$ events without pileup.

b tagger	Without IBL	With IBL	Ratio
IP3D	83 ± 1.5	147 ± 3.4	1.8
IP3D+SV1	339 ± 12	655 ± 32	1.9

Table 3.3: Light jets rejection in $t\bar{t}$ events without pileup for a 60 % *b*-jet efficiency.

3.7.2 Effect of pileup and improvements brought by IBL

The instantaneous luminosity during Phase I (cf. Sec. 2.4) is expected to exceed $2 \times 10^{34} cm^{-2} s^{-1}$ (corresponding to ~ 50 pileup interactions with the LHC machine settings mentioned in Sec. 2.1.4). In-time and out-of-time pileup influence the detector response in many ways as the LHC luminosity increases. For example, calorimeter systems are mostly affected by out-of-time pileup, due to their relatively long integration time ($\tau_{int} >> 25$ ns). For tracking systems, the large background from hits from in-time pileup affects the track reconstruction, which consequently leads to problems for the vertex reconstruction. Additional minimum bias interactions contribute comparatively fewer jets than a high-p_T event such as $t\bar{t}$, but particles produced by the minimum bias interactions can overlay noise

and other soft particles thus raising a low energy deposition above the jet reconstruction threshold or altering the reconstructed jet directions. As a consequence the analysis of high-p_T physics events is affected by the increased jet multiplicity from pileup. A detailed study of jet reconstruction with high level of pileup is beyond the scope of this document. Instead, we will focus briefly on the improvements from the IBL on the track and vertex reconstruction, and in detail on its effects on the b-tagging performance.

3.7.2.1 Tracking

The track reconstruction of events with high luminosity pileup suffers from the increased combinatorial background at all levels, from seeding to track finding and selection of good tracks, up to the reconstruction in the TRT at high occupancy. At the same time the number of shared clusters increases as hits from neighboring tracks merge into single larger clusters, especially at low radius. The track reconstruction needs as well to be robust against possible detector defects (see Sec. 3.7.3) that may develop in time. A more appropriate tighter track selection was proposed in [103]:

- For the current ATLAS geometry: requiring 9 instead of 7 silicon (Pixel, SCT) clusters on track, and removing tracks with a hole in the Pixels.
- For the IBL geometry: 10 silicon (IBL, Pixel, SCT) clusters on track, and allowing for up to one Pixel hole. This latter requirement introduces robustness in the reconstruction against $e.g.$ inefficiencies in the B-layer at high-luminosity.
- For both geometry: the p_T cut is raised from 500 MeV to 900 MeV to reduce the combinatorics from soft tracks from pileup interactions.

This selection results in a modest loss of track reconstruction efficiencies and low rates of additional fake tracks, almost independently of the level of pileup.

It was also shown in [103] (Fig. 11) that the extra tracks accepted without the tighter track selection would lead to a larger rate of tracks with significant d_0 offset and thus can affect the PV reconstruction and b-tagging. Therefore both track selections will be used in the following: the normal selection and the above mentioned tighter selection tuned for high luminosity.

3.7.2.2 Primary Vertex reconstruction

According to [103], the PV resolution (RMS) in z for $t\bar{t}$ events worsens significantly with pileup due to merging of the signal vertex with close-by vertices from pileup. This is especially the case for the nominal track selection, while with the high luminosity track selection the dependence is reduced. Most important is that the improvement in resolution with IBL does not degrade with pileup compared to the current geometry. The resolution at $\sim$ 50 pileup interactions with IBL is even better than the resolution without pileup without IBL.

The vertex reconstruction efficiency, which is very close to 100% without pileup, suffers from the increasing level of pileup. Fortunately, the improved vertex resolution allows to reduce the vertex reconstruction inefficiency. With the high luminosity track selection for events with $2 \times 10^{34} cm^{-2} s^{-1}$ luminosity, it is about halved, from 1.4% without IBL to $\sim$0.6% with IBL.

The correct identification of the interesting PV efficiency is also very close to 100% without pileup. With the high luminosity track selection for events with $2 \times 10^{34} cm^{-2} s^{-1}$ luminosity, it decreases to $\approx$ 96.5% both with and without IBL (slightly higher with IBL). For the nominal track selection, the identification inefficiency is almost doubled.

However, in physics analysis, one can use other means of identifying the correct PV from the set of vertices, like the identified lepton or the tracks associated to the jets from the $t\bar{t}$ decay. For this reason, we will use in the following a MC truth-based algorithm to identify the reconstructed PV, which is justified and much simpler. This also allows the effects of the vertex reconstruction and resolution on the *b*-tagging performance to be studied independently from the inefficiency induced by the vertex identification.

3.7.2.3 *b*-tagging

High-p_T physics events are affected by the increased jet multiplicity due to pileup. Additional tracks and jets from pileup interactions enter the *b*-tagging algorithm and can only degrade their performance, as we will show in this section.

Extra-tracks from pileup jets For $t\bar{t}$ events, the mean number of *b*-tagging quality tracks that can be associated to any reconstructed jet increases by $\approx 25\%$ when increasing the number of pileup interactions from zero to $\sim$50. This huge effect, if one does nothing against it, would lead to a drastic degradation of the *b*-tagging performance. The extra tracks are either from a nearby pileup interaction close to the signal PV, whose tracks contaminate the signal jets; or the reverse situation: tracks from the signal event matching pileup jets. For very high luminosity, given the fact that there is only one 'signal' interaction for many more pileup interactions, one would logically expect this latter effect to be dominant compared to the former. This is confirmed when looking at the mean number of *b*-tagging quality tracks in jets built from MC truth of the signal $t\bar{t}$ event, which only increases of $\sim$2% when increasing the number of pileup interactions from zero to $\sim$50 [103]. This illustrates well that the additional *b*-tagging quality tracks are due to jets from pileup, and the necessity to recognize these jets among signal jets in this very complex situation where several pileup interactions can overlay very close to the primary interaction.

Jet Vertex Fraction The so-called *Jet Vertex Fraction* variable (JVF) of a jet is defined as the momentum sum of all tracks associated to a jet that match the primary vertex over the total momentum sum of all tracks in the jet [104]. This is sketched in Fig. 3.56 (a), showing examples of JVF computation for two jets with respect to two vertices. Fig. 3.56 (b) shows the JVF for all jets entering the *b*-tagging algorithm in $t\bar{t}$ events with $2 \times 10^{34} cm^{-2} s^{-1}$ pileup and only for those jets that are from the signal interaction. It can be clearly seen the discriminating power of this variable to distinguish signal jets from pileup jets which have the tendency towards small JVF values.

In the following of this section, instead of applying a cut on this variable, we will use only *truth level* jets, *i.e.* jets based on true particles stemming only from the signal event. This is done in order to disentangle the effects of jet production in events with pileup from the influence of the IBL on the *b*-tagging performance.

In practice, in physics analysis, it will be particularly useful to apply a cut on the JVF variable, *e.g.* in our search for fourth generation quarks (Chap. 4) in which we will only consider jets with $JVF > 0.75$.

Anti-pileup **cuts** The beam spot describes the envelope of all signal and pileup PVs in an event. The shape of the LHC beam spot (very narrow in the *x*-*y* plane and $\sim$4.5 cm wide in *z*) determines that pileup is likely to affect predominantly the *z* IP significance, while leaving $R\phi$ nearly unchanged. Nearby pileup vertices in *z* are source of additional *b*-tagging quality tracks with significant *z* offsets.

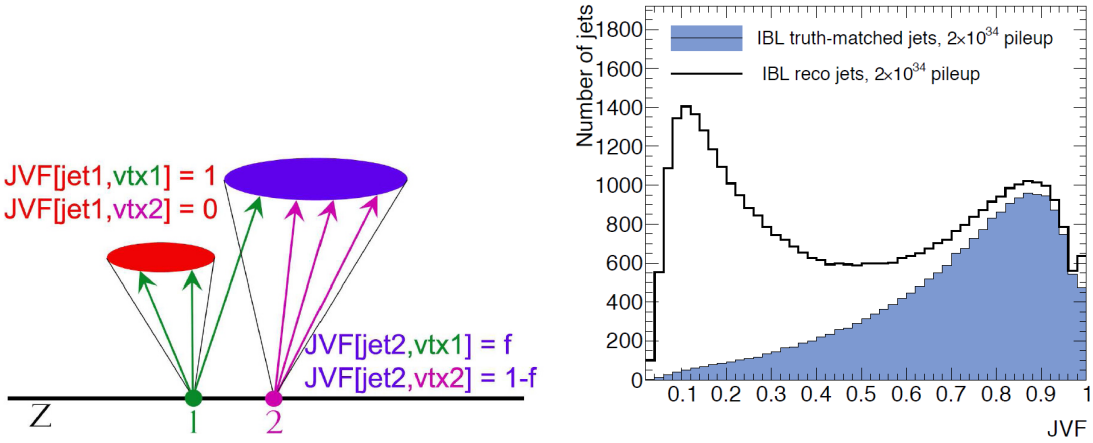

(a) (b)

Figure 3.56: (a) Illustration of the Jet Vertex Fraction of two jets, computed with respect to two different vertices. From [104]. (b) JVF with IBL for all reconstructed jets (with $\eta < 2.5$, $p_T > 15$ GeV, at least one b-tagging quality track) in $t\bar{t}$ events with $2 \times 10^{34} cm^{-2} s^{-1}$ pileup and for the jets from the $t\bar{t}$ interaction itself. From [103].

Fig. 3.57 shows this effect in the IP significance for b-tagging quality tracks from signal and pileup interactions, for $t\bar{t}$ events reconstructed with the IBL and using the high luminosity track selection. The d_0 significance from pileup interactions is symmetric and has the expected shape for tracks in light jets, while the z_0 significance is rather flat as expected for tracks from nearby interactions in z. We have added a cut to the b-tagging software to remove tracks with $|z_0/\sigma(z_0)| > 3.8$ and $|d_0/\sigma(d_0)| < 3$ that are compatible with being from a nearby pileup vertex and would otherwise affect the performance.

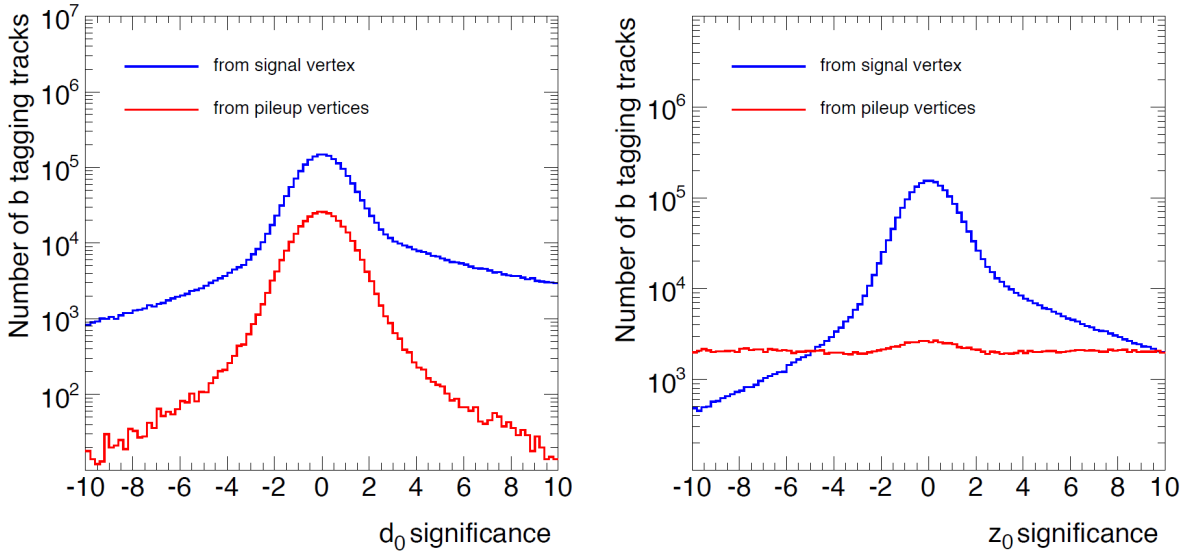

Figure 3.57: Impact parameter significance for b-tagging quality tracks from signal and pileup interactions, (left) for d_0 and (right) for z_0.

Performance As is shown in Fig. 3.58, the performance of the tagging algorithm *IP2D* (which contrary to *IP3D* uses only the $R\phi$ IP information) is rather stable and the improvement with the IBL is almost independent of the level of pileup. Shown as well is the performance of the SV-based tagger *SV1*, which degrades little with pileup and leads to an improved performance with IBL at all luminosities. In both cases, the high luminosity track selection leads to much improved results as additional fake track candidates are removed from the event.

Fig. 3.59 shows the same information as Fig. 3.58 for the tagging algorithms *IP3D* and *IP3D+SV1*. In all cases, *IP3D* does show some remaining degradation with an increasing level of pileup due to the effects in z from nearby pileup vertices discussed before. Still, the results with IBL are much improved. The rejection for the algorithm *IP3D+SV1* at 60% b-jet efficiency with IBL and $2 \times 10^{34} cm^{-2} s^{-1}$ pileup is better than the performance of the current detector at zero pileup.

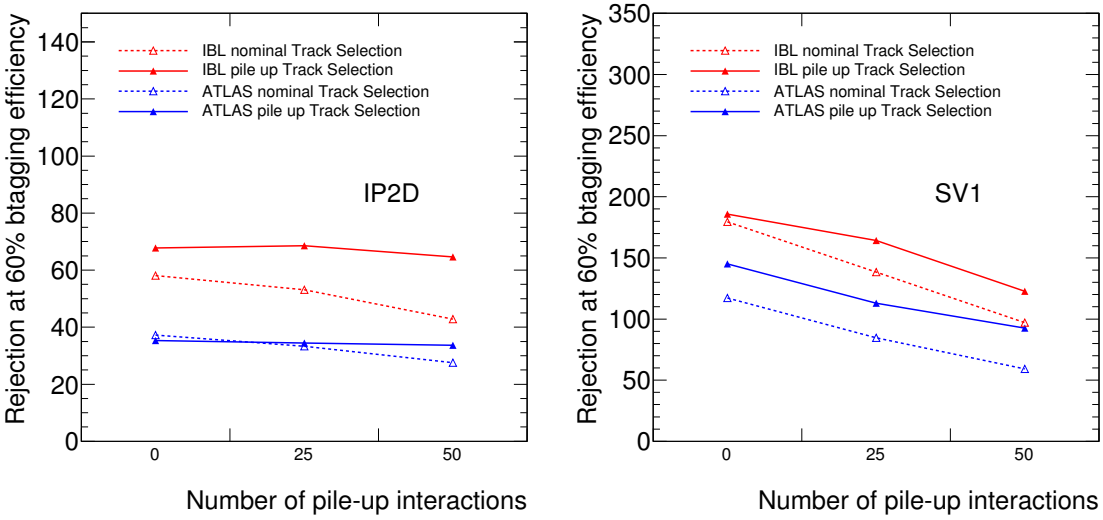

Figure 3.58: Light jet rejection in $t\bar{t}$ events for 60% b-jet efficiency as a function of the average number of pileup events, for the *IP2D* (left) and *SV1* (right) tagger.

3.7.3 Effects of detector defects and readout problems on performance

Due to the high dose of radiation received by the Inner Detector, hard (irreparable) failures in the *B*-layer and in the other layers will inevitably appear with time and can impact tracking and vertexing performance. Failures can affect single channels, or they can impact larger portions of the detector, for instance entire modules, Front-End (FE) chips ($1/16^{th}$ of a module), or all of the modules on a failed cooling loop. We already saw such examples in Fig. 3.11 in Sec. 3.3.4.2, showing maps of dead pixel silicon areas, and in the studies in Sec. 2.3.3.2 about the cooling fluid leaks. In August 2010, 3 cooling loops were considered as leaking (fortunately none of them on the *B*-layer) and 40 modules (including 6 on the *B*-layer) out of 1744 were considered as non-operational, for a total fraction of dead pixels of $\approx 3\%$.

Readout inefficiencies induced by high occupancies will affect the *B*-layer more than other layers (flux $\propto 1/R^2$) and would thereby limit particularly the b-tagging performance. Such inefficiencies will not result in modules with completely missing data, but only in losses of a fraction of the hits. Not

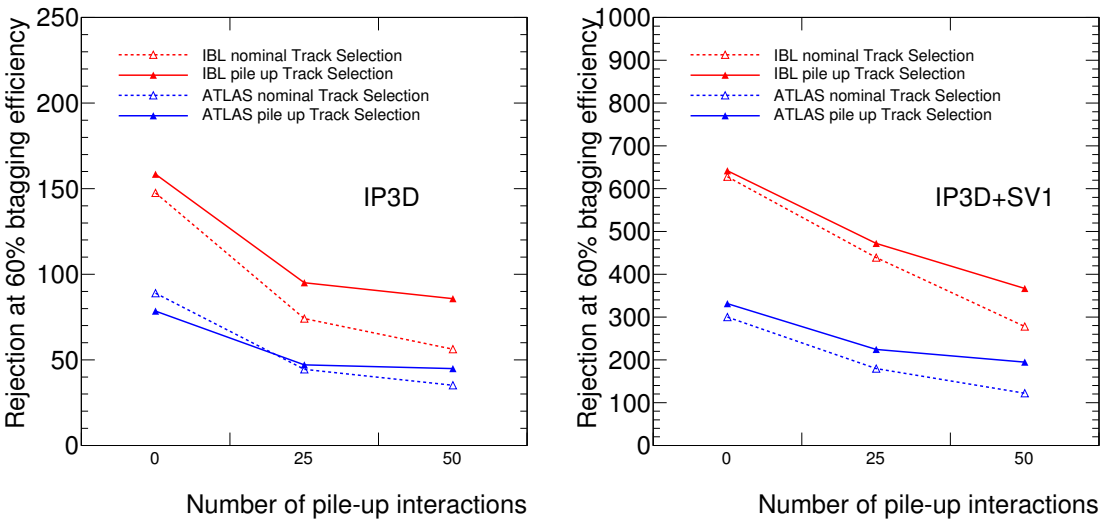

Figure 3.59: Light jet rejection in $t\bar{t}$ events for 60% b-jet efficiency as a function of the average number of pileup events, for the *IP3D* tagger (left) and for the combination *IP3D+SV1* (right).

knowing where hits are lost, the reconstruction software will not be able to recover the affected tracks. For known entire dead modules in the innermost layer, while the tracks themselves can be recovered due to the knowledge of their position, the loss in resolution, especially the loss in IP resolution cannot be recovered as the multiple scattering effects in the extrapolation from layer 1 through the B-layer to the interaction point completely dominates the IP resolution. Known dead modules in other layers than the B-layer can be handled in the reconstruction within limits, but if dead modules line up in too many layers this may lead to tracking inefficiencies even at low luminosity, because the number of layers available to constrain the tracking is reduced. With the IBL, it will be possible to recover tracks with missing hits on the existing B-layer and have a very precise IP resolution. This is part of the reason why the high luminosity track selection for IBL described in Sec. 3.7.2.1 allows for one 'hole' in the Pixels.

For all the considerations just made, different failure scenarios have been studied using dedicated simulation samples[30]:

- Loss of 10% of the clusters in the B-layer *e.g.* due to silicon inefficiencies at high-luminosity;
- A catastrophic failure of the full B-layer as a worse case scenario;
- Disabling 10% of the Readout Drivers in the SCT in order to emulate the effects of known dead modules in several layers in certain $\eta - \phi$ regions.

The first scenario leads to holes in the track reconstruction with IBL. For the two other scenarios, the dead modules are known and the reconstruction can attempt to allow for the failures by adapting the cuts.

Fig. 3.60 shows for all three scenarios the b-tagging performance for *IP3D* and *IP3D+SV1* as a function of the average number of pileup interactions using the high luminosity track selection. In all

[30]These samples were produced centrally by the IBL group.

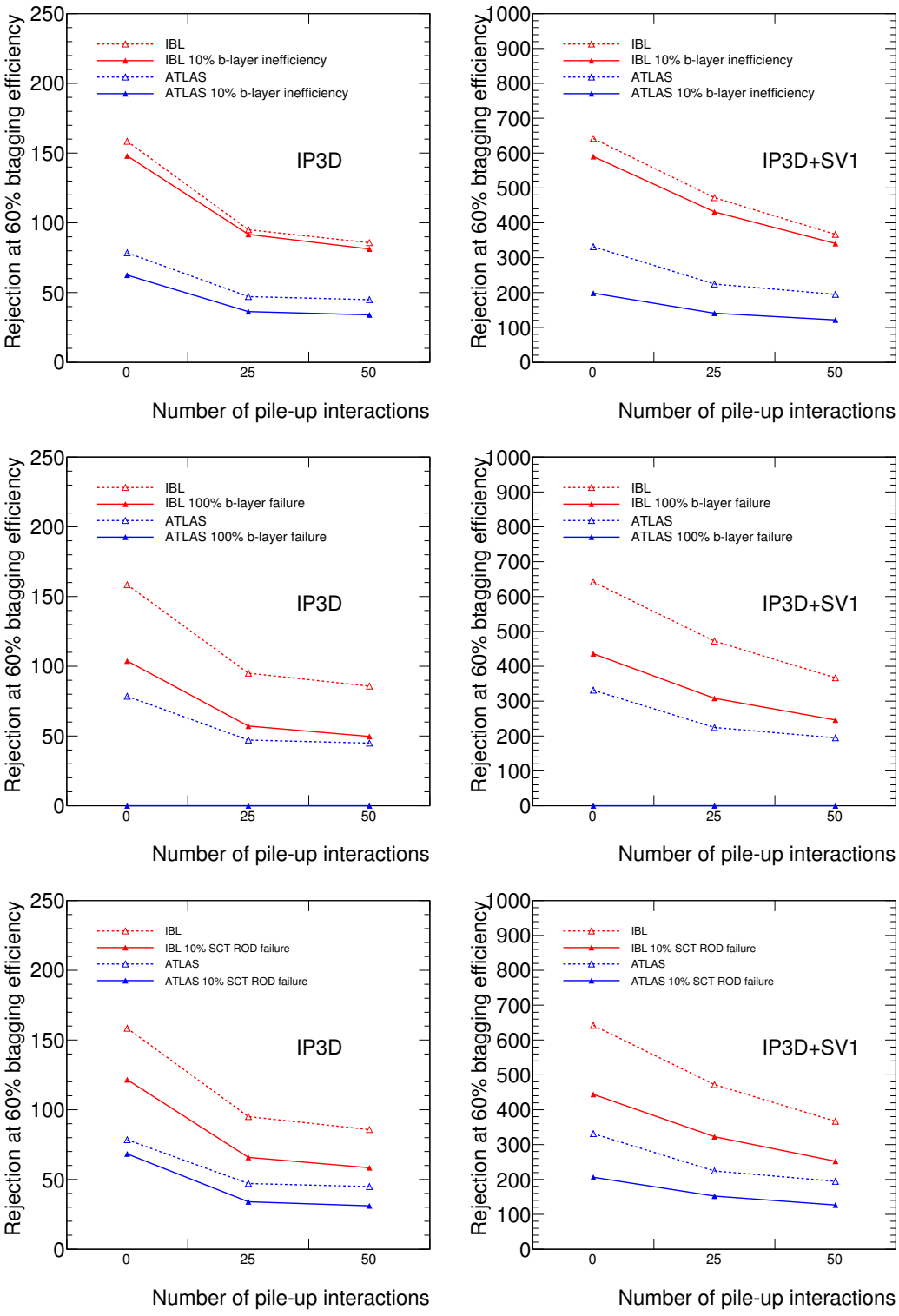

Figure 3.60: Light jet rejection in $t\bar{t}$ events for 60% b-jet efficiency as a function of the average number of pileup events, for the *IP3D* tagger (left) and for the combination *IP3D+SV1* (right), for the three simulated failure scenarios for a detector with and without IBL.

cases, the reconstruction with IBL not only recovers from the failures introduced in the simulation, but exceeds the performance of the current detector without such failures. Even for a complete *B*-layer failure, the IBL recovers good *b*-tagging performance. Without the IBL, one would need to fall back onto tracks with clusters in the second layer, at the price of a much reduced resolution and consequently some very limited light jet rejection. For the third scenario with SCT ROD failures, the IBL leads as well to significant improvements, essentially maintaining the performance of a fully-working ATLAS detector.

3.7.4 Summary

The IBL, with low mass and very close to the interaction point, is expected to improve the quality of the IP reconstruction for tracks and thereby the vertexing and the *b*-tagging performance. Making some justified simplifications (use of the true PV and truth-based jets) in order to disentangle the effect of some issues (that will be addressed later on), and applying 'anti-pileup' cuts, we have drawn some important conclusions: with the IBL, the reconstruction is robust against pileup and hard failures of modules in the *B*-layer and in other silicon layers. The *b*-tagging performance of ATLAS with IBL at $2 \times 10^{34} cm^{-2} s^{-1}$ pileup is similar to the current detector without pileup. In all studied scenarios with detector defects, the IP resolution is recovered and the IBL improves the *b*-tagging performance even in case of a complete *B*-layer failure. As a result, the IBL will lead to a better sensitivity of ATLAS during Phase I for signals in physics involving *b*-jets. It is currently under construction.

3.8 Conclusion

In this chapter, we have studied in the tracking performance of the ATLAS Inner Detector. In particular, we looked at the important features for *b*-tagging, namely the tracking and vertexing performance. The level of data-to-simulation agreement was observed to be very satisfactory at this stage of the experiment.

Building on this work, we contributed to commission, together with [107], the JetProb *early* tagger with the first 900 GeV and 7 TeV LHC data, which ended being usable by physics analyzes in ATLAS. We then concentrated on the commissioning of the high-performance taggers with the 330 pb^{-1} of the 7 TeV data, and we were responsible of the production of the reference histograms used by these taggers. This work led as well to the decision that the data-to-simulation agreement was sufficiently well understood, and that the algorithms could be calibrated in data to absorb the residual data-to-simulation discrepancies, and then used in physics analysis.

Finally, we have studied the effect of the installation of the IBL on the *b*-tagging performance, and concluded that it would allow ATLAS to maintain and improve its physics sensitivity with the coming LHC luminosity upgrades. This work played a significant role in the decision to build the IBL, which demonstrates the crucial importance of *b*-tagging in the ATLAS physics program.

Chapter 4

Search for new heavy top-like quarks

4.1 Introduction

This chapter presents a search for new physics looking for the pair production process:

$$pp \rightarrow t'\bar{t}' \tag{4.1}$$

where t' (or equivalently denoted u_4 in the following) is a hypothetical heavy chiral up-type quark of electric charge $2/3$, such as a fourth-generation quark, decaying into a W boson and a b-quark 100% of the time. We performed the search in the 4.7 fb^{-1} of proton-proton collisions at $\sqrt{s} = 7$ TeV recorded by the ATLAS detector in 2011 at the LHC. The next section gives an overview of the search, which was designed to improve the sensitivity to high-mass u_4 quarks compared to previous searches of ATLAS or similar experiments. This search was also interpreted in the framework of vector-like quarks signals.

In the context of this work, the author presented a poster about *ATLAS New Heavy Quark Searches* [133] at the International Conference *Physics at LHC*, Perugia, June 6–11th 2011, and gave a plenary talk about *ATLAS Exotic Searches* [134] at the International 2011 *Hadron Collider Physics* symposium (HCP-2011), Paris, France, November 14–18th 2011.

The final result of this work was obtained in collaboration with the ATLAS group of the IFAE Barcelona institute. This refers to the final analysis which was approved for publication, that we will describe from Sec. 4.7. Prior to this decision, we particularly worked on preliminary studies to show the feasibility of this novel analysis strategy. Later on, together with IFAE, we mainly focused on defining the final cuts of the analysis including the main systematic uncertainties, and on the statistical analysis. The final result was published in the scientific journal *Physics Letters B* [182].

4.2 Overview of the analysis

How does one discover a new particle with the LHC and a detector such as ATLAS ?

To attempt answering simply this question, let us have a look at the latest particle discovered at the LHC: the particle compatible with the SM scalar boson. Figure 4.1 shows a Feynman diagram of one of the cleanest signature of its decay: $H \to ZZ^{(*)} \to 4\ell$. Fig. 4.2 is one of the observations made at the LHC that contributed to the discovery [52].

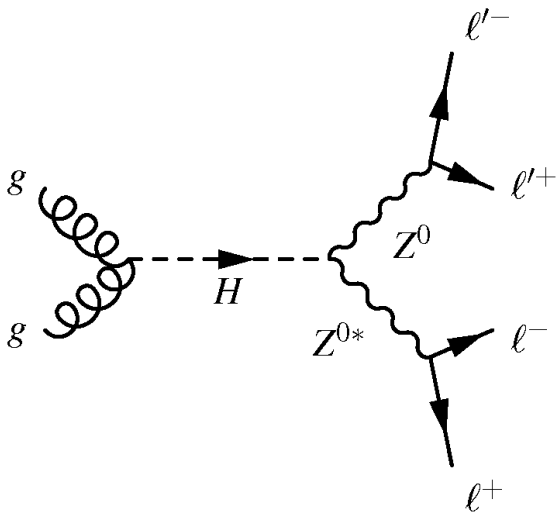

Figure 4.1: Feynman diagram of the SM scalar boson decay to a real and virtual Z boson, where they in turn each decay to leptons with opposite charge.

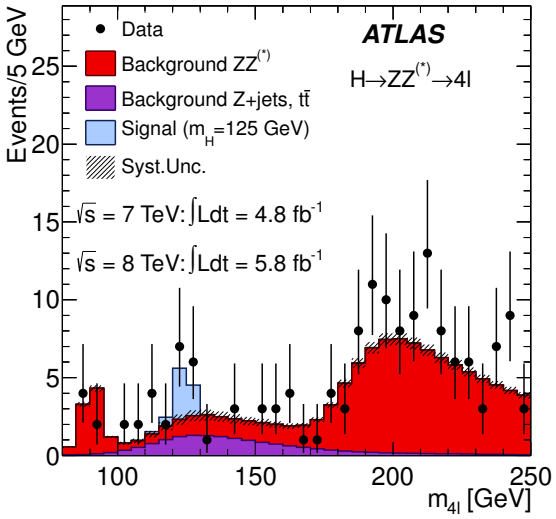

Figure 4.2: Distribution of the four-lepton invariant mass, m_{4l}, for the selected candidates, compared to the background expectation. The signal expectation for a SM scalar boson with $m_H = 125$ GeV is also shown. From [52].

It shows the distribution of the mass of particles reconstructed from two selected pairs of isolated leptons, each of which being comprised of two leptons with the same flavor and opposite charge. The colored histograms are the estimation[1] that one would expect, given the amount of LHC data recorded, for the signal, in light blue, and for other known SM processes that could produce the same kind of signature in the detector as the signal, called 'background' processes, and displayed in purple and red. The shaded area on top of the total background distribution is an estimation of the accuracy on these predictions, in the form of statistical[2] and systematic[3] errors. The black points are the *real* ATLAS data, shown together with the statistical errors in each bin.

After building the kind of distributions above-mentioned, that can play the role of *test statistic*, an hypothesis test (cf. Sec. 3.2.7.2) is generally performed. *E.g.*, if one observes data:

- *not compatible* with the background estimation, one wants to test the $H_0 \equiv$ *Background(B)*

[1] Derived from MC simulation or data-driven techniques.

[2] The statistical (or random) errors come simply from the inability of any measuring device with a non-infinite number of results to give infinitely accurate answers.

[3] Systematic errors are more in the nature of mistakes, which will not necessarily decrease with an higher number of measurements.

only hypothesis, against the $H_1 \equiv$ *Signal(S)+Background* hypothesis. Typically, claiming a discovery requires a level of significance (*i.e.* a probability to reject incorrectly the SM) below $\alpha = 2.9 \cdot 10^{-7}$ for the observed data.

- *not compatible* with the signal prediction, one wants to test the $H_0 \equiv B + \mu_0 S$ hypothesis, against the $H_1 \equiv B + \mu S, \mu < \mu_0$ hypothesis, in order to know what is the hypothesis (or equivalently what μ_0) for which the compatibility with the observed data is lower than a given 'confidence' level (CL) α. Typically, one asks for $\alpha = 5\%$, and μ, the 'quantity of signal', usually equals σ/σ_{SM}. By construction, μ_0 is a 95% CL upper limit on the signal strength. In other words, this test allows to exclude a given quantity of expected signal at a certain CL, when one sees observations compatible with the background only hypothesis.

To summarize, besides constructing the LHC and ATLAS and maintaining their operation, making a discovery (or excluding new physics) is equivalent to perform the following tasks:

- *Construct a Test statistic*: This can be seen as the *core* of the analysis. It consists mainly of reconstructing all the physical objects (cf. Sec. 4.4), applying appropriate event selections, and forming a discriminant (or *test statistic*) that will allow to select the signal with high-efficiency and reject the backgrounds as much as possible. In our case, this will be the reconstructed mass of the heavy quark produced[4] (cf. Secs. 4.6 and 4.7);
- *Signal and backgrounds estimation*: This will be detailed in our case first in Sec. 4.5 and then looking at 'control' regions in Sec. 4.8;
- *Systematic uncertainties estimation*: This task tries to evaluate by how much would vary the signal and backgrounds predictions due to any kind of possible measurement *errors* (cf. Sec. 4.9);
- *Statistical analysis* or *Hypothesis testing*: This last step takes as inputs the predicted distributions of the *test statistic* for the signal and the backgrounds, together with their related uncertainties, and tries to quantify how *certain* we are of seeing (or not seeing) new physics (cf. Sec. 4.10).

4.3 Analysis strategy

4.3.1 Choice of the lepton-plus-jets channel

As introduced previously, we assume in this search that the two u_4 quarks produced in Eq. 4.1 decay 100% of the time to a W boson and b-quark:

$$pp \rightarrow u_4\bar{u}_4 \rightarrow W^+bW^-\bar{b} \tag{4.2}$$

Regarding the decay modes of the two W bosons produced in process (1), we are searching for the final state where one W boson decays $leptonically$ into a lepton and a neutrino, while the other decays $hadronically$ into two quarks. This is illustrated in Fig. 4.3, and would happen $\sim$30% of the time. Experimentally, this relies on the detection of large missing transverse energy, jets and a lepton in the event, which will be described in details in the next sections. The latter requirement is a very clean signature in the detector, that acts to suppress by many order of magnitudes the level of the background from QCD multijet events (see Sec. 4.5.3.2 for a detailed description). This so-called $lepton + jets$ channel is widely-known to be a good compromise between statistics of selected events and background rejection.

[4] Precisely, the *test statistic* will be a function of the reconstructed mass, called a 'Likelihood Ratio'.

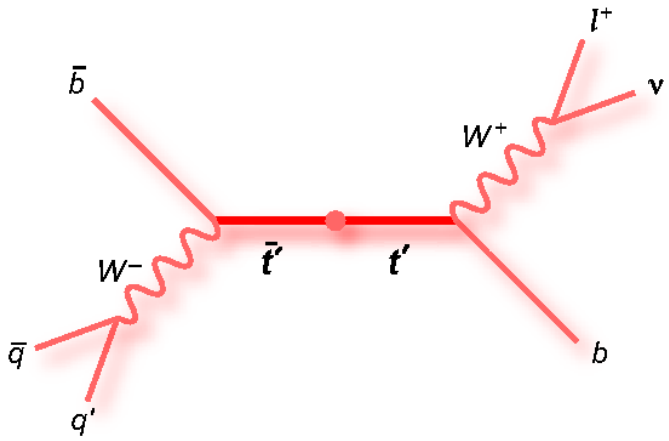

Figure 4.3: Feynman diagram of the kind of t' pair decay we are looking for, where one W boson decays *hadronically* into two jets, while the other decays *leptonically* into a lepton (here a muon) and a neutrino.

4.3.2 Changing the u_4 search paradigm

First direct searches for fourth generation quarks have been conducted at the Tevatron. As $u_4\bar{u}_4$ production leads to the same final states as $t\bar{t}$ production[5], a mass reconstruction of the u_4 quark is necessary. For u_4 masses higher but reasonably close to the top quark mass, a search strategy similar to the original top mass determination was well motivated, and the CDF and D0 collaborations at the Tevatron respectively claimed that its mass could not be lower than 335 GeV [41] and 285 GeV [42] at the 95% confidence level.

Since the start of the LHC, ATLAS and CMS have conducted similar kind of searches, which led respectively to exclude u_4 masses up to 404 GeV [44], using 1 fb^{-1} of data, and 570 GeV [138], using 5 fb^{-1}. The most physically meaningful results of these two analyzes can be found in Fig. 4.4, which shows the final reconstructed mass distributions. Both searches have been conducted in the lepton+jets channel, and assume BR$(u_4 \rightarrow bW) = 100\%$. Searching for short-lived down-type d_4 quark in the signature of trileptons and same-sign dileptons, CMS also excluded $m_{d_4} < 611$ GeV with 4.9 fb^{-1} of data assuming BR$(d_4 \rightarrow tW) = 100\%$ [139].

However, the higher the mass of the fourth generation quarks, the lower the cross-section. For example, the production cross-section of a 600 GeV u_4 quark is $\approx$1300 times lower than the $t\bar{t}$ cross-section, making the search very challenging for the amount of data recorded in 2011. This can be understood in essence by looking at the mass distributions in Fig.4.4, where one can clearly see that the signal starts to be dominated by the $t\bar{t}$ signal in the tail of the distribution for quark masses above 400-500 GeV. In order to perform the search with the currently available dataset, the search strategy inherited from Tevatron had to be revised, as suggested in particular in Refs. [142], [143], [144] and [145].

[5] $t\bar{t}$ production has the same Feynman diagrams as $u_4\bar{u}_4$ production, and given that we assume $BR(u_4 \rightarrow Wb) = 1$, it also shows the same decay modes.

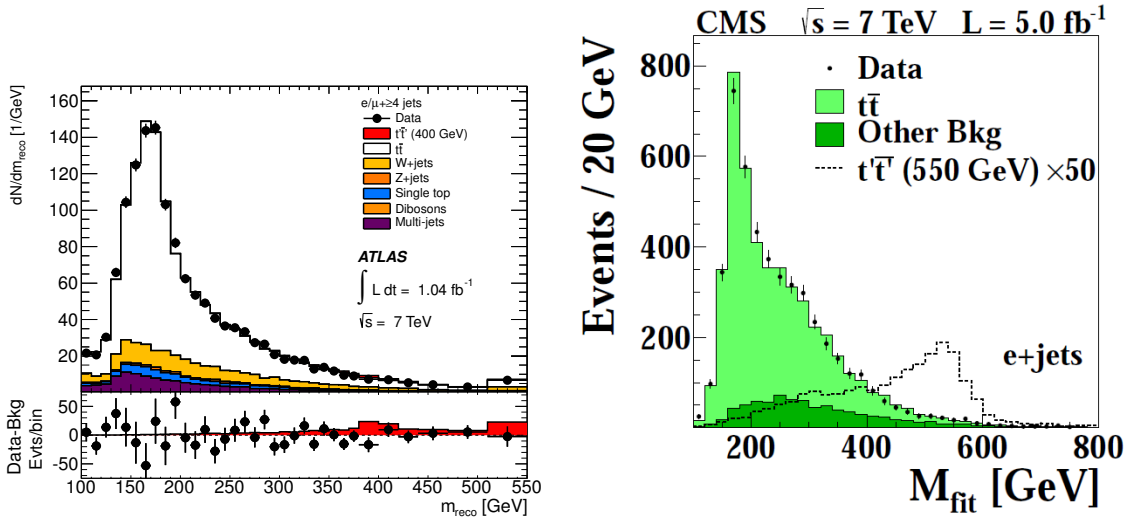

Figure 4.4: Examples of mass distributions obtained from (left) the ATLAS 1fb^{-1} analysis [44], and (right) the CMS 4.7fb^{-1} analysis [138], both in the lepton-plus-jets channel. Note that the signal strength is multiplied by a factor 50 in the CMS search.

4.3.3 Features of the boosted scenario for u_4 search

In this work, we improve upon the previous searches by taking advantage of the kinematic differences that exist between $t\bar{t}$ and $u_4\bar{u}_4$ decays, which are fortunately more and more pronounced as the u_4 quark mass increases. Such differences are illustrated in this section, while the detailed selection and the mass reconstruction strategy will be explained in Secs. 4.6 and 4.7.

Harder decay products The first feature we exploit is the higher transverse energy of u_4 decay products compared to those of the top quark, which arises from the higher mass of the u4. This is illustrated in Monte-Carlo simulation in Fig. 4.5, which shows the distribution normalized to unity of the transverse energy of all objects (the transverse missing energy, the lepton and jets p_T) in the event, a variable called H_T. Fig. 4.6 shows the true p_T of the b-quark originating from the initial u_4 quark, for cases where the W boson produced in $u_4 \to bW$ decays hadronically. Both variables can be seen to have a high discrimination power to distinguish the u_4 signal from the $t\bar{t}$ background.

Collimation of decay products Another important feature crucial in this search is that the W bosons produced will have a much greater boost for the u_4 signal than for the $t\bar{t}$ background, which is sketched in Fig. 4.7. This is illustrated in Monte-Carlo simulation in Fig. 4.8, which shows the distributions normalized to unity of the true ΔR between the two quarks stemming from the decay of the hadronic W boson, as a function of the p_T of the W boson, for the $t\bar{t}$ background and for the u_4 signal. It can be seen that, for the signal, the p_T of the W boson is on average significantly higher, and its decay products are more collinear with its direction. From this simple observation, we can already derive the most important feature of the analysis we are presenting: if one finds a technique that manage to reconstruct a high-p$_T$ W boson, it will select the u_4 signal with high efficiency, while selecting the tails of the $t\bar{t}$ distribution, hence *naturally* rejecting this background. How to reconstruct these W bosons will be detailed extensively in Secs. 4.6 and 4.7.

The fact that decay products from the W bosons are more collimated can also be exploited on the

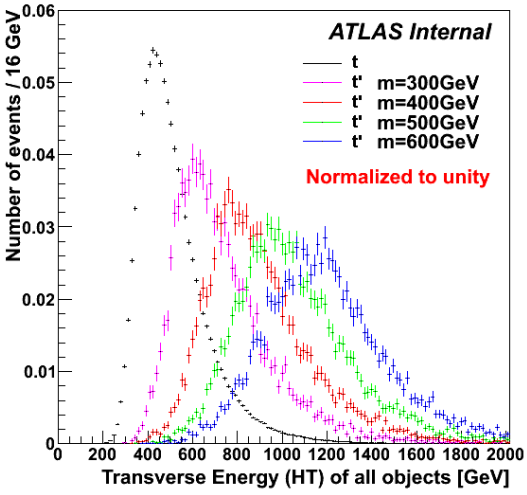

Figure 4.5: Distribution of the true H_T variable (cf. text) for the $u_4\bar{u}_4$ signal events assuming different masses of the u_4 quark, and for $t\bar{t}$ events (dominant physical background). All distributions are normalized to unity.

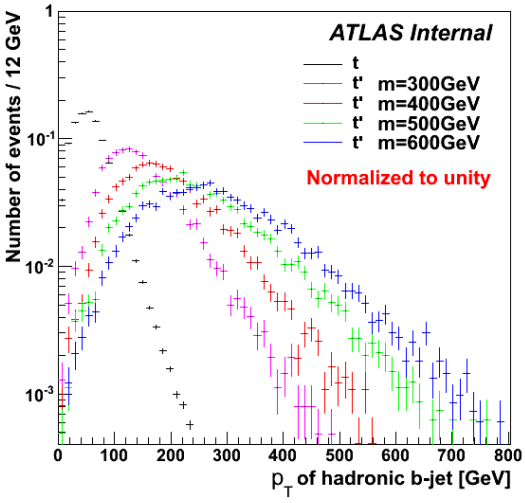

Figure 4.6: Distributions of the true p_T of the b-quark produced together with a W boson that decayed hadronically, for the top quark, and for different masses of the u_4 quark. All distributions are normalized to unity.

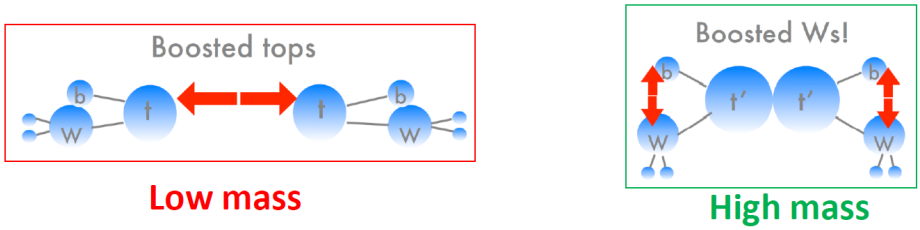

Figure 4.7: Sketch illustrating the differences between low and high mass quark decays.

leptonic side: Fig. 4.9 shows the distribution normalized to unity of the true ΔR between the lepton and the neutrino stemming from the decay of the leptonic W boson, for the $t\bar{t}$ background and for the u_4 signal. We are using this discriminating variable in a way that will be described in Sec 4.7.4.

Isolation of W bosons and their associated b-quark Finally, another important property of the u_4 decays is that the W bosons and their associated b-quark will be more isolated from each other (more 'back-to-back') than in top decays, because in the high-H_T regime the top quarks have large boost and their decays products have smaller ΔR. This can be seen in Fig.4.10, which shows the distribution normalized to unity of the true ΔR between the hadronic W boson and its associated b-quark, for the $t\bar{t}$ background and for the u_4 signal. As b-jets can also come close to a W boson because they are originating from the decay of the *other* heavy quark (top or u_4), we will see in Sec 4.6 that requiring to have W-jets and b-jets isolated from other objects will greatly help to reject further the $t\bar{t}$ background, at the expense of a reasonable loss in signal acceptance.

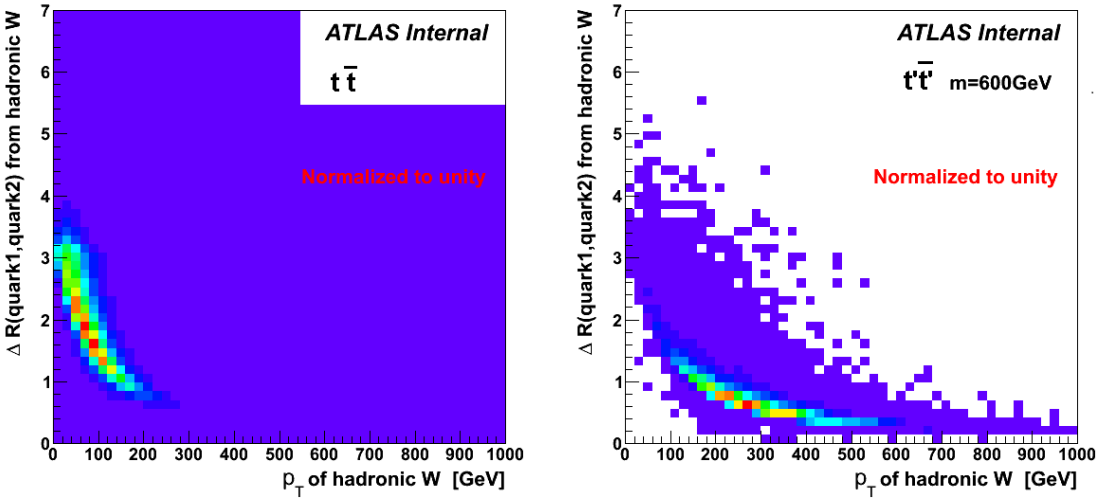

(a) $t\bar{t}$ background

(b) $u_4\bar{u_4}$ signal with $m_{u_4} = 600$ GeV

Figure 4.8: Distributions of the true ΔR between the 2 quarks stemming from the decay of the hadronic W boson, as a function of the p_T of the W boson (in GeV), for (a) the main background and (b) for the signal. All distributions are normalized to unity.

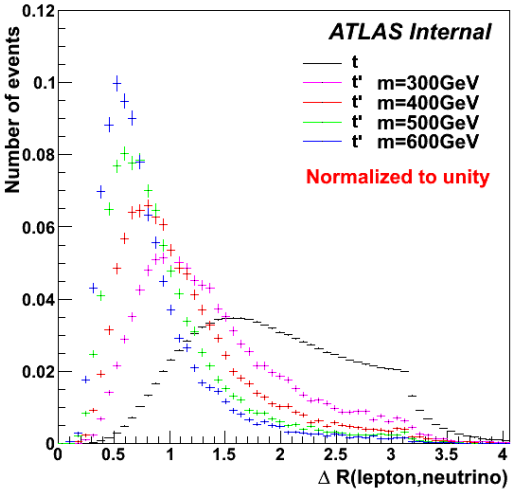

Figure 4.9: Distribution of the true ΔR between the lepton and the neutrino from the decay of the leptonic W bosons, for the top quark background, and for the signal with different masses of the u_4 quark. All distributions are normalized to unity.

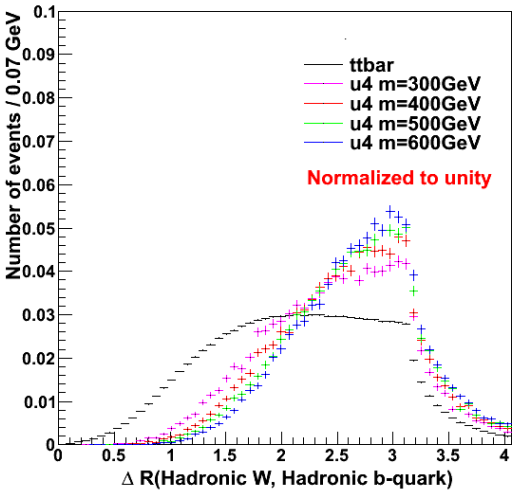

Figure 4.10: Distribution of the true ΔR between the hadronic W boson and its associated b-quark, for the top quark background, and for the signal with different masses of the u_4 quark. All distributions are normalized to unity.

4.3.4 Summary of discriminating options

To conclude this section, we can say that if Nature gave us new heavy quarks, she also gave us three important features to exploit in order to find it:

- The u_4 decay products are harder, opening the possibility to cut on the H_{T} variable, or on the p_T of the b-jets. While not necessary if one is not assuming $\mathrm{BR}(u_4 \to Wb)$ to be 100%, this obviously implies in some sense the possibility to tag beforehand one or two of the b-jets of the event. Fortunately, we have now at our disposition the high-performance taggers that we commissioned in chapter 3.
- The decay products from W bosons are much more collimated for u_4 than for $t\bar{t}$, opening the possibility to reconstruct explicitly W bosons (or 'W-jets), and to exploit the opening angle between the lepton and the neutrino of the events.
- The W bosons are more isolated from their associated b-jets, opening the possibility to exploit the opening angle between the W-jets and the b-jets.

While this will be discussed in detail later, we can however already see that managing to reconstruct the lepton, the neutrino, the W bosons and the b-jets, we have all the ingredients to reconstruct the mass of the originating u_4 quarks very easily, and without requiring the use of complex (and computationally heavy) fitting algorithms usually used for top searches.

4.4 Definition of physical objects and event pre-selection

We will now describe how are reconstructed the various *physics* objects that we will use in our search, and the first level of event selection that we apply.

4.4.1 Primary vertex

The determination on an event-by-event basis of the location of the point where the hard-scattering of two protons occurred, referred to as the primary vertex, is particularly important for an accurate reconstruction of several of the objects used in this analysis, in particular for b-tagging as we know. The number of reconstructed primary vertices is substantially larger than one in the presence of pile-up events: the average number of primary vertex candidates per event was ~ 7 in 2011 data. The strategy is to choose the primary vertex candidate which maximizes $\sum_{\mathrm{tracks}} {p_T}^2$.

4.4.2 Electrons

4.4.2.1 Identification

Electrons are reconstructed up to a pseudorapidity of $|\eta| < 2.47$ by matching clusters of deposited energy in the EM calorimeter with reconstructed tracks in the Inner Detector. The candidates must fulfill $|\eta_{cluster}| < 2.47$ (excluding the transition region of $1.37 < |\eta_{cluster}| < 1.52$) and $E_{\mathrm{T}} > 25$ GeV (where $E_{\mathrm{T}} = E_{cluster}/\cosh(\eta_{track})$). In addition, electrons are required to satisfy the TIGHT++ criteria defined by the e/γ Working group, which include stringent selection cuts on calorimeter, tracking and combined variables that provide good separation between isolated electrons and jets. To suppress further the QCD multijet background, tight isolation cuts are imposed on the electrons using both calorimeter (cone size of $\Delta R < 0.2$) and track isolation ($\Delta R < 0.3$). The cuts chosen correspond to the 90%-efficiency operating point. Further details can be found in Ref. [149].

4.4.2.2 Trigger matching

The offline electron candidates are required to match with an electron trigger as will be defined in Sec. 4.4.9.1. The matching is geometric: $\Delta R(e_{\text{offline}}, e_{\text{trigger}_{EF}}) < 0.15$.

4.4.2.3 Corrections

Several scale factors are applied to correct various efficiencies in simulation with respect to what is measured in data, in particular for the trigger efficiency, the identification efficiency and the isolation cut efficiency. The scale factors have been measured using tag-and-probe techniques mostly on $Z \rightarrow ee$ data samples. The identification scale factors range from 0.8 to 1.2, while for isolation the most extreme scale factor is 0.95 for events with large (12 or more) number of primary vertices. Further details about the binning and the size of these factors can be found in Ref. [149].

4.4.3 Muons

4.4.3.1 Identification

A combination of track measurement from the inner detector and the muon chambers form muon candidates. The refitted track, using the complete track information from both detector systems, is required to satisfy $p_T > 20$ GeV and $|\eta| < 2.5$. The muon candidates are required to fulfill all the track cuts defined by the Muon Combined Performance group. In addition, three isolation cuts are applied, allowing a rejection factor of 5.5 against QCD multijet background (mostly from heavy-flavor production, as seen in Chap. 3). Two of these cuts are based on the amount of energy around the muon candidate in a cone of $\Delta R = 0.3$: one based on calorimeter deposits (< 4 GeV required) and the other one on the Inner Detector tracks (< 2.5 GeV). The third cut requires the muon to be away ($\Delta R > 0.4$) from any jet having $p_T > 25$ GeV and $|JVF| > 0.75$ (see later). Further details can be found in Section 1 of Ref. [149].

4.4.3.2 Trigger matching

The offline muon candidates are required to match with a muon trigger as will be defined in Sec. 4.4.9.1. The matching criterion is the same as for the electrons.

4.4.3.3 Corrections

As for electrons, an extensive set of corrections are applied to correct for (minor) discrepancies between simulation and actual data. All these corrections are implemented following the standard procedure recommended by the Top reconstruction group. The scale factors are derived from tag-and-probe measurements as well. Further details about these factors can be found in Ref. [149].

4.4.4 AntiKt4 Jets

4.4.4.1 Reconstruction, jet-vertex fraction and mass

Jets are reconstructed with the anti-k_t algorithm ($R = 0.4$) using EM-scale topological clusters in the calorimeters. A pile-up subtraction scheme that accounts for the effect of both in-time and out-of-time pile-up is applied to jets at the EM scale. This correction is parametrized according to the number of primary vertices in an event and the number of average interactions in a luminosity block, in bins

of jet pseudorapidity. The jets are then calibrated to the hadronic energy scale, using a p_T- and η-dependent correction factor obtained from simulation (EM+JES scheme). After this calibration, the jets are required to have a $p_T > 25$ GeV.

Some jet candidates are discarded by a standard cleaning procedure aiming at removing fake jets produced by a variety of sources: hardware problems, beam-gas interactions or cosmic rays.

To select jets which originate from the hard-scatter interaction and avoid jets from minimum-bias events piled-up on top of it, the jet-vertex fraction (JVF) (which was introduced in Sec. 3.7.2.3) is used and all the jets considered in the analysis are required to fulfill $|JVF| > 0.75$.

Since the anti-k_t algorithm relies on full 4-vector kinematics, the jets it finds have a meaningful mass[6]. This property will be used in Secs. 4.6 and 4.7 in the so-called CHANNEL 1, where the decay products of the hadronic W are reconstructed as a single jet.

4.4.4.2 Overlap with leptons

A standard procedure designed by the various 'performance' groups is applied to remove overlaps between particles reconstructed as different physical objects, hence removing *fake* particles.

Muons Muons inside jets are mostly from semi-leptonic heavy flavor decays and thus not the muons we want to select. Isolated muon candidates overlapping ($\Delta R < 0.4$) with a selected jet candidate are hence discarded.

Electrons Electrons are almost always reconstructed also as a jet. Jets too close ($\Delta R < 0.2$) to a good electron candidate are hence removed. After this jet-electron overlap removal, if there is another jet found within $\Delta R < 0.4$ of an electron and with $p_T > 20$ GeV, the electron is discarded.

4.4.4.3 b-jet identification

The identification of b-jets is based on the MV1 algorithm. Among the algorithms presented in Sec. 3.5.1.5, it is the one showing the highest performance. In Sec. 4.6, we will use the 60% operating point, which is designed to tag 60% of the actual b-jets in $t\bar{t}$ events, but for the final analysis, we will use the 70% operating point. At this efficiency, the average rejection of light jets having a (p_T,η) spectrum relevant for $t\bar{t}$ physics and with $p_T > 15$ GeV is 140.

However, the b-tagging performance is strongly dependent of the jet p_T, as shown on Figs. 4.11 and 4.12. It is optimal for $p_T \sim 120$ GeV then falls slowly beyond 120 GeV, while it drops sharply as the p_T decreases below ~ 80 GeV. As shown on Fig 4.6, the p_T spectrum of the signal b-jets is more favorable in this respect than the one of the main $t\bar{t}$ background. Therefore, in addition to reject W+jets and QCD events which is the prime motivation to use b-tagging in the analysis, the b-tagging selection should also improve the discrimination against top events.

As described in Sec. 3.6, simulation efficiencies in Monte Carlo for b quarks have to be corrected by p_T-dependent scale factors $\varepsilon_{data}/\varepsilon_{MC}$. Unluckily, the calibrations based on $t\bar{t}$ decays (with lower uncertainties and extending to higher jet-p_T), were not available in the timescale of our analysis, so we used the ones based on p_T^{rel} and *System 8* [128]. These scale factors are of the order of 0.91-0.98 (cf. Fig. 3.53) for b-quarks, and about ~ 1.1 for c quarks, whereas the light jet efficiency has to be scaled up by a factor of ~ 1.2.

[6]The jet four-vector is obtained by summing the four-vectors of the (mass-less) clusters in the calorimeter associated with jets. As the jet components have non-zero opening angle, even jets that result from the hadronization of mass-less gluons or light quarks acquire a non-zero mass.

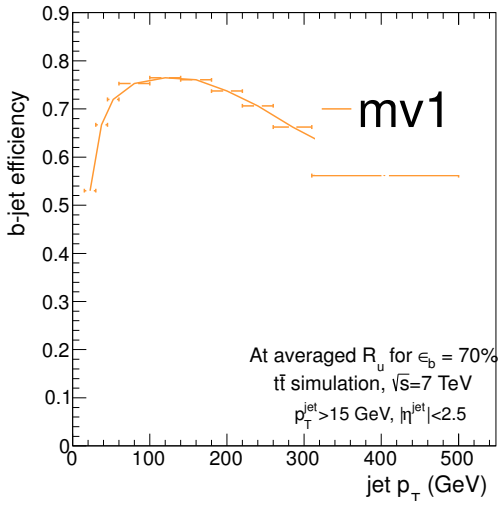

Figure 4.11: Efficiency to tag actual b-jets with the MV1 tagging algorithm at the 70% operating point, as a function of the jet p_T.

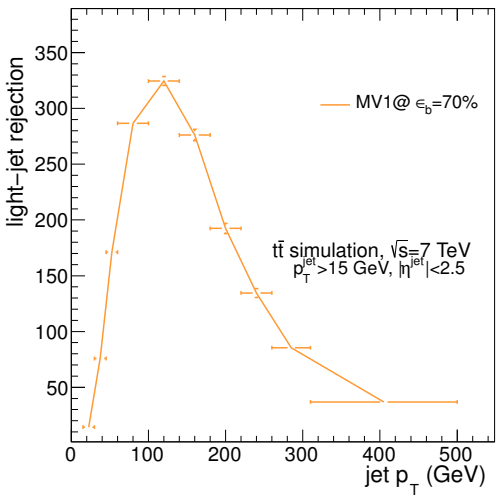

Figure 4.12: Light-jet rejection with the MV1 tagging algorithm at the 70% operating point, as a function of the jet p_T.

The uncertainties applied on these scale factors will be discussed in Sec. C.1 and more information is available in Ref. [149] and references therein.

4.4.5 AntiKt10 Trimmed Jets

A second set of jets will be used in Sec. 4.6 with a radius parameter $R = 1.0$. Such a large cone size will appear particularly useful to capture all the decay products of highly boosted W bosons, and reconstruct the W-jet of the events. Jet *trimming* was applied to this jet collection [146], which is a procedure designed to mitigate the sources of contamination in jets initiated by light partons, such as initial state radiation, multiple interactions, and event pileup. This is especially useful for jets with such big radius.

4.4.6 Missing energy

The magnitude $E_{\mathrm{T}}^{\mathrm{miss}}$ of the missing transverse momentum is constructed from the vector sum of the energy deposits in calorimeter cells associated with topological clusters. Calorimeter cells are associated with a parent physics object in a chosen order: electrons, jets reconstructed with $R = 0.4$, and muons, such that a cell is uniquely associated with a single physics object. Cells belonging to electrons are calibrated at the electron energy scale, and double counting of cell-energies is avoided, while cells belonging to jets are taken at the corrected energy scale used for jets. Finally, the track p_T of muons passing the event selection is included, and the contributions from any calorimeter cells associated with the muons are subtracted. The remaining clusters not associated with electrons or jets included at the EM energy scale.

The exact definition, as well as information on $E_{\mathrm{T}}^{\mathrm{miss}}$ resolution and data/MC comparisons can all be found in Ref. [149].

4.4.7 Leptonic W boson

In order to reconstruct the leptonic W boson of the event, we define the neutrino four-momentum using the E_T^{miss} components in X and Y and computing the p_Z starting from the assumption that

$$P_W^2 = P_l^2 + P_\nu^2 = M_W^2. \tag{4.3}$$

Working out this equation we are left with

$$\alpha = \frac{1}{2}(M_W^2 - M_l^2) \tag{4.4}$$

$$\beta = \alpha + p_{X_\nu} p_{X_l} + p_{Y_\nu} p_{Y_l} \tag{4.5}$$

$$\gamma = -\frac{\beta^2 - E_l^2 \sqrt{p_{X_\nu}^2 + p_{Y_\nu}^2}}{E_l^2 - p_{Z_l}^2} \tag{4.6}$$

$$\lambda = 2\beta \frac{p_{Z_l}}{E_l^2 - p_{Z_l}^2} \tag{4.7}$$

$$\delta = \lambda^2 - 4\gamma \tag{4.8}$$

which gives two possible solutions for the Z component of the neutrino momentum:

$$p_{Z_\nu} = \frac{\lambda \pm \sqrt{\delta}}{2}. \tag{4.9}$$

If no solution is found (negative discriminant), we assume that the neutrino has the same η than the lepton. This approximation is justified by the considerations made in Sec. 4.3.3 about the collimation of the lepton and the neutrino in the regime of high u_4 mass.

If more than one solution is found, only one of them will be chosen, as will be explained in Sec. 4.6.3.

4.4.8 H_{T} variable

An important variable used in the analysis is H_{T}, the scalar sum of the transverse momenta of the objects in the event. In this analysis, the following definition is adopted:

$$H_{\text{T}_4} = E_{\text{T}}^{\text{miss}} + {p_T}^{\text{lepton}} + \sum_{j=1}^{4} {p_T}_j^{\text{jet}}$$

where the jets are ordered by decreasing p_T. Only the first four leading jets are used because we observed better data-to-simulation agreement removing the softer jets from the original H_{T} definition that included all jets, and this was not decreasing significantly its discriminating power.

4.4.9 Event pre-selection

Now that we know how to reconstruct the basic objects of our search, we need to define in detail how the events are selected. We will describe here a first preselection, that will allow us to come close enough to our signal region and to study (in the next sections) better ways to select specifically our signal and reconstruct the mass of the new quark we are searching for.

4.4.9.1 Data sample

The data were collected in 2011 from proton-proton collisions at $\sqrt{s} = 7$ TeV delivered by the LHC and are classified in different periods. The ones of interest for this analysis range from period B to period M. The corresponding integrated luminosities are shown on Table 4.1. Before selecting the good runs fulfilling the detector integrity requirements, the total integrated luminosity collected by ATLAS for 2011 is 5.2 fb^{-1}.

Period	B	D	E	F	G	H	I	J	K	L	M
$\int \mathscr{L} dt$ (pb^{-1})	17	179	50	152	560	278	399	233	660	1568	1121

Table 4.1: Integrated luminosities collected by ATLAS for each data taking period of 2011.

Good run list Only data collected during luminosity blocks corresponding to stable beam periods in which all sub-detectors were fully operational are used, following the Good Runs List established by the Top group. The data fulfilling the GRL requirements correspond to an integrated luminosity of 4.7 ± 0.2 fb^{-1}.

Triggers The presence of leptons in the final state we are looking for is the cleanest signature in the detector. For this reason, we select events using high-p_T lepton triggers. We define two 'channels' for the analysis: the muon and electron channels, for events triggered by a muon or an electron, respectively. The triggers used are the single lepton triggers with the lowest p_T thresholds that are un-prescaled:

- For the muon channel: corresponding to the `EF_mu18`[7] trigger for periods B to I, and to the `EF_mu18_medium`[8] trigger for latter periods.
- For the electron channel: corresponding to the `EF_e20_medium`[9] trigger for periods B-H and `EF_e22_medium`[10] for periods I-K. For periods L-M, the electron trigger was a logical OR of `EF_e22vh_medium1`[11] and `EF_e45_medium1`[12].

These triggers are available in the simulation.

4.4.9.2 Pre-Analysis cuts

- The event must pass our trigger requirements at the Event Filter described just previously.
- The chosen primary vertex of the event must have > 4 tracks associated to it.
- The event must have exactly one good electron or exactly one good muon.

[7] This trigger requires $p_T^\mu > 10$ GeV at the Level 1, and $p_T^\mu >\sim 18$ GeV at the Event Filter.
[8] This trigger requires $p_T^\mu > 11$ GeV at the Level 1, and $p_T^\mu >\sim 18$ GeV at the Event Filter.
[9] This trigger requires $p_T^e > 14$ GeV at the Level 1, and $E_T^e > 20$ GeV at the Event Filter.
[10] This trigger requires $p_T^e > 16$ GeV at the Level 1, and $E_T^e > 22$ GeV at the Event Filter.
[11] 'vh' means that η-dependent thresholds were applied at L1, and that an hadronic leakage requirement was applied, both intended to reduce the L1 rate below an acceptable rate while rejecting backgrounds.
[12] This trigger requires $p_T^e > 30$ GeV at the L1, and $E_T^e > 45$ GeV at the EF. It was added to re-gain some of the efficiency at high-p_T that is cut out because of the 'h' requirement of trigger `EF_e22vh_medium1`.

- Electrons and muons cannot overlap: we reject the event if the electron and muon share an Inner Detector track.
- The event must have a significant amount of missing transverse energy ($E_{\mathrm{T}}^{\mathrm{miss}}$): $E_{\mathrm{T}}^{\mathrm{miss}} > 35$ (20) GeV in the electron (muon) channel. The requirement of $E_{\mathrm{T}}^{\mathrm{miss}} + m_{\mathrm{T}} > 60$ GeV is also added, where m_{T} is the transverse mass [13] of the lepton and $E_{\mathrm{T}}^{\mathrm{miss}}$. Both cuts are intended to reject some of the QCD multijet background.
- The event must also pass some additional (ATLAS specific) data quality cuts[14].

4.5 Signal and backgrounds predictions

Before studying how to apply finer selections to our search, we will now describe the various signal and backgrounds samples to use for the MC prediction of this analysis.

4.5.1 Monte Carlo software version

All the Monte Carlo samples used in this analysis belong to the so-called MC11c production round done by the ATLAS production group [147]. The MC11c tag refers to a given set of software versions (event generation, simulation, reconstruction), detector conditions and pile-up emulation. The most important features of MC11c are briefly described in the following. The common parameters used at the event generation (particle masses, etc) can be found in Ref.[177].

To emulate the varying detector conditions and amount of pile-up events across the full 2011 data sample, all the Monte Carlo samples are simulated in 4 chunks with different conditions and distributions of the number of interactions per bunch crossing in each.

The most important conditions changes that are emulated in the simulated samples are: the number of dead modules in the Tile calorimeter, the number of unavailable Front-End-Boards for the LAr calorimeter, the number of dead pixel modules, and changes in the trigger configuration.

For the pile-up simulation, the minimum bias events generated with PYTHIA[15]. For periods B-H, the mean number of interactions per bunch crossing is $\mu = 6.3$, it goes up to $\mu = 11.6$ for periods L-M.

4.5.2 Signal

Chiral fourth generation The $u_4\bar{u}_4$ samples are generated using PYTHIA[16]. The $u_4 \to W^+b$ decay mode is considered here, and samples were generated separately for the following values of the u_4 mass: 400, 450, 500, 550, 600, 650, 700 and 750 GeV. Each mass point sample comprises 75k events. Events were filtered at the generator level to require at least one lepton with $p_T > 10$ GeV.

[13] The transverse mass is defined by the formula $m_{\mathrm{T}} = \sqrt{2p_{\mathrm{T}}^{\ell}E_{\mathrm{T}}^{\mathrm{miss}}(1-\cos\Delta\phi)}$, where p_{T}^{ℓ} is the p_T of the lepton and $\Delta\phi$ is the azimuthal angle separation between the lepton and $E_{\mathrm{T}}^{\mathrm{miss}}$.

[14] These cuts are mainly intended to reject events with LAr noise bursts, and to deal with some dead Front-End board in the LAr detector. See [149] for details.

[15] PYTHIA 6 [167] generator using the ATLAS AMBT2B(CTEQ6L1) tune [178] are used by default.

[16] PYTHIA 6.421 [167] with the MRST LO* [174] parton density functions (PDFs).

Vector-Like quarks While our analysis was optimized to search for chiral fourth generation quarks, it turned out that it was also sensitive to Vector-Like Quarks (VLQ). In the very last section of this work (Sec. 4.11.5), we will reinterpret our results using a VLQ signal instead of the u_4 one.

The Vector-Like-Quarks (VLQ) samples are generated using PROTOS[17]. Vector-Like-Quarks are pair produced. They can decay in any of the three modes: $t' \to Wb, t' \to tH$ (where H is the SM scalar boson generated with a mass of 125 GeV), and $t' \to tZ$. Default PROTOS mixing where used for the production for the following values of the t' mass: 400, 450, 500, 550, and 600 GeV. They can be found in Table 4.2.

$m_{t'}$ (GeV)	BR(WbWb)	BR(WbtH)	BR(WbtZ)	BR(tHtZ)	BR(tHtH)	BR(tZtZ)
400	0.2625	0.3569	0.1427	0.0969	0.1217	0.0193
450	0.2518	0.3409	0.1583	0.1078	0.1161	0.0250
500	0.2468	0.3282	0.1717	0.1141	0.1092	0.0300
550	0.2448	0.3169	0.1827	0.1183	0.1029	0.0344
600	0.2441	0.3075	0.1923	0.1209	0.0972	0.0379

Table 4.2: Protos Branching Ratios (BR) for vector-like $t'\bar{t}'$ production as a function of $m_{t'}$ as computed by PROTOS.

For each mass point three samples are produced depending on the number of SM scalar bosons: 0, 1 and 2. For the 0/1/2 samples, 10/40/40k events per mass points are produced. Events were filtered at the generator level to require at least one lepton with $p_T > 10$ GeV. ATLAS Fast simulation is used to reconstruct the VLQ signals samples. More details about the VLQ production/validation can be found here [181].

Normalization Signal MC samples are normalized to the theoretical cross section computed at approximate next-to-next-to leading order (NNLO) in QCD using HATHOR[175] and CTEQ66 [176] PDFs. Scale uncertainties are calculated according to recommendations from the HATHOR documentation: a numerical integration of the cross section for each mass point over a range of $m_{u_4}/2$ to m_{u_4} for the negative scale uncertainty and a range of m_{u_4} to $2m_{u_4}$ for the positive scale uncertainty. PDF uncertainties are calculated with HATHOR PDF_SCAN option, which calculates the uncertainty based on the central cross section value and the CTEQ66 error PDFs. The cross section values used are summarized in Table 4.3 for the chiral fourth generation $u_4\bar{u}_4$ production.

From this point and until Sec. 4.11.5, we will only consider chiral fourth generation $u_4\bar{u}_4$ production, and forget momentarily the vector-like quarks.

4.5.3 Backgrounds

Backgrounds are signatures in the detector that can mimic our signal. The typical example in our case is the physics process of $t\bar{t}$ production, that has exactly the same tree-level Feynman diagram as the one of $u_4\bar{u}_4$ production that we showed in Fig. 4.3. As seen previously in Sec. 4.3, we have identified numerous possibilities to reduce this background, but still, we will never know with full certainty if the signature we record comes from a $t\bar{t}$ event or a $u_4\bar{u}_4$ event, and the decision has to be taken on a statistical basis, which will be the last step of the analysis.

[17] PROTOS 2.2 [170] with the CTEQ6l1 [176] parton density functions (PDFs).

m_{u_4} (GeV)	$\sigma(u_4\bar{u}_4)$ (pb)	Scale uncertainties (pb)	PDF and α_s uncertainties (pb)
400	1.406	+0.045/-0.083	+0.176/-0.138
450	0.662	+0.023/-0.040	+0.087/-0.065
500	0.330	+0.012/-0.020	+0.045/-0.032
550	0.171	+0.007/-0.010	+0.024/-0.017
600	0.092	+0.004/-0.006	+0.014/-0.009
650	0.051	+0.002/-0.003	+0.008/-0.005
700	0.029	+0.001/-0.002	+0.005/-0.003
750	0.017	+0.001/-0.001	+0.003/-0.002

Table 4.3: Theoretical cross section at NNLO for chiral fourth-generation $u_4\bar{u}_4$ production as a function of m_{u_4} as computed by HATHOR, and scale and PDF uncertainties.

Another kind of backgrounds are those that come from physics events with different final states but including particles mis-identified by the detector. For example, the QCD multijet background can have jets wrongly reconstructed as electrons, as illustrated in Fig. 4.13(a). Due to the enormous cross-section of such process compared to the rare decays we are looking for, this can represent a substantial background. In the muon channel, such problem can also happen, for example with $b\bar{b}$ production as illustrated in Fig. 4.13(b), in which one can imagine that a c-jet from a W boson in the final state can be tagged wrongly as a b-jet. More details about this QCD multijet background are given in Sec. 4.5.3.2, as well as the method to estimate it using real data.

Another background to our search is what we call W+jets production, which has also a very high cross-section (as seen in Fig. 2.6). It consists mainly of direct W boson production $pp \to W^{(+/-)} \to \ell^{(+/-)}\nu$ (where ℓ can be an electron, a muon or a tau), with possibly additional partons in the final state. Different samples with 0/1/2/3/4/5 such partons are used in this analysis. W boson production associated with quarks production can also occur, as illustrated for example in Fig. 4.13(c). Samples for $Wb\bar{b}$, $Wc\bar{c}$ and Wc processes with 0/1/2/3/4 additional partons are used. The shapes of these backgrounds are predicted from MC simulation but the overall yield and flavor composition are determined using data-driven techniques, as summarized in the next section.

Another background is what we call Z+jets production, which has also a very high cross-section (see also Fig. 2.6), but has much less impact on our search due to the absence of neutrino in the final state. It consists mainly of direct Z boson production $pp \to Z \to \ell^+\ell^-$ (where ℓ can be an electron, a muon or a tau), with possibly additional partons in the final state. Different samples with 0/1/2/3/4/5 such partons are used in this analysis. Z boson production associated with quarks production can also occur, as illustrated for example in Fig. 4.13(d). Samples for $Zb\bar{b}$ processes with 0/1/2/3/4 additional partons are used.

Smaller background contributions arise from single top production[18] (see *e.g.* Fig. 4.13(e)) and di-boson production[19] (see *e.g.* Fig. 4.13(f)). These physics backgrounds, together with Z+jets, are predicted from the MC simulation and are normalized to higher-order theoretical cross sections.

[18]Single top production can occur through three 'channels': the so-called s-channel, in which $pp \to W \to tb$, the t-channel, as seen *e.g.* in Fig. 4.13(e), and the 'W-associated production'. All three of them were used.

[19]Di-boson production consists of three samples: WW, ZZ and WZ production.

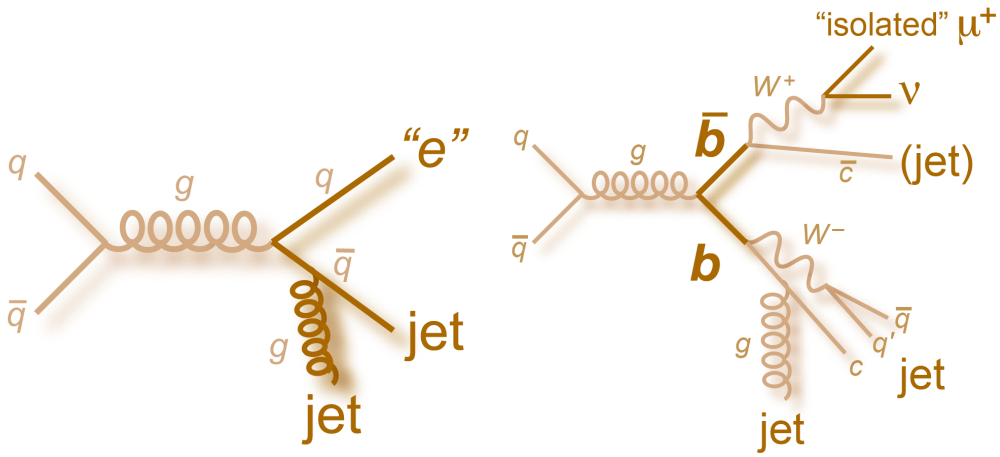

(a) Multijet ($e^{+/-}$)

(b) Multijet ($\mu^{+/-}$)

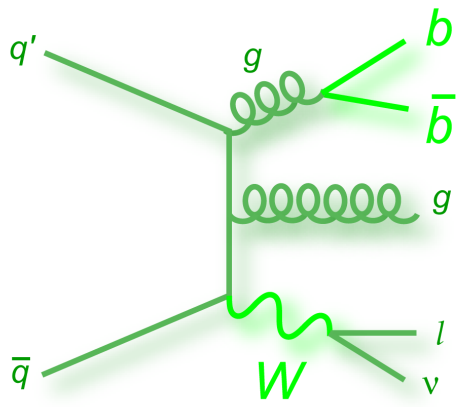

(c) $W + jets$

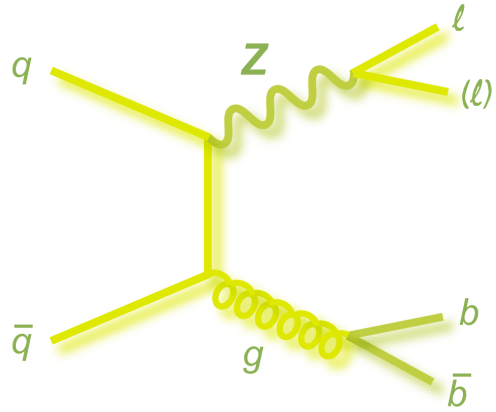

(d) $Z + jets$

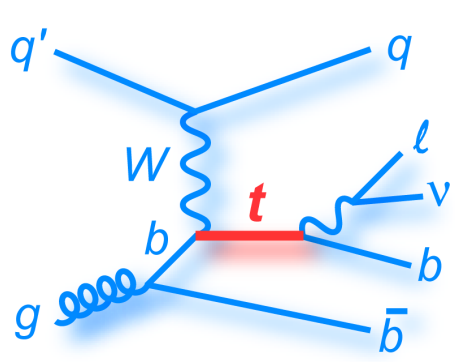

(e) Single-top (t-channel)

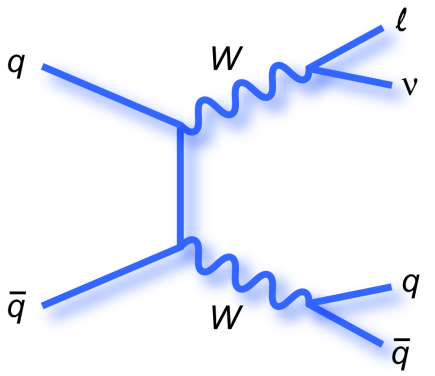

(f) Di-boson

Figure 4.13: Examples of Feynman diagrams for the different backgrounds of our search (see text for details).

4.5.3.1 W+jets background calibration

In proton-proton collisions W+jets production is charge asymmetric[20]. The total number of W+jets events in data, $N_W = N_{W^+} + N_{W^-}$, can be estimated based on the measured difference between positively-charged and negatively-charged W bosons, $(N_{W^+} - N_{W^-})_{meas}$, and the ratio of W^+ to W^-, r_{MC}, determined precisely from simulation:

$$N_W = \left(\frac{r_{MC}+1}{r_{MC}-1}\right)(N_{W^+} - N_{W^-})_{meas}. \tag{4.10}$$

It has been shown that the MC simulation slightly over-predicts the number of W+jets events compared to the data-driven method by up to $\sim 20\%$, depending on the jet multiplicity. Corresponding scale factors to correct the MC prediction have been derived (see Sect. 3.1 of Ref. [149]) and are used in this analysis to calibrate the pre-tag W+jets yields to data.

In addition, by performing measurements of tagged W+jets yields in events with 1 and 2 jets, suitable correction factors to the $Wb\bar{b}$, $Wc\bar{c}$, Wc and W+light jet fractions in MC are derived (see Sect. 3.2 of Ref. [149]), also used in this analysis. The W+jet scale factors for each flavor component are the product of the overall W+jet scale factors and the flavor-specific ones.

4.5.3.2 QCD multijet background

Multijet events can enter the selected data sample through several production and mis-reconstruction mechanisms. In the e+jets channel, the QCD multijet background consists of both non-prompt electrons and fake electrons where the latter include both electrons from photon conversion and misidentified jets with high EM fractions (as seen previously). In the μ+jets channel, the background to "real" (prompt) muons coming from "fake" muons in QCD multijet events, is predominantly due to final states with a non-prompt muon, like b-quark and meson decays in flight. Since the Monte Carlo simulation can not a-priori be expected to model the QCD multijet background with a sufficient level of accuracy, data-driven techniques are developed to determine both its normalization and shape for the distributions of interest.

The QCD multijet background normalization and shape is estimated directly from data by using the so-called "Matrix Method" technique [148]. The matrix method (MM) exploits differences in lepton identification-related properties between prompt isolated leptons from W and Z decays and those where the leptons are either non-isolated or result from mis-identification of photons/jets (referred to as "real leptons" below). For this purpose, two samples are defined after requiring the final kinematic selection criteria, differing only in the lepton identification criteria: a "tight" sample and a "loose" sample, the former being a subset of the latter. The tight selection typically employs the final lepton identification criteria used in the analysis, whereas the loose selection is adjusted in order to satisfy basic requirements for the method to work, which are outlined below. The method assumes that the number of selected events in each sample (N^{loose} and N^{tight}) can be expressed as a linear combination of the numbers of events with real and fake leptons, in such a way that the following system of equations can be defined:

[20]The production asymmetry occurs because the proton contains two valence up quarks and one valence down quark in a sea of quark-antiquark pairs and gluons. So in a proton-proton collision, there is a higher probability of an up and an antidown quark interacting than an antiup quark and a down quark, and hence more positive W bosons (produced most often from the interaction of an up quark and an antidown quark) are produced compared to negative W bosons (produced most often from the opposite combination of a down quark and an antiup quark).

$$\begin{aligned} N^{\text{loose}} &= N^{\text{loose}}_{\text{real}} + N^{\text{loose}}_{\text{fake}}, \\ N^{\text{tight}} &= \varepsilon_{\text{real}} N^{\text{loose}}_{\text{real}} + \varepsilon_{\text{fake}} N^{\text{loose}}_{\text{fake}}, \end{aligned} \tag{4.11}$$

where $\varepsilon_{\text{real}}(\varepsilon_{\text{fake}})$ represents the probability for a real(fake) lepton that satisfies the loose criteria, to also satisfy the tight ones, and are measured in data control samples. For more details about the exact criteria used for both electrons and muon as well as the different validation studies performed see Sect. 2 of Ref. [149]. The actual tools used for the MM prediction are provided in Ref. [150].

4.6 Prototype studies

Before converging to the final analysis that will be presented in much details from Sec. 4.7, we conducted many studies to define what search strategy could show the best compromise in terms of sensitivity and convenience to publish these results in a timely manner[21]. We can only present a fraction of these studies in the present document.

4.6.1 Preliminary remarks

d_4 signal In this section, in addition to $u_4\bar{u_4}$ production, we will also consider the pair production of a fourth-generation chiral down-type quark d_4, which should exist if a u_4 quark exists:

$$pp \rightarrow d_4\bar{d_4} \rightarrow W^- t W^+ \bar{t} \tag{4.12}$$

in which processes $d_4 \rightarrow Wt$ occur 100% of the time. As $BR(t \rightarrow Wb) \simeq 100\%$, the spectacular final state will contain four W bosons. We look for the case where one of them decays leptonically, and the others decay hadronically, as illustrated in Fig. 4.14.

Both $u_4\bar{u_4}$ and $d_4\bar{d_4}$ production are expected to be important if m_{d_4} and m_{u_4} differ by less than the W mass. $u_4\bar{u_4}$ production will be the process of main interest in this study. However, as will be seen later on, the final states of the two processes are sharing similar features. As a consequence, despite the fact that the analysis will be optimized to select the u_4 signal, a non-negligible fraction of the d_4 signal will also be selected by our analysis. We are thus showing in different plots both the u_4 signal, and, for indication purpose, the d_4 signal. We will consider $m_{d_4} = m_{u_4}$, which is an allowed and realistic assumption.

QCD For the prototype studies presented here, we have not included any QCD multijet background estimation for practical matter. This was justified because given the very tight cuts on the p_T of the objects, and the b-tagging requirements (1 or even 2 b-tags in some studies), the contribution of this background was expected to be much lower than the $t\bar{t}$ background.

4.6.2 How to reconstruct W-jets ? CHANNELS 1 & 2

The main idea of this search is to try to reconstruct *boosted W* bosons, which is done in two ways, as explained now.

[21] We recall the reader that at the time the first signs of SM scalar boson appeared in ATLAS, a paper [40] claimed that the best fit for the mass of a u_4 quark was around 625 GeV in the hypothesis of m_H =125 GeV.

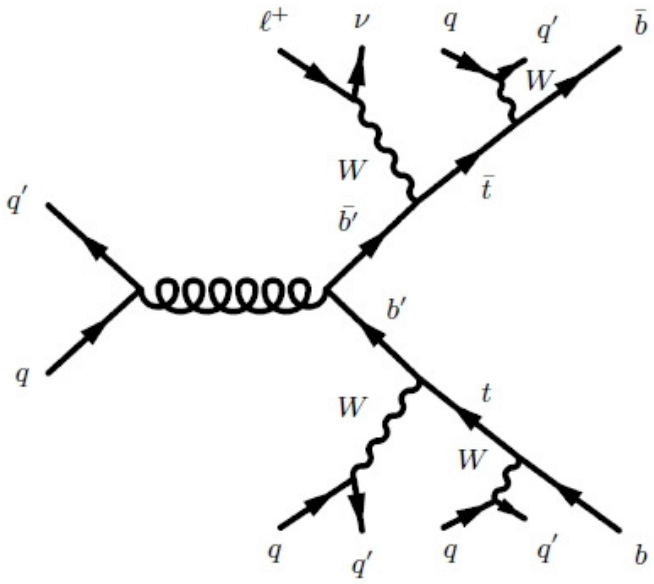

Figure 4.14: Feynman diagram of $d_4\bar{d}_4$ production and decay into four W bosons, one of them decaying leptonically, and the others decaying hadronically.

4.6.2.1 CHANNEL 1

For very high-p_T W bosons, the two resulting jets are so collimated that they can actually be reconstructed as a single jet. This can be seen in Fig. 4.15 which shows the distributions of the mass of the jets with the highest jet mass in an event, for ANTIKT10 jets and ANTIKT4 jets. The events are selected from the 'pre-analysis' cuts defined in Sec. 4.4.9.2, adding the requirement that the event must contain at least one ANTIKT10 or ANTIKT4 jet, respectively.

It can be clearly seen that these distributions show a peak around 80 GeV, the mass of the W boson. For ANTIKT10 jets, the big radius $R = 1.0$ allows to capture almost all of our u_4 signal under the 'W peak'. For ANTIKT4 jets, the smaller radius $R = 0.4$ captures a much lower, but still sizable, fraction of the signal. It is also interesting to note that such 'W-jets' are also present in the d_4 signal.

We also studied jets with cone size $R = 0.6$, and in principle we would have wanted to study other intermediate cone sizes between 0.4 and 1.0. In practice, we have not done so, because it was not forecast in ATLAS to get official systematic uncertainties for such sorts of jets on time for our final result. As these intermediate sizes could be an optimal choice depending on the m_{u_4} range of interest, this should deserve more studies in a future version of this analysis.

We identify single W-jets when their mass m_j falls around the W mass in a certain window:

$$\textbf{W-tagging criteria:} \qquad W_{min} < m_j < W_{max} \tag{4.13}$$

We refer to this way of identifying W-jets as our CHANNEL 1. Numerical values for W_{min} and W_{max} will be given in the following.

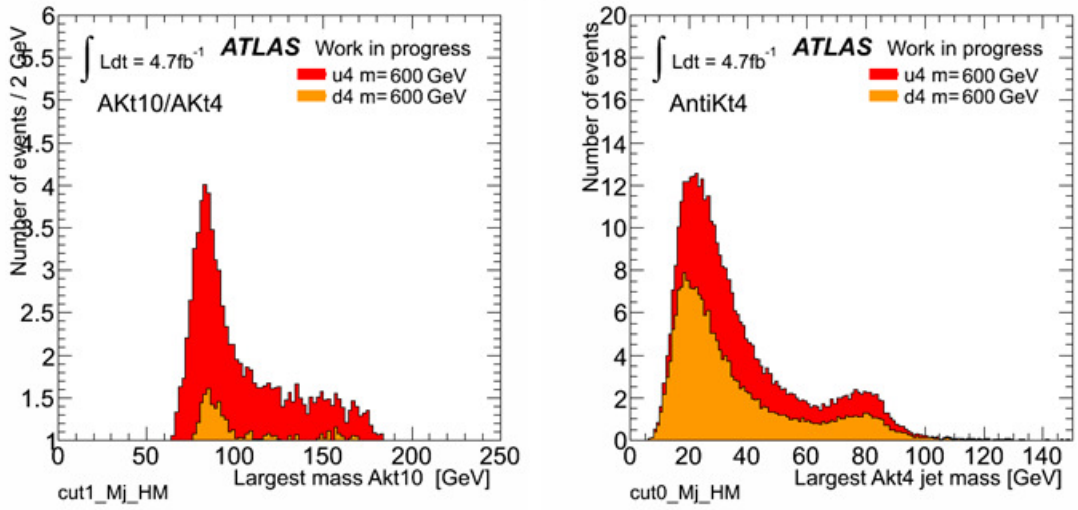

(a) ANTIKT10 jets (b) ANTIKT4 jets

Figure 4.15: Distribution of the largest jet mass for (a) ANTIKT10 jets and (b) ANTIKT4 jets, for the u_4 and d_4 signals (600 GeV mass).

4.6.2.2 CHANNEL 2

When a single W-jet cannot be found, which is especially the case when using ANTIKT4 jets, the two quarks are nevertheless expected to be very close-by. For this reason, we look at the combinations of two jets separated within *e.g.* $\Delta R < 1.0$. Figure 4.16 shows the distribution of the invariant mass of such di-jet systems. The events are selected from the 'pre-analysis' cuts defined in Sec. 4.4.9.2, adding the requirement that the event must contain at least two ANTIKT4 jets. A clear peak at the W boson mass can again be seen.

We tag such di-jet system as a W-jet when its invariant mass lies around the W mass within a certain window:

$$\textbf{W-tagging criteria:} \quad \Delta R(j_1, j_2) < R_{max} \text{ and } W_{min} < m_{j_1 j_2} < W_{max} \tag{4.14}$$

We refer to this way of identifying W-jets as our CHANNEL 2. Numerical values for W_{min} and W_{max} will be given in the following. R_{max} is fixed for now to the value of 1.0.

4.6.2.3 CHANNEL 3

For completeness, we considered in addition a third case (CHANNEL 3) in which no boosted W boson had been identified, but this case was eventually dropped since it was not bringing any significant improvement to the significance of the search.

4.6.3 Mass reconstruction

At this point, if we manage to identify the two b-jets of the event (see later), candidates for all the objects of the $u_4\bar{u}_4$ decay are determined: the two b-jets, one or two solutions for the leptonic W, and the W-jet candidate (whether it is actually a single fat jet or the merging of two jets). Only the pairing

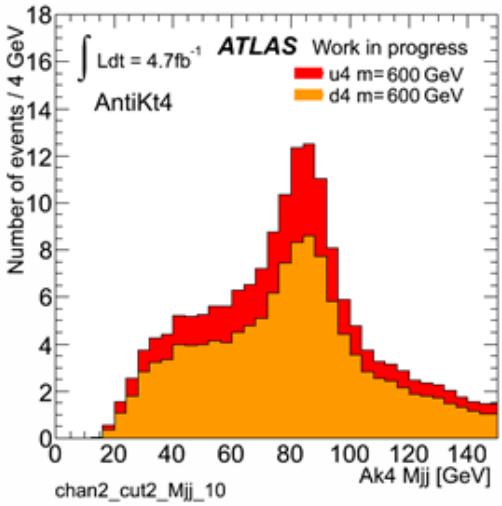

Figure 4.16: Distribution of the invariant mass of di-jet system of jets within $\Delta R < 1.0$, using ANTIKT4 jets, for the u_4 and d_4 signals (600 GeV mass).

of the b-jets with the W's, and the solution of the leptonic W are unknown. We are hence testing all the combinations, and for each one reconstructing:

- a *hadronic* quark t'_{had}, *i.e.* the system formed of the W-jet and a b-jet
- a *leptonic* quark t'_{lep}, *i.e.* the system formed of a leptonic W candidate, and the other b-jet.

and we take the combination that minimizes the mass difference between the hadronic and leptonic u_4 quarks $|M(t'_{had}) - M(t'_{lep})|$. In the following, we will then consider:

- in the rest of this section: the mean of $M(t'_{had})$ and $M(t'_{lep})$;
- from Sec. 4.7: only the hadronic mass $M(t'_{had})$,

and we will refer to it as M_{reco}.

Note that for the chosen solution of the leptonic W, there is also a neutrino solution associated, which will be used later to define a powerful variable for background discrimination.

Note also that knowing the charge of the leptons, the correct association could be obtained determining the initial flavor of the b-jets, *i.e.* whether they are stemming from a b-quark or an anti-b quark. However, such 'jet charge' tagging is known to be very difficult, and as we will see, we do not suffer much from combinatorial effect in the mass reconstruction, as we obtain very nice signal peaks with the simple method stated above. Of course, this should deserve more studies in a future version of this analysis, *e.g.* starting by studying the sign of charged tracks in jets.

We will now describe two ways of exploiting W-jets.

4.6.4 Solution using an AntiKt10/AntiKt4 mix of jets

The first solution we consider is to first use ANTIKT10 jets to tag the W-jets, *a la* CHANNEL 1, *i.e.* looking at jets with mass compatible with the W mass. This is expected to be very efficient due to

the large cone size that can 'capture' the two collimated jets from the W boson decay. An interesting option consists of using also ANTIKT4 jets to tag the b-jets, because the b-tagging in ATLAS is not optimized and calibrated for the ANTIKT10 jet collection. When no W-jet is found using the ANTIKT10 jets, we consider only ANTIKT4 jets and reconstruct W-jets *a la* CHANNEL 2, *i.e.* looking at pairs of close-by jets with invariant mass compatible with the W mass, to recover the few W-jets that were not found in CHANNEL 1. We now describe the detailed steps of this strategy.

From the 'pre-analysis' cuts defined in Sec. 4.4.9.2, we add the following cuts:

- Cut 1: At least two ANTIKT4 jets and at least one ANTIKT10 jet;
- Cut 2: $H_T > 900$ GeV;[22] This cut is motivated by the considerations made in Sec. 4.3.3;

Then, for CHANNEL 1, we require:

- Cut 3: Exactly one W-jet formed among the ANTIKT10 jets. If more than two candidates, we take the one with the mass the closest to m_W;
- Cut 4: $p_T(W_{jet}) > {p_T}^{cut}$ (see below); This cut is motivated by the fact that the merging of jets happens at very high W boson p_T. This will be quantified in Sec. 4.7 in *e.g.* Fig. 4.20(b).
- At this point, we remove from the event ANTIKT4 jets overlapping with the W-jet within $\Delta R < 0.5$[23] as ANTIKT10 jets can also be reconstructed as ANTIKT4 jets, and vice versa;
- Cut 5: At least one ANTIKT4 jet with $p_{TLJ} > {p_T}^{cut1}$ (see below), and another with $p_{TSLJ} > 80$ GeV. We call these two jets 'high-p_T jets';
- Cut 6: The W-jet has to be $\Delta R > 1.0$ away from the high-p_T jets;
- Cut 7: The lepton has to be $\Delta R > 1.0$ away from the high-p_T jets and the W-jet;
- Cut 8: Among the high-p_T jets, at least one of them has to be b-tagged by the MV1 algorithm operating at the 60% operating point;
- Cut 9: The p_T of the b-tagged jet has to be higher than 180 GeV.

For CHANNEL 2:

- If no single W-jet could be found in above 'Cut 3', the event must contain exactly one W-jet as a combination of two close-by ANTIKT4 jets, as explained previously. If more than two candidates, we take the one with the mass the closest to m_W;
- Then the CHANNEL 1 cuts from 'Cut 4' to 'Cut 9' are applied with this W-jet. Obviously, in 'Cut 5', we do not consider the two jets that served to form the W-jet.

Numerical values for all these cuts are summarized in Tab. 4.4. They were chosen after many optimizations based on the statistical significance of the resulting mass plots (see below), and in order to make a fair comparison with the other analysis strategy that we will present in Sec. 4.6.5.

[22] In practice, contrary to the definition of H_{T_4} introduced in Sec. 4.4.8, all jets of the event are considered in the definition of H_T here.

[23] This cut is intended to ensure that there is absolutely no energy overlapping between the two jet collections.

	ANTIKT4 ONLY		ANTIKT10/ANTIKT4	
	CHANNEL 1	CHANNEL 2	CHANNEL 1	CHANNEL 2
$p_T(W_{jet}) >$	250 GeV	150 GeV	150 GeV	150 GeV
$[W_{min}, W_{max}]$	[75,95 GeV]	[75,95 GeV]	[60,100 GeV]	[75,95 GeV]
$p_{T\,LJ} >$	80 GeV	80 GeV	100 GeV	80 GeV

Table 4.4: Numerical values for the different cuts of the proposed solutions using (left) only ANTIKT4 jets, and (right) the ANTIKT10/ANTIKT4 mix of jets.

The resulting distributions of the reconstructed mass M_{reco} are shown in Fig. 4.17 for CHANNEL 1 and CHANNEL 2. Events are from the muon and electron channels combined. The statistical significance is shown for u_4, d_4, and $u_4 + d_4$ hypothesis, as well as the number of signal and background events. We can already notice a very nice signal peak, which can be compared to the one of previous searches *e.g.* in Fig. 4.4. As expected, we can also notice that almost all signal events are coming from CHANNEL 1 ($\sim 90\%$).

4.6.5 Solution using AntiKt4 jets only

The second option to exploit W-jets we consider is to use only ANTIKT4 jets, which are of common use in ATLAS. In this scenario, we naturally expect much less W-jets reconstructed in CHANNEL 1, due to the lower cone size, and much more in CHANNEL 2.

From the 'pre-analysis' cuts defined in Sec. 4.4.9.2, we apply exactly the same cut-flow than in the previous section 4.6.4[24]. Numerical values for all the cuts are summarized in Tab. 4.4.

The resulting distributions of the reconstructed mass M_{reco} are shown in Fig. 4.18 for CHANNEL 1 and CHANNEL 2. Events are from the muon and electron channels combined. As expected, we can notice that most of the signal events are coming from CHANNEL 2 ($\sim 83\%$). For higher u_4 masses, one could expect this latter fraction to decrease, because more jets would be reconstructed as single jets.

4.6.6 Comparison

Figure 4.19 shows the M_{reco} distributions for the combination of CHANNEL 1 and CHANNEL 2 for both solutions.

From the statistical significance values, one can see that both options are roughly equivalent, even if the ANTIKT10/ANTIKT4 mix is slightly better. We base this conclusion also on studies which evaluated the sensitivity (*i.e.* evaluating the statistical power, see Sec. 4.10) of the two options, taking into account the main systematic uncertainties (including the b-tagging systematic and the one on the jet mass of ANTIKT10 jets). We recall that no QCD multijet background estimation was considered for this conclusion.

Another interesting fact is that some non-negligible fraction of the d_4 signal was selected despite the u_4-specific cut-flow and mass reconstruction.

Given the fact that the use of ANTIKT10 jets was very new in ATLAS at the time of this study, while the use of ANTIKT4 jets was very common, it was decided to retain the solution using only ANTIKT4 jets for the final analysis in order to get a result 'publishable' in a timely manner. The

[24]Except that obviously for 'Cut 3', the W-jet candidates are from the ANTIKT4 jet collection, and that no overlap removal between ANTIKT10 and ANTIKT4 jets is needed.

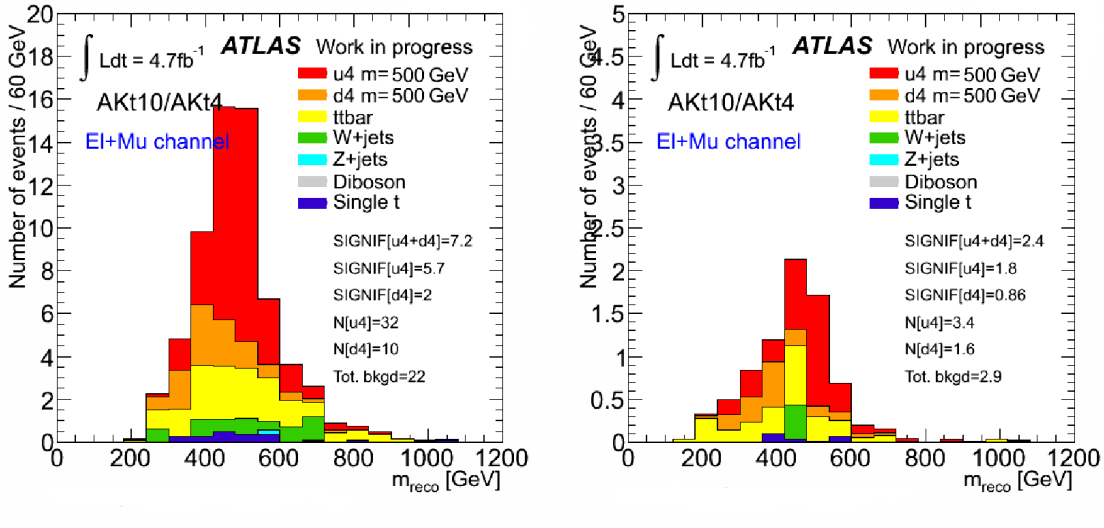

(a) CHANNEL 1 (b) CHANNEL 2

Figure 4.17: Reconstructed mass distributions for (a) CHANNEL 1 and (b) CHANNEL 2 for the option with the AntiKt10/AntiKt4 mixture of jets. The statistical significance is shown for u_4, d_4, and $u_4 + d_4$ hypothesis ($m_{u_4} = m_{d_4} = 500$ GeV), as well as the number of signal and background events.

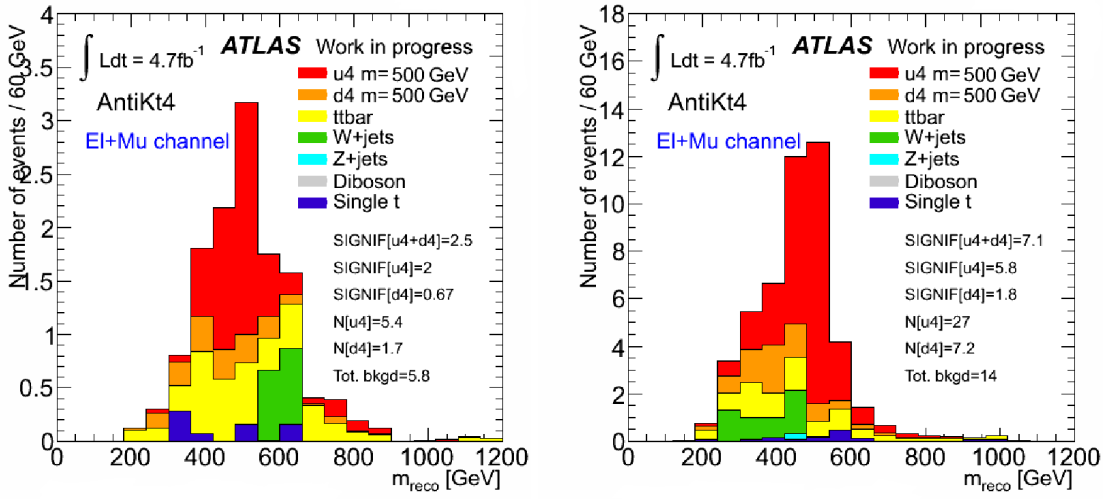

(a) CHANNEL 1 (b) CHANNEL 2

Figure 4.18: Reconstructed mass distributions for (a) CHANNEL 1 and (b) CHANNEL 2 for the option with only AntiKt4 jets. The statistical significance is shown for u_4, d_4, and $u_4 + d_4$ hypothesis ($m_{u_4} = m_{d_4} = 500$ GeV), as well as the number of signal and background events.

consideration of the d_4 signal was abandoned, but this would certainly be an interesting, and physically well-motivated, point in a future version of this work.

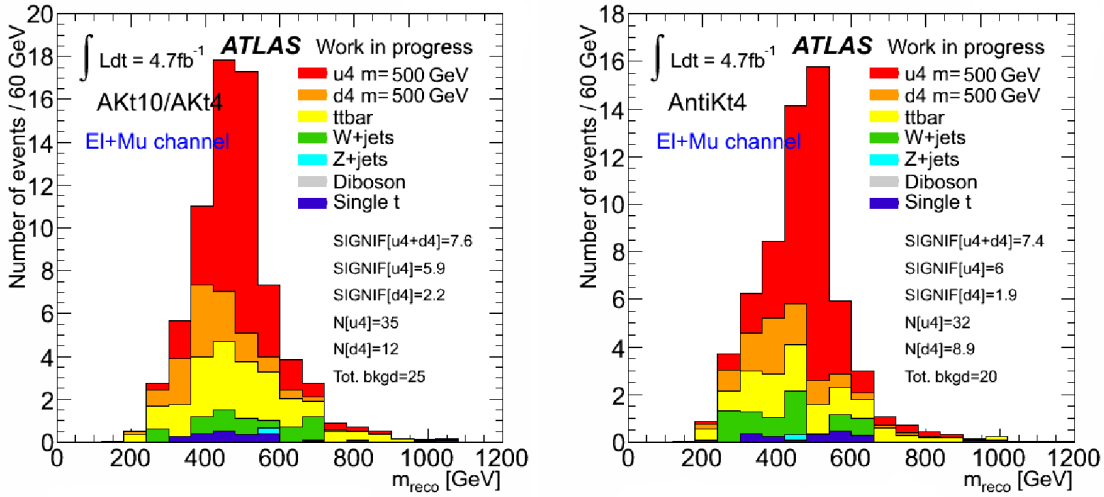

(a) ANTIKT10/ANTIKT4 (b) ANTIKT4 ONLY

Figure 4.19: Reconstructed mass distributions for CHANNEL 1 + CHANNEL 2 for (a) the option with the AntiKt10/AntiKt4 mixture of jets and (b) for the option with only AntiKt4 jets. The statistical significance is shown for u_4, d_4, and $u_4 + d_4$ hypothesis ($m_{u_4} = m_{d_4} = 500$ GeV), as well as the number of signal and background events.

4.7 Solution retained for the final analysis

The final form of the analysis is now described. It will use only ANTIKT4 jets, as introduced in the previous section, but the analysis cuts were slightly re-ordered (one cut was added), and the numerical values for the different cuts were re-optimized. From this point, the work results from a collaboration with the IFAE Barcelona group.

4.7.1 Event pre-selection

From the 'pre-analysis' cuts defined in Sec. 4.4.9.2, we add the following requirements. Events are required to have:

- at least three jets with $p_T > 25$ GeV and $JVF > 0.75$;
- at least one of these jets being tagged by the MV1 algorithm at the $\varepsilon_b = 70\%$ operating point. Subsequently, the two jets with the highest MV1 weights, *i.e.* the ones the more likely to be the actual b-jets of the event, are considered to be the two b-jets of the event. By construction, only one of these two jets is the one that has been formally tagged, but both will be used in the mass reconstruction;
- $H_{T_4} > 750$ GeV.

4.7.2 b-tagging using Tag-Rate-Function method

The stringent selection requirements used in the analysis, designed to strongly suppress the SM backgrounds, cause the available MC statistics to be significantly reduced, leading to large fluctuations in

the resulting templates. This can negatively affect the sensitivity of the analysis, as the corresponding statistical uncertainties on the background templates need to be taken into account in the statistical analysis, and lead to unreliable shape systematics driven by large statistical fluctuations. In addition, the observed limits can be biased depending on how the MC fluctuated relative to the data in the signal region.

In order to mitigate this problem, rather than requiring explicit b-tagging requirements as precised in the previous section, a tag-rate-function (TRF) method has been developed allowing to weight all events in the pre-tag sample to predict the normalization and shapes of the signal and backgrounds shapes one would have obtained using a 'cut-based' b-tagging. This has the effect to increase the number of entries used to evaluate each bins of the templates, and hence decrease the statistical error in the bins. This is particularly useful for backgrounds with small heavy-flavor content, e.g. W+jets, which are significantly suppressed by the b-tagging requirement. Various studies were performed to validate this method.

4.7.3 Reconstruction of the boosted W boson

4.7.3.1 CHANNEL 1

The event is required to have a single jet with a mass close to the W boson mass. Formally, a jet is defined as a W-jet candidate $W_{\text{had}}^{\text{type I}}$ if its mass is between 60 GeV and 110 GeV. This 'W-mass window' was defined using the distribution of largest jet mass in the event, shown in Fig. 4.20(a), in which one can clearly see a peak at the W mass.

Fig. 4.20(b) shows the p_T distribution of such W-jet candidates, and clearly shows that the merging of two jets starts to happen for jets above $\sim$250 GeV in this case where jets are reconstructed with the anti-k_t algorithm and a size parameter of $R = 0.4$. For this reason, we require the W-jet candidates to have a p_T greater than 250 GeV. If more than two candidates fulfill this cut, the one with the mass closest to the W boson mass is chosen.

One important point is that none of the two jets with the highest MV1 weights are considered as W-jets candidates. However no explicit cut or anti-cut is made on the b-tagging weights of the other jets, since jets arising from $W \to c\bar{s}$ decays (55% of the cases for W bosons decaying hadronically) could be tagged.

4.7.3.2 CHANNEL 2

If no W-jet can be found in the way described in the previous section, boosted W bosons are reconstructed in the following way: among all jets but the two ones having the highest MV1 weights, we are testing the invariant mass of all combinations of two jets separated within $\Delta R < 0.8$. If the invariant mass of such a di-jet system falls in the W mass window defined for CHANNEL 1, we define the combination as a W-jet candidate $W_{\text{had}}^{\text{type II}}$. Fig. 4.21(a) shows the distribution of the invariant mass of all di-jet combinations for the u_4 signal, which exhibits a clear peak at the W mass, and compared to the top background. Fig. 4.21(b) shows the distribution of the p_T of the W-jet candidates, and shows that the merging of two close-by jets in the way just defined starts to occur for di-jet systems with p_T above $\sim$150 GeV. For this reason, we require the W-jet candidates to have a p_T greater than 150 GeV. If more than two candidates are remaining, the one with the invariant mass closest to the W boson mass is chosen.

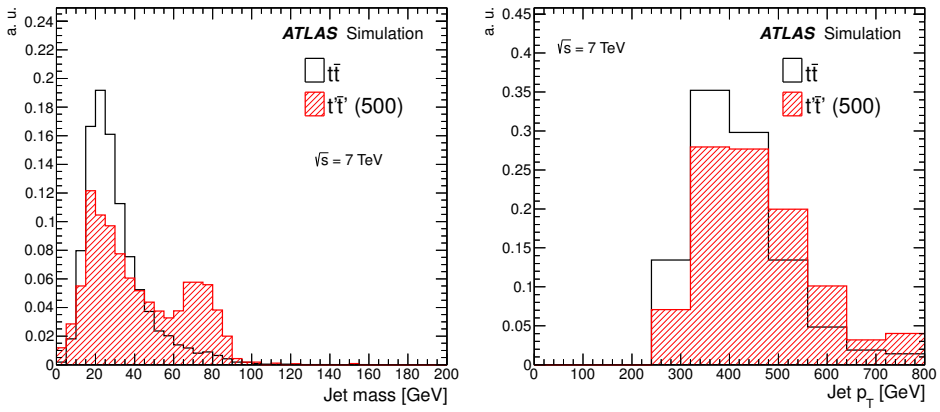

(a) (b)

Figure 4.20: $W_{\text{had}}^{\text{type I}}$ reconstruction: the decay products of the W boson decaying hadronically are selected as a single jet reconstructed with the anti-k_t algorithm with radius parameter $R = 0.4$. Distributions of (a) the highest jet mass, m_{j}, prior to the $60 \leq m_{\text{j}} \leq 110$ GeV requirement, and (b) the p_T of these $W_{\text{had}}^{\text{type I}}$ candidates, after the $60 \leq m_{\text{j}} \leq 110$ GeV requirement, for simulated events satisfying the pre-selection (see text for details). The distributions, normalized to unity, are compared between the dominant $t\bar{t}$ background (black line histogram), and a fourth-generation t' quark with mass $m_{t'} = 500$ GeV (plain red histogram).

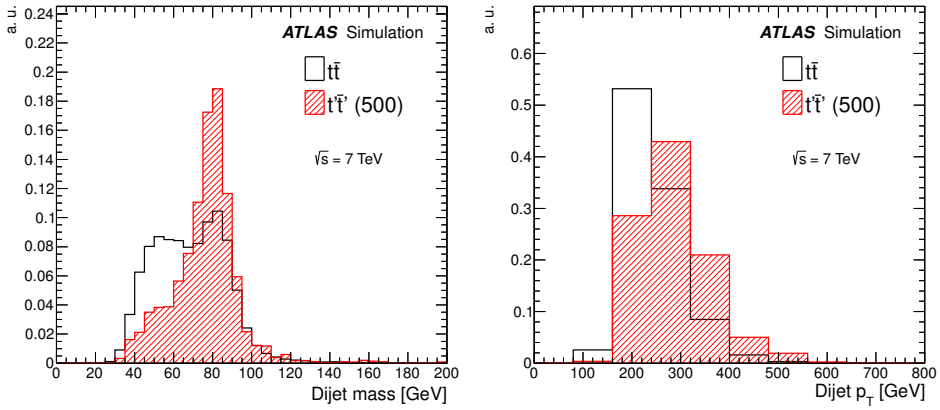

(a) (b)

Figure 4.21: $W_{\text{had}}^{\text{type II}}$ reconstruction: the decay products of the W boson decaying hadronically are selected as a two jets reconstructed with the anti-k_t algorithm with radius parameter $R = 0.4$, satisfying $\Delta R(\text{j},\text{j}) < 0.8$, and excluding the two jets with the highest b-tagging discriminant. Distributions of (a) the dijet invariant mass, m_{jj}, prior to the $60 \leq m_{\text{jj}} \leq 100$ GeV requirement, and (b) the p_T of these $W_{\text{had}}^{\text{type I}}$ candidates, after the $60 \leq m_{\text{jj}} \leq 100$ GeV requirement, for simulated events satisfying the pre-selection (see text for details). The distributions, normalized to unity, are compared between the dominant $t\bar{t}$ background (black line histogram), and a fourth-generation t' quark with mass $m_{t'} = 500$ GeV (plain red histogram).

4.7.4 Final cuts: LOOSE and TIGHT selection

4.7.4.1 LOOSE selection

In order to further reject the different backgrounds, we know apply additional cuts that were motivated in Sec. 4.3.3 using truth information from Monte Carlo simulations of signal and background:

- among the 2 jets considered as b-jets (*i.e.* with the highest MV1 weights), the p_T of the leading jet has to be greater than 160 GeV, and the p_T of the second leading jet has to be greater than 60 GeV. These cuts were optimized from the considerations made in Sec. 4.3.3.
- the ΔR separation between the lepton and the neutrino has to be lower than 1.4. The effect of this cut can be seen in Fig. 4.22, in which the non-$t\bar{t}$ component includes the W+jets, Z+jets, single-top, di-boson and QCD multijet backgrounds.

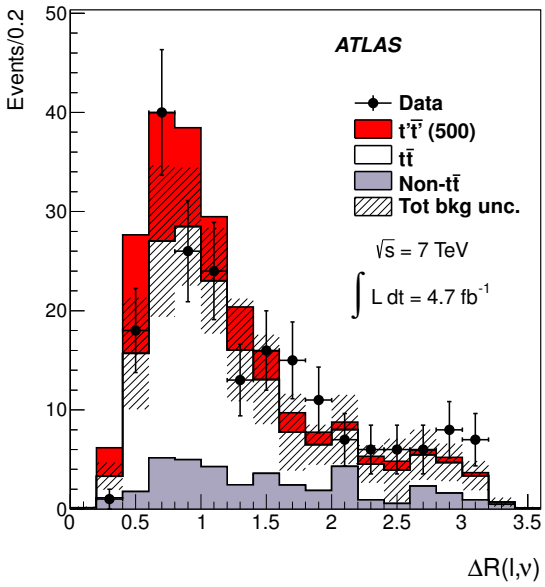

Figure 4.22: Distribution of the angular separation between the lepton and the neutrino, $\Delta R(\ell, \nu)$, for the combined e+jets and μ+jets channels after the *loose* selection, except for the $\Delta R(\ell, \nu) < 1.4$ requirement. The total uncertainty on the background estimation will be discussed in Sec. 4.9, but is already shown here as a black hashed band.

We call this stage of our selection cuts 'LOOSE selection', and corresponding distributions of the reconstructed mass M_{reco} can be found for data (in black solid points) and simulation in Fig. 4.23 for CHANNEL 1 and CHANNEL 2 separately, and in Figs. 4.27(a) for the combination of both channels. Table 4.5 reports the yields in the two channels. A clear peak for the u_4 signal can be seen in all cases, above a rather flat $t\bar{t}$ background. One interesting feature is also the fact that the top mass is clearly visible and well separated from the signal peak, this will allow us to constrain some systematics, as will be described in Sec. 4.10.

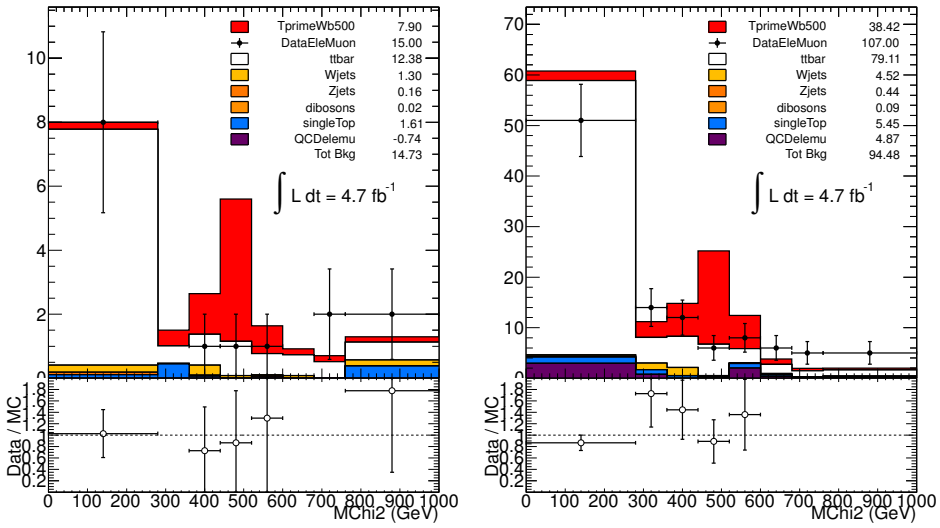

(a) Loose selection CH1 (b) Loose selection CH2

Figure 4.23: M_{reco} distribution for CHANNEL 1 (a), CHANNEL 2 (b) in the LOOSE selection. Please note the non-equidistant bins.

	CHANNELS 1+2		
	Electron	Muon	Electron+Muon
$u_4\bar{u}_4(500)$	22.16 ± 0.56	24.16 ± 0.60	46.32 ± 0.82
$t\bar{t}$	41.03 ± 1.41	50.46 ± 1.54	91.48 ± 2.09
QCD	3.60 ± 5.00	0.53 ± 0.38	4.13 ± 5.02
W+jets	3.39 ± 0.95	2.43 ± 0.68	5.82 ± 1.17
Z+jets	0.26 ± 0.11	0.34 ± 0.15	0.60 ± 0.18
Single top	3.63 ± 0.55	3.43 ± 0.63	7.06 ± 0.84
Dibosons	0.08 ± 0.04	0.03 ± 0.03	0.12 ± 0.05
Total prediction	51.99 ± 5.31	57.22 ± 1.85	109.21 ± 5.62
Data	54	68	122

Table 4.5: Yields for electron and muon channels, separately and combined, in the LOOSE selection for CHANNEL 1 and CHANNEL 2 combined.

4.7.4.2 TIGHT selection

In addition to the LOOSE selection requirements, and in order to reject even further the $t\bar{t}$ background, we apply two more cuts:

- the ΔR separation between the W-jet and both b-jets has to be greater than 1.4. The effect of this cut can be seen in Fig. 4.24.
- the ΔR separation between the lepton and both b-jets has to be greater than 1.4. The effect of this cut can be seen in Fig. 4.25.

These two cuts are motivated by the explanations made in Sec. 4.3.3, *i.e.* to select W bosons and leptons that are well isolated from their associated b-jets.

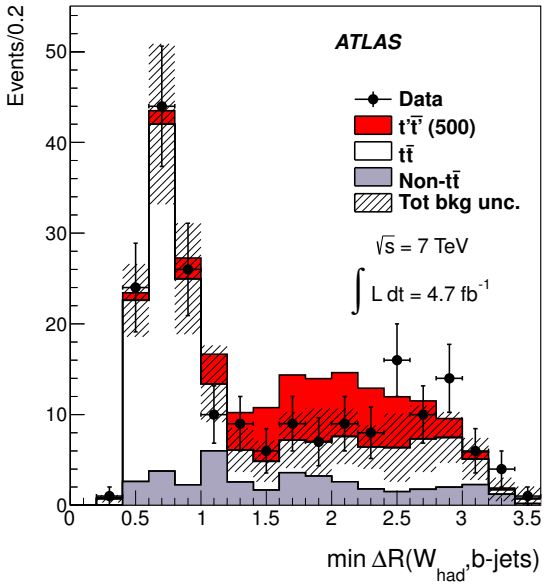

Figure 4.24: Distribution of the minimum angular separation between the selected W_{had} candidate and the b jets, $\min(\Delta R(W_{\mathrm{had}}, b_{1,2}))$, for the combined e+jets and μ+jets channels after the *loose* selection, except for the $\Delta R(\ell, \nu) < 1.4$ requirement.

We call this final stage of our selection cuts 'TIGHT selection', and corresponding distributions of the reconstructed mass M_{reco} can be found in Figure 4.26 for the two channels separately. Figure 4.27(b)shows the same distribution once CHANNEL 1 and CHANNEL 2 are combined. It can be clearly seen that these two extra cuts applied in addition to the LOOSE selection are able to suppress the peak of the top mass, and to further reduce the background under the signal peak. Table 4.6 reports the yields in the two channels for signal, backgrounds and data. Appendix A shows the efficiency of each of the selection cuts on the different signal and background samples.

It should be noted that all the selection cuts we presented were optimized to get a good compromise between signal acceptance and signal over background ratio. Tightening several (or all) of the cuts could in principle allow to reduce the background to an almost as low level as desired, keeping at the same time a substantial signal acceptance. This would be particularly useful for a future version of this analysis with much increased statistics of LHC data.

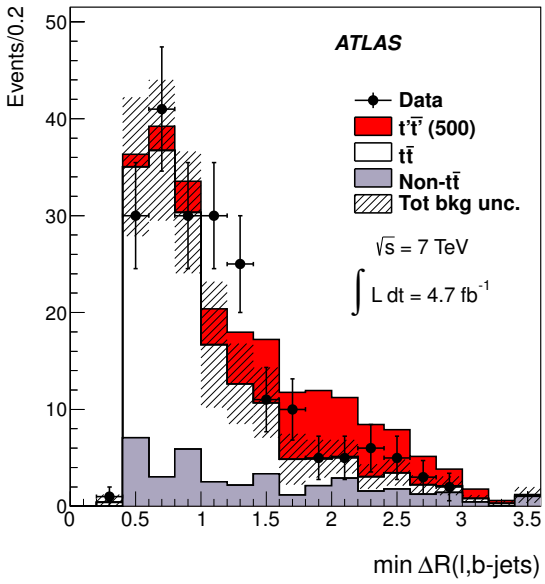

Figure 4.25: Distribution of the minimum angular separation between the lepton and the b jets, $\min(\Delta R(\ell, b_{1,2}))$, for the combined e+jets and μ+jets channels after the *loose* selection, except for the $\Delta R(\ell, \nu) < 1.4$ requirement.

	CHANNELS 1+2		
	Electron	Muon	Electron+Muon
$u_4\bar{u}_4(500)$	12.80 ± 0.42	14.20 ± 0.46	27.00 ± 0.62
$t\bar{t}$	1.56 ± 0.31	2.40 ± 0.38	3.96 ± 0.49
QCD	3.67 ± 2.43	0.14 ± 0.18	3.82 ± 2.44
W+jets	0.93 ± 0.40	1.09 ± 0.45	2.02 ± 0.60
Z+jets	0.07 ± 0.06	0.18 ± 0.13	0.25 ± 0.14
Single top	0.50 ± 0.19	0.60 ± 0.37	1.10 ± 0.42
Dibosons	0.03 ± 0.03	0.01 ± 0.01	0.04 ± 0.03
Total prediction	6.77 ± 2.49	4.43 ± 0.73	11.20 ± 2.60
Data	5	6	11

Table 4.6: Yields for electron and muon channels, separately and combined, in the TIGHT selection for CHANNEL 1 and CHANNEL 2 combined.

4.8 Control regions

4.8.1 Event pre-selection level

At the pre-selection level it is possible to define control regions whose purpose is to validate the modeling of the main backgrounds. These control regions are quite far from the signal region but are nevertheless useful to check with high statistics that the background normalization and kinematics are

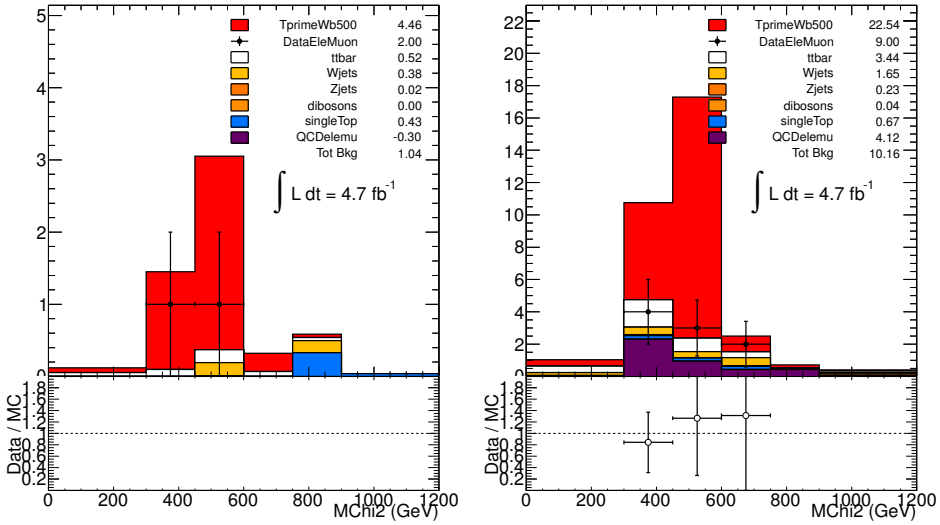

(a) Tight selection CH1 (b) Tight selection CH2

Figure 4.26: M_{reco} distribution for CHANNEL 1 (a) and for CHANNEL 2 (b) in the TIGHT selection.

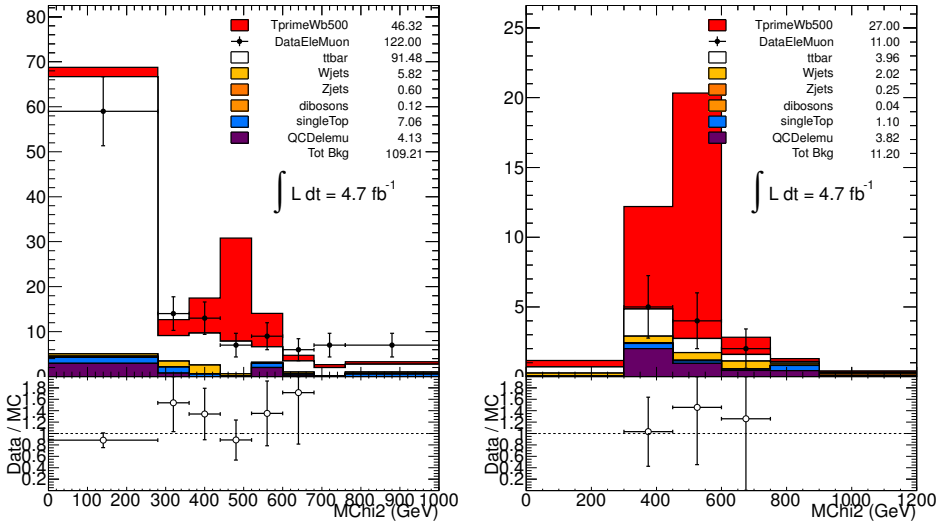

(a) Loose selection CH1+CH2 (b) Tight selection CH1+CH2

Figure 4.27: M_{reco} distribution for the combination of CHANNEL 1 and CHANNEL 2 in the (a) LOOSE and (b) TIGHT selections.

well modeled.

The following control regions are studied:

- $N_{jets} \geq 4$, $N_{\text{b-tags}} = 0$: owing the requirement of no b-tagged jets, this control region is enriched in W+jets and depleted in $t\bar{t}$ and $u_4\bar{u}_4$ signal. Appendix B.1 shows data-to-simulation comparisons for a few selected kinematic variables in the e- and μ-channels. Table 4.7 shows the yields in this control region.

- $N_{jets} \geq 4$, $N_{\text{b-tags}} \geq 1$, $H_T^4 < 700$ GeV: this control region is enriched in $t\bar{t}$ background. H_T is required to be below 700 GeV in order to deplete the sample from signal. Appendix B.3 shows data-to-simulation comparisons for a few selected kinematic variables in the e- and μ-channels. In particular, this control region allows to scrutinize the modeling of the M_{reco} distribution. Table 4.8 shows the yields in this control region.

The mass of the W-jet candidates was also checked for CHANNEL 1 and CHANNEL 2 after pre-selection, and prior to the jet mass requirements. The corresponding distributions are shown in Figs. 4.28(a) and 4.28(b) for the two channels respectively.

In general, good agreement between the data and the background prediction is found.

	Electron	Muon	Electron+Muon
$u_4\bar{u}_4(500)$	10.04 ± 0.15	11.52 ± 0.16	21.56 ± 0.21
$t\bar{t}$	2638.54 ± 5.84	4199.95 ± 7.40	6838.49 ± 9.42
QCD	2126.54 ± 60.83	2526.40 ± 24.21	4652.94 ± 65.47
W+jets	9361.82 ± 67.26	18294.88 ± 98.77	27656.70 ± 119.50
Z+jets	1861.87 ± 22.15	1914.92 ± 28.55	3776.79 ± 36.14
Single top	264.39 ± 2.95	427.87 ± 3.70	692.26 ± 4.73
Dibosons	144.87 ± 2.03	231.98 ± 2.60	376.86 ± 3.30
Total prediction	16398.04 ± 93.60	27596.00 ± 105.98	43994.05 ± 141.40
Data	16129	27350	43479

Table 4.7: Yields for electron and muon channels, separately and combined, in the control region $N_{jets} \geq 4$, $N_{\text{b-tags}} = 0$.

	Electron	Muon	Electron+Muon
$u_4\bar{u}_4(500)$	41.79 ± 0.77	48.54 ± 0.85	90.33 ± 1.14
$t\bar{t}$	13669.44 ± 24.56	22159.87 ± 31.61	35829.30 ± 40.03
QCD	1777.20 ± 83.05	1313.53 ± 15.11	3090.73 ± 84.42
W+jets	1386.91 ± 18.51	2909.60 ± 29.00	4296.51 ± 34.40
Z+jets	192.03 ± 4.27	218.15 ± 5.76	410.18 ± 7.17
Single top	790.94 ± 7.65	1308.70 ± 9.85	2099.63 ± 12.47
Dibosons	28.65 ± 0.62	46.76 ± 0.80	75.41 ± 1.01
Total prediction	17845.17 ± 89.00	27956.60 ± 46.90	45801.76 ± 100.60
Data	18655	30319	48974

Table 4.8: Yields for electron and muon channels, separately and combined, in the control region $N_{jets} \geq 4$, $N_{\text{b-tags}} \geq 1$, $H_T^4 < 700$ GeV.

4.8.2 Analysis level

In order to check the MC modeling in selections closer to the final analysis regions but with still enough statistics to expect reasonable agreement, we took as a baseline the LOOSE selections de-

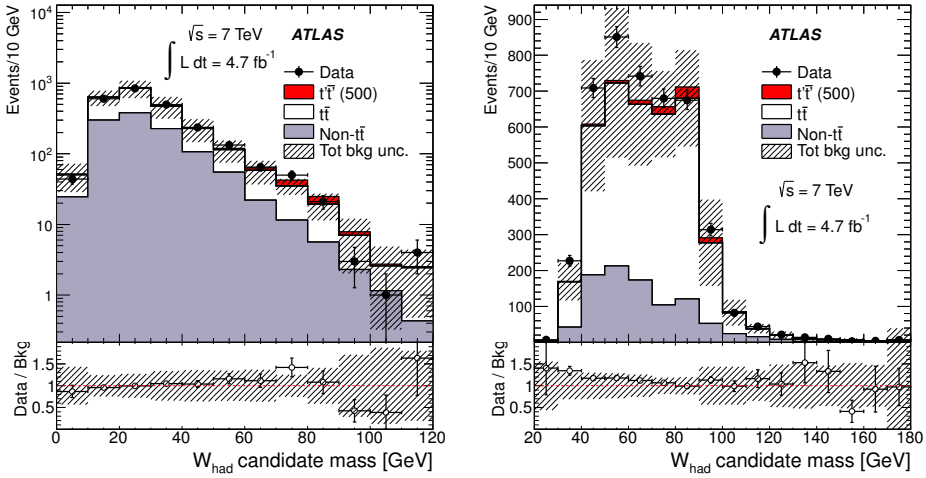

(a) (b)

Figure 4.28: Distribution of the reconstructed mass for (a) $W_{\text{had}}^{\text{type I}}$ and (b) $W_{\text{had}}^{\text{type II}}$ candidates for the combined e+jets and μ+jets channels after pre-selection and prior to the jet mass requirements. Figure (a) corresponds to events with $N_{jets} \geq 3$ and ≥ 1 $W_{\text{had}}^{\text{type I}}$ candidates, while (b) corresponds to events with $N_{jets} \geq 4$ and ≥ 1 $W_{\text{had}}^{\text{type II}}$ candidates (see text for details).

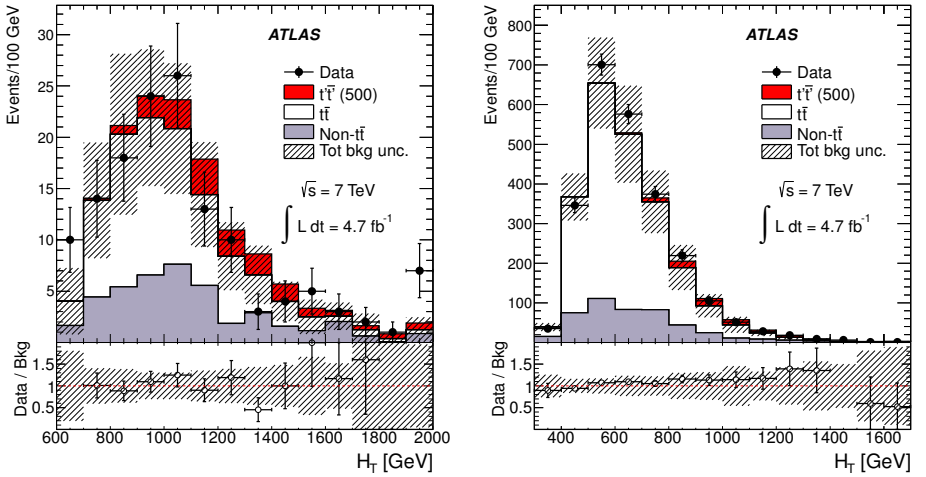

(a) (b)

Figure 4.29: Distribution of H_{T} for events with (a) $N_{jets} \geq 3$ and ≥ 1 $W_{\text{had}}^{\text{type I}}$ candidates and (b) $N_{jets} \geq 4$ and ≥ 1 $W_{\text{had}}^{\text{type II}}$ candidates (see text for details) for the combined e+jets and μ+jets channels after pre-selection.

scribed in Section 4.7.4.1 and defined the following "signal depleted" regions modifying or dropping some cuts:

- same as LOOSE selection except for dropping the H_T^4 cut; The H_{T}^4 distribution was checked for events with $N_{jets} \geq 3$ and ≥ 1 $W_{\text{had}}^{\text{type I}}$ candidates (shown in Fig. 4.29(a)) and events with

	CHANNEL 1+2		
	Electron	Muon	Electron+Muon
$u_4\bar{u}_4(500)$	1.75 ± 0.15	2.17 ± 0.18	3.92 ± 0.23
$t\bar{t}$	27.75 ± 1.12	34.85 ± 1.24	62.61 ± 1.68
QCD	1.78 ± 4.08	0.41 ± 0.30	2.19 ± 4.09
W+jets	0.58 ± 0.47	0.28 ± 0.23	0.86 ± 0.52
Z+jets	0.03 ± 0.02	0.02 ± 0.02	0.04 ± 0.03
Single top	0.76 ± 0.23	0.68 ± 0.22	1.44 ± 0.32
Dibosons	0.00 ± 0.00	0.00 ± 0.00	0.00 ± 0.00
Total prediction	30.91 ± 4.26	36.24 ± 1.32	67.14 ± 4.46
Data	34	34	68

Table 4.9: Yields for electron and muon channels, separately and combined, in the signal depleted region defined as the LOOSE selection except for adding a reversed version of the ΔR cuts between the hadronic W and the two jets with the highest MV1 weight, and of the ΔR cuts between the lepton and the two jets with the highest MV1 weight, for CHANNEL 1 and CHANNEL 2 combined.

$N_{jets} \geq 4$ and ≥ 1 $W_{\text{had}}^{\text{type II}}$ candidates (shown in Fig. 4.29(b)).

- same as LOOSE selection except for dropping the p_T cuts on the two jets with the highest MV1 weight;
- same as LOOSE selection except for dropping the $\Delta R(l, \nu) < 1.4$ cut;
- same as LOOSE selection except for adding a reversed version of the ΔR cuts between the hadronic W and the two jets with the highest MV1 weight, and of the ΔR cuts between the lepton and the two jets with the highest MV1 weight, see Appendix B.5 and the yield Table 4.9.

In general, good agreement between the data and the background prediction is found for all these signal-depleted regions.

4.9 Systematic uncertainties

4.9.1 Overview of treatment

Systematic errors can be seen as biases in a measurement, that lead to situation where the mean of many separate measurements differs significantly from the actual value of the measured attribute [180]. Sources of systematic error may be, *e.g.*:

- *imperfect calibration of measurement instruments.* This is typically the case of the various Scale Factors (SFs) or efficiencies estimated from the various performance groups to the physical objects reconstructed (*e.g* lepton identification SFs, lepton trigger SFs, *b*-, *c*-, light jet efficiencies, etc). As these factors were designed to make the simulation agree better with the real data, they impact the final predicted mass distributions. Hence, an error on their estimation might lead to a bias on the predicted distributions. As a consequence, it is of primary importance to first estimate the error on these factors. This is done in practice by the various performance groups[25],

[25] *e.g.* the *b*-tagging calibration we described in Sec. 3.6.

in the form of *up* (or '+1σ') and *down* (or '-1σ') estimated errors. Our role is then to propagate these errors through the analysis, and see the effect on the final LOOSE M_{reco} distribution of the *b*-tagging systematic, for *up* and *down* variations, shown together with the nominal distributions, for the $u_4\bar{u}_4$ and $t\bar{t}$ samples. All such kind of systematics uncertainties are described in detail in Appendix C.1.

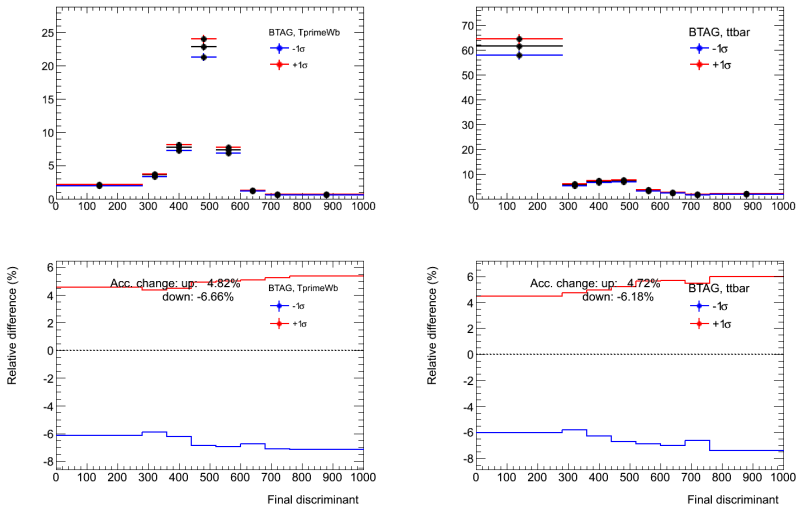

(a) (b)

Figure 4.30: Shape-dependent systematic uncertainty from BTAG on (a) $u_4\bar{u}_4$ signal, and (b) $t\bar{t}$. The event selection corresponds to that of the loose analysis. The top plots show the nominal distribution of m_{reco} (black points) compared to the $+1\sigma$ variation (red points) and the -1σ variation (blue points). The bottom plots show the relative difference between nominal and $\pm1\sigma$ variations.

- *present in the result of an estimate based on a mathematical model or physical law.* This is particularly the case for the simulation samples we use, that are based on Quantum Field Theory calculations. Uncertainties on cross-sections, W+jets and QCD normalizations, $t\bar{t}$ and signal modeling (MC generator, Initial and Final State Radiations, fragmentation, etc) are considered. All details about such kind of systematics uncertainties can be found in Appendices C.2 and C.3.

All systematic uncertainties which have been considered that can affect the normalization of signal and background and/or the shape of their corresponding final discriminant distribution are summarized in Tab. 4.10. This table indicates which sources are considered as normalization uncertainties only and for which ones we also consider shape uncertainties. No smoothing has been applied to shape uncertainties.

4.9.2 Merging of small backgrounds

As detailed extensively previously, this analysis was designed in order to reject a maximum amount of the $t\bar{t}$ background. For this latter background, we do observe a certain shape in the final mass distribution, particularly for the LOOSE selection that shows a resonance at the top quark mass. For the TIGHT selection, the shape is much less pronounced, but still present.

Source	Norm	Shape
Luminosity	YES	NO
Electron factors (ID, reco, trigger)	YES	NO
Muon factors (ID, reco, trigger)	YES	NO
Jet energy scale	YES	YES
Jet energy resolution	YES	YES
Jet mass scale	YES	YES
Jet mass resolution	YES	YES
Jet vertex fraction efficiency	YES	YES
b-tagging efficiency	YES	YES
c-tagging efficiency	YES	YES
Light-tagging efficiency	YES	YES
$t\bar{t}$ cross section	YES	NO
W+jets normalization (all sources combined)	YES	NO
QCD normalization	YES	NO
Single top cross section	YES	NO
Diboson cross section	YES	NO
Z+jets cross section	YES	NO
$t\bar{t}$ modeling: more/less PS	YES	YES
$t\bar{t}$ modeling: fragmentation PS	YES	YES
$t\bar{t}$ modeling: NLO generator	YES	YES
$t'\bar{t}'$ modeling: more/less PS	YES	NO

Table 4.10: Table showing all the systematic uncertainties as considered in the analysis, if they are considered as normalization uncertainties, or shape uncertainties. For small backgrounds, no systematics is treated as shape.

Due to the very low statistics of the remaining backgrounds (W+jets, Z+jets, di-bosons, single top), we are merging all of them into a single component as it will prevent us from pathological behavior in the treatment of some systematic uncertainties, *e.g.* when a bin is empty in the nominal case, while an entry appears in a variation. For the QCD background, showing shaky templates with no real physical meaning, we take the shape of the sum of all the other backgrounds just listed, normalize it to the estimated yield from the Matrix Method, and add it to the sum. The total of all these backgrounds is referred to as '*allSB*' in the following.

This treatment is motivated by the fact that we do not expect any resonance for these backgrounds, which is actually verified. Specific systematic variations of each background, *e.g.* uncertainties on cross-section normalization, are applied separately to each corresponding component, and then added to the others in the nominal case to form a variational histogram of the sum.

Contrary to what was described in Table 4.10, all systematics are considered as normalization only for this small-background component. For the TIGHT selection, we take the values derived from the LOOSE selection, as we do not expect significant difference between the two cases.

4.9.3 Results

A summary of the effect of each sources of systematic uncertainty can be found in Tab. 4.11 for the LOOSE analysis, and in Tab. 4.12 for the TIGHT analysis.

For the LOOSE analysis, the biggest uncertainties can be seen to come from the b-tagging, the Jet Energy Scale, and the QCD estimation. For the TIGHT analysis, the $t\bar{t}$ modeling has the biggest effect.

	$u_4\bar{u}_4$(500 GeV)	$t\bar{t}$	allSB
BTAG	+6.9/-5.1	+6.2/-4.7	-3.8/+3.2
CTAG	+0.3/-0.3	+0.3/-0.3	-3.3/+3.2
ELECTRONIDSF	+1.1/-1.1	+1.0/-1.0	+0.6/-0.6
ELECTRONRECOSF	+0.4/-0.4	+0.4/-0.4	+0.1/-0.1
ELECTRONTRIGSF	+0.3/-0.3	+0.2/-0.2	+0.1/-0.1
Frag	–	+7.8/-7.8	–
JER	+1.7/-1.7	+0.7/-0.7	+2.1/-2.1
JES	+2.7/-2.8	+18.5/-17.9	-9.2/+18.2
JMR	+3.9/-3.9	+0.8/-0.8	+2.2/-2.2
JMS	+1.5/-1.5	+0.7/-2.7	-0.6/+3.0
JVF	+3.5/-4.0	+2.7/-2.8	-2.6/+2.8
LTAG	+0.2/-0.2	+0.3/-0.3	-2.5/+2.4
Luminosity	+3.9/-3.9	+3.9/-3.9	+3.9/-3.9
MUONIDSF	+0.4/-0.4	+0.4/-0.4	+0.0/-0.0
MUONRECOSF	+0.2/-0.2	+0.2/-0.2	+0.2/-0.2
MUONTRIGEFF	+1.1/-1.1	+1.1/-1.1	+0.7/-0.7
NLO	–	+5.1/-5.1	–
PS	+0.7/-0.7	+3.3/-3.3	–
QCD XS stat	–	–	+28.3/-28.3
QCD XS syst	–	–	+11.6/-11.6
WjetsHF $b\bar{b}c\bar{c}$ norm	–	–	-4.8/+5.1
WjetsHF $b\bar{b}c\bar{c}$ scale	–	–	+5.2/-5.2
WjetsHF c scale	–	–	-1.1/+1.2
WjetsHF Light norm	–	–	-3.7/+3.6
Wjets XS	–	–	+15.8/-15.8
Zjets XS	–	–	+1.6/-1.6
dibosons XS	–	–	+0.0/-0.0
singleTop XS	–	–	+1.5/-1.9
ttbar XS	–	+9.9/-10.7	–
Total	+10.3/-9.4	+24.6/-24.3	+37.5/-40.7

Table 4.11: Table summarizing the overall normalization changes (expressed in %) in signal and each of the background processes for each of the systematic uncertainties considered. The selection presented here is the combined e+jets and μ+jets channels in the LOOSE analysis.

4.10 Statistical analysis

4.10.1 Combined log-likelihood

We use the M_{reco} distribution after final selection for each of the two selection studied, which is used in the statistical analysis to test for the presence of a signal at each values of hypothesized u_4 mass:

	$u_4\bar{u}_4$(500 GeV)	$t\bar{t}$	allSB
BTAG	+7.0/-5.1	+6.3/-5.5	+3.2/-3.8
CTAG	+0.3/-0.3	+0.7/-0.7	+3.2/-3.3
ELECTRONIDSF	+1.0/-1.0	+0.9/-0.9	+0.6/-0.6
ELECTRONRECOSF	+0.4/-0.4	+0.3/-0.3	+0.1/-0.1
ELECTRONTRIGSF	+0.3/-0.3	+0.2/-0.2	+0.6/-0.6
Frag	–	+13.7/-13.7	–
JER	+1.3/-1.3	+5.7/-5.7	+2.1/-2.1
JES	+2.7/-2.2	+21.8/-23.9	+18.2/-9.2
JMR	+4.1/-4.1	+1.2/-1.2	+2.2/-2.2
JMS	+1.2/-1.4	+0.5/-5.4	+3.0/-0.6
JVF	+3.6/-4.0	+3.2/-3.5	+2.8/-2.6
LTAG	+0.2/-0.2	+0.6/-0.6	+2.4/-2.5
Luminosity	+3.9/-3.9	+3.9/-3.9	+3.9/-3.9
MUONIDSF	+0.4/-0.4	+0.4/-0.4	+0.0/-0.0
MUONRECOSF	+0.2/-0.2	+0.2/-0.2	+0.2/-0.2
MUONTRIGEFF	+1.1/-1.1	+1.2/-1.2	+0.7/-0.7
NLO	–	+50.4/-50.4	–
PS	+0.2/-0.2	+10.7/-10.7	–
QCD XS stat	–	–	+26.4/-26.4
QCD XS syst	–	–	+33.7/-33.7
WjetsHF $b\bar{b}c\bar{c}$ norm	–	–	+5.1/-4.8
WjetsHF $b\bar{b}c\bar{c}$ scale	–	–	+5.2/-5.2
WjetsHF c scale	–	–	+1.2/-1.1
WjetsHF Light norm	–	–	+3.6/-3.7
Wjets XS	–	–	+13.4/-13.4
Zjets XS	–	–	+1.7/-1.7
dibosons XS	–	–	+0.0/-0.0
singleTop XS	–	–	+0.6/-0.7
ttbar XS	–	+9.9/-10.7	–
Total	+10.3/-9.3	+59.3/-60.5	+49.8/-47.2

Table 4.12: Table summarizing the overall normalization changes (expressed in %) in signal and each of the background processes for each of the systematic uncertainties considered. The selection presented here is the combined e+jets and μ+jets channels in the TIGHT analysis.

400, 450, 500, 550, 600, 650, 700 and 750 GeV.

Hypothesis testing is performed using a Hybrid Bayesian-Frequentist approach based on the CL_s method [163] as implemented in MCLIMIT [164], using a log-likelihood ratio (LLR) as test statistic:

$$LLR = -2\ln\frac{\mathscr{L}(data|H_1)}{\mathscr{L}(data|H_0)} \tag{4.15}$$

where H_1 denotes the test hypothesis, which admits the presence of a $u_4\bar{u}_4$ signal in addition to the SM backgrounds, while H_0 is the null hypothesis, considering only SM backgrounds. For a given hypothesis, the combined likelihood is the product of the likelihoods for the individual channels considered, each of which is a product of Poisson probabilities over the bins of the histogram for the final

discriminant. Therefore, the combined log-likelihood is given by:

$$-2\ln\mathscr{L}(data|H_i) = -2\ln\mathscr{L}(\vec{n}|R,\vec{s},\vec{b},\vec{\theta}) = -2\sum_{i=1}^{N_{chan}}\sum_{j=1}^{N_{bins}}(n_{ij}\ln\mu_{ij}-\mu_{ij}) + \sum_{k=1}^{N_{par}}\theta_k^2 \tag{4.16}$$

where the first sum is over the number of channels N_{chan} and the second sum is over the number of histogram bins N_{bins} containing n_{ij} events in data. The expected number of events for channel i in histogram bin j, μ_{ij}, is given by $\mu_{ij} = Rs_{ij}(\vec{\theta}) + b_{ij}(\vec{\theta})$, where s_{ij} and b_{ij} represent the expected signal and background yields, and R is a scaling parameter applied to the signal to test the sensitivity of the search[26]. In the case of the null-hypothesis, the signal yield in the expression of μ_{ij} is zero. Both signal and background yields per bin are functions of nuisance parameters $\vec{\theta}$ which parametrize the effect of normalization and shape systematics. These parameters are assigned Gaussian penalty terms in the likelihood corresponding to their nominal uncertainties.

4.10.2 CL_s and limits

Given an observed value of *LLR*, $LLR_{\rm obs}$, either in data or a pseudo-experiment, the CL_s method [163] involves computing two p-values, CL_{s+b} and CL_b, which are obtained from the *LLR* distribution for signal-plus-background (H_1) and background-only (H_0) pseudo-experiments, respectively, as given by:

$$\begin{aligned} CL_b &= p(LLR \le LLR_{\rm obs}|H_0), \\ CL_{s+b} &= p(LLR \ge LLR_{\rm obs}|H_1). \end{aligned}$$

The interpretation of these p-values is as follows: $1-CL_b$ represents the probability that a background fluctuation (without the presence of a signal) provides a *LLR* value as signal-plus-background like or more as that observed in the data; CL_{s+b} represents the probability of a downward fluctuation of signal-plus-background in the data. Thus, a small value of CL_{s+b} reflects inconsistency with H_1. However, it is possible that a downward background fluctuation in the data could yield a small value of CL_{s+b}, even if the expected sensitivity is so small that H_1 cannot really be tested by the experiment. To minimize the probability of excluding a signal to which there is insufficient sensitivity (an outcome expected 5% of the time at the 95% C.L.), we use the quantity $CL_s = CL_{s+b}/CL_b$. If $CL_s < 0.05$ for a particular choice of H_1, that hypothesis is deemed to be excluded at the 95% C.L. H_1 is defined in terms of m_{u_4} and $R = \sigma(u_4\bar{u}_4)/\sigma^{\rm th}(u_4\bar{u}_4)$, where $\sigma^{\rm th}(u_4\bar{u}_4)$ is the theoretical prediction. For a given hypothesized m_{u_4}, we report the observed 95% C.L. limit in R, $R_{95}^{\rm obs}$. Whenever $R_{95}^{\rm obs} < 1$, such value of m_{u_4} is excluded at the 95% C.L. Similarly, we report the expected 95% C.L. limit in R, $R_{95}^{\rm exp}$, obtained from the median of the *LLR* distribution for the background-only hypothesis.

4.10.3 Treatment of systematic uncertainties

Systematic uncertainties are included by fluctuating[27] the predictions for signal and background rates in each histogram bin taking into account both Poisson statistical fluctuations as well as Gaussian fluctuations for each of the systematic uncertainties. Individual sources of systematic uncertainty are considered uncorrelated. We maintain correlations of a given systematic uncertainty across processes and channels.

[26] This is the equivalent of the signal strength μ that we introduced in Sec. 4.2.

[27] In the form of the generation of pseudo-experiments.

4.10.3.1 Interpolation method

The standard method implemented in MCLIMIT is to interpolate the histograms between the nominal and the shifted templates, *e.g.* the ones that were shown in Fig. 4.30. Thus a shift of 0.5 sigma will correspond to half way between the nominal and +1 sigma shifted template. This is carried out bin-by-bin. Such an interpolation method is referred to as vertical morphing using a linear interpolation. Some of the uncertainties produce very asymmetric effects. Using only a linear interpolation will in this case produce a non-defined derivative at zero, which can in term cause kinks in the likelihood functions and thus problem with the fitting.

A number of different interpolation methods have been tested that allow a smooth transition between the negative and positive shifts where the derivative at the nominal point is defined. We decided to use a quadratic interpolation for variations <1 sigma absolute differences. For deviations larger than 1 sigma we revert to linear extrapolation. We apply interpolation of all systematic uncertainties and generate pseudo-experiments using these interpolated numbers.

4.10.3.2 Profiling

In order to improve the sensitivity of the analyzes with the LOOSE selection, the log-likelihoods entering the calculation of the *LLR* are separately minimized[28] over a single nuisance parameter representing the overall $t\bar{t}$ yield, subject to a Gaussian penalty term quantifying the total a-priori uncertainty. This uncertainty is assigned a value of 24%, corresponding to the sum in quadrature of all normalization uncertainties (both flat and shaped) affecting the $t\bar{t}$ background.

This procedure takes advantage of the background-dominated low M_{reco} sideband region, which absorbs the cumulative effect of different possible sources of uncertainty affecting the $t\bar{t}$ background normalization.

No profiled parameters are used for the TIGHT selection.

4.10.4 Treatment of statistical uncertainty

The statistical uncertainty of the MC samples is taken into account when computing our likelihoods. The MCLIMIT flag used is 2, meaning we consider the uncertainties as given by the uncertainties of the templates. This allows us to correctly estimate the statistical uncertainty when many templates are merged together with different weights, such as the W+jets.

[28] A procedure also called 'profiling' of a parameter.

4.11 Results

This section presents the results of the combined fit to electrons and muons considering tagged events combining CHANNEL 1 and CHANNEL 2. The four orthogonal channels are merged together into a single channel to gain statistic for the limits setting procedure.

4.11.1 Inputs to the Limits

Figure 4.31 shows the input distribution to the limits with final binning for a u_4 mass of 500 GeV at its expected theoretical cross section for the LOOSE selection on the left and TIGHT selection on the right.

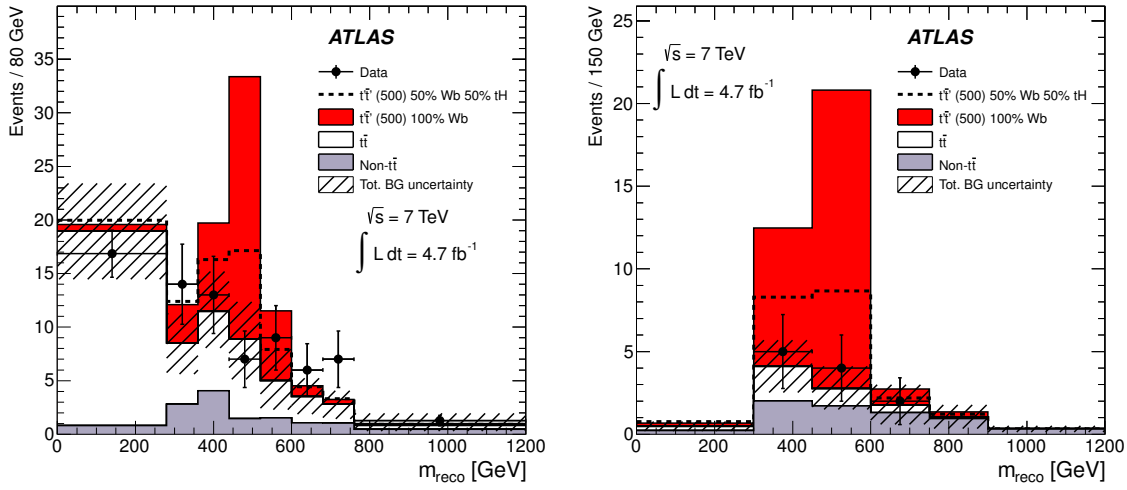

(a) LOOSE selection

(b) TIGHT selection

Figure 4.31: Distribution of m_{reco} for the combined e+jets and μ+jets channels after the (a) *loose* and (b) *tight* selection. The data (solid black points) are compared to the SM background prediction. The total uncertainty on the background estimation is shown as a black hashed band. Also shown, stacked on top of the SM background, are the expected contributions from a signal with mass $m_{t'} = 500$ GeV for the case of $BR(t' \to Wb) = 1$ (plain red histogram), corresponding to a fourth-generation t' quark, as well as the case of $BR(t' \to Wb) = BR(t' \to Ht) = 0.5$ (dashed black histogram). The overflow has been added to the last bin.

All the small backgrounds (W+jets, Z+jets, single-top, di-bosons) are merged together in a single template (in grey), while the main background $t\bar{t}$ (in white) is kept separated. Data points are shown with the black dots. Tables 4.13 and 4.14 summarizes for the TIGHT and LOOSE selection respectively the total expected backgrounds yields with statistic and full systematics as well as expected 500 GeV signal yields and observed data events. We can conclude that within uncertainties our observed data number of events are consistent with predictions, and no significant excess in the limit procedure are expected.

TIGHT selection	
u_4(500 GeV)	$27.00 \pm 0.62\ ^{+3.10}_{-2.82}$
$t\bar{t}$	$3.96 \pm 0.47\ ^{+2.35}_{-2.39}$
allSB	$7.24 \pm 1.12\ ^{+3.61}_{-3.42}$
Total bkg.	$11.20 \pm 1.22\ ^{+4.60}_{-4.37}$
Data	11

Table 4.13: Table summarizing for the TIGHT selection the statistical and total systematic errors for the backgrounds and the signals. Yields have to be compared to data observed events.

LOOSE selection	
u_4(500 GeV)	$46.32 \pm 0.82\ ^{+5.94}_{-5.33}$
$t\bar{t}$	$91.48 \pm 2.09\ ^{+22.49}_{-22.21}$
allSB	$17.73 \pm 1.52\ ^{+6.64}_{-7.22}$
Total bkg.	$109.22 \pm 2.58\ ^{+24.94}_{-25.86}$
Data	122

Table 4.14: Table summarizing for the LOOSE selection the statistical and total systematic errors for the backgrounds and the signals. Yields have to be compared to data observed events.

4.11.2 Log Likelihood Ratio Distributions

Figure 4.32 shows the Log Likelihood ratios for a u_4 mass of 500 GeV at its expected theoretical cross section. The two curves are for the background only hypothesis (blue) and the signal+background hypothesis (red). The black vertical line shows the observed Likelihood value in data.

Plots like these are used to determine the observed and expected confidence level. The integral of the signal+background distribution from the black line to infinity gives the CL_{s+b}. The integral of the background only distribution from minus infinity to the black line gives the CL_b of interest for the signal significance test. The ratio of the two gives the gives the exclusion CL_s value. The bottom two plots show the TIGHT selection case, while the upper two plots show the LOOSE selection case. Left plots show the case where we consider only statistical uncertainties, and the right plots where we do consider all the systematics uncertainties in addition. In both left and right plots the observed value is identical (as there is no profiling involved). Note the change of scale between statistics only and with all systematics which shows the degradation of the Likelihood Ratio Distributions when considering systematics.

Figure 4.33 shows the evolution of the LLR distributions as a function of the u_4 mass including the median and one and two sigma bands for the LOOSE selection on the right and the TIGHT selection on the left. The cut through these plots at 500 GeV corresponds to the plots shown in Fig. 4.32 (b) and (d).

Already from these plots we can tell that we expect to be able to separate background from signal+background hypotheses up to order 500 GeV.

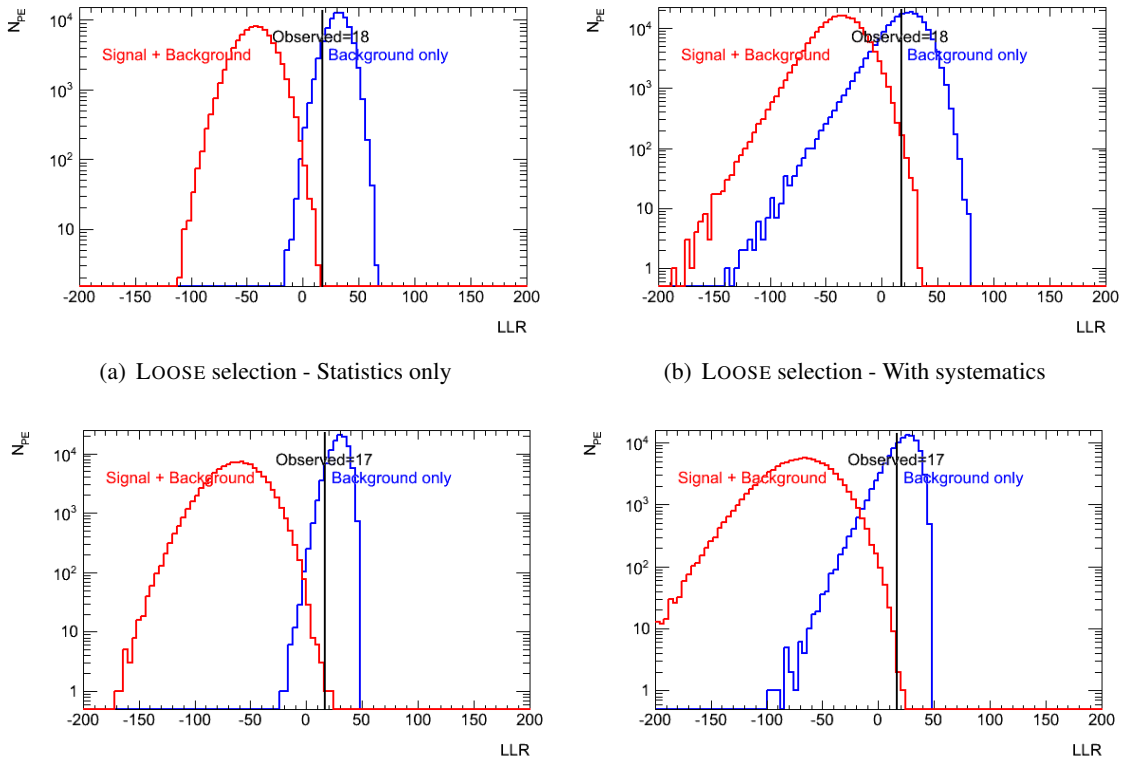

(a) LOOSE selection - Statistics only

(b) LOOSE selection - With systematics

(c) TIGHT selection - Statistics only

(d) TIGHT selection - With systematics

Figure 4.32: Values of the Log Likelihood Ratios for the background only hypothesis (blue) and the signal+background hypothesis (red). Shown as a black vertical line is the observed value in data. The signal hypothesis shown here is for a 500 GeV u_4 quark at its expected cross section. Upper (bottom) plots are for the LOOSE (TIGHT) selection. Left plots show the distributions considering only statistical uncertainties. Right plots include in addition systematic uncertainties.

4.11.3 Signal significance test

We compute CL_b values to evaluate the probability that our data is compatible with the background only hypothesis. Figure 4.34 shows $1 - CL_b$ as a function of m_{u_4} for the LOOSE selection on the left, and the TIGHT selection on the right. From these plots, we can see that the observed data is not significantly un-compatible with the background only hypothesis, for all mass points.

4.11.4 Limit setting

Following the statistical analysis discussed in Sect. 4.10, we derive limits on $\sigma(u_4\bar{u}_4)$ at 95% C.L. as a function of m_{u_4} for the $B(u_4 \to Wb) = 1$ benchmark scenario. Values of $\sigma(u_4\bar{u}_4)$ for which $CL_s < 0.05$ are deemed to be excluded at the 95% C.L.

Figure 4.35 shows the expected CL_s as a function of m_{u_4} for the combination of four channels, the LOOSE selection is represented on the left, and the TIGHT selection on the right. The observed CL_s is also shown as the black solid line. Those include all the statistical and systematic uncertainties.

Table 4.15 compares the ratios of the median expected and observed 95% C.L. limits on $\sigma(u_4\bar{u}_4)$

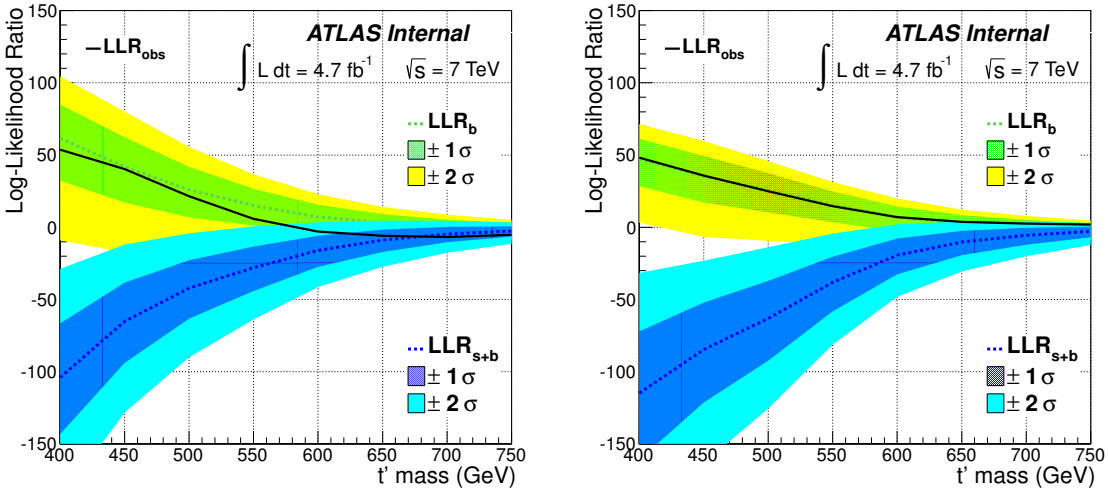

(a) LOOSE selection (b) TIGHT selection

Figure 4.33: Observed and expected Likelihood ratio for b-only (green tones) and s+b (blue tones) hypothesis as a function of m_{u_4} from the combination of the four channels in the $B(u_4 \to Wb) = 1$ benchmark scenario. The green line and bands correspond to the b-only hypothesis ± 1 standard deviation (s.d.) and 2 s.d. intervals. The blue line and bands correspond to the s+b hypothesis ± 1 standard deviation (s.d.) and 2 s.d. intervals. The black line corresponds to the observed Likelihood ratio. Left plot is show the LOOSE selection and right plot the TIGHT selection

relative to the theoretical prediction for the $B(u_4 \to Wb) = 1$ benchmark scenario, with and without including systematic uncertainties. Those mass values for which this ratio is below 1 are excluded at 95% CL.

The resulting observed and expected upper limits on the $u_4\bar{u}_4$ production cross-section are shown in Fig. 4.36 as a function of m_{u_4}, and compared to the theoretical prediction. An observed (expected) 95% CL limit $m_{u_4} > 580\,(633)$ GeV is derived for the LOOSE selection. An observed (expected) 95% CL limit $m_{u_4} > 656\,(638)$ GeV is derived for the TIGHT selection, which is the most stringent limit to date on the mass of a fourth-generation u_4 quark decaying exclusively into a W boson and a b quark.

In terms of production cross-section for u_4u_4, the expected sensitivity is $\sigma(u_4u_4) < 63$ fb at 95% C.L. limit while the observed upper limit is $\sigma(u_4u_4) < 118$ fb for the LOOSE analysis. The expected sensitivity is $\sigma(u_4u_4) < 59$ fb at 95% C.L. limit while the observed upper limit is $\sigma(u_4u_4) < 55$ fb for the TIGHT analysis.

An important remark is that the analysis was conducted in a 'blinded' way, which means that we have not looked at the real data before choosing (or *freezing*) the final cuts of the analysis. Due to the better expected sensitivity of the TIGHT selection, it was decided before *un-blinding* the data to chose this selection for the publication.

4.11.5 Vector like Quark interpretation

The same analysis is used to derive exclusion limits on vector-like t' quark production, for different values of $m_{t'}$ and as a function of the two branching ratios $BR(t' \to Wb)$ and $BR(t' \to Ht)$. The

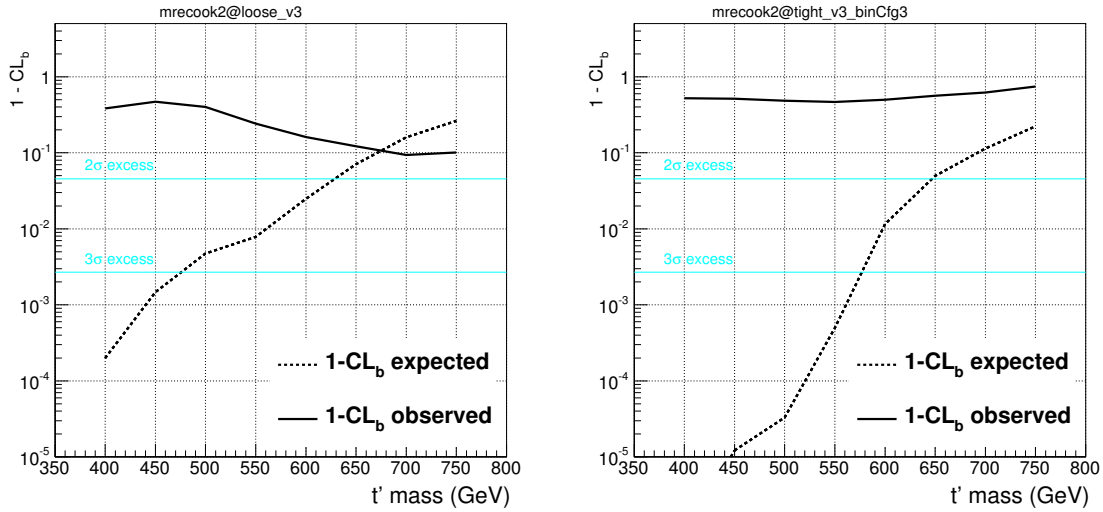

(a) LOOSE selection (b) TIGHT selection

Figure 4.34: Comparison of observed and expected $1-\mathrm{CL_b}$ as a function of m_{u_4} for the combination of the four channels. The grey line corresponds to the expected $1-\mathrm{CL_b}$ in presence of a $u_4\bar{u}_4$ signal assuming the $B(u_4 \to Wb) = 1$ benchmark scenario, while the black line corresponds to the observed $1-\mathrm{CL_b}$, in both cases including systematic uncertainties. The LOOSE selection, is represented on the left, TIGHT selection on the right

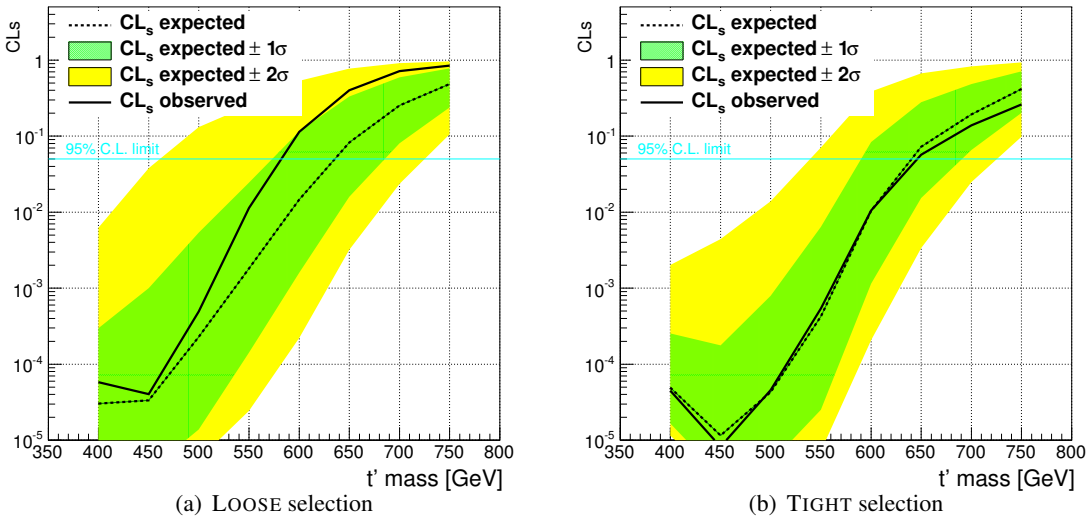

(a) LOOSE selection (b) TIGHT selection

Figure 4.35: Expected CLs for the LOOSE (a) and TIGHT (b) selection, with all sources of systematic uncertainties included. Shaded bands are the associated errors. The solid black line is the observed CLs.

branching ratio $BR(t' \to Zt)$ is fixed by $BR(t' \to Zt) = 1 - BR(t' \to Wb) - BR(t' \to Ht)$. To probe this two-dimensional branching-ratio plane, the signal samples with the original branching ratios as

m_{u_4} (GeV)	400	450	500	550	600	650	700	750
e+jets and μ+jets combined								
Expected LOOSE (pb) (Stat)	0.214	0.133	0.087	0.061	0.048	0.040	0.036	0.033
Expected LOOSE (pb)	0.384	0.243	0.145	0.094	0.072	0.059	0.053	0.050
Expected LOOSE +1 s.d.	0.246	0.158	0.097	0.063	0.047	0.038	0.034	0.032
Expected LOOSE -1 s.d.	0.621	0.383	0.235	0.149	0.113	0.094	0.086	0.081
Observed LOOSE (pb)	0.431	0.239	0.159	0.130	0.111	0.102	0.097	0.090
Expected TIGHT (pb) (Stat)	0.216	0.131	0.078	0.056	0.049	0.042	0.036	0.034
Expected TIGHT (pb)	0.312	0.190	0.109	0.075	0.066	0.057	0.048	0.046
Expected TIGHT +1 s.d.	0.203	0.123	0.072	0.050	0.043	0.038	0.032	0.030
Expected TIGHT -1 s.d.	0.500	0.301	0.171	0.118	0.104	0.089	0.075	0.068
Observed TIGHT (pb)	0.317	0.195	0.115	0.080	0.067	0.053	0.041	0.035

Table 4.15: Expected and observed cross section 95% C.L. limits (in pb) on $\sigma(u_4\bar{u}_4)$ for the $B(u_4 \to Wb) = 1$ benchmark scenario, as a function of m_{u_4}. Limits are quoted with statistical and systematic uncertainties fully accounted for, and with statistical uncertainties only ("Stat").

generated by PROTOS are weighted. The resulting 95% CL exclusion limits are shown in Fig. 4.37 for different values of $m_{t'}$. For instance, a t' quark with mass of 550 GeV and $BR(t' \to Wb) > 0.63$ is excluded at $\geq 95\%$ CL, regardless of the value of its branching ratios to Ht and Zt. All the decay modes contribute to the final sensitivity when setting limits. For example, assuming $m_{t'} = 550$ GeV, the efficiency of the *tight* selection with at least four jets is 2.67%, 0.64%, 0.81%, 0.27%, 0.24% and 0.25%, for decays to $WbWb$, $WbHt$, $WbZt$, $ZtHt$, $ZtZt$ and $HtHt$, respectively. The default predictions from PROTOS for the weak-isospin singlet and doublet cases are also displayed. A weak-isospin singlet t' quark with $400 \leq m_{t'} \leq 500$ GeV is excluded at $\geq 95\%$ CL. It should be noted that since this analysis is optimized for $m_{t'} \gtrsim 400$ GeV (recall the $H_{\mathrm{T}} > 750$ GeV requirement), it is not sensitive for vector-like quark scenarios where $m_{t'} < 400$ GeV. The doublet scenarios are shown on Fig. 4.37 to illustrate the fact that this analysis has no sensitivity in these cases.

4.12 Conclusion

We searched for pair-production of a sequential 4^{th} generation quark with its antiparticle followed by their decays to a W boson and a b-quark, $u_4\bar{u}_4 \to W^+bW^-\bar{b}$, based on 4.7 fb^{-1} of proton-proton collisions at $\sqrt{s} = 7$ TeV collected in 2011 by the ATLAS detector at the Large Hadron Collider.

A novel strategy in the lepton-plus-jets channel was presented. It is based on the explicit reconstruction of high-momentum W bosons, identified either as single jets, or as pairs of two close-by jets, and on the use of b-tagging. Signal over background ratio was shown to be extremely high compared to previous searches conducted at the Tevatron and at the LHC, even for u_4 quark masses as high as ≈ 650 GeV.

Inspired by ideas from [142], we initiated this project showing studies using jets with a size $R = 1.0$, compared to studies using only jets with size $R = 0.4$. We concluded that under a few assumptions, the two solutions were roughly equivalent. We initiated a collaboration with the IFAE

Barcelona group, which lead to the publication of [182].

No significant excess over the expected SM background was observed. We set upper limits on the $u_4\bar{u}_4$ production cross section, which translated into an observed (expected) 95% CL limit $m_{u_4} > 656\,(638)$ GeV of a fourth-generation u_4 quark decaying exclusively into a W boson and a b quark.

The strategy followed in this search, directly exploiting the distinct boosted signature expected in the decay of a heavy u_4 quark, has resulted in the most stringent limits to date on a fourth-generation u_4 quark decaying exclusively into a W boson and a b quark. This approach shows great promise for improved sensitivity in future LHC searches at higher center-of-mass energy and integrated luminosity. This search was also interpreted more generically in the context of vector-like quark models, resulting in the first quasi-model independent exclusions in the two-dimensional plane of $BR(t' \to Wb)$ vs $BR(t' \to Ht)$, for different values of the t' quark mass.

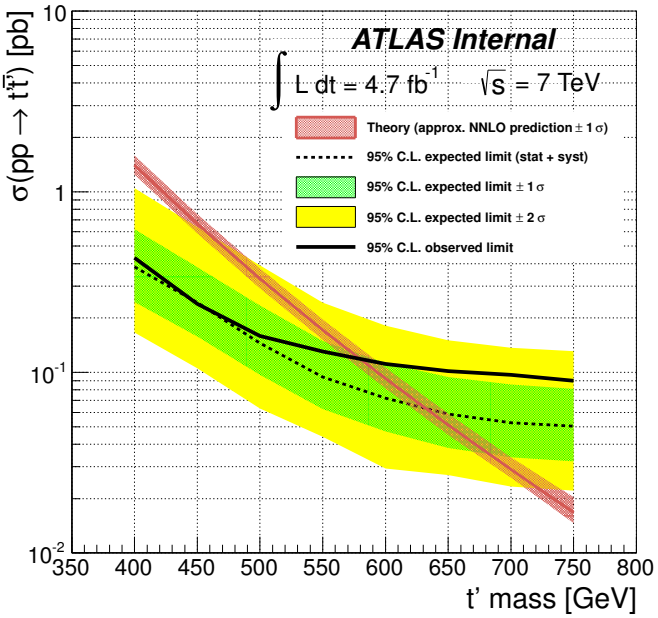

(a) LOOSE selection

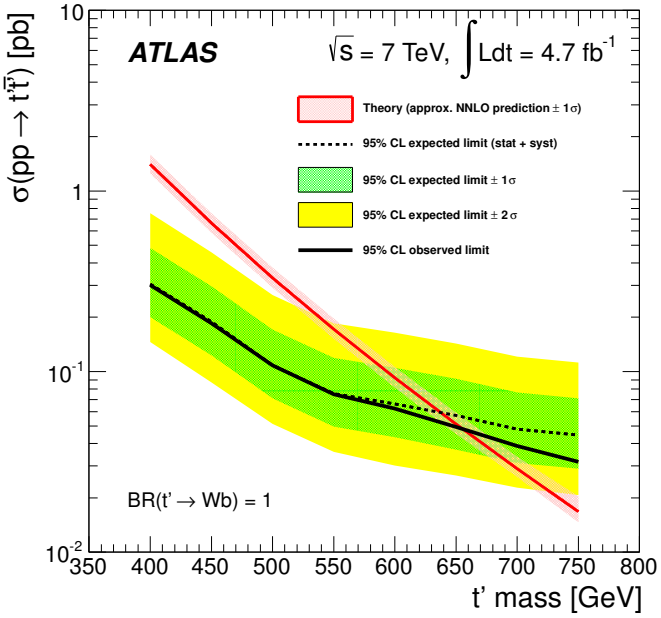

(b) TIGHT selection

Figure 4.36: Observed (solid line) and expected (dashed line) 95% CL upper limits on the $u_4\bar{u}_4$ cross-section as a function of the u_4 quark mass, for the LOOSE and TIGHT selections. The surrounding shaded bands correspond to the ± 1 and ± 2 standard deviations around the expected limit. The thin red line and band show the theoretical prediction and its ± 1 standard deviation uncertainty.

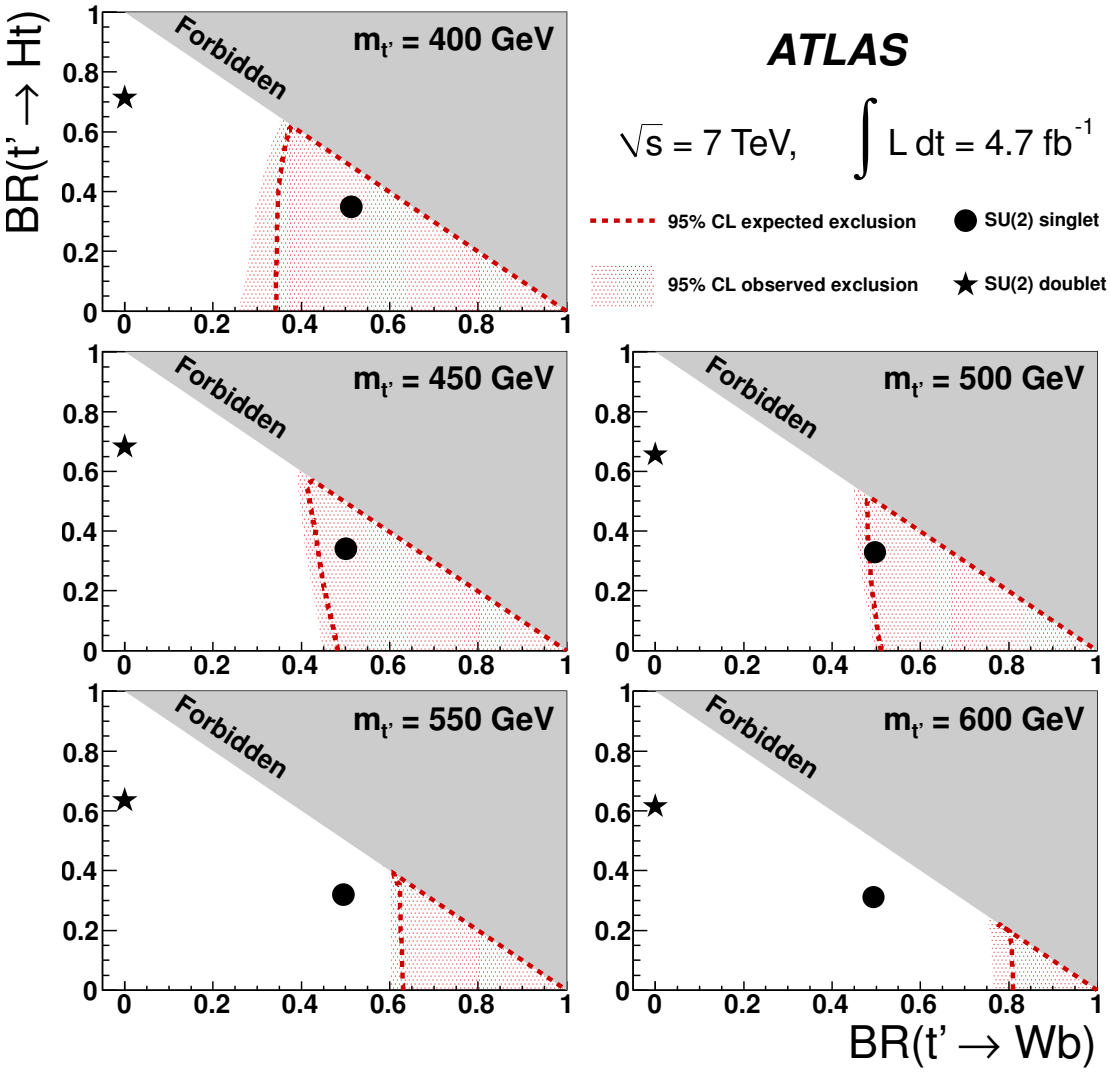

Figure 4.37: Observed (red filled area) and expected (red dashed line) 95% CL exclusion on the plane of $BR(t' \to Wb)$ vs $BR(t' \to Ht)$, for different values of the vector-like t' quark mass. The grey solid area corresponds to the unphysical region where the sum of branching ratios exceeds unity. The default branching ratio values from the PROTOS event generator for the weak-isospin singlet and doublet cases are shown as plain circle and star symbols, respectively.

Conclusion and perspectives

Thanks to the outstanding performance of the LHC which started to deliver its first collisions a few months after the beginning of this thesis, we were extremely lucky to work during such an exciting period, which saw the re-discovery of the Standard Model, and the observation of a new boson ! We had the opportunity to work on many aspects of experimental particle physics.

Regarding detector-related aspects, we participated in many shifts of the pixel detector - which performance is crucial for *b*-tagging capabilities - which was the occasion to get more familiar with the functioning and calibration procedures of this amazing detector, and with LHC operation cycles. We also contributed to a sonar system intended to detect coolant leaks in the pixel detector volume, that could potentially destroy irreversibly some junctions on the modules, hence affecting the entire ATLAS experiment. In particular, it allowed to detect one leaking stave. We also contributed to the Technical Design Report of the 'Insertable B-Layer' upgrade project, by assessing and optimizing the *b*-tagging performance in different configurations with this extra layer of detection. These results played an important role in the decision to build this new detector, which is currently being constructed, and which should be inserted in ATLAS before the LHC starts again in 2014.

Regarding *performance*-related aspects, which is the interface between the detectors and the physical objects, we made tracking studies with the first 900 GeV LHC data. We commissioned and optimized the JetProb *b*-tagging algorithm that turned out to be usable for first ATLAS physics analysis in 2010. Typically, this algorithm can reach a light jet rejection of $\sim$20 for a 70% *b*-tagging efficiency working point. Later on, with 330 pb^{-1} of the 2011 7 TeV data, we commissioned the much more complex algorithms based on Likelihood Ratios and Neural Network techniques, the most advanced *b*-tagging algorithms that were developed thanks to many years of study before the LHC start-up. This work led the ATLAS *b*-tagging group to declare in July 2011 that the agreement between data and simulation was good enough to allow their calibration in data, and their use in ATLAS physics analyzes. During all these periods, we were responsible of the production of the 'reference histograms', allowing the proper functioning of *b*-tagging algorithms, which was of key importance during the various ATLAS data re-processings. Light jet rejection factors of these *high-performance* taggers can reach $\sim$145 for a 70% *b*-tagging efficiency working point. Such rejection power for such a high efficiency working point is quite remarkable, and is especially promising for searches of low cross-section processes. At the same time, the CMS experiment was still using its *early* taggers. Given the numerous ATLAS analyzes that used *b*-tagging since the start of the LHC, we can claim that this work contributed to increase ATLAS physics reach as well as the competitiveness of the experiment.

Building on this work on *b*-tagging, we searched for new heavy quarks. This was motivated initially by the model of fourth generation, which is one of the simplest extensions to the SM. This model was shown to have numerous attractive features, *e.g.* in cosmology, and its search appeared very well motivated both before and after the recent observation at the LHC. Prior to it, such model could for example have allowed to break dynamically the electroweak symmetry of the SM, replacing the minimal solution which is the SM scalar boson. After the recent observation, this model is still viable in

many scenarios, which keeps justifying searching directly for the production and decay of such heavy quarks. In particular, we looked at one of the most interesting processes we isolated: the decay of pair-produced up-type quarks $t' \to Wb$ in the lepton plus jets channel assuming BR$(t' \to Wb) = 100\%$. We presented a novel search strategy that exploits specifically the kinematic differences between top and t' quarks decays, with 4.7 fb^{-1} of the 7 TeV LHC data. This search takes its strength mainly from the explicit reconstruction of a high-p$_T$ W boson decaying hadronically – using single jets, or very close-by jets – and also from the use of the b-tagging algorithms that we commissioned previously. We initiated this project presenting prototype studies using different jet cone sizes. Then, we initiated a collaboration with the Barcelona group which allowed to make this work public. Most importantly, we were sensitive for the first time to t' masses higher than 570 GeV, which was the exclusion limit previously set by the CMS experiment with the same amount of data. While we observed no significant excess of events above the SM background expectation, an observed (expected) 95% CL lower limit $m_{t'} > 656\ (638)$ GeV was derived, which is hence the most stringent limit to date. The observed (expected) limit (sensitivity) of our analysis is $\sim$250 (240) GeV better than the previous ATLAS limit (using only 1 fb^{-1} of data though), and $\sim$90 (50) GeV better than the current best CMS limit, and even better than the b' observed exclusion limit of 611 GeV. This search strategy was also seen to be quite generic, *e.g.* being directly applicable to Vector-Like quarks, and resulted in the first quasi-model independent exclusions in the two-dimensional plane of $BR(t' \to Wb)$ vs $BR(t' \to Ht)$, for different values of the t' quark mass, which is especially relevant after the recent observation of a particle compatible with the SM scalar boson. Such results demonstrate that the strategy followed in this search shows a much improved sensitivity compared to previous searches, and great promise in future LHC searches at higher center-of-mass energies and integrated luminosities. As an example, the reconstruction of W-jets might also be useful in searches for signatures with more W bosons in the final states (*e.g.* considering $t' \to b'$ decays), scenarios where new heavy quarks could also hide.

Appendices

Appendix A

Efficiency of cuts for signals and backgrounds

Here we present the yields after each cut for the background samples and the signal samples as well as the cut efficiency (which, in the case of the backgrounds, is defined as the rejection efficiency). Table A.1 reports the definition of the cuts with the schematic name that will be used in Tables A.2, A.3, A.4 and A.5 where the cutflow for electron and muon channels for background and signal in CHANNEL 1 and CHANNEL 2 respectively are shown.

Table A.1:

	CHANNEL 1	CHANNEL 2
preCut0	$\geq$ 3jets ($p_T > 25$ GeV)	
preCut1	$\geq 1b$tag	
preCut2	$H_T > 750$ GeV	
preCut3	$\geq$ 1 Wjet	$= 0$ Wjets
preCut4	—-	$\geq$ 4jets ($p_T > 25$ GeV)
preCut5	—-	$\geq$ 1 hand-merged Wjet
Cut0	$b\text{jet}_pT > 160, 60$ GeV	
Cut1	$\Delta R(l,\nu) < 1.4$	
Cut2	$\Delta R(Wj, bjets) > 1.4$	
Cut3	$\Delta R(l, bjets) > 1.4$	

Table A.2: Cutflow and cut rejection efficiency for background samples in the electron (top) and muon (bottom) CHANNEL 1.

	$t\bar{t}$		QCDele		Wjets		Zjets		singleTop		Dibosons	
	N	cut eff	N	cut eff	N	cut eff	N	cut eff	N	cut eff	N	cut eff
preCut0	33969.01 ± 41.59	n/a	13687.08 ± 158.88	n/a	57502.16 ± 196.77	n/a	7834.97 ± 49.65	n/a	4085.26 ± 18.29	n/a	1171.46 ± 6.22	n/a
preCut1	28013.89 ± 34.85	17.53%	17637.01 ± 415.94	-28.86%	6748.04 ± 42.30	88.26%	704.77 ± 7.98	91.00%	3010.24 ± 13.72	26.31%	186.45 ± 1.52	84.08%
preCut2	753.95 ± 6.10	97.31%	17715.22 ± 2006.49	-0.44%	258.70 ± 7.86	96.17%	37.37 ± 1.98	94.70%	91.83 ± 2.66	96.95%	3.42 ± 0.21	98.17%
preCut3 CH1	33.76 ± 1.33	95.52%	17801.05 ± 21890.40	-0.48%	5.61 ± 1.06	97.83%	1.49 ± 0.38	96.03%	4.96 ± 0.62	94.60%	0.21 ± 0.06	93.89%
Cut0 CH1	8.00 ± 0.69	76.31%	17800.44 ± 38682.32	0.00%	0.50 ± 0.21	91.08%	0.08 ± 0.04	94.51%	1.14 ± 0.32	76.97%	0.03 ± 0.03	84.29%
Cut1 CH1	6.32 ± 0.59	21.01%	17799.67 ± 23321.00	0.00%	0.41 ± 0.20	18.88%	0.04 ± 0.03	47.07%	0.72 ± 0.26	37.11%	0.03 ± 0.03	8.73%
Cut2 CH1	2.08 ± 0.35	67.02%	17799.06 ± 9258.18	0.00%	0.35 ± 0.20	14.10%	0.02 ± 0.02	57.10%	0.47 ± 0.23	34.07%	0.03 ± 0.03	0.00%
Cut3 CH1	0.18 ± 0.13	91.57%	17798.85 ± 17798.85	0.00%	0.07 ± 0.04	80.99%	0.00 ± 0.00	100.00%	0.13 ± 0.10	73.44%	0.00 ± 0.00	100.00%

	$t\bar{t}$		QCDmu		Wjets		Zjets		singleTop		dibosons	
	N	cut eff	N	cut eff	N	cut eff	N	cut eff	N	cut eff	N	cut eff
preCut0	52604.36 ± 51.85	n/a	26834.38 ± 83.28	n/a	118518.36 ± 291.43	n/a	10266.57 ± 73.48	n/a	6647.83 ± 23.01	n/a	2060.70 ± 8.30	n/a
preCut1	43972.62 ± 43.96	16.41%	6894.25 ± 35.19	74.31%	14318.14 ± 66.89	87.92%	1590.53 ± 14.57	84.51%	5003.20 ± 17.60	24.74%	438.83 ± 2.26	78.70%
preCut2	900.24 ± 6.73	97.95%	41.34 ± 2.76	99.40%	384.58 ± 12.14	97.31%	42.83 ± 2.44	97.31%	102.15 ± 2.82	97.96%	4.78 ± 0.24	98.91%
preCut3 CH1	40.16 ± 1.45	95.54%	2.95 ± 0.73	92.87%	12.35 ± 1.86	96.79%	1.48 ± 0.42	96.55%	5.93 ± 0.78	94.19%	0.13 ± 0.04	97.34%
Cut0 CH1	10.00 ± 0.70	75.11%	0.80 ± 0.36	72.73%	1.59 ± 0.55	87.15%	0.05 ± 0.04	96.46%	1.62 ± 0.46	72.62%	0.01 ± 0.01	96.02%
Cut1 CH1	6.51 ± 0.55	34.83%	−0.03 ± 0.01	103.96%	0.86 ± 0.36	45.55%	0.05 ± 0.04	0.00%	0.93 ± 0.41	42.81%	0.00 ± 0.00	100.00%
Cut2 CH1	2.71 ± 0.38	58.43%	−0.02 ± 0.01	48.25%	0.29 ± 0.16	66.12%	0.05 ± 0.04	0.00%	0.78 ± 0.39	15.61%	0.00 ± 0.00	n/a
Cut3 CH1	0.34 ± 0.16	87.57%	−0.01 ± 0.01	64.22%	0.19 ± 0.15	36.50%	0.02 ± 0.02	70.42%	0.34 ± 0.35	56.24%	0.00 ± 0.00	n/a

Table A.3: Cutflow and cut efficiency for signal samples in the electron (top) and muon (bottom) CHANNEL 1.

	$u_4\bar{u}_4400$		$u_4\bar{u}_4450$		$u_4\bar{u}_4500$		$u_4\bar{u}_4550$		$u_4\bar{u}_4600$		$u_4\bar{u}_4650$		$u_4\bar{u}_4700$		$u_4\bar{u}_4750$	
	N	cut eff	N	cut eff	N	cut eff	N	cut eff	N	cut eff	N	cut eff	N	cut eff	N	cut eff
preCut0	562.58 ± 6.07	n/a	281.23 ± 3.00	n/a	143.69 ± 1.51	n/a	77.69 ± 0.81	n/a	43.64 ± 0.45	n/a	24.30 ± 0.25	n/a	14.03 ± 0.17	n/a	8.11 ± 0.10	n/a
preCut1	504.73 ± 5.48	89.72%	252.97 ± 2.71	89.95%	129.81 ± 1.37	90.34%	70.47 ± 0.73	90.71%	39.54 ± 0.41	90.61%	22.07 ± 0.23	90.85%	12.78 ± 0.16	91.08%	7.39 ± 0.09	91.16%
preCut2	259.24 ± 3.94	51.36%	174.52 ± 2.27	68.99%	104.79 ± 1.23	80.73%	62.01 ± 0.69	88.00%	36.56 ± 0.39	92.45%	21.08 ± 0.22	95.49%	12.35 ± 0.16	96.64%	7.22 ± 0.09	97.67%
preCut3 CH1	14.70 ± 0.94	5.67%	13.45 ± 0.63	7.70%	9.66 ± 0.38	9.22%	6.91 ± 0.23	11.15%	5.00 ± 0.15	13.66%	3.58 ± 0.09	16.99%	2.42 ± 0.07	19.55%	1.59 ± 0.04	22.03%
Cut0 CH1	5.62 ± 0.58	38.21%	6.20 ± 0.43	46.09%	5.06 ± 0.28	52.39%	4.20 ± 0.18	60.82%	3.25 ± 0.12	65.04%	2.51 ± 0.08	70.18%	1.76 ± 0.06	72.84%	1.21 ± 0.04	76.17%
Cut1 CH1	4.68 ± 0.53	83.35%	5.12 ± 0.39	82.60%	4.33 ± 0.26	85.50%	3.59 ± 0.17	85.32%	2.83 ± 0.11	87.14%	2.24 ± 0.07	89.11%	1.58 ± 0.06	89.68%	1.12 ± 0.04	92.07%
Cut2 CH1	2.96 ± 0.43	63.13%	3.34 ± 0.31	65.31%	3.46 ± 0.23	79.93%	2.92 ± 0.15	81.35%	2.25 ± 0.10	79.42%	1.80 ± 0.07	80.31%	1.25 ± 0.05	79.32%	0.86 ± 0.03	77.29%
Cut3 CH1	1.22 ± 0.27	41.22%	1.77 ± 0.23	53.05%	2.33 ± 0.19	67.51%	2.07 ± 0.13	70.98%	1.52 ± 0.08	67.74%	1.32 ± 0.06	73.45%	0.88 ± 0.04	70.07%	0.63 ± 0.03	72.74%

	$u_4\bar{u}_4400$		$u_4\bar{u}_4450$		$u_4\bar{u}_4500$		$u_4\bar{u}_4550$		$u_4\bar{u}_4600$		$u_4\bar{u}_4650$		$u_4\bar{u}_4700$		$u_4\bar{u}_4750$	
	N	cut eff	N	cut eff	N	cut eff	N	cut eff	N	cut eff	N	cut eff	N	cut eff	N	cut eff
preCut0	651.67 ± 6.53	n/a	309.21 ± 3.14	n/a	154.05 ± 1.56	n/a	83.07 ± 0.83	n/a	45.24 ± 0.45	n/a	24.98 ± 0.25	n/a	13.90 ± 0.17	n/a	8.27 ± 0.10	n/a
preCut1	583.08 ± 5.87	89.48%	276.71 ± 2.82	89.49%	137.96 ± 1.41	89.55%	74.39 ± 0.75	89.55%	40.47 ± 0.41	89.44%	22.33 ± 0.23	89.36%	12.67 ± 0.16	91.17%	7.54 ± 0.09	91.15%
preCut2	287.78 ± 4.14	49.35%	182.75 ± 2.30	66.04%	108.53 ± 1.25	78.67%	63.68 ± 0.69	85.60%	36.95 ± 0.39	91.31%	20.95 ± 0.22	93.83%	12.18 ± 0.16	96.16%	7.35 ± 0.09	97.45%
preCut3 CH1	19.87 ± 1.07	6.91%	13.17 ± 0.61	7.21%	8.89 ± 0.36	8.20%	6.98 ± 0.23	10.96%	4.91 ± 0.14	13.28%	3.59 ± 0.09	17.14%	2.33 ± 0.07	19.10%	1.65 ± 0.04	22.43%
Cut0 CH1	8.64 ± 0.72	43.49%	7.01 ± 0.45	53.20%	5.10 ± 0.27	57.35%	4.20 ± 0.18	60.15%	3.25 ± 0.12	66.25%	2.43 ± 0.07	67.62%	1.68 ± 0.06	72.33%	1.21 ± 0.04	73.62%
Cut1 CH1	5.87 ± 0.59	67.89%	5.42 ± 0.39	77.33%	3.98 ± 0.24	78.09%	3.43 ± 0.16	81.65%	2.71 ± 0.11	83.41%	2.01 ± 0.07	82.97%	1.44 ± 0.05	85.57%	1.06 ± 0.04	87.46%
Cut2 CH1	3.81 ± 0.47	64.95%	4.01 ± 0.34	74.02%	3.33 ± 0.22	83.66%	2.76 ± 0.15	80.62%	2.20 ± 0.09	80.99%	1.64 ± 0.06	81.31%	1.13 ± 0.05	78.41%	0.84 ± 0.03	79.29%
Cut3 CH1	2.03 ± 0.34	53.35%	2.37 ± 0.26	59.04%	2.28 ± 0.18	68.35%	1.82 ± 0.12	65.76%	1.52 ± 0.08	69.37%	1.14 ± 0.05	69.87%	0.82 ± 0.04	72.51%	0.63 ± 0.03	74.45%

Table A.4: Cutflow and cut rejection efficiency for background samples in the electron (top) and muon (bottom) CHANNEL 2.

	$t\bar{t}$		QCDele		Wjets		Zjets		singleTop		Dibosons	
	N	cut eff	N	cut eff	N	cut eff	N	cut eff	N	cut eff	N	cut eff
preCut0	33969.01 ± 41.59	n/a	13687.08 ± 158.88	n/a	57502.16 ± 196.77	n/a	7834.97 ± 49.65	n/a	4085.26 ± 18.29	n/a	1171.46 ± 6.22	n/a
preCut1	28013.89 ± 34.85	17.53%	17637.01 ± 415.94	-28.86%	6748.04 ± 42.30	88.26%	704.77 ± 7.98	91.00%	3010.24 ± 13.72	26.31%	186.45 ± 1.52	84.08%
preCut2	753.95 ± 6.10	97.31%	17715.22 ± 2006.49	-0.44%	258.70 ± 7.86	96.17%	37.37 ± 1.98	94.70%	91.83 ± 2.66	96.95%	3.42 ± 0.21	98.17%
preCut3 CH2	720.19 ± 5.95	4.48%	158.03 ± 17.90	99.11%	253.09 ± 7.79	2.17%	35.88 ± 1.94	3.97%	86.88 ± 2.59	5.40%	3.21 ± 0.21	6.11%
preCut4 CH2	631.28 ± 5.66	12.35%	305.81 ± 34.43	-93.52%	164.42 ± 6.47	35.04%	26.48 ± 1.66	26.19%	62.77 ± 2.32	27.75%	1.77 ± 0.16	44.95%
preCut5 CH2	175.31 ± 3.04	72.23%	348.50 ± 70.73	-13.96%	18.83 ± 2.15	88.55%	3.86 ± 0.68	85.44%	15.76 ± 1.20	74.90%	0.31 ± 0.07	82.58%
Cut0 CH2	48.49 ± 1.59	72.34%	359.46 ± 141.88	-3.14%	4.67 ± 1.13	75.19%	0.71 ± 0.29	81.52%	4.54 ± 0.67	71.19%	0.05 ± 0.03	82.42%
Cut1 CH2	37.09 ± 1.37	23.50%	365.39 ± 218.23	-1.65%	2.51 ± 0.78	46.21%	0.09 ± 0.04	87.68%	3.08 ± 0.49	32.03%	0.05 ± 0.03	12.22%
Cut2 CH2	8.71 ± 0.70	76.52%	367.07 ± 444.88	-0.46%	1.25 ± 0.49	50.12%	0.07 ± 0.04	24.82%	1.53 ± 0.34	50.50%	0.05 ± 0.03	3.26%
Cut3 CH2	1.63 ± 0.31	81.25%	370.47 ± 205.89	-0.93%	0.80 ± 0.39	36.40%	0.03 ± 0.02	60.02%	0.33 ± 0.15	78.08%	0.03 ± 0.03	32.19%

	$t\bar{t}$		QCDmu		Wjets		Zjets		singleTop		dibosons	
	N	cut eff	N	cut eff	N	cut eff	N	cut eff	N	cut eff	N	cut eff
preCut0	52604.36 ± 51.85	n/a	26834.38 ± 83.28	n/a	118518.36 ± 291.43	n/a	10266.57 ± 73.48	n/a	6647.83 ± 23.01	n/a	2060.70 ± 8.30	n/a
preCut1	43972.62 ± 43.96	16.41%	6894.25 ± 35.19	74.31%	14318.14 ± 66.89	87.92%	1590.53 ± 14.57	84.51%	5003.20 ± 17.60	24.74%	438.83 ± 2.26	78.70%
preCut2	900.24 ± 6.73	97.95%	41.34 ± 2.76	99.40%	384.58 ± 12.14	97.31%	42.83 ± 2.44	97.31%	102.15 ± 2.82	97.96%	4.78 ± 0.24	98.91%
preCut3 CH2	860.09 ± 6.57	4.46%	38.39 ± 2.67	7.13%	372.24 ± 12.00	3.21%	41.35 ± 2.41	3.45%	96.22 ± 2.71	5.81%	4.65 ± 0.24	2.66%
preCut4 CH2	761.54 ± 6.27	11.46%	29.14 ± 2.34	24.09%	243.77 ± 8.46	34.51%	29.40 ± 2.08	28.91%	69.31 ± 2.42	27.96%	2.10 ± 0.15	54.86%
preCut5 CH2	219.87 ± 3.40	71.13%	7.05 ± 1.17	75.82%	31.01 ± 3.12	87.28%	4.55 ± 0.90	84.51%	16.96 ± 1.26	75.53%	0.38 ± 0.06	82.08%
Cut0 CH2	66.50 ± 1.80	69.76%	1.47 ± 0.56	79.09%	3.88 ± 1.24	87.48%	0.93 ± 0.28	79.66%	5.59 ± 0.70	67.05%	0.04 ± 0.03	89.50%
Cut1 CH2	43.94 ± 1.44	33.92%	0.56 ± 0.38	61.89%	1.56 ± 0.58	59.75%	0.29 ± 0.14	68.62%	2.50 ± 0.48	55.24%	0.03 ± 0.03	12.70%
Cut2 CH2	9.52 ± 0.75	78.33%	0.18 ± 0.23	67.72%	1.14 ± 0.47	26.90%	0.21 ± 0.13	27.91%	1.21 ± 0.36	51.59%	0.03 ± 0.03	0.00%
Cut3 CH2	2.06 ± 0.34	78.35%	0.15 ± 0.18	16.91%	0.90 ± 0.43	20.77%	0.17 ± 0.13	19.53%	0.26 ± 0.12	78.91%	0.01 ± 0.01	72.07%

Table A.5: Cutflow and cut efficiency for signal samples in the electron (top) and muon (bottom) CHANNEL 2.

	$u_4\bar{u}_4400$		$u_4\bar{u}_4450$		$u_4\bar{u}_4500$		$u_4\bar{u}_4550$		$u_4\bar{u}_4600$		$u_4\bar{u}_4650$		$u_4\bar{u}_4700$		$u_4\bar{u}_4750$	
	N	cut eff	N	cut eff	N	cut eff	N	cut eff	N	cut eff	N	cut eff	N	cut eff	N	cut eff
preCut0	562.58 ± 6.07	n/a	281.23 ± 3.00	n/a	143.69 ± 1.51	n/a	77.69 ± 0.81	n/a	43.64 ± 0.45	n/a	24.30 ± 0.25	n/a	14.03 ± 0.17	n/a	8.11 ± 0.10	n/a
preCut1	504.73 ± 5.48	89.72%	252.97 ± 2.71	89.95%	129.81 ± 1.37	90.34%	70.47 ± 0.73	90.71%	39.54 ± 0.41	90.61%	22.07 ± 0.23	90.85%	12.78 ± 0.16	91.08%	7.39 ± 0.09	91.16%
preCut2	259.24 ± 3.94	51.36%	174.52 ± 2.27	68.99%	104.79 ± 1.23	80.73%	62.01 ± 0.69	88.00%	36.56 ± 0.39	92.45%	21.08 ± 0.22	95.49%	12.35 ± 0.16	96.64%	7.22 ± 0.09	97.67%
preCut3 CH2	244.54 ± 3.83	94.33%	161.07 ± 2.18	92.30%	95.13 ± 1.17	90.78%	55.10 ± 0.65	88.85%	31.56 ± 0.36	86.34%	17.50 ± 0.20	83.01%	9.94 ± 0.14	80.45%	5.63 ± 0.08	77.97%
preCut4 CH2	216.23 ± 3.62	88.42%	141.26 ± 2.05	87.70%	82.54 ± 1.10	86.77%	47.72 ± 0.61	86.60%	27.18 ± 0.34	86.10%	15.02 ± 0.19	85.87%	8.56 ± 0.13	86.14%	4.78 ± 0.08	84.89%
preCut5 CH2	76.21 ± 2.16	35.24%	53.07 ± 1.26	37.57%	33.53 ± 0.70	40.63%	20.22 ± 0.40	42.38%	11.90 ± 0.22	43.79%	6.67 ± 0.13	44.40%	4.01 ± 0.09	46.78%	2.15 ± 0.05	45.06%
Cut0 CH2	42.21 ± 1.60	55.38%	33.10 ± 0.99	62.37%	23.39 ± 0.59	69.76%	15.11 ± 0.35	74.74%	8.88 ± 0.19	74.64%	5.17 ± 0.11	77.46%	3.21 ± 0.08	80.13%	1.73 ± 0.05	80.42%
Cut1 CH2	33.30 ± 1.42	78.91%	27.96 ± 0.91	84.46%	20.08 ± 0.54	85.86%	13.28 ± 0.32	87.85%	7.92 ± 0.18	89.13%	4.62 ± 0.10	89.39%	2.86 ± 0.08	89.09%	1.57 ± 0.04	90.70%
Cut2 CH2	24.71 ± 1.22	74.20%	21.16 ± 0.79	75.69%	15.48 ± 0.48	77.09%	9.95 ± 0.28	74.93%	5.99 ± 0.16	75.65%	3.37 ± 0.09	72.88%	2.11 ± 0.07	73.80%	1.16 ± 0.04	73.90%
Cut3 CH2	17.10 ± 1.02	69.19%	15.79 ± 0.69	74.62%	11.68 ± 0.41	75.44%	7.95 ± 0.25	79.93%	4.92 ± 0.15	82.16%	2.71 ± 0.08	80.64%	1.77 ± 0.06	83.81%	0.99 ± 0.03	84.90%

	$u_4\bar{u}_4400$		$u_4\bar{u}_4450$		$u_4\bar{u}_4500$		$u_4\bar{u}_4550$		$u_4\bar{u}_4600$		$u_4\bar{u}_4650$		$u_4\bar{u}_4700$		$u_4\bar{u}_4750$	
	N	cut eff	N	cut eff	N	cut eff	N	cut eff	N	cut eff	N	cut eff	N	cut eff	N	cut eff
preCut0	651.67 ± 6.53	n/a	309.21 ± 3.14	n/a	154.05 ± 1.56	n/a	83.07 ± 0.83	n/a	45.24 ± 0.45	n/a	24.98 ± 0.25	n/a	13.90 ± 0.17	n/a	8.27 ± 0.10	n/a
preCut1	583.08 ± 5.87	89.48%	276.71 ± 2.82	89.49%	137.96 ± 1.41	89.55%	74.39 ± 0.75	89.55%	40.47 ± 0.41	89.44%	22.33 ± 0.23	89.36%	12.67 ± 0.16	91.17%	7.54 ± 0.09	91.15%
preCut2	287.78 ± 4.14	49.35%	182.75 ± 2.30	66.04%	108.53 ± 1.25	78.67%	63.68 ± 0.69	85.60%	36.95 ± 0.39	91.31%	20.95 ± 0.22	93.83%	12.18 ± 0.16	96.16%	7.35 ± 0.09	97.45%
preCut3 CH2	267.90 ± 4.00	93.09%	169.57 ± 2.21	92.79%	99.64 ± 1.20	91.80%	56.70 ± 0.65	89.04%	32.04 ± 0.36	86.72%	17.36 ± 0.20	82.86%	9.86 ± 0.14	80.90%	5.70 ± 0.08	77.57%
preCut4 CH2	238.38 ± 3.79	88.98%	148.83 ± 2.08	87.77%	87.03 ± 1.12	87.34%	49.63 ± 0.61	87.53%	27.87 ± 0.34	86.99%	15.10 ± 0.19	86.98%	8.55 ± 0.13	86.73%	4.89 ± 0.08	85.89%
preCut5 CH2	87.43 ± 2.31	36.68%	55.90 ± 1.29	37.56%	35.73 ± 0.73	41.06%	20.96 ± 0.40	42.22%	12.54 ± 0.23	45.00%	6.85 ± 0.13	45.39%	3.98 ± 0.09	46.59%	2.26 ± 0.05	46.14%
Cut0 CH2	50.28 ± 1.75	57.52%	35.74 ± 1.04	63.92%	24.86 ± 0.61	69.59%	15.24 ± 0.34	72.71%	9.44 ± 0.20	75.28%	5.43 ± 0.11	79.23%	3.19 ± 0.08	80.18%	1.80 ± 0.05	79.79%
Cut1 CH2	37.85 ± 1.52	75.27%	27.75 ± 0.91	77.64%	20.18 ± 0.55	81.16%	12.83 ± 0.31	84.20%	7.98 ± 0.18	84.57%	4.65 ± 0.11	85.57%	2.74 ± 0.07	85.90%	1.58 ± 0.04	87.44%
Cut2 CH2	28.72 ± 1.32	75.87%	21.43 ± 0.80	77.23%	15.32 ± 0.48	75.92%	9.70 ± 0.27	75.61%	6.02 ± 0.16	75.39%	3.50 ± 0.09	75.38%	2.03 ± 0.06	74.09%	1.16 ± 0.04	73.63%
Cut3 CH2	20.94 ± 1.12	72.90%	16.24 ± 0.70	75.79%	11.92 ± 0.42	77.79%	7.74 ± 0.24	79.80%	5.02 ± 0.14	83.35%	2.92 ± 0.08	83.30%	1.68 ± 0.06	82.91%	0.97 ± 0.03	84.00%

Appendix B

Data/MC comparisons in control regions

B.1 *e*-channel: $N_{jets} \geq 4$, $N_{\text{b-tags}} = 0$

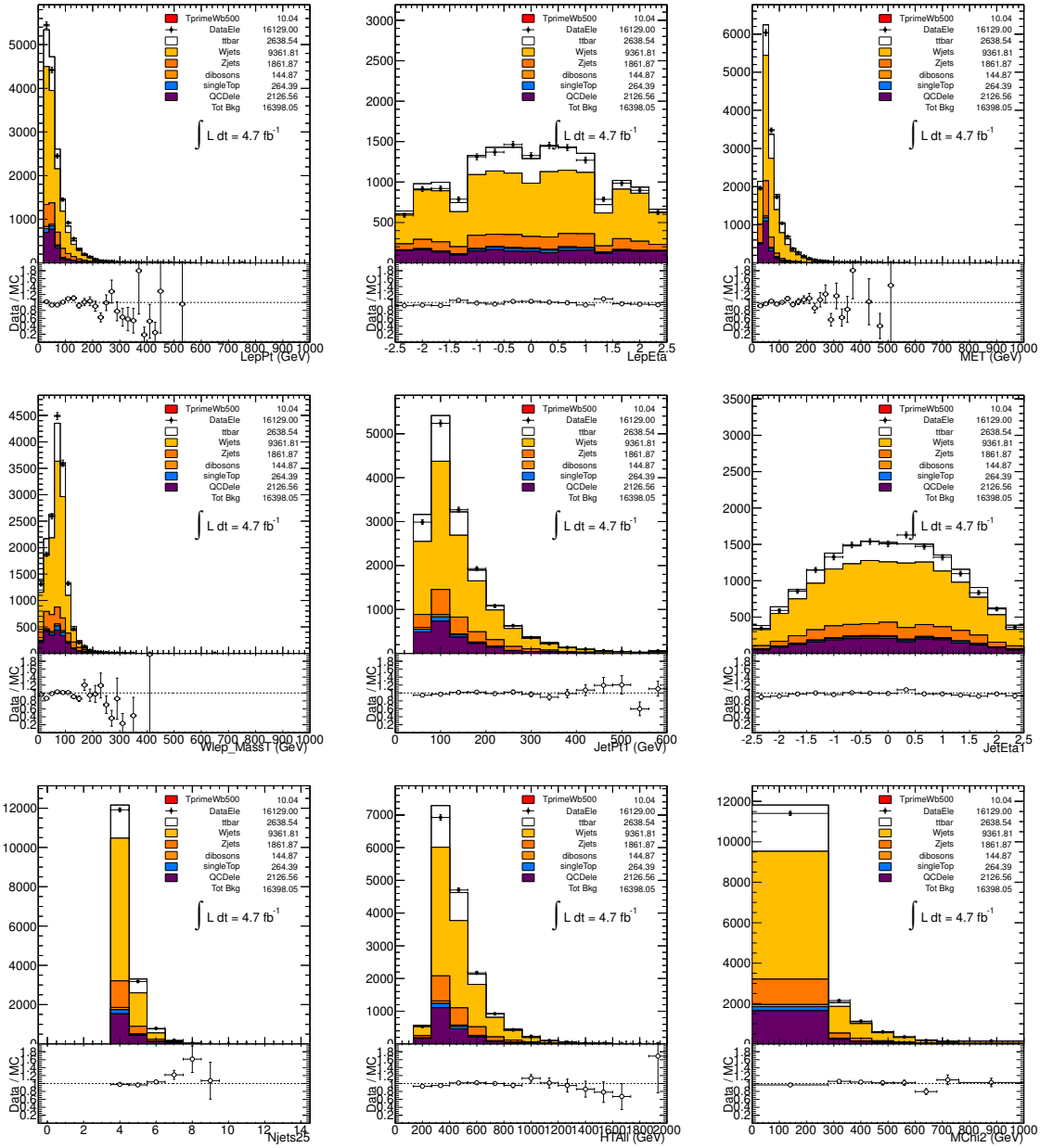

Figure B.1: Comparison between data and prediction for a number of kinematic variables in the *e*-channel, $N_{jets} \geq 4$, $N_{\text{b-tags}} = 0$ control region. From top to bottom and left to right, the variables displayed are: lepton p_T, lepton η, $E_{\text{T}}^{\text{miss}}$, leading jet p_T, leading jet η, H_T^4 and M_{reco}. Only statistical uncertainties are shown.

B.2 μ-channel: $N_{jets} \geq 4$, $N_{\text{b-tags}} = 0$

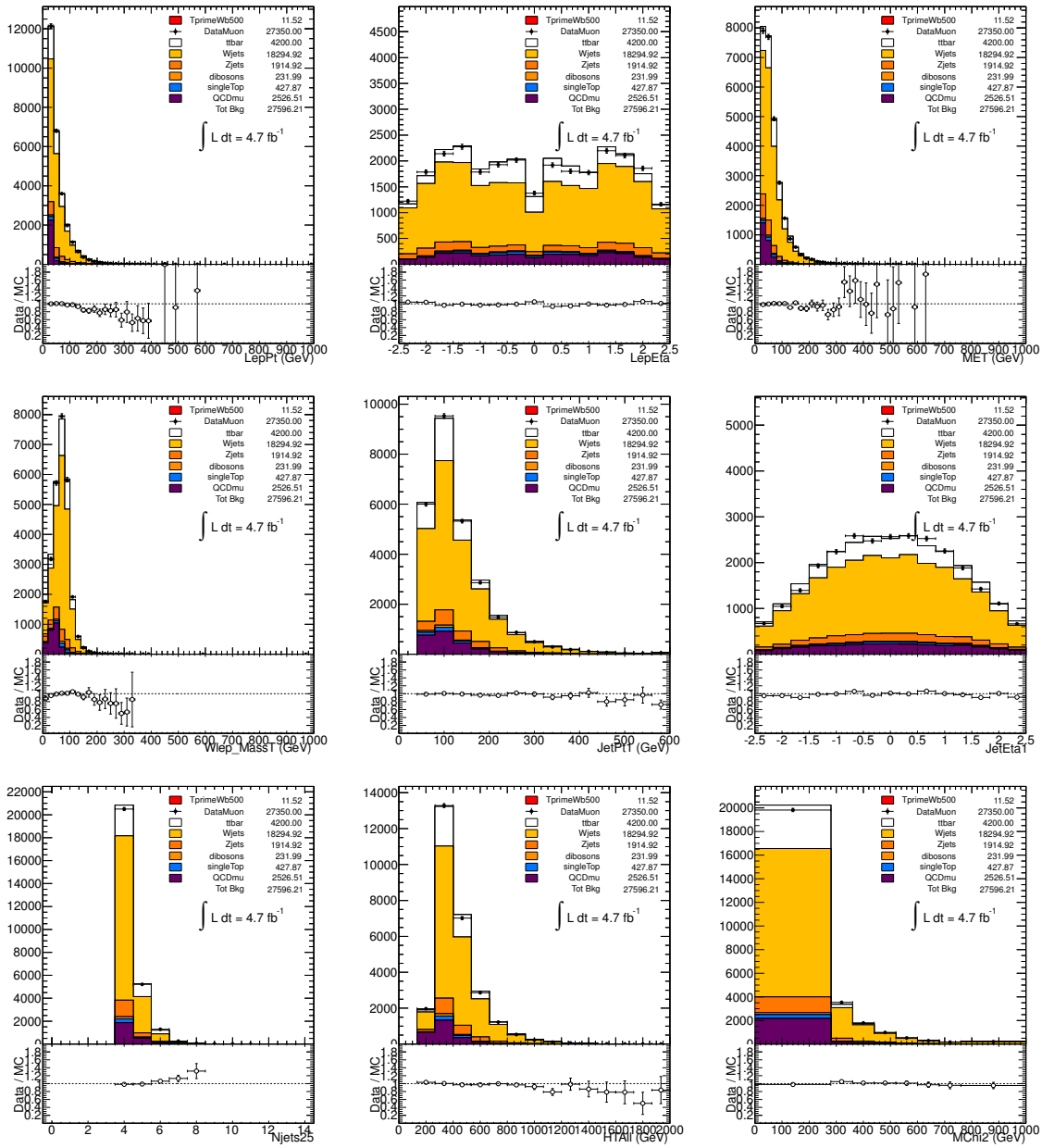

Figure B.2: Comparison between data and prediction for a number of kinematic variables in the μ-channel, $N_{jets} \geq 4$, $N_{\text{b-tags}} = 0$ control region. From top to bottom and left to right, the variables displayed are: lepton p_T, lepton η, $E_{\text{T}}^{\text{miss}}$, leading jet p_T, leading jet η, H_T^4 and M_{reco}. Only statistical uncertainties are shown.

B.3 *e*-channel: $N_{jets} \geq 4$, $N_{\text{b-tags}} \geq 1$, $H_T^4 < 700$ GeV

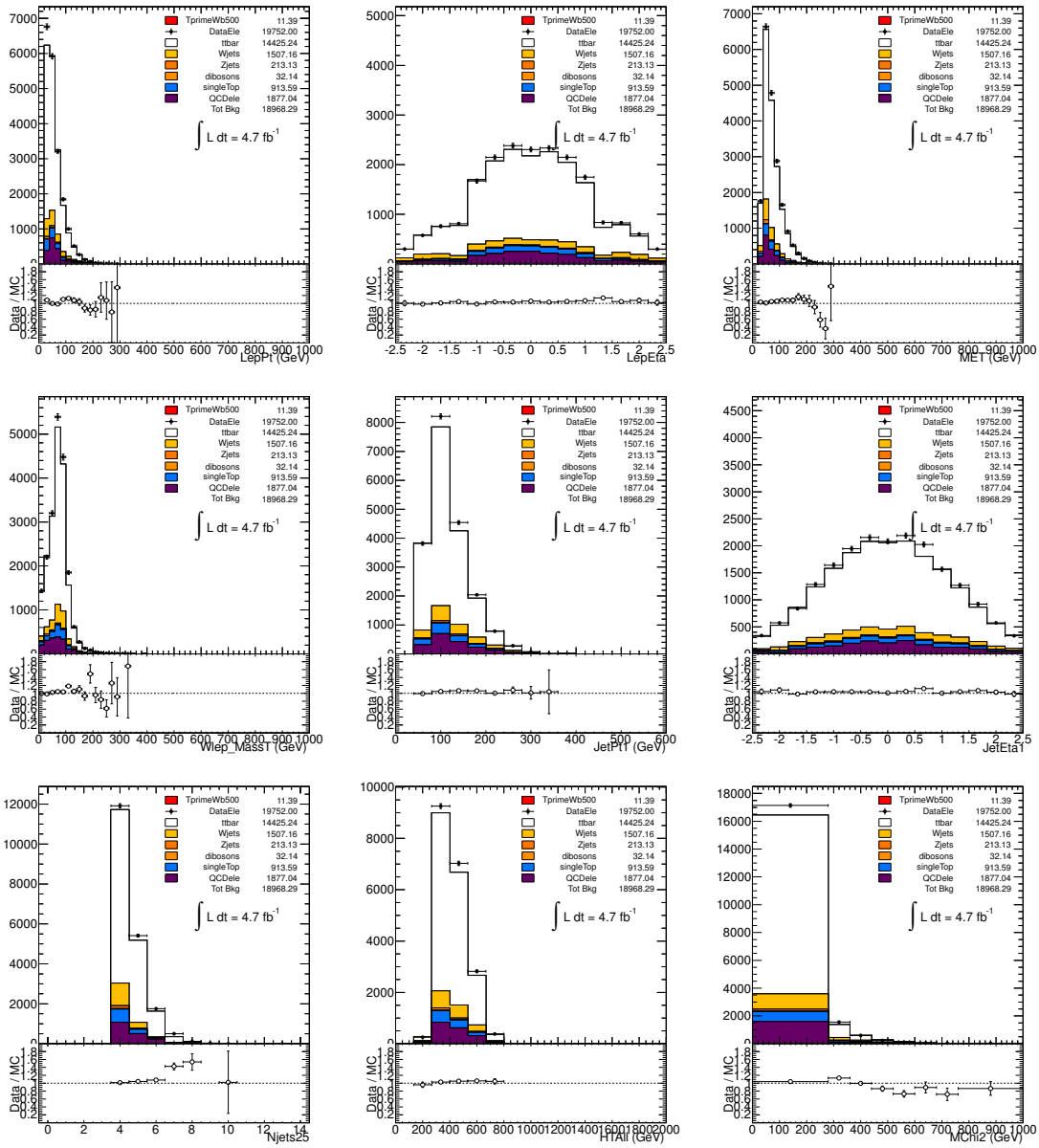

Figure B.3: Comparison between data and prediction for a number of variables in the *e*-channel, $N_{jets} \geq 4$, $N_{\text{b-tags}} \geq 1$, $H_T^4 < 700$ GeV control region. From top to bottom and left to right, the variables displayed are: p_T^{lepton}, η^{lepton}, $E_{\text{T}}^{\text{miss}}$, p_{TLJ}, η_{LJ}, H_T and M_{reco}. Only statistical uncertainties are shown.

B.4 μ-channel: $N_{jets} \geq 4$, $N_{\text{b-tags}} \geq 1$, $H_T^4 < 700$ GeV

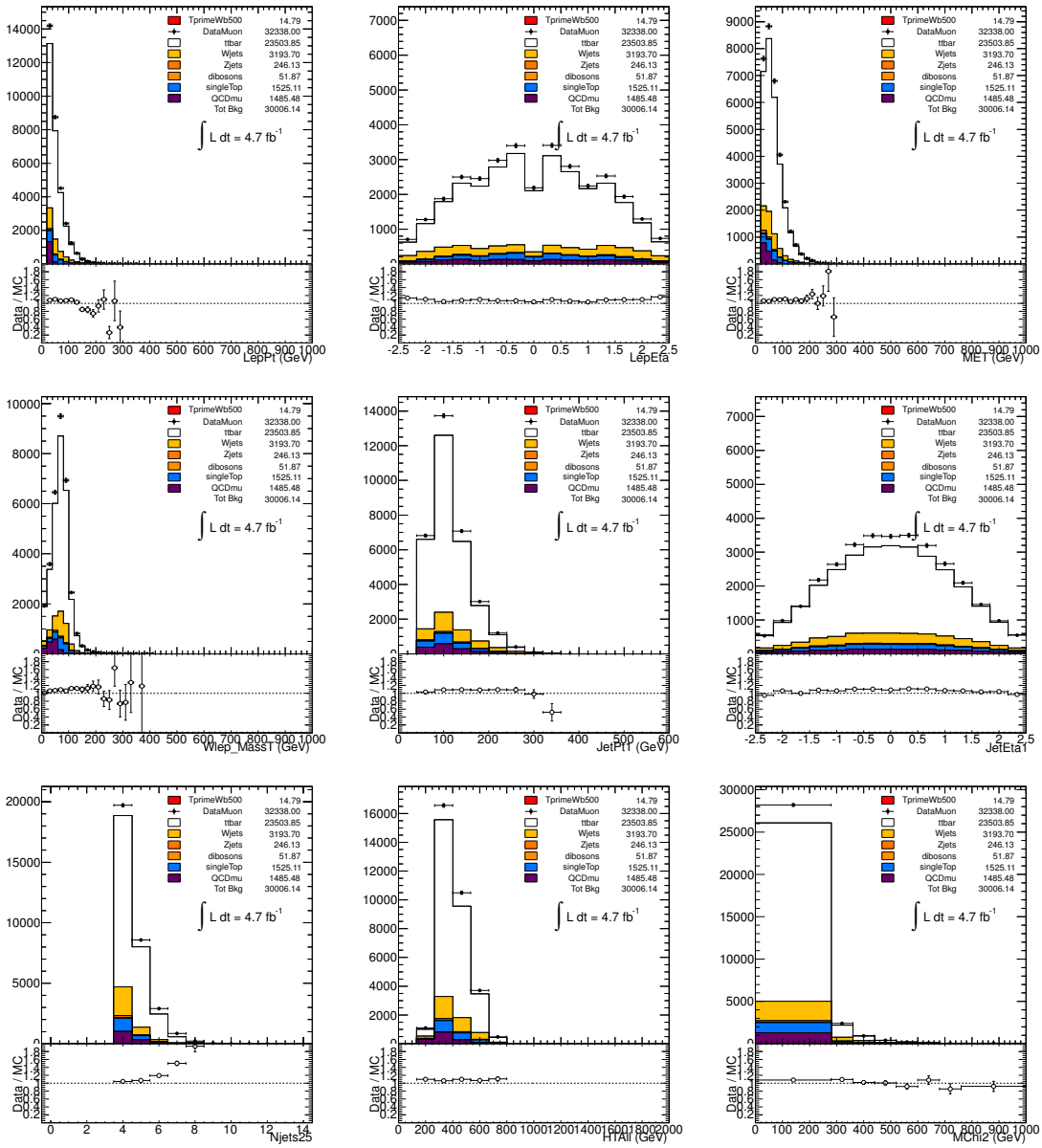

Figure B.4: Comparison between data and prediction for a number of variables in the μ-channel, $N_{jets} \geq 4$, $N_{\text{b-tags}} \geq 1$, $H_T^4 < 700$ GeV control region. From top to bottom and left to right, the variables displayed are: p_T^{lepton}, η^{lepton}, $E_{\text{T}}^{\text{miss}}$, p_{TLJ}, η_{LJ}, H_T and M_{reco}. Only statistical uncertainties are shown.

B.5 *e*-channel - Loose analysis - Reversing ΔR cuts

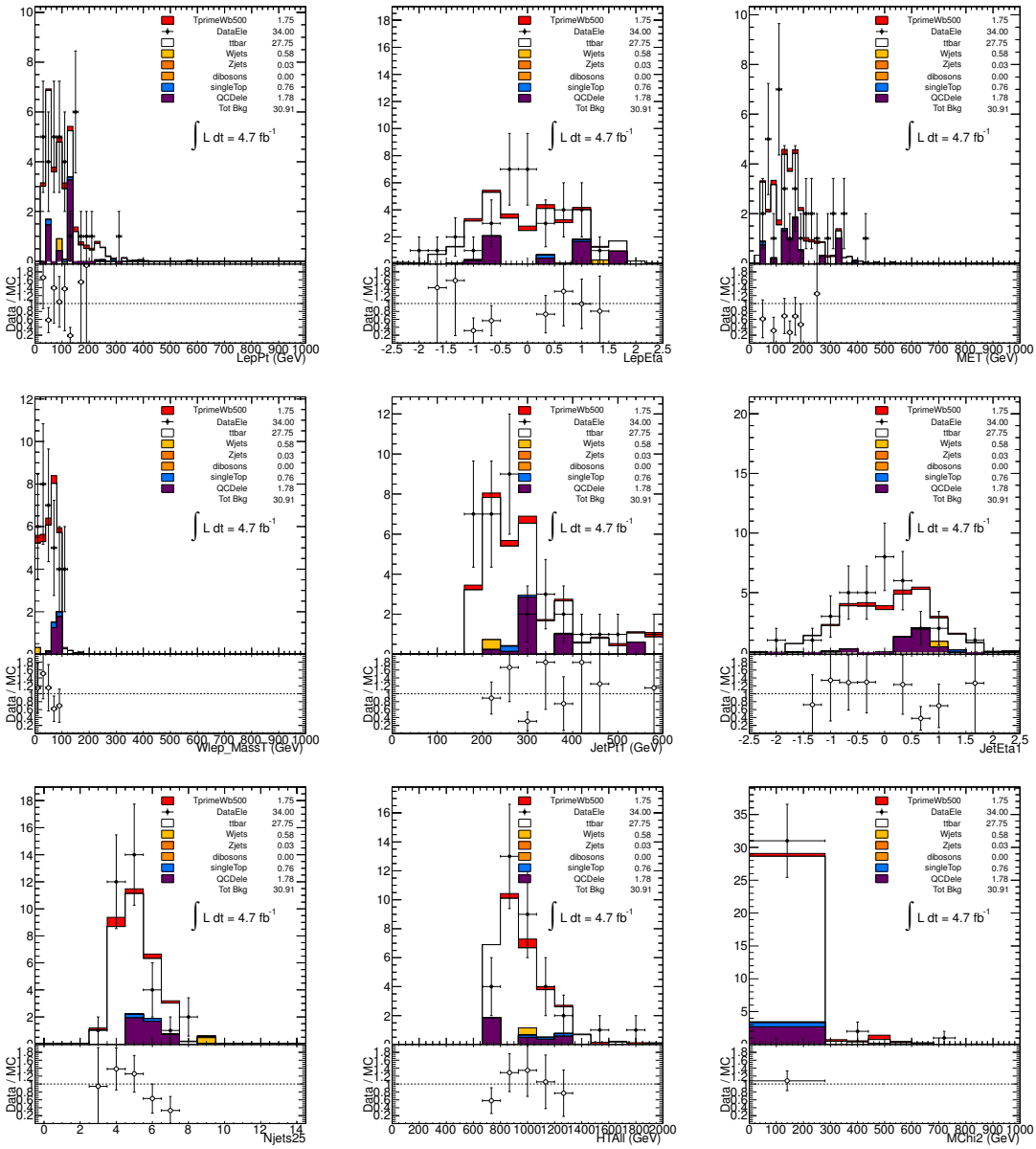

Figure B.5: Comparison between data and prediction for a number of kinematic variables in the *e* Loose Channel 1 and 2 combined, in the control region selected by adding inverted isolation cuts between the W_{had} and the *b* jets and between the lepton and the *b* jets ($\Delta R < 1.4$). From top to bottom and left to right, the variables displayed are: lepton p_T, lepton η, $E_{\text{T}}^{\text{miss}}$, leading jet p_T, leading jet η, H_T and M_{reco}. Only statistical uncertainties are shown.

B.6 μ-channel - Loose analysis - Reversing ΔR cuts

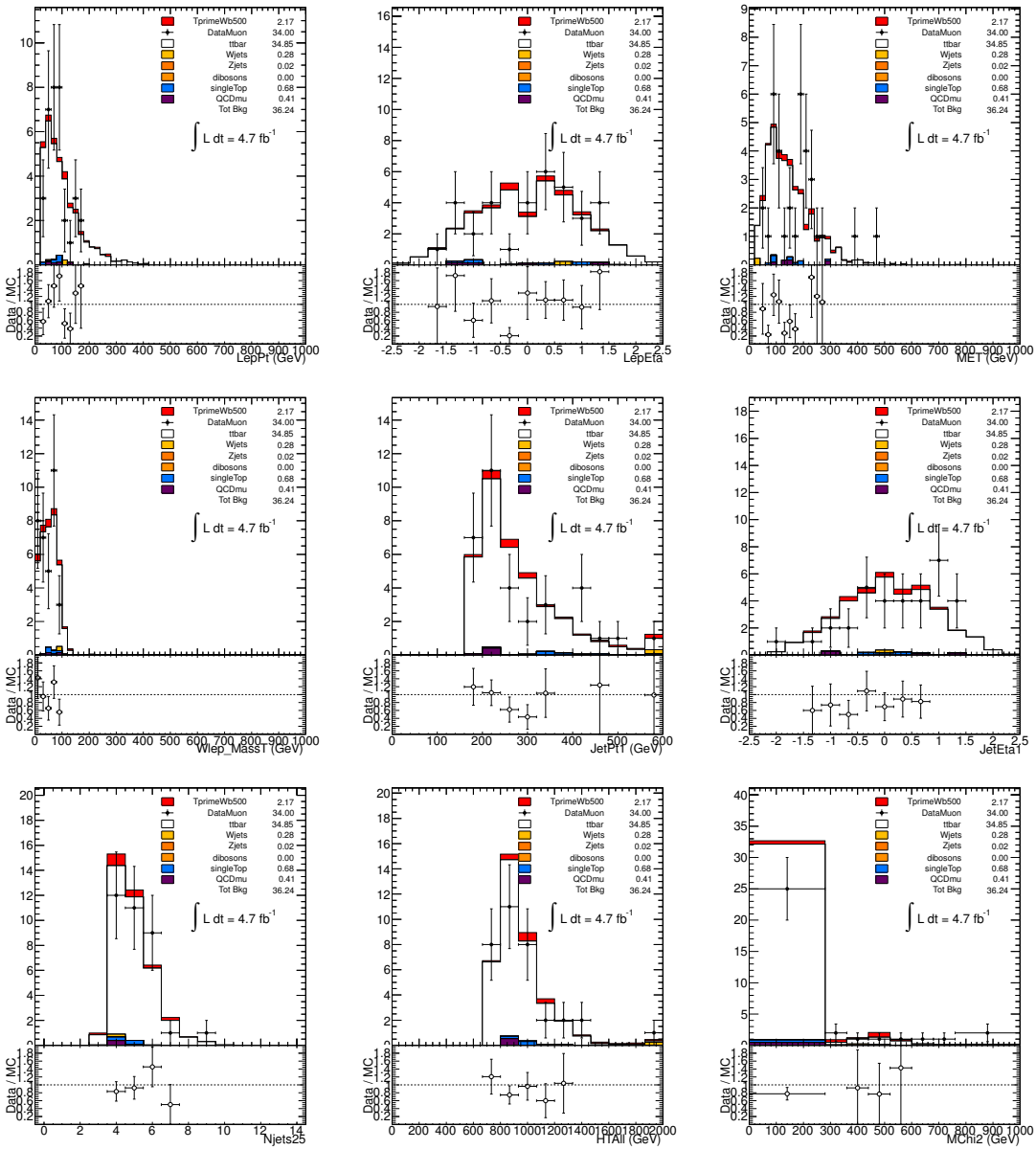

Figure B.6: Comparison between data and prediction for a number of kinematic variables in the μ Loose Channel 1 and 2 combined, in the control region selected by adding inverted isolation cuts between the W_{had} and the b jets and between the lepton and the b jets ($\Delta R < 1.4$). From top to bottom and left to right, the variables displayed are: lepton p_T, lepton η, $E_{\text{T}}^{\text{miss}}$, leading jet p_T, leading jet η, H_T and M_{reco}. Only statistical uncertainties are shown.

Appendix C

Systematics

Luminosity

The luminosity estimate has an uncertainty of 3.9% [151]. This systematic uncertainty is applied to the signal and all physics backgrounds modeled via the MC simulation (i.e. all processes but QCD multijet events).

C.1 Uncertainties on object definitions

Lepton identification and trigger

As seen previously, the reconstruction and identification efficiency of electrons and muons, as well as the efficiency of the trigger used to record the events, differ between data and MC. Scale factors are derived using tag-and-probe techniques on $Z \to \ell^+\ell^-$ ($\ell = e, \mu$) data and MC samples to correct for the simulation for these discrepancies. For each source of uncertainty, the quadratic sums of the statistical and systematic uncertainties on the corresponding scale factor is taken as the overall systematic uncertainty. For these uncertainties only the effect on acceptance for signal and backgrounds is considered. A total per-lepton uncertainty of 1.3% and 1.3% is taken for electrons and muons, respectively.

Jet vertex fraction efficiency

The per-jet efficiency to satisfy the $|JVF| > 0.75$ requirement is measured in $Z(\to \ell^+\ell^-)$+1-jet events in data and MC, selecting separately events enriched in hard-scatter jets and events enriched in pileup jets. Dedicated efficiency and inefficiency scale factors are measured separately for both type of jets. In particular, the efficiency SF for hard-scatter jets is larger than 1, decreasing from ~ 1.03 at $p_T = 25$ GeV to ~ 1.01 for $p_T > 150$ GeV. The product of all per-jet SFs define a per-event weight used to calibrate the MC to data. The effect on acceptance for signal and backgrounds of this uncertainty is 2.5–3.5%.

Jet energy scale

The jet energy scale and its uncertainty have been derived combining information from test-beam data, LHC collision data and simulation. The 'MultijetJESUncertaintyProvider' tool [152] can be used to access up to 16 individual uncertainty values corresponding to uncorrelated systematic sources.

This analysis is currently using a single JES systematic uncertainty, corresponding to the sum of quadrature of all sources. At the time of this work, studies were underway to determine whether this approximation is sufficient, which is expected to be the case because: (1) the JES uncertainty is not profiled, (2) this analysis is mostly focused on $p_T > 100$ GeV, which automatically limits the number of systematic sources which are relevant, and (3) treating all jets as correlated when varying their jet energies up and down should maximize the impact on acceptance and mass reconstruction, which makes this treatment conservative. A comparison of the total acceptance systematic on signal and $t\bar{t}$ background between the current treatment of a single JES uncertainty and the recommended breakdown into the 16 JES nuisance parameters has been conducted, and concluded that using one global parameter for JES is conservative.

The missing transverse energy is corrected according to the varied p_T of the jets in each event, by adding the original transverse energy of each jet and subtracting the varied one, weighted by the provided object weight. All jet-related kinematic variables are recomputed accordingly.

Jet energy resolution

The jet energy resolution (JER) has been derived based on data/MC studies using two in-situ techniques. The 'JERUncertaintyProvider' tool [153] was used to obtain the expected fractional p_T resolution for a given jet as a function of its p_T and rapidity. A systematic uncertainty is taken by smearing the jet energy by the shift in resolution provided by the tool and comparing to the nominal value in MC. The nominal value is used as the default in the analysis. This JER uncertainty is assumed to be fully correlated point-by-point.

In order to propagate the uncertainty in the p_T resolution, for each jet in MC a random number r is drawn from a Gaussian distribution with mean 0 and sigma equal to the difference in quadrature between the fractional p_T resolution with the tool and the nominal one. The jet 4-momentum is then scaled by a factor $1+r$. By definition, such uncertainty is one-sided (also termed as "up uncertainty"), since jets in MC cannot be under-smeared. We compute the normalization and shape uncertainties in the final discriminant and symmetry them to define a corresponding "down uncertainty".

Jet mass scale and resolution

The jet mass is used in one of the analysis channels (CHANNEL 1) to preselect the most energetic W bosons that have been reconstructed as single jets. Since this variable is only used to select one of the jets and is not used in other kinematic discriminants like the final reconstructed mass, the impact of uncertainties affecting the jet mass determination is deemed small but should nevertheless be taken into account.

The uncertainties affecting the jet mass have been extensively studied previously in Ref. [154]. The primary approach relies on in-situ comparison of the usual calorimeter-based jets with their track-based counterparts, and on several MC samples from different generators, various hadronic shower models and amounts of dead material. We are currently using the uncertainties stated in Ref. [154]: those have been derived for larger anti-k_t jets ($R = 1.0$)[1] . It is reasonable to think that those are conservative when applied to smaller $R = 0.4$ jets using the refined calibration from release 17. This is confirmed by preliminary results [156] obtained with release 17 and $R = 0.4$ anti-k_t jets, which show for instance that the uncertainty on the jet mass resolution is more likely to be 10% than the 20% we use.

[1] And in the so-called 'Release 16' reconstruction, the previous version of the current version we are using for our samples: 'Release 17'

For jets with $p_T < 400$ GeV (NB: our W-jets always fulfill $p_T > 250$ GeV as shown in Fig. 4.20(b) in section 4.7.3.1), the systematic on the jet mass scale (JMS) is taken to be 4.5%, while it is 6.0% for jets with $400 < p_T < 600$ GeV (table 18 of Ref. [154]). For jets with $p_T > 600$ GeV, the latter uncertainty of 6.0% is used as well. In all cases, an additional uncertainty of 1% is added in quadrature, to account for mis-modeling of additional (pile-up) interactions that is not fully covered by the previous JMS uncertainty, following the prescription used for the boosted top analysis in Ref. [155].

For the jet mass resolution (JMR), the uncertainty is taken to be 20%, regardless of the jet p_T (table 18 of Ref. [154]). The same symmetrization prescription described for the JER uncertainty is applied. The JMS and JMR are treated as uncorrelated with JES and JER.

Heavy- and light-flavor tagging

The effects of uncertainties in efficiencies for the heavy flavor tagging of jets by the MV1 tagger have been evaluated by applying the uncertainties on the scale factors described in Sec. 4.4.4.3.

These uncertainties are situated between 6% and 20% for b-jets, between 12% and 22% for c-jets, and $\sim 16\%$ for light jets. The scale factors and uncertainties are retrieved for each jet in MC depending on its flavor, p_T and η using the 'BTaggingCalibrationDataInterface' [157].

Of particular importance for this analysis is the extrapolation of the b and c tagging calibration to high-p_T jets (above 200 GeV). The current prescriptions for extrapolating the scale factors and uncertainties to high p_T are preliminary and based on an old study using the SV0 tagger (50%), which has the largest disagreement between data and MC compared to other taggers. Therefore, these uncertainties are expected to be quite conservative and should be improved in the final Rel17 recommendation. The preliminary recommendation implemented involves taking the last measured b-jet efficiency SF (bin 140-200 GeV) and adding the following errors in quadrature: 0.11 (200-300 GeV) and 0.12 (300-500 GeV). In the case of c jets, above 200 GeV the SF and the uncertainty from the 90-140 GeV bin is taken and the following errors are added in quadrature: 0.16 (200-300 GeV) and 0.17 (300-500 GeV).

The systematic uncertainty is taken uncorrelated between b, c jets, and light flavor jets. A per-jet weighting procedure [158] is applied to Monte Carlo to propagate the calibration of b-tagging and the related uncertainties.

C.2 Uncertainties on normalizations

Cross-sections

A $+9.9\%/-10.7\%$ uncertainty has been assumed on the inclusive $t\bar{t}$ production cross section evaluated at approximate NNLO using HATHOR[135]. A $+4.7\%/-3.7\%$ and 5% uncertainty has been assumed for the theoretical cross sections of the single top [160] and diboson [161] backgrounds, respectively.

The Z+jets cross sections from ALPGEN are affected by large uncertainties because they are a leading-order calculation. The inclusive Z+jets cross section is assigned a 4% uncertainty. Then, a 24% normalization uncertainty is assigned for each additional jet, added in quadrature. This prescription results in an uncertainty of 48% applied to events with ≥ 4 jets.

W+jets normalization

The overall W+jets normalization uncertainty results from the combination of uncertainties associated with data-driven methods used (see Sect. 4.5.3.1). An estimated uncertainty of 48% is assumed, corresponding to the Top group-recommended MC-based normalization uncertainty. Additional normalization uncertainties are assigned associated with the calibration factors for the $WQ\bar{Q}$ ($Q = b, c$) and W+light fractions as measured in W+2 jets data, as well as the MC-based extrapolation of uncertainties to higher jet multiplicity for the $WQ\bar{Q}$ and Wc fractions.

QCD normalization

The statistical uncertainty on the QCD multijet background estimate via the Matrix Method represents the largest uncertainty due to the limited statistics of the loose and tight (referring to the MM lepton definitions) samples after final selection, being larger than 100%. Systematic uncertainties originate from the difference between estimates obtained using different control regions and from the calibration of the method using simulated multijet events. The uncertainty assessed for the QCD multijet estimation is 50%.

C.3 Uncertainties on signal and background modeling

Signal modeling

The signal is modeled using PYTHIA, which is based on a leading-order matrix element interfaced to a parton shower. Previous studies [159] using a similar generator, AcerMC+ PYTHIA, have shown that this provides a reasonably accurate modeling of kinematic distributions in $t\bar{t}$ events, when compared to MC@NLO. The main exception is the p_T of the $t\bar{t}$ system where, as expected, not enough hard radiation from the initial state is provided by AcerMC+ PYTHIA.

To assess the systematic uncertainty on the ISR and FSR samples with modified PYTHIA parameters[2] in order to maximize (minimize) the amount of parton shower (PS) have been generated using the AFII simulation. In contrast with previous MC productions, in MC11 these alternative parameter choices are data-driven exploiting measurements such as the jet fraction in dileptonic $t\bar{t}$ events and jet shapes in QCD multijet events. For more details see Ref. [162]. The recommended prescription is to evaluate this systematic uncertainty as half the difference between the 'morePS' and 'lessPS' samples, and propagate the relative effect to the PYTHIA fully simulated signal sample. Since the only signal MC samples generated with these variations correspond to the 400, 500 and 600 GeV mass points, this uncertainty is considered as acceptance-only and interpolated for the 450, 550 and 650 GeV mass points.

$t\bar{t}$ modeling

The $t\bar{t}$ modeling uncertainties considered are: more/less PS, fragmentation and NLO vs matrix-element+parton-shower. These uncertainties are assessed by comparing different Monte Carlo generators.

More/less PS This uncertainty is estimated following the same prescription as discussed in Sect. C.3. In this case, the alternate AFII $t\bar{t}$ samples were generated using AcerMC.

[2] PARP(67), PARP(64) and PARP(72)

Fragmentation The effect of uncertainties on the parton shower simulation are studied comparing two different hadronization models applied to the same parton level generator (POWHEG): HERWIG and PYTHIA[3]. These two samples have been processed through the AFII simulation. The relative uncertainty between POWHEG/PYTHIA and POWHEG/HERWIG AFII samples is symmetrized and propagated to the MC@NLO fully simulated sample.

MC generator comparison The effect of uncertainties on the parton level modeling of $t\bar{t}$ is obtained by comparing the distributions from MC@NLO and from POWHEG+HERWIG. Both are NLO MCs interfaced to HERWIG, with differences in the details on how the NLO calculation is interfaced with the parton shower. These two samples have been processed through the AFII simulation. The relative uncertainty between POWHEG/HERWIG and MC@NLO AFII samples is symmetrized and propagated to the MC@NLO fully simulated sample.

[3]Pythia is based on the Lund string hadronization model. Herwig is based on a so-called 'cluster' model of hadronization.

Bibliography

Bibliography

[1] S. Glashow, *Partial-symmetries of weak interactions*, Nucl. Phys. 22, (1961) 579.

[2] A. Salam and J.C. Ward, *Electromagnetic and weak interactions*, Phys. Rev. Lett. 13, (1964) 168.

[3] S. Weinberg, *A model of leptons*, Phys. Rev. Lett. 19, (1967) 1264.

[4] S. Glashow, I. Iliopoulos and L. Maini, *Weak interactions with lepton-hadron symmetry*, Phys. Rev. D2, (1970) 1285.

[5] F. Englert and R. Brout, *Broken symmetry and the mass of gauge vector mesons*, Phys. Rev. Lett. 13 (1964) 321.

[6] P. W. Higgs, *Broken symmetries, massless particles and gauge fields*, Phys. Lett. 12 (1964) 132.

[7] P. W. Higgs, *Broken Symmetries and the Masses of Gauge Bosons*, Phys. Rev. Lett. 13 (1964) 508.

[8] G. S. Guralnik *et al.*, *Global Conservation Laws and Massless Particles*, Phys. Rev. Lett. 13 (1964) 585.

[9] P. W. Higgs, *Spontaneous Symmetry Breakdown without Massless Bosons*, Phys. Rev. 145 (1966) 1156.

[10] Gargamelle Neutrino Collaboration, *Observation of neutrino-like interactions without muon or electron in the Gargamelle neutrino experiment*, Phys. Lett. B 46, (1973) 138.

[11] G. Zweig, *An SU(3) Model for Strong Interaction Symmetry and its Breaking (I & II)*, CERN Report No.8182/TH.401 & CERN Report No.8419/TH.412(1964).

[12] M. Gell-Mann, *A Schematic Model of Baryons and Mesons*, Phys. Lett. 8 (3) (1964) 214-215.

[13] J.-E. Augustin *et al.*, *Discovery of a Narrow Resonance in e^+e^- Annihilation*, Phys. Rev. Lett. 33, 1406–1408 (1974).

[14] J.J. Aubert *et al.*, *Experimental Observation of a Heavy Particle J*, Phys. Rev. Lett. 33, 1404–1406 (1974).

[15] S.W. Herb *et al.*, *Observation of a Dimuon Resonance at 9.5 GeV in 400-GeV Proton-Nucleus Collisions*, Phys. Rev. Lett. 39, 252–255 (1977).

[16] UA1 Collaboration, *Experimental observation of isolated large transverse energy electrons with associated missing energy at $\sqrt{s} = 540$ GeV*, Phys. Lett. B 122 (1983) 103 .

[17] UA2 Collaboration, *Observation of single isolated electrons of high transverse momentum in events with missing transverse energy at the CERN $p\bar{p}$ collider*, Phys. Lett. B 122 (1983) 476.

[18] UA1 Collaboration, *Experimental observation of lepton pairs of invariant mass around 95 GeV/c^2 at the CERN SPS collider*, Phys. Lett. B 126 (1983) 398.

[19] UA2 Collaboration, *Evidence for $Z^0 \rightarrow e^+e^-$ at the CERN $p\bar{p}$ collider*, Phys. Lett. B 129 (1983) 130.

[20] N. Cabibbo, *Unitarity symmetry and leptonic decays*, Phys. Rev. Lett. 10, (1963) 531.

[21] M. Kobayashi and T. Maskawa, *CP violation in the renormalizable theory of weak interaction*, Prog. Theor. Phys. 49, (1973) 65.

[22] S. W. Herb *et al.*, *Observation of a Dimuon Resonance at 9.5 GeV in 400-GeV Proton-Nucleus Collisions*, Phys. Rev. Lett. 39, 252–255 (1977).

[23] J. Hagelin, MIU-THP-86-015, p1-55, Mod.Sci. & Vedic Sci.1: 29 (1986).

[24] M.E. Peskin, D.V. Schroeder (1995). An introduction to quantum field theory. Addison-Wesley.

[25] Super-Kamiokande Collaboration, *Measurements of the Solar Neutrino Flux from Super-Kamiokande's First 300 Days*, Phys. Rev. Lett. 81 (1998) 1158-1162; Erratum-ibid. 81 (1998) 4279 [hep-ex/9805021].

[26] CDF Collaboration, *Observation of top quark production in $p\bar{p}$ collisions*, Phys. Rev. Lett. 74 (1995) 2626.

[27] D0 Collaboration, *Observation of the top quark*, Phys. Rev. Lett. 74 (1995) 2632.

[28] ALEPH Collaboration, *Determination of the number of light neutrino species*, Phys. Lett. B 231 (4) 519-529 (1989).

[29] ALEPH, DELPHI, L3, OPAL, SLD Collaborations, LEP Electroweak Working Group, SLD Electroweak and Heavy Flavour Groups, *Precision Electroweak Measurements on the Z Resonance*, Phys. Rept. 427 : 257-454, 2006 [arXiv:hep-ex/0509008].

[30] http://map.gsfc.nasa.gov/universe/uni_matter.html

[31] L3 Collaboration, *Search for Heavy Neutral and Charged Leptons in e+ e- Annihilation at LEP*, Phys. Lett. B 517, 75-85 (2001) [arXiv:hep-ex/0107015].

[32] W.S. Hou, *Source of CP Violation for Baryon Asymmetry of the Universe*, Chin. J. Phys. 47 (2009) 134 [arXiv:0803.1234].

[33] K.M. Belotsky *et al.*, *Heavy neutrinos of 4th generation in searches for dark matter*, Gravitation & Cosmology, Vol. 11 (2005), No. 1–2 (41–42), pp. 16–26.

[34] M.Y. Khlopov, *Composite dark matter from 4th generation*, Pisma Zh. Eksp. Teor. Fiz. 83 (2006) 3-6 [arXiv:astro-ph/0511796].

[35] S. Sultansoy, *Flavor Democracy in Particle Physics*, AIPConf. Proc. 899, 49-52 (2007) [arXiv:hep-ph/0610279].

[36] B. Holdom *et al.*, *Four Statements about the Fourth Generation*, PMC Physics A 3 (2009) 4 [arXiv:0904.4698].

[37] CDF Collaboration, Phys. Rev. Lett. 100 (2008) 161802.

[38] D0 Collaboration, Phys. Rev. Lett. 101 (2008) 241801.

[39] S.A. Cetin, G.W.-S. Hou, V.E. Özcan, A.N. Rozanov, S. Sultansoy, *Status of the Fourth Generation*, (2011) [arXiv:1112.2907].

[40] O. Eberhardt *et al.*, *Joint analysis of Higgs decays and electroweak precision observables in the Standard Model with a sequential fourth generation*, (2012) [arXiv:1204.3872].

[41] CDF Collaboration, *Search for Heavy Top t' $\rightarrow Wq$ in Lepton Plus Jets Events in* $\int \mathscr{L} dt = 4.6 fb^{-1}$, (2010) [CDF Note 10110].

[42] D0 Collaboration, *Search for a Fourth Generation t' Quark in* $p\bar{p}$ *Collisions at* $\sqrt{s}$ *=1.96 TeV*, (2011) [Phys. Rev. Lett. 107, 082001 ; DOI: 10.1103/PhysRevLett.107.082001].

[43] ATLAS Collaboration, *Search for pair-produced heavy quarks decaying to Wq in the two-lepton channel at* $\sqrt{s} = 7$ *TeV with the ATLAS detector*, Phys. Rev. D 86 (2012) 012007 [arXiv:1202.3389].

[44] ATLAS Collaboration, *Search for pair production of a heavy quark decaying to a W boson and a b quark in the lepton+jets channel with the ATLAS detector*, (2012) [arXiv:1202.3076].

[45] CMS Collaboration, *Search for heavy, top-like quark pair production in the dilepton final state in pp collisions at* $\sqrt{s} = 7$ *TeV*, (2012) [arXiv:1203.5410].

[46] M.S. Chanowitz, M.A. Furman and I. Hinchliffe, *Weak interactions of ultra heavy fermions*, Phys. Letters 78 B, 2,3 (1978).

[47] J. Beringer *et al.*, (*Particle Data Group*), Phys. Rev. D86, 010001 (2012).

[48] Tevatron Electroweak Working Group [CDF and D0 Collaborations], arXiv:0801.1326.

[49] CMS Collaboration, Phys. Rev. Lett. 107, 091802 (2011) [arXiv:1106.3052].

[50] B. Pontecorvo, *Neutrino experiments and the question of leptonic-charge conservation*, Sov. Phys. JETP 26, 984 (1968).

[51] Z. Maki, M. Nakagawa and S. Sakata, *Remarks on the unified model of elementary particles*, Prog. Theor. Phys. 28, 870 (1962).

[52] ATLAS Collaboration, *Observation of a new particle in the search for the Standard Model Higgs boson with the ATLAS detector at the LHC*, Phys. Lett. B 716 (2012) 1-29 (2012), [arXiv:1207.7214].

[53] CMS Collaboration, *Observation of a new boson at a mass of 125 GeV with the CMS experiment at the LHC*, Phys. Lett. B 716 (2012) 30-61 (2012), [arXiv:1207.7235].

[54] A. Lenz, *Constraints on a fourth generation of fermions from Higgs boson searches*, Submitted to AHPE, (2012).

[55] M. Bobrowski *et al.*, *How much space is left for a new family?*, Phys. Rev. D 79, 113006 (2009) [arXiv:0902.4883].

[56] M. S. Chanowitz *et al.*, *Weak interactions of ultra heavy fermions (II)*, Nucl. Phys. B 153, 402 (1979).

[57] M. S. Chanowitz, *Bounding CKM Mixing with a Fourth Family*, Phys. Rev. D 79 (2009) 113008 [arXiv:0904.3570].

[58] C. Promberger, *The Fourth Generation: A Comprehensive Analysis*, PHD-thesis, TU Munich 2011; http://inspirehep.net/record/1122720/files/1078088.pdf

[59] M. Buchkremer *et al.*, *Closing in on a perturbative fourth generation*, April 2012 [arXiv:1204.5403].

[60] M. Maltoni *et al.*, *Extra quark-lepton generations and precision measurements*, Phys. Lett. B 476 (2000) 107 [hep-ph/9911535].

[61] V. A. Novikov *et al.*, *Extra generations and discrepancies of electroweak precision data*, Phys. Lett. B 529 (2002) 111-116 [hep-ph/0111028].

[62] V. A. Novikov *et al.*, *Mass of the higgs versus fourth generation masses*, JETP Lett. 76 (2002) 127-130; Pisma Zh. Eksp. Teor. Fiz. 76 (2002) 158-161 [hep-ph/0203132].

[63] A. N. Rozanov and M.I. Vysotsky, *Tevatron constraints on the Higgs boson mass in the fourth-generation fermion models revisited*, Phys. Lett. B 700, 313-315 (2011) [arXiv:1012.1483].

[64] ATLAS Collaboration, *Update of the Combination of Higgs Boson Searches in 1.0 to 2.3 fb^{-1} of pp Collisions Data Taken at $\sqrt{s} = 7$ TeV with the ATLAS Experiment at the LHC*, ATLAS-CONF-2011-135 (2011).

[65] CMS Collaboration, *Combined results of searches for a Higgs boson in the context of the standard model and beyond-standard models*, CMS PAS HIG-12-008 (2012).

[66] G. D. Kribs *et al.*, *Four Generations and Higgs Physics*, Phys. Rev. D 76, 075016 (2007) [arXiv:0706.3718].

[67] H. -J. He *et al.*, *Extra Families, Higgs Spectrum and Oblique Corrections*, Phys. Rev. D 64, 053004 (2001) [hep-ph/0102144].

[68] J. Alwall *et al.*, *Is Vtb=1 ?*, Eur.Phys.J. C49 (2007) 791-801 [arXiv:hep-ph/0607115].

[69] O. Eberhardt *et al.*, *Impact of a Higgs boson at a mass of 126 GeV on the standard model with three and four fermion generations*, [arXiv:1209.1101].

[70] P.Q. Hung and M. Sher, *Experimental constraints on fourth generation quark masses*, Phys. Rev. D 77, 037302 (2008) [arXiv:0711.4353].

[71] H. Murayama *et al.*, *Saving fourth generation and baryon number by living long*, Phys. Lett. B 705 208-211 (2011) [arXiv:1012.0338].

[72] N. Chen and H.J. He, *LHC Signatures of Two-Higgs-Doublets with Fourth Family*, JHEP 04 (2012) 062 [arXiv:1202.3072].

[73] R. Bates *et al.*, *An On-Line Acoustic Fluorocarbon Coolant Mixture Analyzer for the ATLAS Silicon Tracker*, IEEE Transactions on Nuclear Science, 59 5 2367-2374, October 2012.

[74] R. Bates *et al.*, *A combined ultrasonic flow meter and binary vapour mixture analyzer for the ATLAS silicon tracker*, Submitted to JINST, October 2012 [arXiv:1210.4835].

[75] R. Bates *et al.*, *Development of a custom on-line ultrasonic vapour analyzer/flowmeter for the ATLAS inner detector, with application to gaseous tracking and Cherenkov detectors*, Paper in preparation (2012).

[76] L. Evans and P. Bryant, *LHC machine*, JINST 3 (2008) S08001

[77] S. DÃ¼rr *et al.*, *Ab Initio Determination of Light Hadron Masses*, Science Vol. 322 no. 5905 pp. 1224-1227 (2008) [arXiv:0906.3599].

[78] ALICE Collaboration, *The ALICE Experiment at the CERN Large Hadron Collider*, JINST 3 (2008) S08002.

[79] ATLAS Collaboration, *The ATLAS Experiment at the CERN Large Hadron Collider*, JINST 3 (2008) S08003.

[80] CMS Collaboration, *The CMS Experiment at the CERN Large Hadron Collider*, JINST 3 (2008) S08004.

[81] LHCb Collaboration, *The LHCb Experiment at the CERN Large Hadron Collider*, JINST 3 (2008) S08005.

[82] ATLAS Collaboration, *Measurement of the Inelastic Proton-Proton Cross-Section at sqrts=7 TeV with the ATLAS Detector*, Nat. Commun. 2 (2011) 463, arXiv:1104.0326.

[83] Campbell, J., Huston, J., Stirling, J., *Hard interactions of quarks and gluons : a primer for LHC physics*, Rept. Prog. Phys. 70:89 (2007) [hep-ph/0611148]

[84] M. Paulini, *B Lifetimes, Mixing and CP Violation at CDF*, Int.J.Mod.Phys.A14:2791-2886 (1999), [arXiv:hep-ex/9903002].

[85] http://www.bw-grid.de/projekte/2012/05/11/monte-carlo-generator-for-the-lhc/

[86] http://www.borborigmi.org/2012/06/28/rivelatori-di-particelle-a-lhc-ottava-parte-spray-di-particelle-ovvero-come-si-vedono-quark-e-gluoni/

[87] M. Cardoso *et al.*, *Lattice QCD computation of the colour fields for the static hybrid quark-gluon-antiquark system, and microscopic study of the Casimir scaling*, Phys. Rev. D 81, 034504 (2010).

[88] http://cms.web.cern.ch/news/jets-cms-and-determination-their-energy-scale

[89] http://en.wikipedia.org/wiki/Radiation_length

[90] http://wlcg.web.cern.ch/

[91] N. Bousson, for the ATLAS Collaboration, Poster *ATLAS Upgrade Plans*, 105^{th} LHCC meeting, CERN. ATL-PHYS-SLIDE-2011-158 [https://cdsweb.cern.ch/record/1345765].

[92] G. Aad *et al.*, *ATLAS pixel detector electronics and sensors*, JINST 3, P07007 (2008).

[93] L. Rossi, P. Fischer, T. Rohe, N. Wermes, *Pixel Detectors, From Fundamentals to Applications*, Springer (2006).

[94] G. Hallewell *et al.*, *Properties of saturated fluorocarbons: Experimental data and modeling using perturbed-chain-SAFT*, Fluid Phase Equilibria, Volume 292, Issues 1-2, 25 May 2010, Pages 64-70.

[95] G. Hallewell *et al.*, *A sonar-based technique for the ratiometric determination of binary gas mixtures*, Nucl. Inst. and Meth. in Physics Research A264 (1988) 219-234.

[96] G. Hallewell, *Aspects of the use of saturated fluorocarbon fluids in high energy physics*, HDR, Université Aix-Marseille, CPPM-HDR-2011-001.

[97] J. Gross and G. Sadowski, *Perturbed-chain SAFT: An equation of state based on a perturbation theory for chain molecules*, Ind. Eng. Chem. Res. 40, 1244–1260 (2001).

[98] E. W. Lemmon, R Span, *Short Fundamental Equations of State for 20 Industrial Fluids*, J. Chem. Eng. Data, 2006, 51 (3), 785–850.

[99] B.E. Poling *et al.*, *The properties of Gases and Liquids*, fifth ed., McGraw-Hill Int. Editions, New York, 2001.

[100] M. Barbero *et al.*, *A new ATLAS pixel front-end IC for the upgraded LHC luminosity*, Nucl. Instrum. Meth. A 604 (2009) 397.

[101] M. Cacciari, G. P. Salam, and G. Soyez, The anti-k_t jet clustering algorithm, JHEP 04 (2008), arXiv:0802.1189v2 [hep-ph].

[102] ATLAS Collaboration, *Jet energy measurement with the ATLAS detector in proton-proton collisions at* $\sqrt{s} = 7$ *TeV*, CERN-PH-EP-2011-191 (2011) [arXiv:1112.6426].

[103] M. Capeans *et al.*, *ATLAS Insertable B-Layer Technical Design Report* CERN-LHCC-2010-013, ATLAS-TDR-019, CERN, Geneva (2010).

[104] D. Miller *et al.*, *Jet-Vertex Association Algorithm* ATL-COM-PHYS-2008-008

[105] L. Vacavant, *Etiquetage des quarks b par un détecteur de vertex à pixels dans l'expérience ATLAS auprès du LHC*, Thesis, Université de la Méditerranée - Aix-Marseille II (13/06/1997), Delpierre Pierre (Dir.).

[106] R. Zaidan, *Recherche du boson de Higgs chargé dans le canal* $H^+ \rightarrow tb$ *et étiquetage des jets b avec l'expérience ATLAS auprès LHC*, Thesis, Université de la Méditerranée - Aix-Marseille II (2009).

[107] C. Lapoire, *Mise en oeuvre de l'étiquetage des jets issus de quarks beaux dans l'expérience ATLAS au LHC*, Thesis, Université de la Méditerranée - Aix-Marseille II (2010).

[108] S. Aoun, *Mise en oeuvre du détecteur à pixels et mesure de la section efficace différentielle de production des jets issus de quarks beaux auprès de l'expérience ATLAS au LHC*, Thesis, Université de la Méditerranée - Aix-Marseille II (2011).

[109] N. Tannoury, *Calibration of the early b-tagging algorithms using the System8 method and measurement of the tt differential cross section as function of the $t\bar{t}$ mass and $t\bar{t}$ rapidity using 7 TeV p-p collisions with the ATLAS detector at the LHC*, Thesis, Université Aix-Marseille (2012).

[110] N.G. Piacquadio, *Identification of b-jets and investigation of the discovery potential of a Higgs boson in the $WH \to \ell\nu b\bar{b}$ channel with the ATLAS experiment.*, Thesis, Albert-Ludwigs-Universität Freiburg (2009).

[111] ATLAS Collaboration, *Performance of primary vertex reconstruction in pp collisions at $\sqrt{s} = 7$ TeV in the ATLAS experiment*, ATLAS-CONF-2010-069 (2010).

[112] T. Cornelissen *et al.*, *Concepts, Design and Implementation of the ATLAS New Tracking (NEWT)*, Tech. Rep. ATL-SOFT-PUB-2007-007, CERN, Geneva (2007).

[113] C. Amsler et al. (Particle Data Group), Physics Letters B 667, 1 (2008), Section 27.3.: *Multiple scattering through small angles*.

[114] D. Grandjean, G. Gaycken, *Impact Parameter Resolution Studies*, ECFA Workshop Durham September 2004.

[115] F. James, Statistical Methods in Experimental Physics, 2nd Edition, World Scientific Publishing (2006).

[116] ATLAS Collaboration, *Charged-track multiplicities in pp interactions at $\sqrt{s} = 900$ GeV*, ATL-STDM-2010-001, (2010).

[117] M. Frank and D. Brown, Tagging B hadrons using track impact parameters, ALEPH 92-135.

[118] ATLAS Collaboration, *Tracking studies for b-tagging in 900 GeV collision data with the ATLAS detector*, ATLAS-CONF-2010-003, http://cdsweb.cern.ch/record/1273190 (2010).

[119] ATLAS Collaboration, *Performance of the ATLAS secondary vertex b-tagging algorithm in 7 TeV collision data*, ATLAS-CONF-2010-042 (2010).

[120] ATLAS Collaboration, *Tracking Studies for b-tagging with 7 TeV Collision Data with the ATLAS Detector*, ATLAS-CONF-2010-040 (2010).

[121] ATLAS Collaboration, *Tracking Studies for b-tagging with 7 TeV Collision Data with the ATLAS Detector*, ATLAS-CONF-2010-070.

[122] ATLAS Collaboration, *First look at the JetProb b-tagging algorithm in 900 GeV collision data*, ATLAS-CONF-2010-010 (2010).

[123] ATLAS Collaboration, *Performance of impact parameter-based b-tagging algorithms with the ATLAS detector using pp collisions at $\sqrt{s} = 7$ TeV*, ATLAS-CONF-2010-091 (2010).

[124] ATLAS Collaboration, *Commissioning of the ATLAS high-performance b-tagging algorithms in the 7 TeV collision data*, ATLAS-CONF-2011-102 (2011).

[125] N. Bousson, for the ATLAS Collaboration, Poster *ATLAS high-performance b-tagging algorithms*, EPS 2011, Grenoble, France, ATL-PHYS-SLIDE-2011-431 [https://cdsweb.cern.ch/record/1371932].

[126] G. Piacquadio, C. Weiser, *A new inclusive secondary vertex algorithm for b-jet tagging in ATLAS*, J.Phys.Conf.Ser. 119 032032 (2008).

[127] ATLAS Collaboration, *Calibrating the b-tag Efficiency and Mistag Rate in 35/pb of Data with the ATLAS Detector*, ATLAS-CONF-2011-089 (2011).

[128] ATLAS Collaboration, *Measurement of the b-tag Efficiency in a Sample of Jets Containing Muons with 5^{-1} of Data from the ATLAS Detector*, ATLAS-CONF-2012-043, March 2012.

[129] ATLAS Collaboration, *Measuring the b-tag efficiency in a $t\bar{t}$ sample with 4.7 fb^{-1} of data from the ATLAS detector*, ATLAS-CONF-2012-097, June 2012.

[130] ATLAS Collaboration, *Measurement of the Mistag Rate of b-tagging algorithms with 5 fb^{-1} of Data Collected by the ATLAS Detector*, ATLAS-CONF-2012-040, March 2012.

[131] ATLAS Collaboration, *Statistical combination of top quark pair production cross-section measurements using dilepton, single-lepton, and all hadronic final states at $\sqrt{s} = 7$ TeV with the ATLAS detector*, ATLAS-CONF-2012-024, March 2012.

[132] GEANT4 Collaboration, S. Agostinelli et al., *GEANT4: A simulation toolkit*, Nucl. Instrum. Meth. A506 (2003) 250.

[133] N. Bousson, for the ATLAS Collaboration, Poster *ATLAS New Heavy Quark Searches*, PLHC 2011, Perugia, Italy, Conference website: https://indico.cern.ch/conferenceDisplay.py?confId=141546, ATL-PHYS-SLIDE-2011-425 [https://cdsweb.cern.ch/record/1371924].

[134] N. Bousson, for the ATLAS Collaboration, Plenary talk *ATLAS Exotic Searches*, HCP-2011, Paris, France, Conference website: http://hcp2011.lpnhe.in2p3.fr/Indico.html, Talk: ATL-COM-PHYS-2011-1523 [https://cdsweb.cern.ch/record/1395560], Proceedings: ATL-PHYS-PROC-2012-024 [http://arxiv.org/abs/1201.5256].

[135] M. Aliev *et al.*, *HATHOR - Hadronic top and heavy quarks cross section calculator*, Comput. Phys. Commun. bf 182, 1034 (2011).

[136] CMS Collaboration, CMS-PAS-EXO-11-051, http://cdsweb.cern.ch/record/1369546

[137] CMS Collaboration, CMS-PAS-EXO-11-036, http://cdsweb.cern.ch/record/1377864

[138] CMS Collaboration, *Search for the pair production of a top-like t' quark in events with a lepton and at least four jets in pp collisions at $\sqrt{s} = 7$ TeV*, Submitted to Phys. Lett. B. (2012) [arXiv:1209.0471].

[139] CMS Collaboration, *Search for heavy bottom-like quarks in 4.9 inverse femtobarns of pp collisions at $\sqrt{s} = 7$ TeV*, JHEP 05 (2012) 123, [arXiv:1204.1088].

[140] CMS Collaboration, *Combined search for the quarks of a sequential fourth generation*, Submitted to Phys. Rev. D (2012), [arXiv:1209.1062].

[141] B. Holdom, *Heavy Quarks and Electroweak Symmetry Breaking*, Phys. Rev. Lett. 57, 2496–2499 (1986).

[142] B. Holdom, *t' at the LHC: the physics of discovery*, JHEP 03 (2007) 063 [arXiv:hep-ph/0702037v3]

[143] B. Holdom, *The heavy quark search at the LHC*, JHEP 08 (2007) 069 [arXiv:0705.1736v1]

[144] B. Holdom, *Approaching a strong fourth family*, Phys.Lett. B 686 (2010) 146 [arXiv:1001.5321v2]

[145] B. Holdom, *Exotic versus strong*, (2011) [arXiv:1201.0074v1]

[146] D. Krohn *et al.*, *Jet Trimming*, JHEP 1002:084,2010 [arXiv:0912.1342]

[147] ATLAS Production TWiki:
https://twiki.cern.ch/twiki/bin/view/AtlasProtected/AtlasProductionGroup

[148] B. Abbott *et al.* (D0 Collaboration), Phys. Rev. D 61, 072001 (2000).

[149] B. Acharyia *et al.*, *Object selection and calibration, background estimations and MC samples for the Summer 2012 Top Quark analyses with 2011 data*, ATL-COM-PHYS-2012-1197 [https://cdsweb.cern.ch/record/1472525] (2012).

[150] TopFakes TWiki for ICHEP2012:
https://twiki.cern.ch/twiki/bin/viewauth/AtlasProtected/TopFakesICHEP2012

[151] ATLAS Collaboration, *Luminosity Determination in pp Collisions at sqrt(s) = 7 TeV using the ATLAS Detector in 2011*, ATL-CONF-2011-116.

[152] https://twiki.cern.ch/twiki/bin/viewauth/AtlasProtected/MultijetJESUncertaintyProvider
We are using tag JetUncertainties-00-05-07.

[153] https://twiki.cern.ch/twiki/bin/viewauth/AtlasProtected/JetEnergyResolutionProviderForPhysicsAnalysis
We are using tag JetResolution-01-00-00.

[154] R. Alon *et al.*, *Backup note for jet mass and substructures in QCD jets with the ATLAS experiment*, ATL-COM-PHYS-2011-1319.

[155] A. Arce *et al.*, *A Search for Resonances in Lepton+Jets $t\bar{t}$ Events with Highly Boosted Top Quarks in 2 fb^{-1} of pp Collisions at $\sqrt{s} = 7$ TeV, backup document*, ATL-COM-PHYS-2011-1692.

[156] D. Adams, K. Terashi, *JMS and JMR studies for anti-k_t jets with $R = 0.4$ in release 17*, https://indico.cern.ch/conferenceDisplay.py?confId=189874,
https://indico.cern.ch/getFile.py/access?contribId=10&sessionId=5&resId=1
&materialId=slides&confId=172364.

[157] https://twiki.cern.ch/twiki/bin/viewauth/AtlasProtected/BTaggingCalibrationDataInterface

[158] M. Bosman *et al.*, *Weighting method to propagate heavy-flavor tagging calibrations and related uncertainties*, ATL-COM-PHYS-2010-331.

[159] A. Shibata *et al.*, *Understanding Monte Carlo generators for Top physics*, ATL-COM-PHYS-2009-334.

[160] N. Kidonakis, Phys. Rev. D 83, 091503(R) (2011); N. Kidonakis, Phys. Rev. D 81, 054028 (2010); N. Kidonakis, Phys. Rev. D 83, 091503(R) (2011).

[161] ATLAS Collaboration, Eur. Phys. J. C 71, 1577 (2011) [arXiv:1012.1792v2 [hep-ex]].

[162] Liza Mijovic's talk at the MC Generator Group:
https://indico.cern.ch/getFile.py/access?contribId=2&resId=0&materialId=slides&confId=172994.

[163] T. Junk, *Confidence level computation for combining searches with small statistics*, Nucl. Instrum. Meth. A 434 (1999) 435-443; A. L. Read, *Modified Frequentist analysis of search results (the CL_s method)*, in F. James, L. Lyons and Y. Perrin (eds.), *Workshop on Confidence Limits*, CERN Report 2000-005.

[164] MCIMIT webpage:
http://www-cdf.fnal.gov/ trj/mclimit/production/mclimit.html

[165] W. Fisher, *Systematics and Limit Calculations*, (2006) FERMILAB-TM-2386-E.

[166] ATLAS Collaboration, *Expected performance of the ATLAS Detector, Trigger and Physics*, CERN-OPEN-2008-020, arXiv:0901.0512 (2009).

[167] *PYTHIA 6.4 physics and manual*, T. Sjöstrand, S. Mrenna and P. Skands, JHEP 0605 (2006) 026.

[168] *A Brief Introduction to PYTHIA 8.1.*, T. Sjostrand et al., CERN-LCGAPP-2007-04. LU TP 07-28. FERMILAB-PUB-07-512-CD-T (2007) [arXiv:0710.3820]

[169] A. D. Martin, W. J. Stirling, R. S. Thorne, and G. Watt, *Parton distributions for the LHC*, Eur. Phys. J. C63 (2009) 189, arXiv:hep-ph/0901.0002;
A. Sherstnev and R. S. Thorne, *Different PDF approximations useful for LO Monte Carlo generators*, arXiv:hep-ph/0807.2132.

[170] *PROTOS physics and manual*, J. A. Aguilar-Saavedra http://www-ftae.ugr.es/protos/

[171] J. A. Aguilar-Saavedra *Identifying top partners at LHC*, JHEP 11 (2009) 0911

[172] F. del Aguila, M. J. Bowick, Nucl. Phys. B 224 (1983) 107.

[173] R. Contino, R. Franceschini and M. Peskin, *A Module for Vectorlike Heavy Top Quarks*, www.lhcnewphysics.org/wiki/images/6/60/Tprime.pdf

[174] A. Sherstnev and R. S. Thorne, *Parton Distributions for LO Generators*, Eur. Phys. J. C 55 (2008) 553-575 [arXiv:0711.2473].

[175] M. Aliev, H. Lacker, U. Langenfeld, S. Moch, P. Uwer and M. Wiedermann, *HATHOR: HAdronic Top and Heavy quarks crOss section calculatoR*, Comput. Phys. Commun. 182 (2011) 1034-1046.

[176] P. M. Nadolsky et al., *Implications of CTEQ global analysis for collider observables*, Phys. Rev. D 78 (2008) 013004 [arXiv:0802.0007].

[177] Twiki page: The common parameters used for ATLAS MC production 2011. https://twiki.cern.ch/twiki/bin/viewauth/AtlasProtected/McProductionCommonParameters

[178] ATLAS Collaboration, *ATLAS tunes of Pythia 6 and Pythia 8 for mc11*, ATL-PHYS-PUB-2011-1493 (2011).

[179] b-tagging efficiency maps used are available here:
http://marwww.in2p3.fr/ vacavant/btagparam/effimaps_mv1_ttjx_v6e.root

[180] http://en.wikipedia.org/wiki/Systematic_error

[181] More information about the Vector-Like-Quarks production/validation can be found here:
https://twiki.cern.ch/twiki/bin/viewauth/AtlasProtected/VectorLikeTops

[182] ATLAS Collaboration, *Search for pair production of heavy top-like quarks decaying to a high-p_T W boson and a b quark in the lepton plus jets final state at $\sqrt{s} = 7$ TeV with the ATLAS detector*, Phys. Lett. B 718 (2013) 1284-1302 [arXiv:1210.5468].

Résumé

L'hypothèse d'une quatrième famille de *fermions* – les particules de *matière* décrites au sein du Modèle Standard (MS) de la physique des particules – est un des plus simples modèles de nouvelle physique encore non exclu et accessible au démarrage du Large Hadron Collider (LHC) – le plus puissant collisionneur hadronique au monde depuis 2009. Cette thèse s'intéresse à la production d'une paire de quarks t' se désintégrant chacun en un boson W et un quark b. La recherche se focalise sur le domaine des très hautes masses, où la production peut être distinguée de la production de bruit de fond d'une paire de quark top en exploitant la cinématique des produits de désintégration des collisions proton-proton produites au centre du détecteur ATLAS. Nous présentons une stratégie originale exploitant en particulier la collimation des produits de la désintégration des bosons W de très grande impulsion transverse, permettant leur reconstruction explicite. L'analyse s'appuie sur un travail de mise en oeuvre des algorithmes d'identification des jets résultants de la fragmentation des quarks de saveur b. Ces algorithmes se basent sur la reconstruction très précise de la trajectoire des particules chargées, des vertex d'interactions primaires et des vertex de désintégrations secondaires présents au sein des jets. L'étiquetage-b permet à l'expérience ATLAS d'améliorer la (re)découverte du MS, ainsi que la sensibilité à la nouvelle physique. Il sera ainsi d'une grande importance pour les futures années d'opération du LHC, raison pour laquelle nous présentons une étude de prospective de ses performances attendues avec l'extension du détecteur à *pixels* d'ATLAS – détecteur clé de l'étiquetage-b – dénommée *IBL* et actuellement en construction. Notre recherche de quark t' quant à elle a permis d'établir une limite inférieure à la masse du quark t' de 656 GeV à partir des 4.7 fb^{-1} de données 7 TeV collectées en 2011, ce qui est la meilleure limite à ce jour en recherche directe, avec également une interprétation dans le cadre du modèle de quarks dits 'vecteurs'.

Summary

The hypothesis of a fourth generation of *fermions* – the *matter* particles described in the Standard Model (SM) of particle physics – is one of the simplest model of new physics still not excluded and accessible at the start of the Large Hadron Collider (LHC) – the world most powerful hadron collider since 2009. We search for the pair production of up-type t' quarks decaying to a W boson and a b-quark. The search is optimized for the high quark mass regime, for which the production can be distinguished from the top background by exploiting kinematic features of the decay products arising from the proton-proton collisions occurring at the center of the ATLAS detector. We present a novel search strategy reconstructing explicitly very high-p_T W bosons from their collimated decay products. The analysis benefits from the commissioning of algorithms intended to identify jets stemming from the fragmentation of b-quarks. These algorithms are based on the precise reconstruction of the trajectory of charged particles, vertices of primary interaction and secondary vertices in jets. The b-tagging ability allows for ATLAS to improve the (re)discovery of the SM, and the sensibility to new physics. It will hence play an important role in the future of the LHC, the reason why we study the expected performance with an upgrade of the ATLAS *pixel* detector, called *IBL* and currently under construction. Our search of t' quark, using 4.7 fb^{-1} of the 7 TeV data collected in 2011, has resulted in the world most stringent limit, excluding t' masses below 656 GeV, with also an interpretation in the framework of vector-like quarks.